Midori E. Amano Patiño

Balliol College

University of Oxford



A thesis submitted to the

Board of the Faculty of Physical Sciences

in partial fulfilment of the requirements

for the degree of Doctor of Philosophy

Trinity Term 2016

Topochemical Manipulation of Some Complex Transition Metal Oxides

This thesis is comprised of three parts. The first part concerns the investigation of the topochemical reduction of $LaSrNiRuO_6$ in order to prepare $LaSrNiRuO_4$ via anion deintercalation. The second part discusses the oxide-for-hydride anion exchanges performed in $SrV_{1-x}Ti_xO_3$, and the resulting $SrV_{1-x}Ti_xO_{2-y}H_{1+y}$ reduction products. Finally, the results from redox-neutral topochemical cation exchange reactions conducted in the three-dimensional perovskite structure of $NaTaO_3$ are presented along with the characterisation of a novel product of composition $Ni_{0.5}TaO_3$.

The topochemical reduction of $LaSrNiRuO_6$ using CaH_2 was carried out to produce a novel extended oxide phase with composition $LaSrNiRuO_4$. This phase is composed of sheets of apex-linked $Ni^{1+}O_4$ and $Ru^{2+}O_4$ squares in a checkerboard ordered arrangement. To the best of our knowledge, this material is the first example of a B-cation ordered infinite-layer oxide phase. The low oxidation states of the transition-metal cations are confirmed by DFT calculations from which a spin moment S = ½ is determined for the nickel while the ruthenium centres adopt an intermediate-spin S = 1 configuration. $LaSrNiRuO_4$ behaves paramagnetically at room temperature. However, upon cooling ($T < 250$ K) a phase transition is observed in which the nickel spins interact ferromagnetically, while the ruthenium cations appear to undergo a change in spin configuration to a diamagnetic spin state. A possible explanation is given for this observation based on an ordered arrangement of local Jahn-Teller distortions.

While investigating the preparation of $LaSrNiRuO_4$, it was observed that different samples of the $LaSrNiRuO_6$ starting materials exhibited markedly different reactivity. The observed differing reactivity is inconsistent with the crystal structure and composition of the $LaSrNiRuO_6$ samples, from which all the materials are identical. Careful investigation of the X-ray diffraction data collected from the $LaSrNiRuO_6$ materials revealed that the reactivity of the samples is a consequence of the microstructure. By quenching or slow-cooling the materials during their synthesis, the size of the crystalline domains formed is affected and this in turn is observed to define the extent to which the topochemical deintercalation of oxide anions takes place. A mechanism to explain this effect is presented in which the greater 'plasticity' of small crystalline domains helps to limit the influence of lattice strain during the reaction.

Similar with the observations for the $LaSrNiRuO_6$ phases, it was found that the reactivity of $SrV_{0.95}Ti_{0.05}O_3$ samples towards topochemical oxide-for-hydride exchange is also determined by the characteristics of the starting materials. The cooling rate can lead to phase segregation in $SrV_{0.95}Ti_{0.05}O_3$ samples which in turn affects the reduction behaviour. A modification of the energy profile for the oxide-for-hydride exchange in $SrV_{1-x}Ti_xO_3$ phases is proposed on the basis of the electronic configuration that the transition-metal cations adopt upon reduction (d^2,V^{3+} and d^1,Ti^{3+}).

Finally, topochemical exchange reactions can also be carried out between cations in complex transition metal oxides when the mobility of the species to be exchanged is sufficiently greater with respect to the host lattice. The preparation of $Ni_{0.5}TaO_3$ from exchange of Na^+ by Ni^{2+} in $NaTaO_3$ represents a synthetic approach not yet widely explored in the long-standing challenge that the preparation of magnetoelectric multiferroic materials represents.

The topochemical reactions studied in this work highlight the possibility of directing and modifying the product phases, by tuning features of the reagents. This is in contrast with the limited control available in thermodynamic processes.

Declaration

The work described in this thesis was carried out at the Inorganic Chemistry Laboratory at the University of Oxford between October 2012 and October 2016 under the supervision of Dr. Michael A. Hayward. The work presented in this document is my own except where I have either given reference to a published source, or acknowledged help from a named person. This work has not been submitted by the author for any other degree at any other university.

Midori E. Amano Patiño

October 2016

To Susana and Noriko, in the memory of Esteban

Acknowledgements

First I would like to thank Prof. Michael Hayward for giving me the invaluable opportunity to come and work with him. The determination that he puts into his research is truly admirable. I learned much more than I could ever have imagined and feel lucky to have been the recipient of his seemingly inexhaustible knowledge of Chemistry during this DPhil.

I thank CONACYT and Balliol College (and generosity of Martin Foley-Béjar) for their scholarships. Special thanks goes to the Praefectus Prof. Thomas Melham for his unconditional support during these past months.

I also need to thank all the researchers who contributed to this work: Prof. P. Shiv Halasyamani with SHG activity measurements, Prof. John MacGrady and MSc Dihao Zeng with DFT calculations, Prof. Stephen Blundell with collection of μSR data, Dr. Robert Jacobs and Dr. Ashley Shepherd for their help at the SAF at the CRL, and the beam scientists Dr. Ron Smith and Dr. Emma Suard, with their help at ISIS, Diamond and the ILL, France.

Thanks to the MAH group. Each member that I've worked with has taught me something new. I thank the students (now Doctors) who received me when I arrived in the group, Dr. Fabio Denis and Dr. Kun Luo. Special thanks to Dr Fabio Denis who helped me so much when I was learning all the techniques and who didn't mind me for continuing to bug him even when he tried to escape to the other side of the world. In addition and in order of arrival, thanks to the DPhil students Miss Ronghuan Zhang with whom I have shared so much (madness) and who has given me invaluable support in the most demanding times. Thanks to the MChem Jacob Page (the glovebox chose you), Miss Lun Jin and MChem Nijat Hasanli who have been keen to learn and to help other students including myself. To Dr. Antonio and MSc. Eva for always being willing to help as well during their visit. Thanks to the part II students of years 2013-14, 14-15 and 15-16 for all that bad (but fun) football, for the (also bad but fun) bowling, for the much better (and delicious) baking contests.

I feel immensely lucky to have found myself surrounded by an amazing team of colleagues and friends. There are no words apt enough that I can think of to describe how meaningful and defining their support has been for the completion of this thesis. I would

really like to thank the SJC group for having (literally) opened a door for me (to their office). Thanks to Prof. Simon Clarke for this and special thanks to Dr. Danny Woodruff, Dr. Simon Cassidy and MChem. Jack Blandy for trying to solve all sorts of questions that I came up with and for sharing with me not only their time and resources (food, coffee, Lab-ware), but also their knowledge and their impressive collection of skills.

Thanks to the team that keeps the ICL running with instruments and workshops (I also bugged all of the following people): Dr. P. Wiseman for SQUIDs and X-ray diffractometers' matters, Mrs Terri Adams for glass-ware, Mr Nenad Vranjes for furnace matters (and tons of industrial wool), Chris and Jennie for allowing me to borrow stuff from the Teaching Labs that would save the day. Thanks to Jonathan, Dan, Martin and Dave for almost every other matter.

These acknowledgments would not be complete without expressing my admiration to the body of incredibly committed teachers at UNAM, Mexico, who make wonders with the amount of resources that they have and enable students to make it this far. Special thanks go to MSc. María Castellanos for sharing with me her passionate insight to Solid State Chemistry and Materials Sciences which defined my career. I also thank Prof. Raúl Valenzuela for practically taking me as a member of his group by constantly helping me and teaching me (as well as allowing me to participate in his group meetings and letting me into his students' office). Thanks to Prof. Israel Betancourt for his supervision during my bachelors research project which founded the roots for coming to Oxford.

Finally, I would like to thank all of those whom I believe also genuinely contributed with their help in this thesis by reading me, cooking a delicious meal for me so that I can keep going (or bringing food for me to the ICL), by working and studying next to me, advising me and solving problems even at indecent times during the night… In alphabetical order: Adán, Alex, Amit, Andrea, Andy, Ernesto (mi infalible camarada), Gaby, Jed, Johanna, Karen, Laia, Marisol (representando a todos "los Químicos"), Natasha (for supporting me and staying with me until the end).

Table of Contents

Topochemical Manipulation of Some Complex Transition Metal Oxides I

Declaration III

Acknowledgements VII

Table of Contents XI

Chapter 1

Introduction

1.1 Complex Transition Metal Oxides 1

1.1.1 Complex Transition Metal Oxides Adopting the Perovskite Structure 1

1.2 The Electronic Structure of Complex Transition Metal Oxides 6

1.2.1 The Goodenough-Kanamori Rules 10

1.3 Topochemical Manipulation 12

1.3.1 Low-Temperature Reductive Chemistry Using Binary Metal Hydrides 12

1.3.2 Cation Exchange Reactions 16

Chapter 2

Experimental Techniques

2.1 Syntheses of Starting Materials 19

2.1.1 Ceramic Methods 19

2.1.2 Citrate-gel Method 19

2.1.3 Arc-melt Furnace 20

2.2 Oxide Anion Deintercalations and Oxide-Hydride Anion Exchanges 21

2.2.1 Reactions with CaH_2 in sealed tubes 22

2.2.2 Pressure Venting Apparatus 22

2.2.3 Removal of Reagents and Reaction By-products 23
2.3 Cation Exchange Reactions 23
2.3.1 Drying Metal Chlorides 23
2.4 Powder Diffraction 24
2.4.1 X-ray Powder Diffraction 26
2.4.2 Neutron Powder Diffraction 29
2.5 Rietveld Refinement 33
2.5.1 Size and Strain from the Refined Peak Profile 34
2.6 SQUID Magnetometry 35
2.6.1 Ferrosubtraction Measurements 37
2.6.2 Curie-Weiss Law 38
2.7 Thermogravimetric Analysis (TGA) 39
2.8 Manganometric Titrations 39
2.9 Bond Valence Sums 40
2.10 Muon-Spin Relaxation Spectroscopy (μSR) 40
2.11 Second Harmonic Generation (SHG) 41

Chapter 3

Synthesis of $LaSrNiRuO_6$ – Microstructural Aspects of the Starting Materials for $LaSrNiRuO_4$

3.1 Introduction 43
3.2 Experimental 45
3.2.1 Synthesis of $LaSrNiRuO_6$ 45
3.2.2 X-ray Powder Diffraction Experiments 46
3.2.3 Thermogravimetric Measurements 46
3.3 Results 46
3.3.1 Structure of $LaSrNiRuO_6$ from X-ray Powder Diffraction 46

3.3.2 Composition of Slow-Cooled and Quenched $LaSrNiRuO_6$ Samples from Thermogravimetric Measurements 48

3.3.3 Comparison of X-ray Powder Diffraction Data of Slow-Cooled and Quenched $LaSrNiRuO_6$ Samples 50

3.3.4 Comparison of the Broadness of Peaks of Slow-Cooled and Quenched $LaSrNiRuO_6$ Samples 54

3.4 Discussion 55

3.4.1 Slow-cooled and Quenched $LaSrNiRuO_6$ Samples 55

3.4.2 The Topochemical Reduction of Slow-cooled and Quenched $LaSrNiRuO_6$ Samples. 57

3.5 Conclusions 60

Chapter 4

The Topochemical Reduction of $LaSrNiRuO_6$

4.1 Introduction 61

4.2 Experimental 61

4.2.1 Reduction of Slow-Cooled and Quenched $LaSrNiRuO_6$ Samples 61

4.2.2 Thermogravimetric Measurements 62

4.3 Results 62

4.3.1 Reactivity of $LaSrNiRuO_6$ Starting Materials 62

4.3.2 The Reduction Product $LaSrNiRuO_4$ 67

4.4 Discussion 73

4.4.1 The Topochemical Reduction of $LaSrNiRuO_6$ 73

4.4.2 Reduction behaviour of Slow-Cooled and Quenched $LaSrNiRuO_6$ Starting Materials 74

4.4.3 The Reactivity of Slow-Cooled and Quenched $LaSrNiRuO_6$ Starting Materials 76

4.5 Conclusions 79

Chapter 5

Synthesis and Characterisation of $LaSrNiRuO_4$

5.1 Introduction 81
5.2 Experimental 81
5.2.1 Synthesis of $LaSrNiRuO_4$ 81
5.3 Results 82
5.3.1 Thermogravimetric Analysis 82
5.3.2 X-ray Powder Diffraction 83
5.3.3 Neutron Powder Diffraction Data Collected at Room Temperature 85
5.3.4 Magnetisation Measurements 87
5.3.5 Neutron Powder Diffraction at Low Temperature 88
5.3.6 Density Functional Theory Calculations 93
5.4 Discussion 97
5.4.1 High Temperature Structural and Magnetsiation Data 98
5.4.2 Low Temperature Structure and Magnetic Behaviour of $LaSrNiRuO_4$ 98
5.4.3 The Electronic Structure of $LaSrNiRuO_4$ 100
5.5 Conclusions 102

Chapter 6

The Topochemical Reduction of $SrV_{0.95}Ti_{0.05}O_3$

6.1 Introduction 103
6.2 Experimental 106
6.2.1 Synthesis of the $SrV_{1-x}Ti_xO_3$ (x = 0.05) starting materials 106
6.2.2 Reduction of the $SrV_{1-x}Ti_xO_3$ (x = 0.05) Samples Prepared via the Ceramic and Arc-Melt Methods 106
6.3 Results 106

6.3.1 X-ray Powder Diffraction Data of the $SrV_{1-x}Ti_xO_3$ (x = 0.05) Starting Materials 106

6.3.2 Reduction of the $SrV_{0.95}Ti_{0.05}O_3$ Samples Prepared via the Ceramic and Arc-Melt Methods 108

6.3.3 Structural Characterisation of the C-R and A-R Reduction Products 110

6.3.4 Chemical Characterisation of the C-R and A-R Reduction Products 114

6.3.5 Magnetic Characterisation of the C-R and A-R Reduction Products 119

6.3.6 Muon Spin Relaxation (μSR) Spectroscopy of $SrV_{1-x}Ti_xO_{1.5}H_{1.5}$ 124

6.4 Discussion 126

6.4.1 Reduction Behaviour of the $SrV_{0.95}Ti_{0.05}O_3$ Starting Materials Prepared via the Ceramic and Arc-Melt Methods 126

6.4.2 Disorder in the Vanadium-Titanium Oxyhydrides 128

6.4.3 The Kinetic Trap in the Formation of $SrVO_2H$ 131

6.4.4 Titanium Content in the $SrV_{1-x}Ti_xO_3$ Starting Materials 133

6.5 Conclusions 133

Chapter 7

The Synthesis of $SrV_{0.95}Ti_{0.05}O_3$

7.1 Introduction 134

7.2 Experimental 135

7.2.1 Synthesis of $SrV_{0.95}Ti_{0.05}O_3$ via the Ceramic Method – Sample C 135

7.2.2 Synthesis of $SrV_{0.95}Ti_{0.05}O_3$ Using the Arc-Melt Furnace – Sample A 135

7.3 Results 136

7.3.1 X-Ray Powder Diffraction Data 136

7.3.2 $SrV_{0.95}Ti_{0.05}O_3$ Samples Prepared via the Ceramic Method at Higher Temperatures 139

7.3.3 $SrV_{1-x}Ti_xO_3$ Samples with x = 0.40, 0.50 142

7.3.4 $SrV_{1-x}Ti_xO_3$ Solid-Solutions 146
7.3.5 Phase Segregation in a $SrV_{0.95}Ti_{0.05}O_3$ Sample Prepared via Arc-Melt 148
7.4 Discussion 152
7.5 Conclusions 154

Chapter 8

Cation Exchanges in $NaTaO_3$ and $NaNbO_3$

8.1 Introduction 155
8.2 Experimental 158
8.2.1 Synthesis of $NaNbO_3$ and $NaTaO_3$ 158
8.2.2 Preparation of Anhydrous $NiCl_2$ and $CuCl_2$ 158
8.2.3 Synthesis of $Ni_{0.5}TaO_3$ and $Cu_{0.5}TaO_3$ Phases 158
8.2.4 Cation Exchanges in $NaNbO_3$ 159
8.3 Results 159
8.3.1 $Ni_{0.5}TaO_3$ 160
8.3.2 $Cu_{0.5}TaO_3$ 165
8.4 Discussion 171
8.4.1 Topochemical Cation Exchange Reactions 171
8.4.2 The Structural Change on Cation Exchange Reaction from $NaTaO_3$ to $Ni_{0.5}TaO_3$ 172
8.4.3 Comparison Between $Ni_{0.5}TaO_3$ and $LiTaO_3$ 173
8.4.4 The structure of $Cu_{0.5}TaO_3$ 175
8.4.5 Exchanges with Other Divalent Cations in $NaTaO_3$ 176
8.4.6 Cation Exchange in Three Dimensional Perovskite Structures 179
8.5 Conclusions 180

Chapter 9

Summary, Conclusions and Future Work

Appendix 1: Bibliography.....189

Appendix 2: Details of the Ferromagnetic Subtraction Experiment for $LaSrNiRuO_4$ 194

Appendix 3: Table of Figures 196

Appendix 4: Table of Tables.....206

Chapter 1

Introduction

1.1 Complex Transition Metal Oxides

Complex transition metal oxides are an extensively studied class of compounds in the search for new materials with scientifically interesting and technologically appealing properties, due to the diverse electronic and magnetic behaviour they exhibit.[1,2] In these materials, the coupling and correlation between the crystallographic, orbital and spin structures often results in a wide range of emerging features including multiferroicity, colossal magnetoresistance, superconductivity, catalytic activity and energy storage capability, among others.[3-8]

These properties arise from the ability of transition metals to adopt a range of oxidation states that result in partially-filled *d*-orbitals. The electrons in these partially filled *d*-orbitals can couple to each other either by direct mixing with neighbouring transition-metal centres or via the 2*p* orbitals of the bridging oxygen ligands. The complex electronic states that result from these couplings are a function of the identity, oxidation state, and coordination geometry of the transition metal centres that form the extended metal-anion network.[9]

1.1.1 Complex Transition Metal Oxides Adopting the Perovskite Structure

The orbital overlap between the transition metal *d*-states and the 2*p* oxygen states in an extended solid oxide is maximised when the B-O-B bond angle is 180º, while the overlap decreases as the angle changes away from 180°. Complex transition-metal oxides that adopt the perovskite structure of basic formula ABO_3, where B is a transition metal and A is a larger cation from the *s*-, *d*- or *f*-block, are of particular relevance. This structure consists of apex-linked BO_6 octahedra forming a three-dimensional network, in which the

A-cations occupy 12-coordinate cubo-octahedral cavities. The aristotype perovskite structure is cubic and all B-O-B angles are 180º so the orbital overlap is optimal.

The BO_6 octahedra in the perovskite structure can twist and tilt changing the 180º B-O-B bond angle, and/or be subject to Jahn-Teller effects which allow additional energetic stabilisations (Figure 1.1).[9,10] The Jahn-Teller effects can be of first or second order. First Order Jahn-Teller effects arise from incomplete shells of degenerate orbitals (*e.g.* d^9 orbitals in an octahedral crystal field), while Second Order Jahn-Teller (SOJT) effects arise from the mixing of filled and empty orbitals which are close in energy (and which transform into the same irreducible representation in the lower symmetry).[10] The SOJT effects involve the coupling of a non-degenerate ground state with a low-lying excited state. Transition-metal cations with d^0 configurations occupying the B-sites of the perovskite structure are susceptible to SOJT effects. The geometric distortions produced by each type of Jahn-Teller effect are different. The FOJT effect lifts the degeneracy and leads to significant distortions (Figure 1.1a). The SOJT effect breaks the inversion symmetry by displacing the cations off-centre within their coordination polyhedra (Figure 1.1b) and can also lead to large distortions.[11] The schematisation of a first order Jahn-Teller effect for a *d*-metal is presented in Figure 1.1a. Figure 1.1b, depicts the shift of the metal centre along an apical direction in its coordination polyhedra (cations can also shift towards one of the triangular phases of the octahedra).

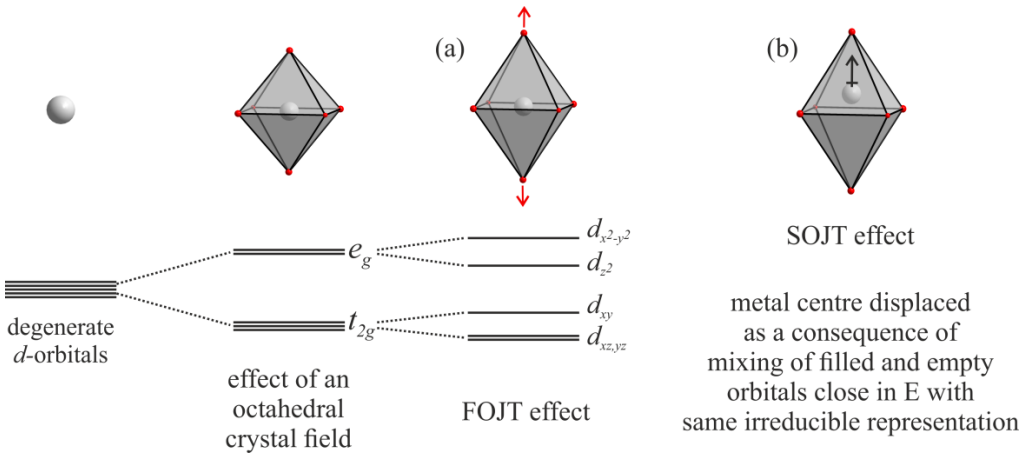


Figure 1.1. Schematisation of an example of (a) FOJT and (b) SOJT effects on a *d*-metal in an octahedral environment. The electrons in the *d* orbitals in (a) have been omitted for simplicity but d^9 configurations represent a good example.

For d^0 metal cations in the B-sites of a perovskite structure, the off-centring leads to a loss in the symmetry of inversion of the BO_6 structural units (Figure 1.2). The presence of such non-centrosymmetric units is particularly relevant, as they can arrange to yield polar structures such as that of $BaTiO_3$.[12] A net polarisation is condition for ferroelectricity as will be discussed in Chapter 8.

The 'flexibility' conferred by the aforementioned distortions in the perovskite structure gives access to a vast range of compositions with diverse species both in the A-sites and in the B-sites, and has allowed the study of a plethora of properties. Given that the B–O–B bond angle changes the coupling interactions between the electrons of the transition metal centres, and that different species leading to different geometric distortions change the electronic distribution in the lattice, changing such structural aspects makes it possible to tune the physical properties in materials adopting the perovskite structure.[9]

The Goldschmidt tolerance factor is a useful metric to quantify the level of distortion of a perovskite structure from the ideal cubic aristotype:[13]

$$\boldsymbol{t} = \frac{\boldsymbol{<A-O>}}{\sqrt{\boldsymbol{2}}\boldsymbol{<B-O>}} \qquad (1.1)$$

In the above expression, <A-O> and <B-O> correspond to the bond lengths between the oxide ions and the A and B cations respectively.

The tolerance factor *t*, takes the value of $t = 1$ for the perfect cubic case. When $t < 1$, the A-site cations are smaller than the ideal size for the cubo-octahedral cavities, which drives cooperative twists and tilts of the BO_6 octahedra forming the network.[14] The perovskite structure deviates from a perfect cubic symmetry (by becoming either orthorhombic or rhombohedral) and the B–O–B bond angles are less than 180º. On the other hand, when $t > 1$, larger A-site cations (with respect to the ideal case) need to be accommodated, and the network of octahedra distorts to give way to hexagonal systems.[14]

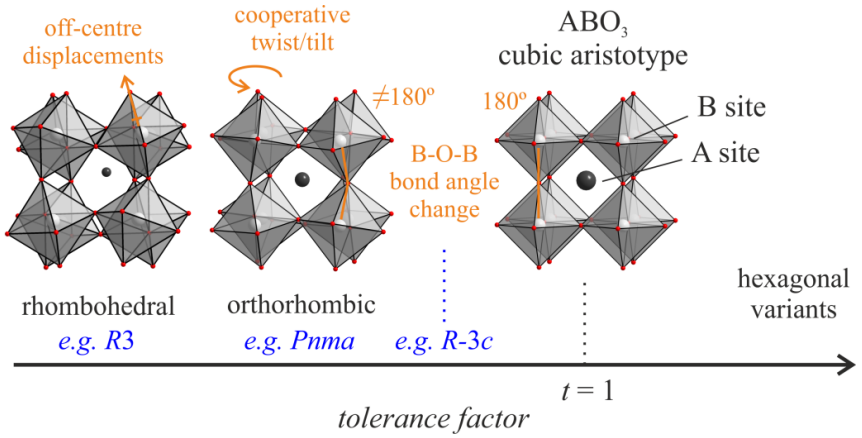


Figure 1.2. Schematisation of the distortions that occur in the perovskite structure. Representative examples of space groups observed for the different values of the tolerance factor *t* are given in blue.

The orbital overlap between the *d*-states and the 2*p* oxygen states in the perovskite structure permit the transition metal centres to strongly couple to each other giving rise to the wide range of electronic properties observed. Such properties can be tuned by changing the B–O–B bond angles and with this the coupling interactions between the electrons of the transition metal centres. The tolerance factor therefore represents a parameter for the control of properties in the resulting materials: chemical substitutions can be made onto both cation sites, A and B, and onto the oxygen anion sites. Furthermore, the latter can accommodate high concentrations of vacancies without the structure collapsing.

A regular stacked intergrowth of perovskite blocks ABO_3, and cations (or cationic structural units) forming rock salt layers (AO), can give way to the perovskite-related Ruddlesden-Popper structures, of which two examples are shown in Figure 1.3. These layered structures can be described by the general formula $AO(ABO_3)_n$, of which the three dimensional perovskite structure is the $n = \infty$ end member.

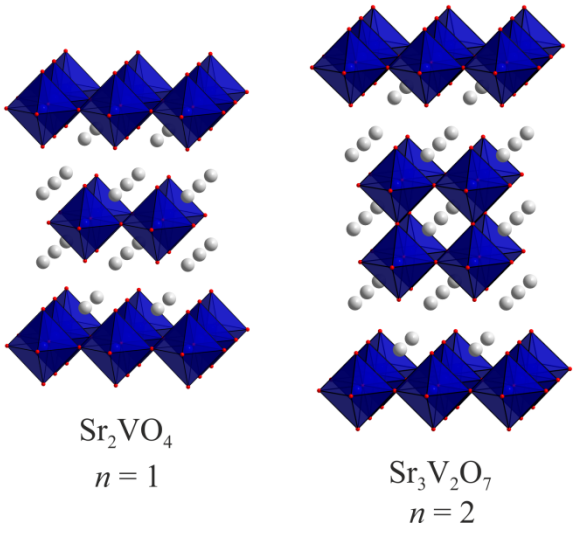


Figure 1.3. The Ruddlesden-Popper structures of Sr_2VO_4 and $Sr_3V_2O_7$.

1.1.1.1 Cation Order in the Perovskite Structure

When more than one type of ion occupies the same site in the perovskite structure (either A, B or O), they can: (i) distribute statistically, or (ii) arrange in a pattern. The latter leads to ion-ordered structures, which have very successfully expanded the number of possibilities for engineering new materials, as the choice of the additional species represents an extra degree of freedom to their tunability.[8]

The ion-ordering is favoured when there is a significant difference in the size and charge between the species involved.[8] The patterns that can form in cation-ordered perovskite structures are summarised in Figure 1.4. The cation-ordering in the B-sites leads to structures $A_2BB'O_6$ which are referred to as *double perovskite* structures.

The cation-ordering is observed to have a profound influence on the physical properties of the perovskite structures. For example, a combined ferromagnetic and insulating behaviour is not possible to realise in disordered ABO_3 perovskite structures, whilst it is observed in the ordered structures A_2MnNiO_6 and A_2MnCoO_6 (A = La, Bi).[15,16] Similarly, both the dielectric properties of Pb_2ScTaO_6 and the magnetotransport properties of Sr_2FeMoO_6, are highly sensitive to the degree of the B/B' ordering.[17,18]

The reduction of the double perovskite structure $LaSrNiRuO_6$ will be studied in Chapters 3-5.

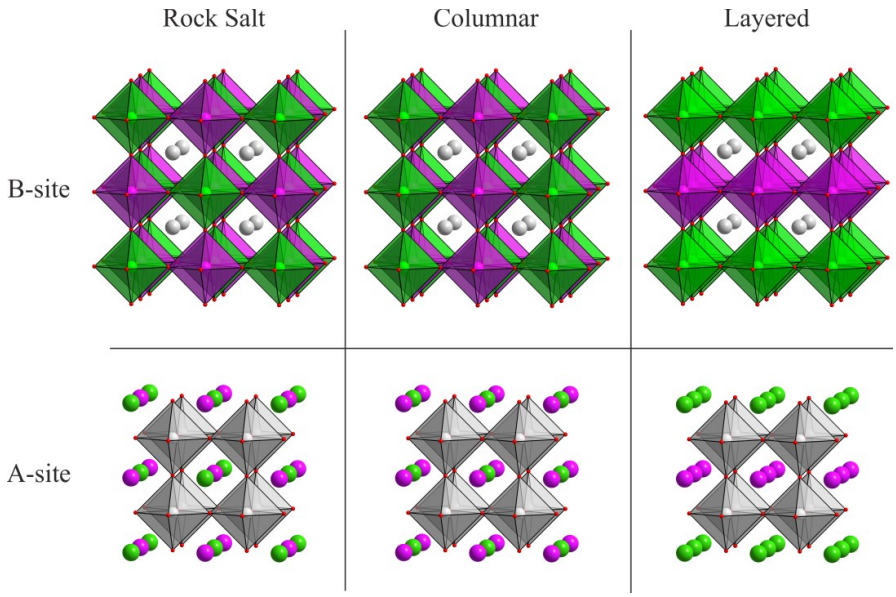


Figure 1.4. Table of different ordering schemes in perovskites.[8]

1.2 The Electronic Structure of Complex Transition Metal Oxides

For an extended array of atoms, the electron wave functions resulting from interaction of the atomic orbitals can be understood as being 'spread out' throughout the solid. The crystal orbitals are formed into an *energy band*, where the differences between energy levels are so small that they can be described as a continuous distribution of states (Figure 1.5).

The occupancy of atomic orbitals determines the occupancy (or filling) of a band. The energy of the highest occupied level is known as the *Fermi level*. A partially occupied band can give rise to metallic conductivity as unpaired electrons near the Fermi level are excited into orbitals where they delocalise and move freely, and thus transport charge. However, for solids in which the interatomic orbital overlap is small, narrow bands are formed and electron-electron repulsion is observed to become important. In such cases electrons are localised by mutual repulsion and the conducting behaviour is not observed. For example, despite having partially filled *d*-bands, NiO and CoO are not metallic but antiferromagnetic insulators.[14]

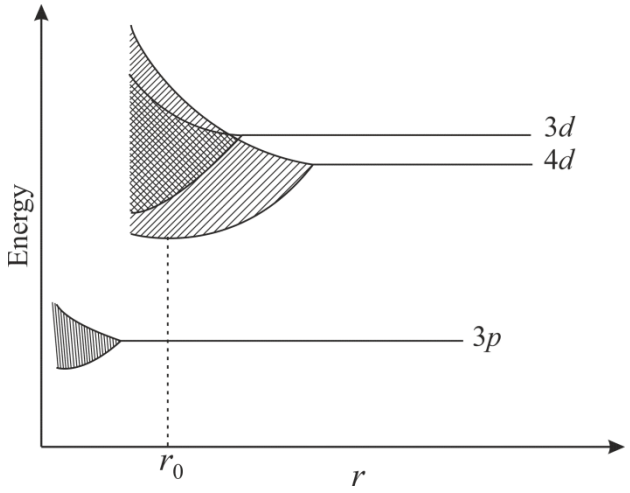


Figure 1.5. Schematisation of atomic levels splitting into energy bands where the equilibrium interatomic distance is r_0.[19]

The Hubbard model (Figure 1.6) represents one of the most simple ways to describe how the interactions between the electrons in a solid result in the conducting and insulating behaviours observed in transition metal oxides.[9]

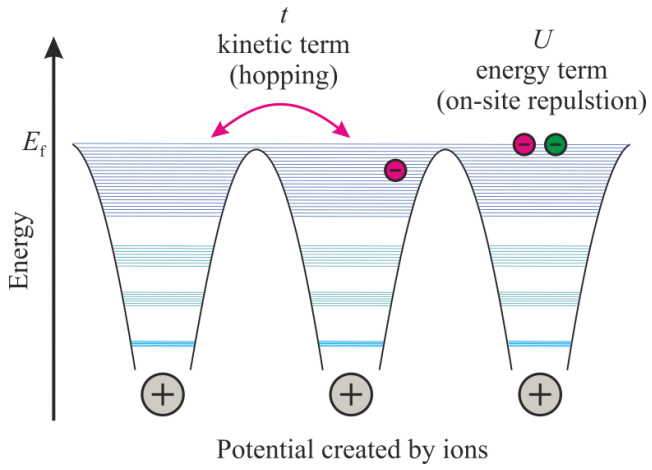


Figure 1.6. Schematisation of the hopping (*t*) and energy (*U*) terms in the Hubbard model.[20]

The Hubbard model is an extension of the *tight-binding* model (a method used to describe the electronic band structure of a crystal), in which the total energy of the interaction between electrons of atoms in neighbouring sites in a lattice, is described as the contribution of two terms (in the Hubbard Hamiltonian): a kinetic term *t* and a potential energy term *U*. The term *t* allows for tunneling ('hopping') of the electrons between the neighbouring sites of the lattice. This kinetic term favours itinerant electrons. Meanwhile,

U describes the Coulombic repulsion between two electrons on the same atom and can be thought as the difference between the ionisation energy and the electron affinity. This repulsion is assumed to be the only interaction between the electrons in the model.[9]

The Hubbard model therefore describes the competition between chemical bonding (*t*) and short range on-site Coulomb repulsion (*U*). The relative strength between the two terms can be compared by using the dimensionless ratio *t*/*U*.

The transfer of an electron from an atom to its neighbour 'costs' the energy penalty *U* as a consequence of the on-site repulsion, which leads to the formation of sub-bands separated by a Mott-Hubbard gap (of magnitude *U*, as depicted in Figure 1.7(a)). Such a system is insulating when the interatomic orbital overlap is small.

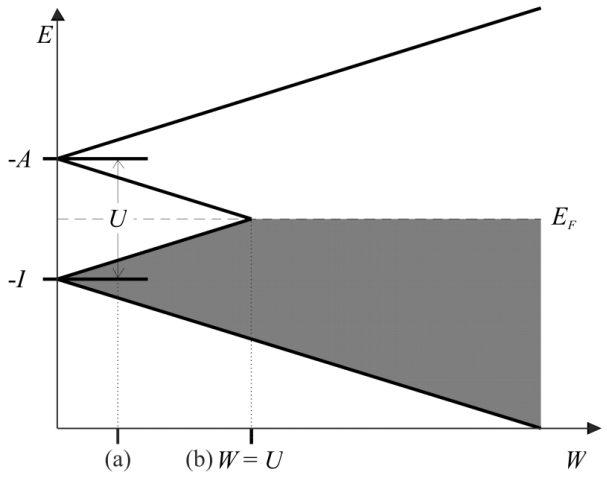


Figure 1.7. Hubbard sub-bands as a function of the band width *W*. On the energy coordinate *E*, *-I* represents the ionisation energy and *-A* the electron affinity.[2]

As the interatomic orbital overlap increases, the sub-bands become broader until there is a critical value at which the width *W* and the repulsion parameter *U* are approximately equal (*W* = *U* in Figure 1.7(b)). The energy gap *U* becomes negligible after this point (*W* > *U*) and the system becomes metallic.[20]

When $U \approx W$, the competition between forces that favour localisation (*e.g.* on-site repulsion) and those that favour delocalisation (*e.g.* the band width) often result in the system adopting a 'third option' in which various energetic requirements need to be satisfied. Many interesting electronic properties of complex transition metal oxides arise

under these conditions. For example, Sr_2RuO_4 has been shown to exhibit antiferromagnetic, ferromagnetic, and superconducting instabilities from the competing localisation-delocalisation interactions.[21] The result of these competing instabilities is that Sr_2RuO_4 is the only known material to exhibit *p*-wave superconducting behaviour (T_c ~ 1.5 K).[22]

The 4*d* and 3*d* transition metal oxides represent particularly interesting systems. The relatively large 4*d* and 3*d* orbitals yield small *U* values, while the better orbital overlap leads to an increase in the width of the bands.[2] TiO and VO display metallic behaviour, while MnO and FeO are insulators.[23] Similarly, $SrFeO_3$ and $SrMnO_3$ are insulating, while $SrRuO_3$ displays metallic behaviour.[24] Additionally, reduction of the 4*d* and early 3*d* transition metal oxides appears to be especially conducive to phases exhibiting correlated electronic behaviour.[21]

The electronic behaviour of complex transition metal oxides is strongly dependent upon the crystal structure. For example, coming back to the only known *p*-wave superconductor Sr_2RuO_4, this oxide has a Ruddlesden-Popper tetragonal structure in which the Ru–O–Ru bond angles are 180° (Figure 1.8).[25,26] For the Ca_2RuO_4 phase on the other hand, Ru-O-Ru bond angles deviate from 180° due to tilting of the RuO_6 octahedra. In contrast to Sr_2RuO_4, Ca_2RuO_4 is a Mott insulator (also in Figure 1.8).[27] Another example is Sr_2IrO_4, in which twisting of the octahedra also leads to deviation from a perfect 180° Ir–O–Ir bond angle as shown in Figure 1.8, resulting in insulating behaviour.[26,28] Upon substitution the B-sites of Sr_2IrO_4 with ruthenium to form $Sr_2Ru_xIr_{1-x}O_4$ phases, a metal-insulator transition (*i.e.* an itinerant-localised transition) is observed at x = 0.7.[29]

The cation-ordering is another structural parameter that can change the electronic behaviour in complex transition metal oxides. For perovskite structures containing both 3*d* and 4*d* metals either in the A-sites or in the B-sites, the cation-ordering determines the correlation interactions between electrons in the different *d*-states.[30,31] This aspect will be discussed in Chapters 3 to 5.

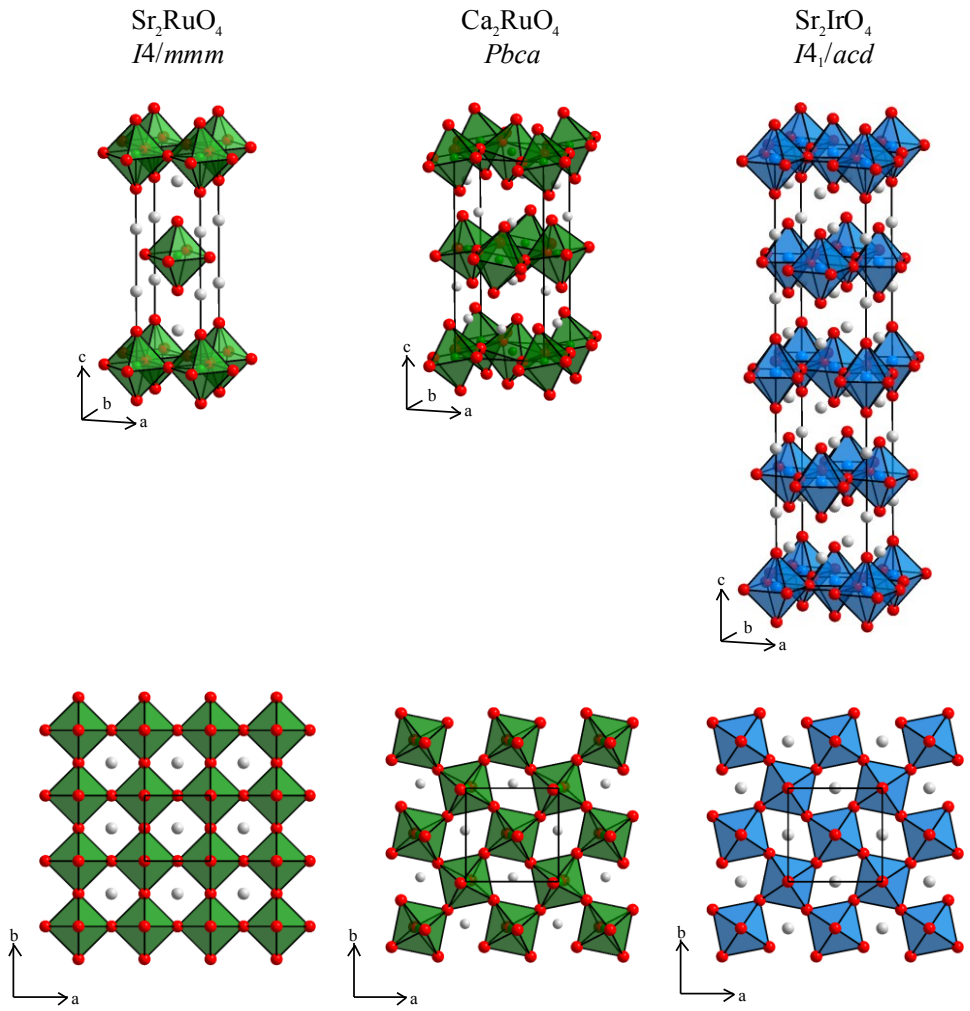


Figure 1.8. Structures of Sr_2RuO_4 (left), Ca_2RuO_4 (middle) and Sr_2IrO_4 (right).[32]

1.2.1 The Goodenough-Kanamori Rules

A system of semi-empirical rules was developed by Goodenough and Kanamori,[33] based on Anderson's work,[34] for the prediction of the type of magnetic coupling expected from the superexchange interactions between electrons in the *d*-levels of magnetic ions, separated by a ligand. These rules have been able to explain the magnetic order for a wide variety of materials. According to the Goodenough-Kanamori rules an M-O-M 180º superexchange interaction (where M is a magnetic ion with partially filled *d*-orbitals) results in strong antiferromagnetic coupling (Figure 1.9). On the other hand, an M-O-M 90º superexchange interaction results in a weak ferromagnetic coupling (Figure 1.9).

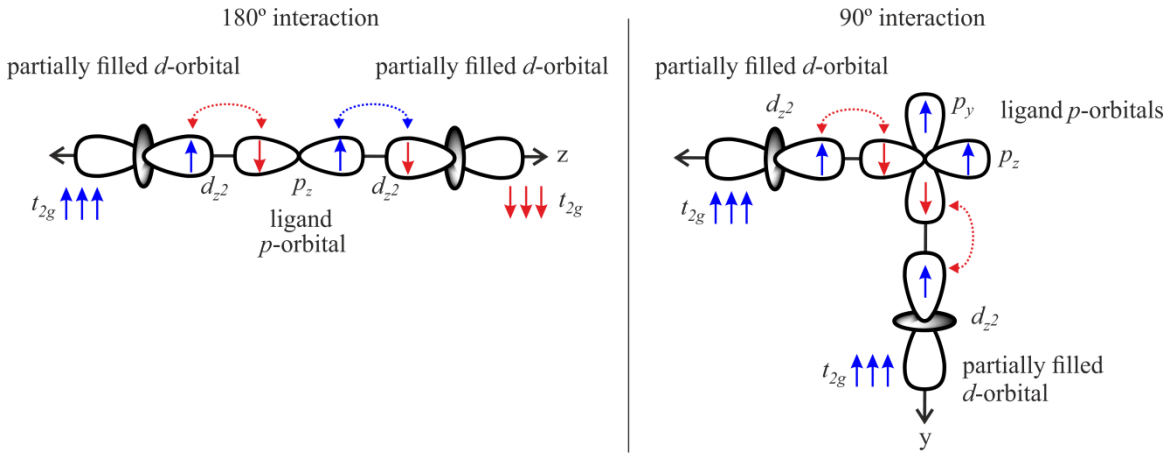


Figure 1.9. Schematic examples of M-O-M 180º and 90º, *d-p-d* orbital interactions resulting in the magnetic coupling predicted by the Goodenough-Kanamori rules.

When two magnetic ions have lobes pointing towards each other (*i.e.* the M-O-M bond angle is 180º), the following predictions arise:

(i) The interaction between a half-filled orbital and either a filled or an empty orbital, favours ferromagnetic coupling.

(ii) The interaction between two half-filled orbitals favours antiferromagnetic coupling.

(iii) The interaction between a filled and an empty orbital favours antiferromagnetic coupling.

The structural aspects that change the orbital overlap and the M-O-M bond angles have an effect on the coupling interactions in transition metal oxides and thus define the interactions that give way to the electronic and magnetic behaviour. Thus, by rationalising the design of solids with carefully chosen structural and compositional features, selected physical and electronic behaviours can be targeted for the understanding and development of new materials.

1.3 Topochemical Manipulation

The synthesis of complex transition metal oxides is typically carried out at high temperatures to overcome the large energy barriers to ion diffusion in the solid state. These energy barriers are often comparable for a set of possible (competing) reactions, given a set of solid reagents. At these elevated synthesis temperatures, the energy requirements for a range of possible pathways are satisfied, with the products of all the competing reactions becoming readily accessible. The result in this high temperature regime is therefore invariably the set of most thermodynamically stable phases, while a range of metastable phases exhibiting novel oxidation states and/or coordination geometries are not generally observed.

Given that the electronic structure of the complex-transition metal oxides is a function of the lattice connectivity (crystal structure), in combination with the orbital and electron counts (defined by the local coordination geometry and oxidation state of the metal centres), the preparation of phases where these aspects can be explored is of central interest in the search for new materials.

Low-temperature synthetic methods can give access to metastable phases that permit the exploration of unusual properties. By utilising the different rates of solid-state diffusion of the cation lattice with respect to the anion lattice or *vice versa*, selected species can be exchanged, inserted, or removed, while the surrounding less mobile species preserve the main topology of the starting material. Such kinetic control is a defining characteristic of the topochemical processes.

1.3.1 Low-Temperature Reductive Chemistry Using Binary Metal Hydrides

Reductive deintercalation using binary metal hydrides has enabled the preparation of a wide range of materials at relatively low temperatures (180 °C to 630 °C) to form anion-deficient metastable phases.[35-37] The topochemical reduction of $LaNiO_3$ to form $LaNiO_2$ (Figure 1.10), represents a prime example of this type of reaction.[35] As shown in Figure 1.10, during the reaction, oxide ions are selectively removed while the cation framework

remains intact. In order to maintain charge neutrality, the transition metal centres are reduced.

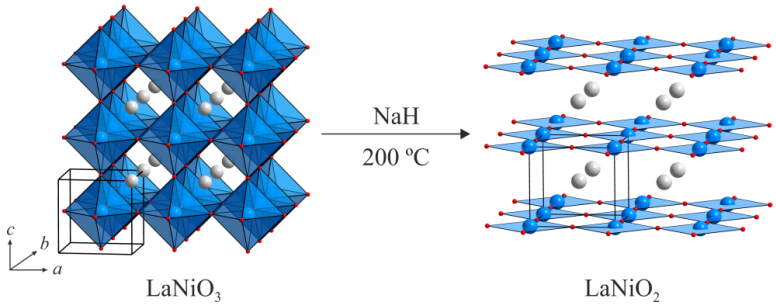


Figure 1.10. Reaction of $LaNiO_3$ with NaH to form the reduction product $LaNiO_2$.

This topochemical reductive deintercalation approach applied to other perovskite-related oxides has enabled the possibility of locating other transition-metal cations in square planar sites in extended phases for the first time, such as Co^{+} in $LaBaCo_2O_{4.25}$ (Figure 1.11), and Ru^{2+} in $SrFe_{0.5}Ru_{0.5}O_2$ (further discussed in Chapters 3 and 4).[38]

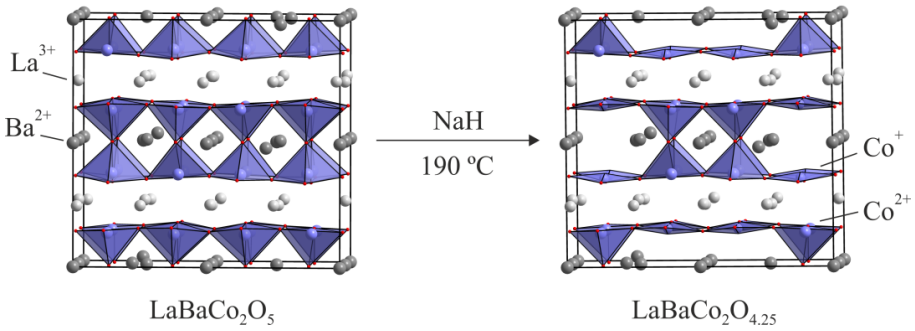


Figure 1.11. The reduction of $LaBaCo_2O_5$ with NaH resulting in the $LaBaCo_2O_{4.25}$ phase with square planar Co^{+} centres (occupying 50% of the anion-defficient sites).

The structure-conserving nature of the topochemical reactions allows the preparation of target phases by enabling directed chemical changes. The observation of Ru^{2+} centres in $SrFe_{0.5}Ru_{0.5}O_2$ is of particular relevance, as complex transition metal oxides containing 4*d* and 5*d* metal centres are expected to transform/decompose all the way into the elements upon reduction. However, the low oxidation state of the ruthenium 4*d* metal centres can be stabilised by the robust Sr-Fe-O 3*d* metal lattice, which is preserved throughout the reduction process.

Strong interaction between the anion and cation lattices can also exert control over the reduction behaviour of complex transition metal oxides. For example, the reduction of the isostructural and isoelectronic phases $YBaCo_2O_5$ and $LaBaCo_2O_5$ with NaH proceed to form markedly different products due solely to the directing behaviour of the A-cation identity (Figure 1.12).[39]

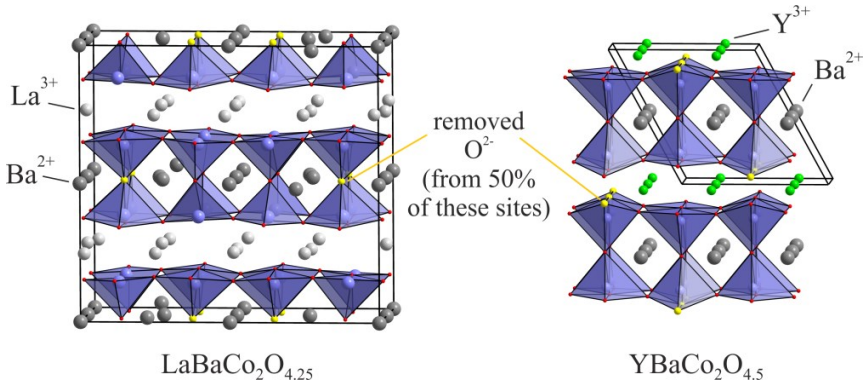


Figure 1.12. The structures of the topochemically reduced phases $LaBaCo_2O_{4.25}$ and $YBaCo_2O_{4.5}$.

The removal of oxide ions during topochemical reduction processes can also be directed by the influence of the B-cations over the selectivity of the topochemical reduction reactions. For instance, the n = 2 Ruddlesden-Popper phases $Sr_3Mn_2O_{7-\delta}$ and $Sr_3Fe_2O_{7-\delta}$ can be topochemically reduced to form phases with composition $Sr_3Mn_2O_{6+\delta}$ and $Sr_3Fe_2O_6$. As shown in Figure 1.13, in the manganese-containing phases the oxide ions are removed from the equatorial sites, whereas they are removed from the bridging apical sites in the iron case (Figure 1.13).[40,41]

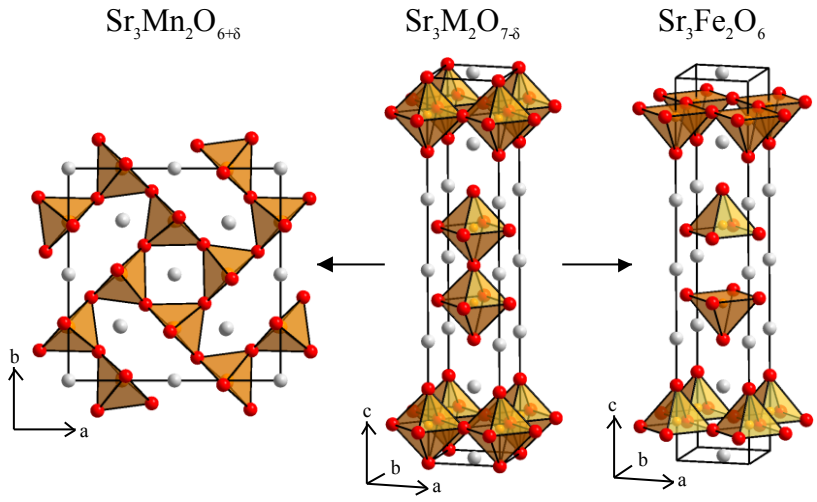


Figure 1.13. The n = 2 Ruddlesden-Popper phases $Sr_3M_2O_7$ (M = Mn, Fe) and their reduction products.[32]

The selectivity of anion deintercalation during topochemical reductions reveals differing rates of oxygen diffusion along different directions for a given structure. This is clear from the studies of $SrFeO_{3-\delta}$ to $SrFeO_2$ on thin films. Different orientations of the starting material ($SrFeO_{3-\delta}$) on the substrate lead to different reduction rates.[42,43]

In contrast to the limited control available during processes under thermodynamic control (in which only the relative stabilities of the products to be formed can be adjusted), the kinetic control during topochemical processes involves a combination of conditions that can be used to tune the reaction rate from the starting materials, rather than the products of reaction.

The topochemical reduction of complex transition metal oxides can result in replacement of oxide anions for hydride. The resulting *oxyhydride* phases are rare and not many of them have been reported. Some important examples are shown in Figure 1.14, where $SrVO_2H$ (along with the $Sr_{n+1}V_nO_{2n+1}H_n$ phases from reduction of the n = 1, 2 Ruddlesden-Popper structures shown in Figure 1.3), was the first oxyhidride reported to exhibit both stoichiometric exchange of oxide for hydride and a rigorous oxide/hydride anion order.[44-48] The $Sr_{n+1}V_nO_{2n+1}H_n$ phases are discussed in Chapters 6 and 7.

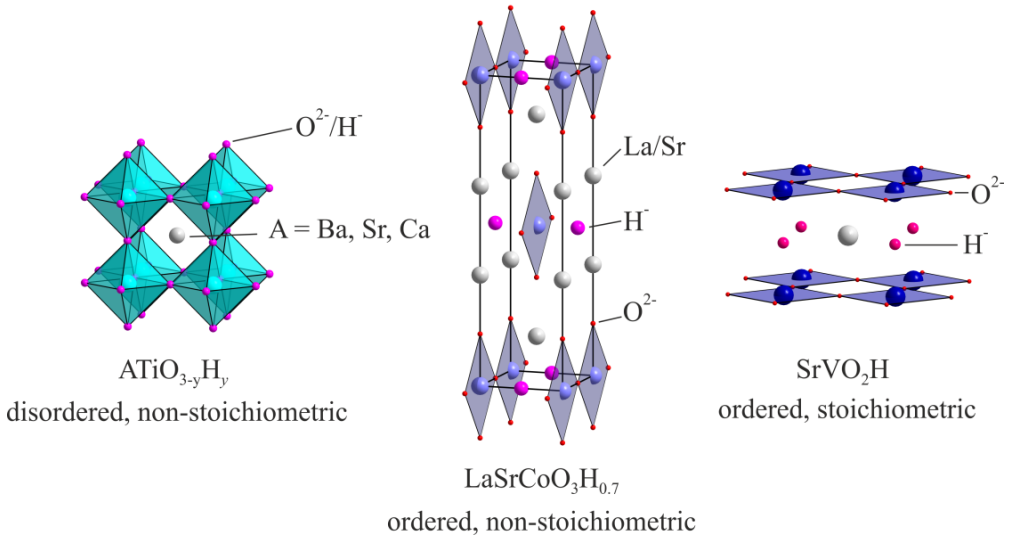


Figure 1.14. The structure of $ATiO_{3-y}H_y$ (A = Ba, Sr, Ca), $LaSrCoO_3H_{0.7}$ and $SrVO_2H$.

As will be discussed in Chapters 6 and 7, the nature of the H^- as a ligand makes the oxyhydrides phases very interesting from an electronic point of view. The hydride ligands are known to represent very good sigma donors in discrete molecular systems and the

exchange interactions with transition metal cations has been observed to lead to unconventional electronic and magnetic behaviours.[48]

1.3.2 Cation Exchange Reactions

Cations (in general) tend to be more tightly bound within their coordination polyhedra in extended solids. Therefore, a very low or null mobility is expected from the cations in complex transition metal oxides at the low temperatures at which the topochemical processes are performed.

Reductive and oxidative deintercalations and intercalations of small electropositive cations, such as Li^+, are observed to readily take place in (highly charged) metal-oxide host phases containing suitable cation vacancies. Two examples of cation insertions are depicted in Figure 1.15.[49,50]

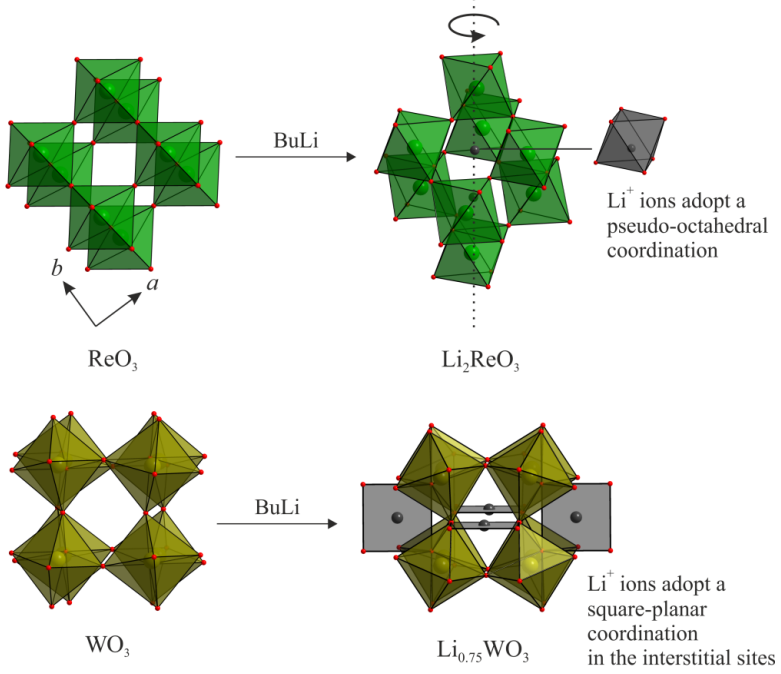


Figure 1.15. The lithium insertion into the ReO_3 and WO_3 perovskite structures.[49]

For redox-neutral topochemical cation substitution reactions to take place, further conditions need to be met. In addition to the species being significantly mobile within the host lattice at the reaction temperature, and the product being kinetically stable (both conditions that also apply for deintercalation/intercalation reactions); the redox-neutral reactions must be spontaneous ($\Delta G < 0$), as there are no thermodynamically driven electron transfer processes to drive the reaction.

The exchange of large cations for smaller cations (with concomitant increase in the lattice energy of reaction products), can lead to spontaneous cation exchange topochemical reactions. Such is the case of the substitution of Na^+ for Co^{2+} in the Ruddlesden-Popper phase $Na_2La_2Ti_3O_{10}$ (Figure 1.16).[49] The Co^{2+} cations in this case are inserted within the perovskite layers.

$$Na_2La_2Ti_3O_{10} + CoCl_2 \rightarrow Co^{II}La_2Ti_3O_{10} + NaCl$$

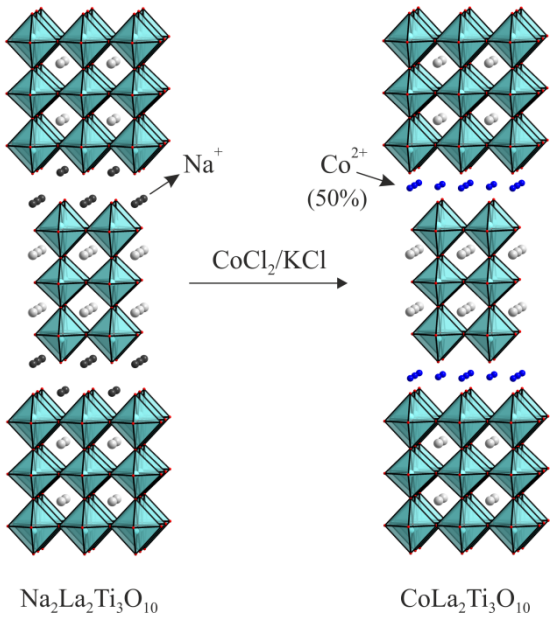


Figure 1.16. The cation exchange of Co^{2+} for Na^+ in the Ruddlesden-Popper phase $Na_2La_2Ti_3O_{10}$. The Co^{2+} cations occupy half of the tetrahedral interlayer sites.[49]

Factors such as the differences in the oxidation states of the cations being substituted, along with the formation of vacancies are expected to favour the occurrence of cation exchange.

The preparation of magnetoelectric multiferroic materials (which exhibit coupled magnetic and ferroelectric behaviour) represents a long-standing synthetic challenge (Chapter 8). This is because in the majority of solids, the requirements for magnetic coupling seem to exclude those for ferroelectric coupling and *vice versa*.[51]

In this work a novel approach in the challenge of obtaining magnetoelectric multiferroic materials was taken by utilising perovskite structures (such as $NaTaO_3$ and $NaNbO_3$) in which higher mobility of the A-site cations, with respect to the B-site cations, is realised. An unprecedented (to the best of our knowledge) redox-neutral topochemical cation-exchange process in $NaTaO_3$ allowed for small paramagnetic metal cations to substitute on the A-sites, yielding the new material $Ni_{0.5}TaO_3$ in which large geometric distortions through octahedral rotations are observed.

Chapter 2

Experimental Techniques

2.1 Syntheses of Starting Materials

2.1.1 Ceramic Methods

As highlighted in Section 1.1, the ceramic method involves the use of high temperatures (typically above 1000°C) to overcome the energy barriers to diffusion for ions in the solid state. For all the ceramic methods used, reagents were thoroughly mixed using an agate pestle and mortar in order to minimise the necessary diffusion length for reaction. In most syntheses, the resulting powder mixtures were then pressed into 13 mm pellets (5 tonnes). Pellets were heated at the corresponding temperature for periods of time of at least 12 hours. In some cases the mixtures were reacted as loose powder (Section 7.2). Exact details of the procedures for each phase are included in the appropriate chapters. Reaction progress was monitored via X-ray powder diffraction.

As will be further discussed in Chapters 3, 4 and 7, the cooling rate can have an influence on the products that are formed. Slow cooling can favour the growth of large crystalline domains, while metastable configurations made out of smaller domains can be trapped by rapid cooling.

2.1.2 Citrate-gel Method

The citrate-gel method is a sol-gel synthetic technique among the range of 'wet' procedures that have emerged for the preparation of homogeneous precursors for solid-state reactions.[52] In the citrate-gel method, the precursor formed is a citrate polymer in which the metals desired in the final composition are chelated.[53] This polymer is then transformed into the precursor of the desired product by pyrolysis in air.

Suitable quantities of the appropriate starting materials (metal oxides, chlorides or carbonates) were dissolved in a 1:1 solution of nitric acid in distilled water. An excess of citric acid was added, followed by ethylene glycol. The solution was then heated to drive the polymerisation of citric acid which results in the formation of a polyester network in which a homogeneous array of the metal cations are chelated.[52] The resulting homogeneous powders were then treated as in standard ceramic synthesis. Exact details of the procedures for each phase are included in the appropriate chapters.

2.1.3 Arc-melt Furnace

An arc-melt furnace consists of two electrodes between which a voltage is applied in order to form an electric arc. The electric arc can heat samples contained in the furnace to very high temperatures, typically in the range $3000 \leq T\ (^{o}C) \leq 4000$ depending on the applied current (at which most solids will melt).[54] For the arc-melt furnace used, a current of approximately 75 A was applied with a DC Inverter Arc Welding Power Source (150 TE).[55] The electrodes are a copper stage (on which the samples rest within the furnace, Figure 2.1), and a tungsten tip. The copper stage is water-cooled throughout the arc-melting process, and the melting process is carried out under a flowing argon atmosphere.

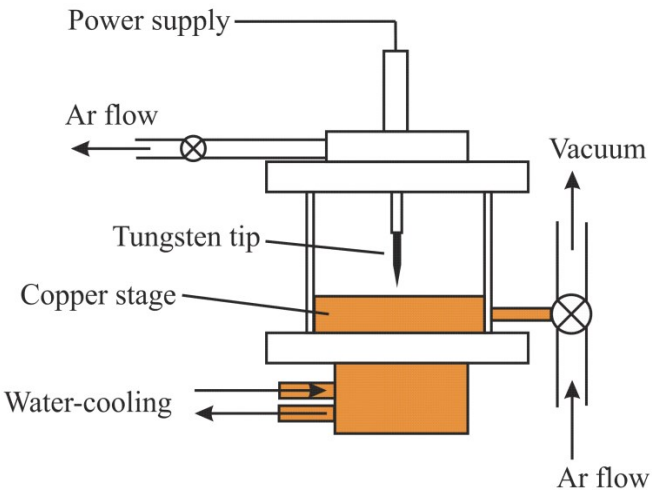


Figure 2.1. The arc-melt furnace.

For the heating treatments, powder samples pressed into 13 mm diameter pellets of intimately mixed precursors were placed on a copper stage. The chamber was pump-filled three times with argon and then placed under a flowing argon atmosphere. A DC arc welding torch operating with a 60 amp current was used to ionise the argon gas. The hot plasma was then repeatedly passed over the pellet until it melted. The pellet was then allowed to cool to room temperature, at which point it was flipped over and melted once again. This process was repeated a minimum of four times. Reaction progress was monitored via X-ray powder diffraction.

2.2 Oxide Anion Deintercalations and Oxide-Hydride Anion Exchanges

The reduction of complex transition metal oxides with binary metal hydrides such as NaH, CaH_2 and LiH allows the preparation of anion-deficient metastable phases at relatively low temperatures ($180 \leq T\ (°C) \leq 630$).[35,37] The choice of the binary metal hydride to be used as reducing agent for a particular phase can be made using the reaction temperature as a criterion.[49] For the phases studied in this work, preliminary exploratory reactions were carried out to find the temperatures of reaction. When reactions were found to require temperatures in the range $250 \leq T\ (ºC) \leq 630$, CaH_2 was used as the reducing agent.[37]

The reduction of an ABO_3 perovskite-structure phase with CaH_2 can be written as:[49]

$$ABO_3 + xCaH_2 \rightarrow ABO_{3-x} + xCaO + xH_2 \qquad (2.1)$$

The binary metal hydrides are air and moisture-sensitive, therefore the reaction mixtures had to be handled using air-sensitive techniques (*i.e.* once prepared, mixtures were kept under an inert atmosphere at all times).

Samples to be reduced were typically ground with an excess of CaH_2 in a glovebox and then placed within a suitable reaction vessel.

2.2.1 Reactions with CaH_2 in sealed tubes

Pyrex (T < 350 ºC) or silica sealed evacuated ampoules are very convenient reaction vessels for the reductions with binary metal oxides. The volume can be scaled in order to contain the gas pressure generated during reaction (Reaction 2.1), and the reactions can be easily handled during thermal treatments and transferred inside a glove box of inert atmosphere.

Generally, the air sensitive reaction mixtures were loaded inside an argon-filled glovebox and then transferred to a vacuum line using a system of taps or Teflon stopcocks which prevent exposure to the atmosphere. The argon was evacuated from the tubes and then these were sealed. The reaction mixtures contained in the sealed tubes were heated to the desired temperatures at a ramp rate of 1 °C min^{-1} to ensure that the temperature of the furnace did not overshoot the relatively low reaction temperatures. After being held at the required temperature for a suitable length of time, the ampoules were opened in the glovebox and the sample reground. Reaction progress was monitored using X-ray powder diffraction.

2.2.2 Pressure Venting Apparatus

For the reactions in which the H_2 pressure generated during reduction with CaH_2 (Reaction 2.1) exceeded the safe working levels (samples of sizes greater than 1.5 g), the venting apparatus shown in Figure 2.2 was used.[37]

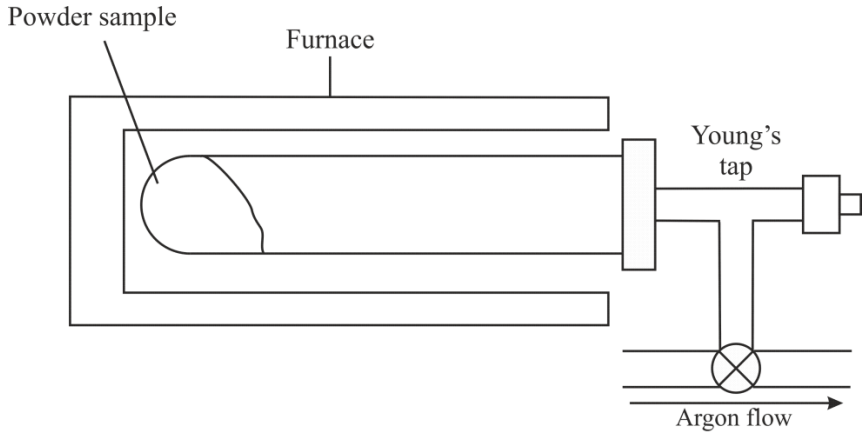


Figure 2.2. The venting apparatus.

Reactants were ground together and placed in a 19 mm silica tube sealed with a Young's tap. After purging the venting system using a flow of argon, the reaction vessel was connected to an argon flow, and heated to the appropriate reaction temperature. Upon completion of a heating cycle, the tube was evacuated using the vacuum line and purged into the glovebox to allow reaction monitoring using X-ray powder diffraction.

2.2.3 Removal of Reagents and Reaction By-products

The by-product CaO (Reaction 2.1) and unreacted CaH_2 were removed from the products of reduction by washing with NH_4Cl, using standard Schlenk line techniques. The resulting mixtures after reaction were removed from the glovebox without being exposed to air, and stirred under nitrogen with solutions of NH_4Cl (Fisher Scientific, > 99%) in methanol (Sigma-Aldrich, ≥ 99.9%).

Samples were then recovered by filtration, and washed with clean methanol to remove any remaining NH_4Cl, before drying under vacuum. The concentration of the NH_4Cl solution used is given in each chapter.

2.3 Cation Exchange Reactions

2.3.1 Drying Metal Chlorides

Anhydrous metal chlorides for their use in cation exchange reactions (Chapter 8), were prepared from the hydrated form according to the following process:

$$MCl_n \cdot yH_2O \xrightarrow{\Delta,\ \text{Ar flow}} MCl_n + yH_2O_{(vap)} \qquad (2.2)$$

where M = Ni^{2+}, Cu^{2+}, Mn^{2+}, Fe^{2+}, Co^{2+} and Δ is the drying temperature of the chlorides determined from thermogravimetric analysis (Section 2.7).

Initially, the hydrated materials were heated at 1 ºC min^{-1} to 150 ºC under flowing argon and held at this temperature for 2 hours, to eliminate the absorbed water. Materials were then heated at 5 °C min^{-1} to T = Δ, to remove all the water of crystallisation. The anhydrous chloride was then transferred and stored in an argon filled glove box without

exposure to air. The efficiency of this drying procedure was confirmed by thermogravimetric analysis and X-ray powder diffraction.

Effectively drying the MCl_2 reagents without forming $M(OH)_2$ during the procedure was vital for the success of the cation exchange reactions, and required strict adherence to the heating procedure described above. It was observed that if the MCl_2 reagent was not completely dry, or if any $M(OH)_2$ was present, reaction tubes would explode at the reaction temperature (Section 8.2.3), due to the high water vapour pressure produced within the silica ampoules.

2.4 Powder Diffraction

Powder diffraction techniques are some of the most important and widely used methods for the characterisation of crystalline materials. X-ray and neutron powder diffraction were the main methods used for the characterisation of the phases presented in this work.

Diffraction is a characteristic behaviour of waves which occurs when they irradiate scattering obstacles of comparable size to the wavelength. X-ray and neutron radiations have wavelengths that are comparable to the spacing between the lattice planes formed by atoms periodically arranged within a crystal. X-rays and neutrons are scattered in a process known as elastic scattering, in which each centre of the periodic array becomes equivalent to a new point source of secondary waves. The regular array of scatterers produces a regular array of waves. In most directions, these waves will cancel out through destructive interference; however, a few specific directions will result in constructive interference. This is known as diffraction and the geometrical conditions for it to be observed are given by Bragg's Law:[56]

$$\boldsymbol{n\lambda = 2d_{hkl}sin(\theta)} \qquad (2.1)$$

where λ is the wavelength of the incident beam, d_{hkl} is the interplanar distance and θ is the angle between the beam and the lattice planes depicted in Figure 2.3. Assuming that the source and detector in a diffraction experiment are at an infinite distance from the sample, then the incident and scattered beams can be considered parallel.

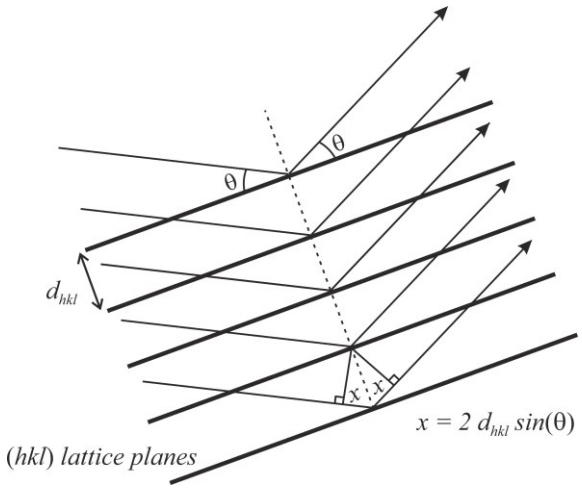


Figure 2.3. Bragg's construction for diffraction of monochromatic radiation by a set of parallel lattice planes.[56]

In a diffraction pattern, the position of a given reflection is defined by the *d*-spacing (d_{hkl}) and therefore the unit cell dimensions. The intensity (I_{hkl}) is given by:

$$\boldsymbol{I_{hkl} \propto LmA|F_{hkl}|^2} \qquad (2.2)$$

where L is the sample-independent Lorentz-polarisation function, m is the reflection multiplicity, A is the absorption factor and F_{hkl} is the *structure factor*, which depends on the crystal structure.[57]

The structure factor describes how the intensity is affected by the particular atomic contents of the unit cell as follows:

$$\boldsymbol{F(hkl) = \sum_j f_j(\theta) \cdot \exp[2\pi i(hx_j + ky_j + lz_j)] \cdot \exp(-8\pi^2 U_{isoj} sin^2\,\theta/\lambda^2)} \qquad (2.3)$$

where f_j is the atomic scattering factor (a function of the Bragg angle θ), x_j, y_j, z_j are the coordinates of the atoms in the unit cell relative to the origin. The second exponential factor, containing the isotropic displacement parameter $Uiso_j$, determines how the intensity decreases as a function of the scattering angle.

Powder samples can be assumed to be a large number (effectively infinite) of randomly oriented crystals, representing an equal distribution of all possible directions. Any particular allowed reflection will be generated by each of the individual crystals when the Bragg's law is satisfied. Every orientation is statistically represented, and for a given Bragg angle and intensity, the allowed reflections will give raise to diffracted beams in

more than one absolute orientation. Diffraction in all possible orientations generates Debye-Scherrer cones around the sample (Figure 2.4).[57] Collecting the diffracted cones and measuring their intensity as a function of the scattering angle yields a pattern in two dimensions, rather than the discrete Laue spots observed in single crystal diffraction.

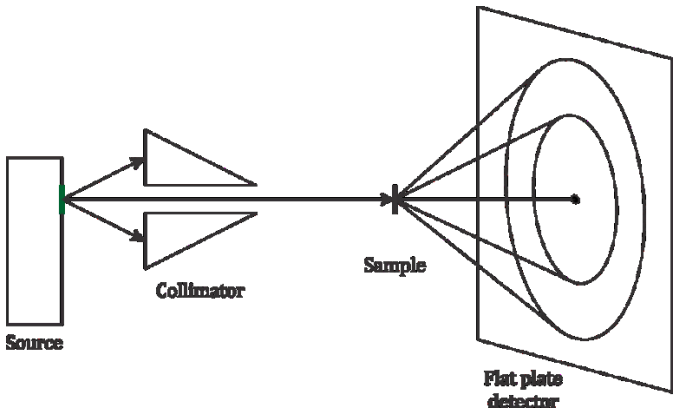


Figure 2.4. Schematisation of the Debye-Scherrer cones from diffraction by a powder sample, and their projection on a flat plate detector.[58]

2.4.1 X-ray Powder Diffraction

Bragg diffraction of X-rays is primarily due to the scattering from electrons of the atoms forming a crystal structure. This is known as Thomson scattering. In X-ray diffraction, a given atom's scattering factor (f_j) is therefore related to its atomic number (Z).

The reverse Fourier transform of an X-ray diffraction pattern, gives the value of the electron density at every point in the unit cell as follows:

$$\boldsymbol{\rho(xyz) = \frac{1}{V}\sum_{hkl} F(hkl)\exp[-2\pi i(hx + ky + lz)]} \qquad (2.4)$$

where V is the volume of the unit cell and all the structure factors $F(hkl)$ are being summed.

2.4.1.1 Laboratory X-ray Diffractometers

X-ray powder diffraction experiments were carried out using the K_α emission profile of copper, consisting of the doublet $K_{\alpha 1}$ (1.5405 Å) and $K_{\alpha 2}$ (1.5443 Å) in a 2:1 ratio. In some of the instruments (as will be specified in the respective sections), the $K_{\alpha 2}$ radiation

was eliminated using a germanium monochromator. The geometry used was Bragg-Brentano, consisting of a planar sample with normal axis coinciding with the direction of the scattering vector. Optical slits were used to focus and Soller slits to collimate, both the incident and diffracted beams.

In all measurements, unless otherwise stated in the relevant sections, the beam mask used was of 10 mm and the Soller slits of 0.02 radians. In both instruments, programmable divergence slits and fixed anti-scatter silts of 1º were used for the incident beam optics. For the diffracted beam optics, a fixed anti-scatter slit of 4º and receiving slit of 1º were used in the X'Pert instrument, and an anti-scatter fixed slit of 1/2º was used in the Empyrean. The scan speed was of 0.02º s^{-1} in all experiments.

X-ray powder diffraction data from air-stable samples were collected on either an aluminium plate (recess of dimensions 20 mm x 10 mm x 0.5 mm), or onto a silicon wafer (cleaved along the systematically absent [110] plane) coated with a thin layer of Dow-Corning high vacuum grease.

For experiments with air-sensitive samples, a gas-tight holder shown in Figure 2.5 was used. The samples were loaded on a glass slide coated with a small amount of Dow-Corning high-vacuum grease in an argon filled glovebox. This was then placed inside a gas-tight holder equipped with a thin acetate window and sealed with a rubber o-ring and a brass cap. Data were collected over the range $10 < 2\theta$ (º) < 70 using a continuous scan speed of 0.02 °s^{-1} to compensate for the intensity loss due to absorption by the acetate window.

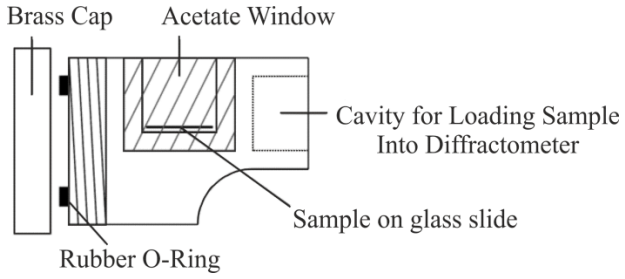


Figure 2.5. Gas-tight holder for the collection of X-ray powder diffraction data from air-sensitive samples.

2.4.1.1.1 Philips Instrument PW1710

A Philips diffractometer PW1710, equipped with a fixed Cu X-ray source and a detector on the 2θ axis, was routinely used to monitor reaction progress. This instrument has a secondary monochromator and the $K_{\alpha 2}$ copper lines are not removed (so both the $K_{\alpha 1}$ and $K_{\alpha 2}$ copper wavelengths are present in the incident beam). The divergence and the receiving slits are fixed, and no Soller slits were used. The standard measurements carried out with this instrument are in the range $3 < 2\theta\ (°) < 70$ with a continuous scan speed of $0.04° \ s^{-1}$. Slower scans were ran in the range $10 < 2\theta\ (°) < 70$ at $0.02º \ s^{-1}$.

2.4.1.1.2 PANalytical X'Pert and Empyrean Instruments

PANalytical X'Pert and Empyrean diffractometers were used to collect data suitable for Rietveld Refinement (Section 2.5). In this instruments a Ge(111) monochromator on the incident beam selects $K_{\alpha 1}$ radiation exclusively, and the beam optics can be adjusted by the choice of beam mask, anti-scatter and Soller slits.

The Empyrean Instrument yields data of higher intensity with respect to the X'Pert diffractometer. However, an improved signal to noise ratio compared to the Empyrean is attained with the X'pert diffractometer by fitting an angle sensitive detector (+/- 1.5º from θ).[59,60]

2.4.1.2 Synchrotron X-ray Powder Diffraction

Synchrotron radiation results from acceleration of charged particles generated by electromagnetic radiation which is forced to change direction around a curved path (by a magnetic field) and with this accelerated at speeds approaching the speed of light. synchrotron X-rays have a range of high frequencies and high quality powder diffraction can be collected by using this radiation.[61]

The data presented in this work were collected on the I11 high resolution powder diffraction beamline at the Diamond Light Source Facility. The I11 beamline is equipped with an undulator source that produces X-rays ranging from 5 to 30 keV.[61] A Si(111) double-crystal-monochromator is used to select the desired beam energy. Samples are

placed in a sealed glass capillary fixed to the centre of a brass ferrule. The brass ferrule is secured into a magnetic base that engages with a precision engineered spinner pre-aligned with the diffractometer's centre of rotation. Scans were performed using the position sensitive detector (PSD) which uses MYTHEN-II silicon microchip technology to provide wide-angle powder diffraction data (2θ = 0-150º) of resolution $\Delta d/d \approx 10^{-3}$-$10^{-4}$.[62]

The GSAS suite of programs was used for all the refinements against X-ray diffraction data (Section 2.5).[63,64] When using this set of software for refinements against synchrotron X-ray diffraction data, an underestimation of the standard uncertainties can arise as a consequence of the high signal to noise ratio, and the large amount of data points.[65] This yields a disproportionately small error for the data sets and leads to values of χ^2 (parameter discussed in Section 2.5) which are much larger than expected. Other parameters (such as the R-factors) were used to evaluate the statistical fit in this case.

2.4.2 Neutron Powder Diffraction

As mentioned in Section 2.4.1, the contribution to the diffracted X-ray intensity is related to the atomic number.[57] This means that determining the changes in the fractional occupancy or position of atomic sites occupied by light elements can become difficult (and unreliable) in the presence of relatively heavy elements. This is the case in the complex transition metal oxides studied in this work, which contain mixtures of light and heavy elements. Therefore, the complete structural characterisation of the samples was not always possible using X-ray powder diffraction data only. Neutron powder diffraction experiments were used in these cases.

Neutrons interact directly with the nuclei of the atoms, and the contribution to the diffracted intensity is different for each isotope. In particular, the nuclei of both anions studied in this work, oxide and hydride, exhibit significant coherent scattering lengths (5.803 and -3.739 fm respectively) and thus are readily 'visible' in a neutron diffraction experiment.[66]

In contrast with the X-ray scattering form factor, which decreases rapidly with the scattering angle, the neutron scattering form factor is essentially constant since the size of the scatterer (nucleus) is not as large compared to the size of the radiation (neutrons).

Neutrons are particles with half-integer spin and they interact with the magnetic moments (from unpaired electrons) of atoms. For magnetically-ordered materials, this interaction results in the presence of additional reflections in the neutron powder diffraction data. The intensity of the magnetic scattering is comparable to that of the nuclear scattering. However, in contrast with the latter, the form factor for the magnetic scattering has an angular dependence which decays even faster than the form factor in X-ray diffraction. This is because magnetic scattering results from the interaction (of neutrons) with the outer-most electrons.[67]

The magnetic scattering structure factor (F_{mag}^{hkl}) for an unpolarised neutron source can be expressed as follows:[68]

$$\boldsymbol{F_{hkl,mag} = \sum_j q_j p_j e^{2\pi i h x_j}} \qquad (2.5)$$

where q_j is the magnetic interaction vector, p_j is the magnetic form factor, h the magnetic scattering vector and x_j the position vector of magnetic atoms in the unit cell. The observed intensity of a magnetic reflection ($I_{hkl,mag}$) is proportional to the square of the projection of the magnetic structure factor onto the scattering vector:[68]

$$\boldsymbol{I_{hkl,mag} = |F_{hkl,mag}|^2 cos^2 \alpha} \qquad (2.6)$$

where α is the angle between the magnetic scattering structure and the relevant lattice plane.

Given that the neutron scattering interaction is relatively weak, large scale samples (of a minimum of 1.5 g) were prepared for the experiments. Samples were loaded in vanadium cans which have a relatively small contribution as the vanadium exhibits a low coherent scattering length (-0.3824 fm).[66]

Neutrons can be generated by nuclear reactor sources (in which the neutron radiation arises from a fission process), or by spallation sources (where the neutrons are expelled from a heavy metal target being hit by pulses of accelerated high-energy protons). The former is the source used at the Institut Laue-Langevin (ILL) in Grenoble, France, and the latter at ISIS neutron facility, Rutherford Appleton Laboratory in Oxfordshire. The neutron powder diffraction data in this work were collected at these two facilities.[69,70]

2.4.2.1 D2B Instrument

The D2B Instrument (Figure 2.6) is a high-resolution powder diffractometer at ILL. The ILL neutron source provides neutrons with an extremely high intensity (energies in the meV range) from fission of ^{235}U. The fission process is sustained by reducing the energy of produced neutrons by a moderator filled with D_2O. The neutrons resulting from this process are of suitable energies to perform diffraction experiments, with appropriate wavelengths (maximum flux at 1.2 Å) which can be further moderated by using a crystal monochromator.

The D2B is a two-axis diffractometer with a high take-off angle (135°) for the monochromator. Scans were performed over the range $5 < 2\theta\ (°) < 160$ with several scans being summed to improve the statistics. The wavelength of the incident neutron beam can be selected by rotation within the (*hhl*) plane of a Ge crystal monochromator. A wavelength of 1.594 Å was used for all experiments in this investigation.

For a constant wavelength diffractometer the resolution is a function of the variation of the full width at half maximum (FWHM) of a Bragg reflection with respect to the scattering angle. The Cagliotti function describes this relation:[71]

$$\boldsymbol{\sigma^2 = \frac{FWHM^2}{8ln2} = Utan^2(\theta) + Vtan(\theta) + W} \qquad (2.7)$$

Both instrumental parameters (such as the monochromator geometry and beam collimation), and sample parameters (structural features), contribute to *U*, *V* and *W*.

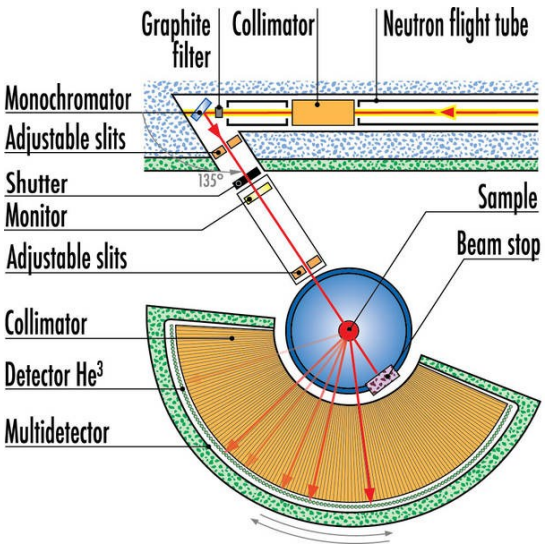


Figure 2.6. D2B diffractometer at ILL, Grenoble, France.[72]

2.4.2.2 POLARIS Instrument

The POLARIS Instrument (Figure 2.7) is a high-intensity, medium resolution powder diffractometer at the Rutherford Appleton laboratory at ISIS neutron facility. A pulsed neutron beam is generated in this facility, by firing high energy protons at a tungsten target. The process is achieved by accelerating hydride ions into a synchrotron, which ionises the hydride ions to protons and fires them in pulses at the target at 50 Hz. Neutron pulses generated by this process have very high thermal energies and must be slowed down using a hydrogenous moderator (H_2O in the case of the POLARIS instrument) so that their wavelength is suitable for diffraction. This method produces a pulse of neutrons with a range of wavelengths suitable for time-of-flight measurements.[73]

Time-of-flight diffractometers use an energy dispersive mode with detectors at fixed scattering angles around the sample to measure diffraction patterns as a function of the wavelength. The time-of-flight over a known distance can be related to the wavelength using the de Broglie relation:

$$\boldsymbol{\lambda} = \frac{\boldsymbol{h}}{\boldsymbol{m}} \times \frac{\boldsymbol{t}}{\boldsymbol{L}} \qquad (2.8)$$

where h is Planck's constant, m the neutron mass, and t the time taken to travel distance L from the moderator to the detector via the sample.

The POLARIS Instrument is equipped with six banks of detectors (Figure 2.7, Table 2.1).[74]

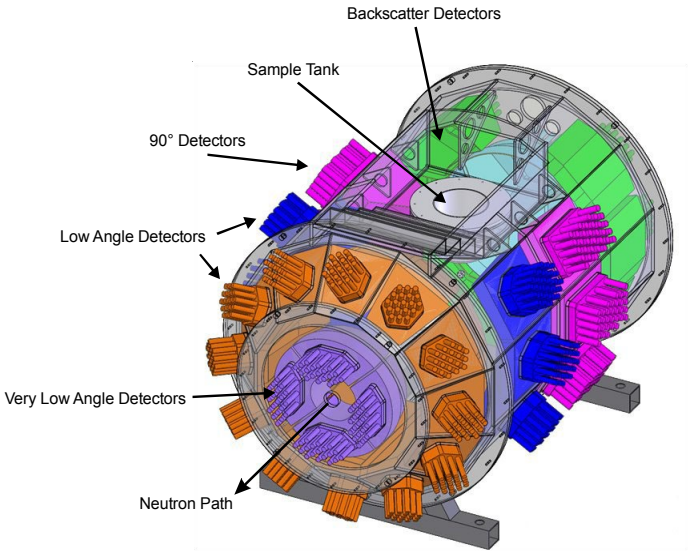


Figure 2.7. New POLARIS instrument at the ISIS facility.[74]

Table 2.1: Detector banks following the POLARIS upgrade.

Detector Bank		**2θ Range / °**	**d_{max} / Å**
Very Low Angle	1	6 – 14	19.6
Low Angles	2	19 – 34	8.7
	3	40 – 67	7.0
90 °	4	75 – 113	3.2
Back-scattering	5	135 – 143	2.7
	6	146 – 168	2.7

For a time-of-flight diffractometer, the resolution $R(d)$ is given by the width of a reflection Δd over its position in d-space, and is dependent on the uncertainty in the time-of-flight (Δt), the uncertainty in path-length over which the neutron has travelled (ΔL), and the uncertainty in the diffracted angle ($\Delta\theta$):[75]

$$\boldsymbol{R(d) = \frac{\Delta d}{d} = \sqrt{\Delta\theta^2 cot^2(\theta) + \left(\frac{\Delta t}{t}\right)^2 + \left(\frac{\Delta L}{L}\right)^2}} \qquad (2.9)$$

2.5 Rietveld Refinement

The Rietveld method was used to analyse X-ray and neutron powder diffraction data with the GSAS suite of programs.[64] The extraction of structural information is inherently difficult from powder diffraction data, where peak overlap and d_{hkl} degeneracy prevent exact structure factors to be calculated from reflection intensities. The Rietveld method allows for a structural model, which is a starting point close to the real structure, to be

compared against the observed diffraction pattern so that when the model is correct the 'true' values for the intensities can be predicted.[63]

During a Rietveld refinement experiment, the intensity of the reflections in the structural model are compared to those observed in the collected data via the relation:

$$\boldsymbol{S = \sum_i w_i (y_{io} - y_{ic})^2} \qquad (2.10)$$

where w_i is the weighting factor, y_{io} the observed intensity at point i in the diffraction pattern, and y_{ic} the calculated intensity at point i. Diffraction and structural parameters are then refined against the experimental data using a least squares optimisation technique in order to minimise S.

The statistical fit to the data is assessed using three parameters: reduced χ^2, the residual function (R_p) and the weighted residual function (wR_p). These functions are defined as follows:

$$\boldsymbol{\chi^2 = \frac{\sum w_i (y_{io} - y_{ic})^2}{n_{obs} - n_{var}}} \qquad (2.11)$$

$$\boldsymbol{R_p = 100 \times \frac{\sum |y_{io} - y_{ic}|}{\sum y_{io}} \%} \qquad (2.12)$$

$$\boldsymbol{wR_p = 100 \times \sqrt{\left(\frac{\sum w_i (y_{io} - y_{ic})^2}{\sum w_i y_{io}^2}\right)} \%} \qquad (2.13)$$

where n_{obs} is the number of observations in all histograms and n_{var} is the number of variables in the least squares refinement.

2.5.1 Size and Strain from the Refined Peak Profile

The description of the observed peak shapes in the diffraction patterns is central during a Rietveld analysis (the 'goodness of fit' depends strongly on it). The peak shapes were modelled in GSAS using a pseudo-Voigt function which convolutes Gaussian and Lorentzian components.[64,76] The Gaussian full-width at half-maximum (FWHM), Γ_g, is defined as:[77]

$$\boldsymbol{\Gamma_g = \sqrt{(8ln2)\sigma^2}} \qquad (2.14)$$

which has a 2θ dependence of :

$$\boldsymbol{\sigma^2 = U \tan^2 \theta + V \tan \theta + W} \qquad (2.15)$$

The Lorentzian coefficient, γ, has a 2θ dependence:

$$\boldsymbol{\gamma = \frac{LX}{\cos\theta} + LY \tan\theta} \qquad (2.16)$$

There are both instrumental and sample-dependent contributions to the peak widths in a powder diffraction experiment. In this work, for the purpose of comparison between samples, the Lorentzian components were taken to be mainly a contribution from the sample while the Gaussian components were assumed to be mainly a contribution form the instrument.

The coefficients LX and LY can be used to calculate the average size of the crystalline domains and the isotropic strain present in a sample.

2.5.1.1 Particle size broadening

Using the Lorentzian isotropic particle size broadening term LX, the particle size *p* (in Å) was calculated using the following relation:[64]

$$\boldsymbol{p = \frac{18000K\lambda}{\pi(LX)}} \qquad (2.17)$$

where the units of LX are hundredths of a degree (and hence the term 18000 arises), K is the Scherrer constant taken to be 1 and λ is the copper $K_{\alpha 1}$ wavelength 1.5406 Å.

2.5.1.2 Strain broadening

Using the Lorentzian isotropic strain broadening term LY, the strain in percentage was calculated as:[64]

$$\boldsymbol{strain(\%) = 100\%(LY)\left(\frac{\pi}{18000}\right)} \qquad (2.18)$$

where the units of LY are hundredths of a degree.

2.6 SQUID Magnetometry

The magnetic susceptibility of the samples was measured using a Quantum design MPMS XL Superconducting Quantum Interference Device. The SQUID magnetometers consist of a superconducting ring with two weak link insulating barriers known as Josephson Junctions.[78] Upon application of an electric current (which in some SQUIDs can be either

direct or alternating), Cooper pairs are able to tunnel across the junctions with phase coherence (Figure 2.8).[79]

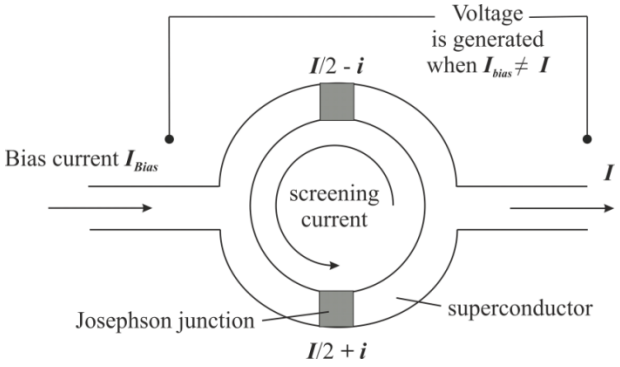


Figure 2.8. Schematic representation of the principal component in a SQUID magnetometer.[78]

The application of a magnetic field on this system, induces an opposing current in the coil which, after surpassing a critical value (a *critical current*), 'breaks' the superconductivity of the coil and impedes the tunnelling of the cooper pairs through the Josephson Junctions.

During a SQUID measurement, samples are moved through a pickup coil, which is connected to the superconducting detection coil depicted in Figure 2.8, while an external magnetic field is applied. The magnetic flux induced by the moving sample interrupts the supercurrent in the detection coil. An applied bias current is then applied to re-establish the supercurrent in the coil. This bias current is directly related to the magnetic flux produced by the sample and when the magnitude is greater than the critical current, a voltage is produced across the SQUID and this voltage is measured.[80]

For the measurements in this work, samples of approximately 20 mg were weighed and placed in a gelatine capsule inside a drinking straw, with four empty capsules on either side. The outermost capsules were covered in a layer of diamagnetic tape to hold the sample in place. Air sensitive samples were prepared in the glovebox and kept under an inert atmosphere until they could be loaded into the chamber of the SQUID.

Magnetisation data from samples were collected either as a function of temperature (zero-field cooled and field cooled susceptibility data) or as a function of the applied field (M/H isotherms). The magnetic susceptibility as a function of temperature was normally measured in the range $5 \leq T\ (K) \leq 300$ at an applied field of 100 Oe. The field range for the isotherms was $-50000 \leq H\ (Oe) \leq 50000$ at a constant temperature (*e.g.* 5 K, 300 K).

2.6.1 Ferrosubtraction Measurements

When ferromagnetic impurities were present in the samples a *ferromagnetic subtraction* was performed. The method used for this work consisted of fitting a linear function to the data of magnetisation-field isotherms at values of field at which the ferromagnetic impurities are normally saturated (Figure 2.9).[81] The magnetisation of the samples was measured in a series of 5 fields in the range $30000 \leq H\ (Oe) \leq 50000$. The gradient of the linear functions fitted to the magnetisation-field isotherms is equal to the paramagnetic susceptibility and the intercept is equal to the saturated ferromagnetic contribution.

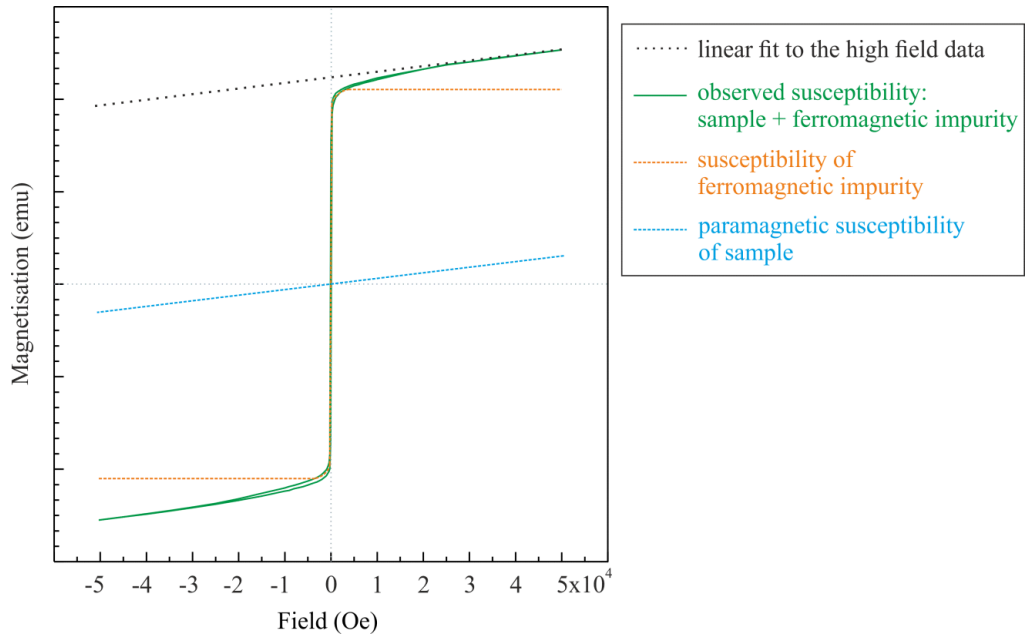


Figure 2.9. Schematisation of a magnetisation-field isotherm of a sample consisting of a paramagnetic phase and a ferromagnetic impurity phase. The dotted line indicates the region used for a ferromagnetic subtraction experiment.

All fits had at least 4 data points with data points with large errors being excluded (see Appendix 2). This procedure was repeated at 5 K intervals between 5 K and 300 K to measure the temperature dependent susceptibility of samples.

2.6.2 Curie-Weiss Law

The paramagnetic susceptibility of a material (denoted as χ_m in this work) can be defined as the magnetic dipole density (*M*) in the material, induced by an applied field (*H*).[82] The expression for the paramagnetic susceptibility is normally expressed as:

$$\boldsymbol{\chi_m = \frac{M}{H}} \qquad (2.19)$$

where the three parameters in Equation 2.19 are vectors (χ_m in particular a tensor), however, since they tend to be parallel, this equation is very often written in the scalar form. The magnetic susceptibility can be derived from the partial derivatives of the components of the vector ***M*** with respect to ***H***.

The paramagnetic susceptibility of a material can be modelled using the Curie-Weiss law:

$$\boldsymbol{\chi_m = \frac{C}{T-\theta}} \qquad (2.20)$$

where θ is the Weiss constant, a measure of the strength of the interactions present, and *C*, the Curie constant which can be defined as:[82]

$$\boldsymbol{C = \frac{N_A \mu_B g^2 S(S+1)}{3k_B} \approx \frac{1}{8}\mu_{eff}^2} \qquad (2.21)$$

N_A in the expression for the Curie constant is Avogadro's number, μ_B is the Bohr magneton, *g* is the Landé factor, *S* is the spin quantum number of the magnetic ion, k_B is Boltzmann's constant and μ_{eff} is the effective magnetic moment.

A temperature-independent paramagnetic contribution can be accounted for in the Curie-Weiss law by the inclusion of a further constant *K*:

$$\boldsymbol{\chi_m = \frac{C}{T-\theta} + K} \qquad (2.22)$$

The number of magnetic atoms present in the sample can be determined from the definition of the Curie constant.[19] The latter was used in Chapter 8 (concerning cation exchange reactions) to evaluate the level of substitution from magnetic transition-metal cations (Section 8.3.1.1 and 8.3.2.1).

2.7 Thermogravimetric Analysis (TGA)

Thermogravimetric analysis consists of measuring the mass of a sample as a function of temperature. By heating the sample under a reactive gas flow (e.g. a reducing gas flow or an oxidising one), chemical information about samples can be obtained. In this work, reductive and oxidative decompositions were useful for determining the composition of the samples, and in particular the content of oxygen.

For a generic, reduced ABO_{3-x} perovskite:

$$ABO_{3-x(s)} + O_{2(g)} \rightarrow ABO_{3(s)} \qquad (2.3)$$

$$ABO_{3-x(s)} + H_{2(g)} \rightarrow AO_{(s)} + B_{(s)} + H_2O_{(g)} \qquad (2.4)$$

In both cases, from knowledge of the mass of the sample at the beginning and end points, together with the compositions at the end point (normally from X-ray diffraction data), the amount of oxygen gained or lost was calculated. From the latter data, the initial composition of the samples can be proposed.

All measurements were carried out using the Mettler Toledo TGA/DSC 1 STARe system. The TGA balance furnace was loaded with 20-50 mg of sample in an alumina can and accurately weighed. The maximum error of the TGA balance for the data reported in this thesis was determined to be 0.003% of the measurement plus/minus an absolute error of 20 micrograms using standard 1 gram weights. Details of the (reductive or oxidative) conditions used in each case are given in the relevant sections.

2.8 Manganometric Titrations

Chapters 6 and 7 concern the characterisation of samples containing vanadium. For these samples, the vanadium oxidation state was determined via titration with $KMnO_4$ using the method described by Niwa and Murakami.[83] Samples were dissolved in 4.5 M H_2SO_4 and the resulting solution was titrated against a $KMnO_4$ solution of known concentration, determined by standardisation with dried samples of $Na_2C_2O_4$.[84]

Reduced vanadium ions in solution are oxidised by $KMnO_4$ to V^{5+} as follows:

$$z\left(MnO_4^- + 8\,H^+ + 5\,e^- \longrightarrow Mn^{2+} + 4\,H_2O\right) \quad (2.5)$$

$$5\left(V^{(5-z)+} \longrightarrow V^{5+} + z\,e^-\right) \quad (2.6)$$

For the experiments, approximately 25 mg of the samples were accurately weighed in an argon filled glove box. After being transferred outside of the glove box (in a sealed three necked flask), samples were dissolved in a 1:1 solution of H_2SO_4 in deionised water. The resulting solutions were titrated using a 0.0035(2) M $KMnO_4$ solution which was standardised by titrating against $Na_2C_2O_4$. An argon flow was used to avoid oxidation of the samples by air throughout the titrations. The errors reported for the calculated oxidation state come from the standard deviation in the measurement of the mass and the volume of titre used for each titration trial.

2.9 Bond Valence Sums

The valence of an ion, V_i, can be estimated by considering the sum of the valences of all the individual bonds within the coordination sphere of the ion.[85] This approximation can be written as:

$$\boldsymbol{V_i = \sum_j v_{ij}} \quad (2.23)$$

where the valence v_{ij} of a bond between atoms i and j is given by:

$$\boldsymbol{v_{ij} = e^{(R_{ij} - d_{ij})/b}} \quad (2.24)$$

where b is an empirical constant (taken to be 0.37)[86], R_{ij} is the 'bond-valence parameter', and d_{ij} is the bond length. Bond valence calculations performed in this investigation used R_{ij} values published by Brese and O'Keefe.[85]

2.10 Muon-Spin Relaxation Spectroscopy (μSR)

Muon-Spin Relaxation Spectroscopy (μSR) is a technique that uses the muon spin to examine structural and dynamical processes in a material with which insight into the magnetic and electronic properties is gained. It consists of implanting spin polarised muons within a material and then measuring the decay process. The muons decay emitting a *fast decay positron* (an anti-electron) preferentially along the direction of the

muons' spin. The decay of positrons from 'a bunch' of muons deposited at the same conditions allows the determination of the statistical average direction of the spin polarisation of the implanted muon ensemble. The time evolution of the muon spin polarisation depends sensitively on the spatial distribution and dynamical fluctuations of the magnetic environment.[87]

Muons are produced by collisions between high-energy protons and a light element target such as graphite, which produce pions that subsequently decay into leptons (muons or electrons in a ratio of approximately 8000:1) and neutrinos with mean lifetime of 26×10^{-9} seconds. Beampipes are then used to focus the muon beam and discard unwanted particles, guiding the muons into the sample such that they arrive with correct energies and practically 100% spin polarised.[87]

μSR data were collected at the Paul Scherrer Institute in Switzerland by Prof. Stephen J. Blundell.

2.11 Second Harmonic Generation (SHG)

The Second Harmonic Generation (SHG) is an optical effect that occurs when photons interact with a medium that lacks inversion symmetry. In such a medium, photons interact non-linearly and effectively 'combine' to give way to 'new' photons with twice the energy (and therefore twice the frequency or half the wavelength), of the initial photons. Such non-linear effects were only possible to observe after the extreme intensities of the laser were realised in 1960.[88] The induced polarisation, P, occurring in a material when irradiated with a large optical field can be expressed by the expansion:

$$P_i = \chi_{ij}E_j + \chi_{ijk}E_jE_k + \chi_{ijkl}E_jE_kE_l + \ldots \qquad (2.25)$$

where χ_{ij} is the linear electric susceptibility, and the later terms arise due to various non-linear effects. The first non-linear term (E_jE_k) containing the third-rank susceptibility tensor χ_{ijk}, corresponds to the SHG. The inequality $\chi_{ijk} \neq 0$ holds only in a non-centrosymmetric environment. Experimentally, the observation is the conversion of a specific wavelength, *e.g.* an Nd-YAG laser with wavelength of 1064 nm, into half its original, *i.e.* a green laser with wavelength of 532 nm.

It is only possible for a phase to exhibit a net spontaneous electric polarization if it crystallises in a non-centrosymmetric structure, and as well as ferroelectricity, other interesting physical properties such as piezoelectricity and pyroelectricity, can only arise in phases which lack inversion symmetry. Therefore, determining the SHG activity can be a powerful technique for probing the properties of new materials. In this work, SHG activity measurements were carried out on powder samples, using a modified Kurtz-Powder Laser system.[88] The representation of the experimental setup used for the measurements is shown in Figure 2.10.

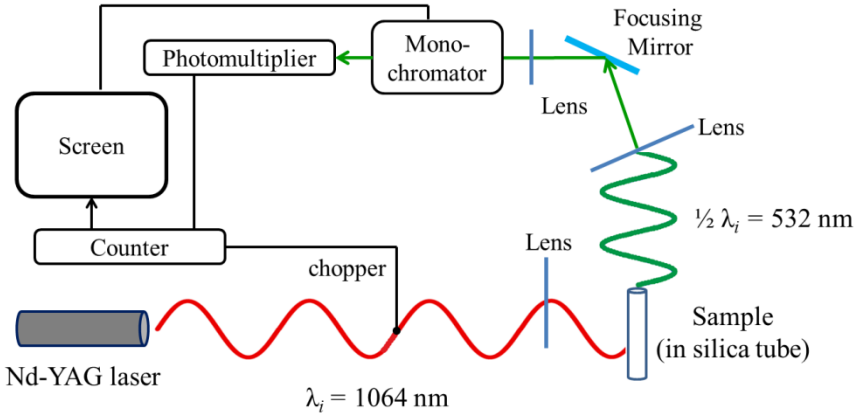


Figure 2.10. Schematic representation of the experimental setup for the SHG measurements using a Kurtz-Powder Laser System.

Approximately 50 mg of sample, were placed in a fused silica tube, and irradiated with a pulsed Nd-YAG laser (λ = 1064 nm). The resulting polarisatrion was compared with that of α-SiO_2 (non-phase-matchable) and $LiNbO_3$ (phase-matchable). Since the powder SHG efficiency has been shown to depend strongly on particle size,[89] samples were ground and sieved into distinct particle size ranges, and the comparisons were made with same particle size ranges of the ground and sieved references of α-SiO_2 and $LiNbO_3$.

Chapter 3

Synthesis of $LaSrNiRuO_6$ – Microstructural Aspects of the Starting Materials for $LaSrNiRuO_4$

3.1 Introduction

The low-temperature topochemical reduction of complex metal oxides using binary metal hydrides has enabled the preparation of a wide range of novel metastable materials, as discussed in Section 1.3.1. These structure-conserving reactions can give access to unusual transition-metal oxidation states and coordination geometries, which result in interesting electronic and magnetic properties such as multiferroic behaviour, high-temperature superconductivity and metal-insulator transitions.[39,48,49,81]

Mixed 3*d*/4*d* and 3*d*/5*d* metal oxides can exhibit complex electronic and magnetic behaviour arising from coupling interactions between the compact 3*d* orbitals and the more extended 4*d* and 5*d* orbitals. For example, the double perovskite phase Sr_2FeMoO_6 exhibits half-metallic ferromagnetic behaviour, which arises from the magnetic coupling between electrons localized in 3 d^5 iron states and those in delocalized bands derived from the molybdenum 4*d* orbitals.[90] This modulated coupling interaction has raised interest in this type of mixed transition metal oxides.

Attempts to topochemically reduce *4d* and *5d* transition metal oxides usually result in reduction to the elements. However, coupling the reduction of *4d* and *5d* cations to the formation of a robust, stable framework prevents them from being reduced all the way to their elemental state. Examples of such stabilisation are the products of reduction of the perovskite phase $SrRu_{0.5}Fe_{0.5}O_3$, and the Ruddlesden-Popper phase $Na_2La_2Ti_2RuO_{10}$, to give $Sr(Ru_{0.5}Fe_{0.5})O_2$ and $Na_2La_2Ti_2RuO_{10-x}$ respectively (Figure 3.1).[38,91] In these phases, the robustness of the *3d* transition metal lattice (Sr-Fe-O and Na-La-Ti-O), allows access

to extended oxide phases containing low-valent ruthenium via topochemical reduction. $SrFe_{0.5}Ru_{0.5}O_2$ was the first reported extended oxide containing Ru^{2+} centres, and the first reported diamagnetic Ru^{2+} centres were observed in the phases $Na_2La_2Ti_2RuO_{10-x}$ ($0 < x < 1$).

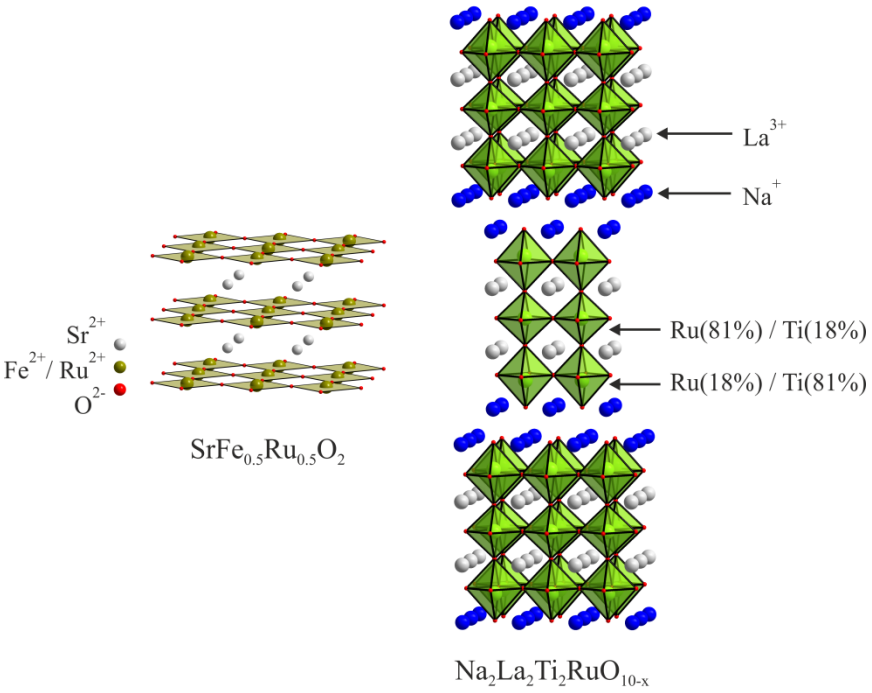


Figure 3.1. Structures of $Sr(Ru_{0.5}Fe_{0.5})O_2$ and $Na_2La_2Ti_2RuO_8$.

Building on this work, further investigations into the extent to which the highly reduced Ru^{2+} oxidation state can be stabilised by *3d* transition metals were carried out. In particular, the possibility of reducing the cation ordered double perovskite phase $LaSrNiRuO_6$ (depicted in Figure 3.2), to form an anion-deficient phase analogous with $SrFe_{0.5}Ru_{0.5}O_2$ was investigated.

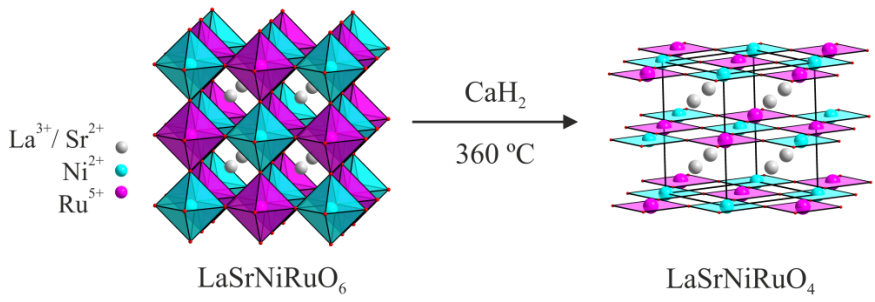


Figure 3.2. Reduction of $LaSrNiRuO_6$ to form $LaSrNiRuO_4$.

The formation of $LaSrNiRuO_4$ proved challenging. The comparison of reduction reactions after identical periods of time and under the same conditions revealed an inconsistent progress of reduction for different samples of $LaSrNiRuO_6$. Exploration of the experimental variables involved in the reduction reactions (described in Chapter 4) narrowed the difference in reactivity down to the cooling rate used during the synthesis of the $LaSrNiRuO_6$ starting materials. Two different cooling rates were used after the last heating period during the synthesis of the starting materials: slow-cooling and rapid-cooling (quenching). The influence of the cooling rate on the $LaSrNiRuO_6$ resulting material was investigated. The focus of this chapter is on these investigations. Chapter 4 discusses the reactivity towards reduction of the different $LaSrNiRuO_6$ starting materials with the characterisation of $LaSrNiRuO_4$ being presented in Chapter 5.

3.2 Experimental

3.2.1 Synthesis of $LaSrNiRuO_6$

Samples of $LaSrNiRuO_6$ were prepared via a citrate gel method (Section 2.1.2). Suitable stoichiometric ratios of La_2O_3 (Alfa Aesar 99.999%), $SrCO_3$ (Alfa Aesar 99.99%), Ni powder (Alfa Aesar 99.996%), and RuO_2 (from RuO_2 hydrate Alfa Aesar 99.99%, dried at 800°C) were dissolved in a minimum quantity of 6 M nitric acid. 3 molar equivalents of citric acid and 5 ml of analar ethylene glycol were added and the solution heated with constant stirring on a hotplate. The citrate gel precursors thus formed were subsequently ground into a fine powder (using an agate mortar and pestle), placed in an alumina crucible and heated at 1 °C min^{-1} to 900 °C in air. The powders were then reground, pressed into 13 mm pellets and then heated at 1200 ºC in air for 2 periods of 24 hours. After the final heating period, two different cooling methods were used:

- Method 1: samples were cooled from 1200 ºC to room temperature at 4 ºC min^{-1}.
- Method 2: samples were taken out of the furnace at 1200 ºC and allowed to equilibrate rapidly to room temperature.

Method 1 will be referred as slow-cooling and method 2 as quenching.

3.2.2 X-ray Powder Diffraction Experiments

X-ray powder diffraction data were collected from the slow-cooled and quenched $LaSrNiRuO_6$ samples using the PANalytical X'Pert and Empyrean instruments described in Section 2.4.1.1. To eliminate any instrumental contributions, the same instrument with identical conditions and beam optics was used to collect equivalent data sets from the samples being compared. The conditions are detailed in Section 3.3.4.

3.2.3 Thermogravimetric Measurements

The composition of the slow-cooled and quenched $LaSrNiRuO_6$ samples was determined from reductive thermogravimetric measurements by considering the following decomposition reaction:

$$LaSrNiRuO_{6-x} \xrightarrow[10\%\ H_2\ in\ N_2]{T = 900\ ^oC} 1/2\ La_2O_3 + SrO + Ni + Ru + (9/2-x)\ H_2O \quad (3.1)$$

Decompositions were performed by heating a small amount of the $LaSrNiRuO_6$ samples (~ 10.0 mg) at 900 ºC under a 10% H_2 in N_2 flow. The products La_2O_3, SrO, Ni and Ru (Reaction 3.1), were confirmed via X-ray powder diffraction.

3.3 Results

3.3.1 Structure of $LaSrNiRuO_6$ from X-ray Powder Diffraction

Figure 3.3 shows the X-ray powder diffraction data collected from a slow-cooled ('SC', top), and a quenched ('Q', bottom) $LaSrNiRuO_6$ sample. A model based on a monoclinic cell of space group $P2_1/n$ was refined against both sets of data.[92] Table 3.1 shows the refined Ni/Ru order and lattice parameters. Results from refinement of the Ni/Ru order led to a 5.9(3)% and 8.3(4)% antisite disorder in the slow-cooled and quenched samples respectively, confirming that both phases are close to B-cation ordered. The refined lattice parameters are in good agreement with the literature values (a = 5.575(1) Å, b = 5.542(1) Å, c = 7.849(1) Å, β = 90.00(1)º).[92] A small amount of NiO was observed as a secondary phase (weight fractions = 1.15(1)%, 1.11(1)%).

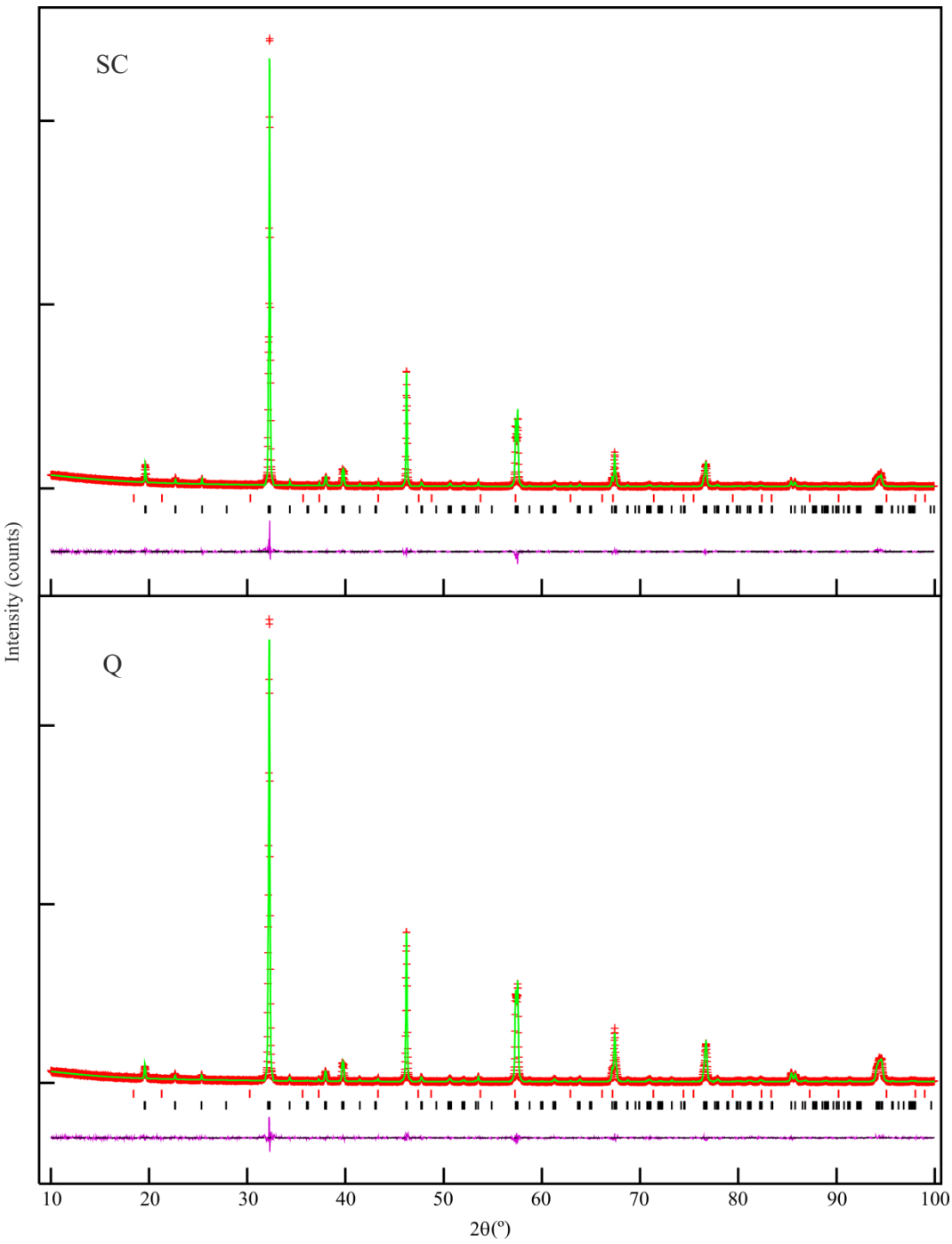


Figure 3.3. Observed, calculated, and difference plots from refinement of the structural model of $LaSrNiRuO_6$ in space group $P2_1/n$ against X-ray powder diffraction data collected from a slow-cooled and a quenched samples. The upper set of tick marks corresponds to the NiO secondary phase.

Table 3.1. Lattice parameters and Ni/Ru atomic fractions in the structural model of $LaSrNiRuO_6$ in space group $P2_1/n$ refined against X-Ray powder diffraction data of a slow-cooled and a quenched sample.

Slow-Cooled Sample						
atom	**Wyck.**	***x***	***y***	***z***	**fraction**	U_{iso} **(Å^2)**
Ni(1)/Ru(1)	*2c*	1/2	0	1/2	0.941(3)/0.059(3)	0.0353(3)
Ru(2)/Ni(2)	*2d*	1/2	0	0	0.941(3)/0.059(3)	0.0353(3)
Lattice parameters:						
a **(Å)**	***b*** **(Å)**	***c*** **(Å)**		***β*** **(º)**	***V*** **(Å^3)**	
5.575(1)	5.545(1)	7.853(1)		89.99(1)	242.8(1)	
$\chi^2 = 1.296$; $wR_p = 8.46\%$, $R_p = 5.93\%$						
NiO: space group *Fm*-3*m*; *a* = 8.355(1) Å; weight fraction = 1.15(1)%						
Quenched Sample						
atom	**Wyck.**	***x***	***y***	***z***	**fraction**	U_{iso} **(Å^2)**
Ni(1)/Ru(1)	*2c*	1/2	0	1/2	0.915(4)/0.085(4)	0.0161(4)
Ru(2)/Ni(2)	*2d*	1/2	0	0	0.915(4)/0.085(4)	0.0161(4)
Lattice parameters:						
a **(Å)**	***b*** **(Å)**	***c*** **(Å)**		***β*** **(º)**	***V*** **(Å^3)**	
5.574(1)	5.543(2)	7.851(2)		89.99(1)	242.6(2)	
$\chi^2 = 1.748$; $wR_p = 10.14\%$, $R_p = 6.95\%$						
NiO: space group *Fm*-3*m*; *a* = 8.355(1) Å; weight fraction = 1.11(1)%						

3.3.2 Composition of Slow-Cooled and Quenched $LaSrNiRuO_6$ Samples from Thermogravimetric Measurements

Thermogravimetric data collected during the reductive decomposition of the slow-cooled and quenched samples of $LaSrNiRuO_6$ are shown in Figure 3.4. An additional quenched sample, which will be described in Section 3.3.3, is shown in Figure 3.5. The resulting mass loss, together with the X-ray diffraction data collected from the products of decomposition, suggest that all three samples had the same composition and content of oxygen as summarised in Table 3.2. The secondary phase NiO was accounted for in the calculations and the reported error for the oxygen content of the samples was estimated from the expected value.

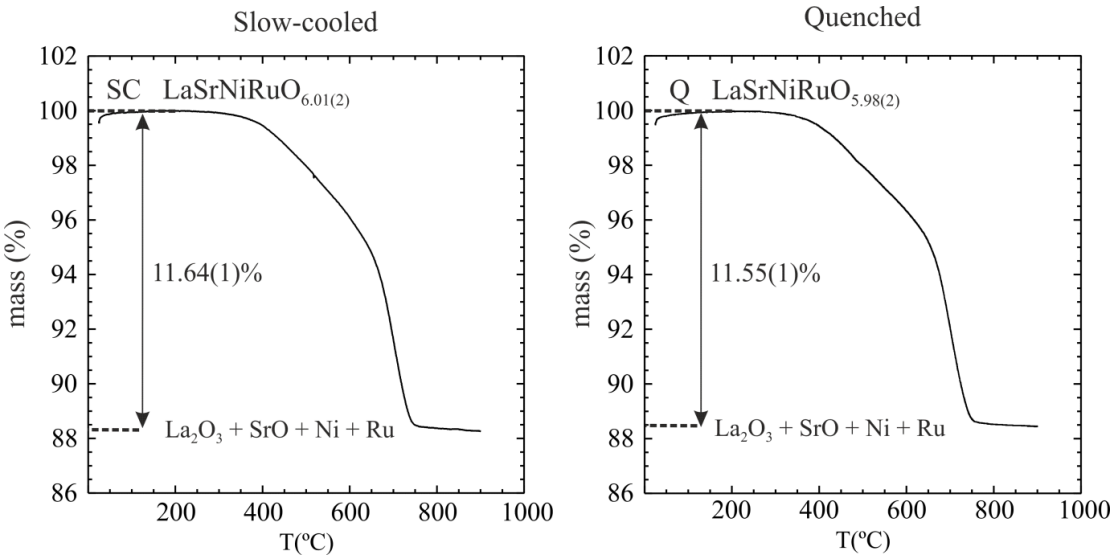


Figure 3.4. Thermogravimetric data collected during the reduction of slow-cooled and quenched $LaSrNiRuO_6$ samples to La_2O_3, SrO, Ni and Ru.

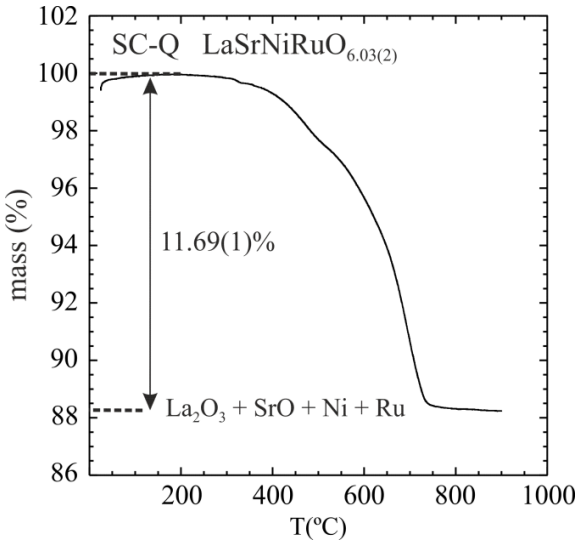


Figure 3.5. Thermogravimetric data collected during the reduction of a quenched $LaSrNiRuO_6$ sample to La_2O_3, SrO, Ni and Ru.

Table 3.2. Summary of results from thermogravimetric analysis of slow-cooled and quenched $LaSrNiRuO_6$ samples.

Sample	Mass loss (%)	RMM*	Oxygen content
Slow-cooled 'SC'	11.64(1)	482.45	6.01(2)
Quenched 'Q'	11.55(1)	481.97	5.98(2)
Quenched 'SC-Q'	11.69(1)	482.77	6.03(2)

* The RMM in were calculated considering that the mass loss expected from an exact $LaSrNiRuO_6$ composition (RMM 482.29), is 11.61%.

3.3.3 Comparison of X-ray Powder Diffraction Data of Slow-Cooled and Quenched $LaSrNiRuO_6$ Samples

Results from refinement of the structures of both slow-cooled and quenched samples in combination with the TGA data demonstrate that the two sets of samples are indistinguishable in terms of their crystal structure and composition. However, closer inspection of the X-ray diffraction data revealed differences in the peak profile shapes. Figure 3.6 shows the highest intensity peaks in the X-ray powder diffraction patterns collected from the slow-cooled and quenched $LaSrNiRuO_6$ samples. The 200, 112, -112 and 020 reflections, which constitute the main peaks in the X-ray powder diffraction pattern of a monoclinic cell of space group $P2_1/n$, are indexed for the data collected from the slow-cooled sample (Figure 3.6 left).

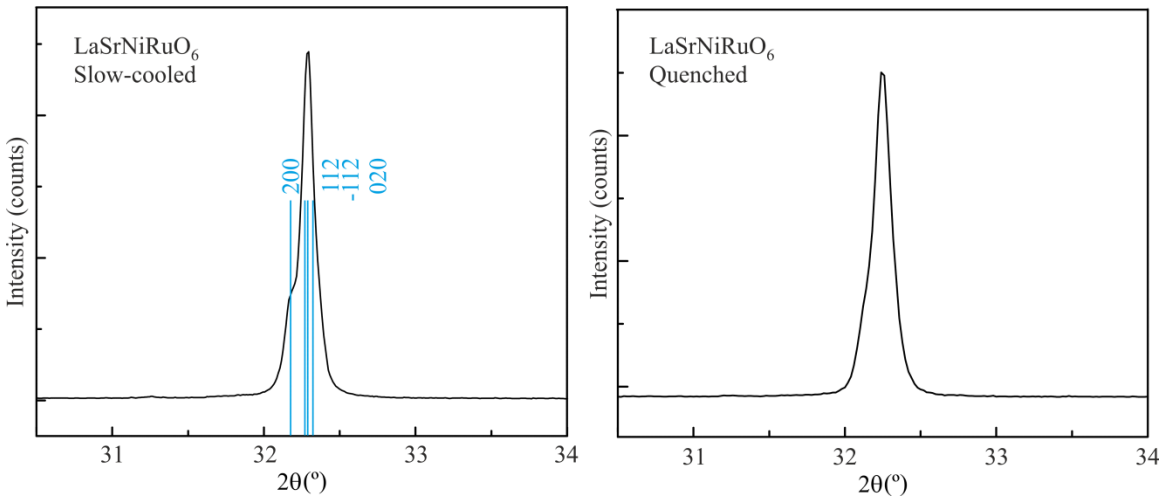


Figure 3.6. Region 30 < 2θ(º) < 35 of the X-ray powder diffraction patterns collected from a slow-cooled (left) and a quenched (right) $LaSrNiRuO_6$ sample.

Upon inspection of both diffraction patterns it became apparent that while the main reflections 200, 112, -112 and 020 yield well defined peaks in the diffraction pattern of the slow-cooled sample (this is particularly clear for the peak corresponding to the reflection 200), all the reflections seem to overlap for the quenched sample. Given that both samples have identical lattice parameters within error, the observed difference suggests that the peaks are broader for the quenched sample.

For a better comparison of the X-ray diffraction data of slow-cooled and quenched $LaSrNiRuO_6$ samples, a fraction of the slow-cooled $LaSrNiRuO_6$ sample was heated at 1200 ºC in air for 2 hours, and then rapidly quenched to room temperature (cooling method 2, Section 3.2.1). A comparison of the X-ray diffraction data collected from this 'slow-cooled subsequently quenched' sample (denoted as SC-Q) with the data of the original SC slow-cooled sample, is shown in Figure 3.7. The data shows that in addition to the differences previously described for the main peaks at $2\theta(^o) \approx 32.25$. The differences in broadness of peaks are also observed for the sets at $2\theta(^o) \approx 56$, 85.5 and 94.5.

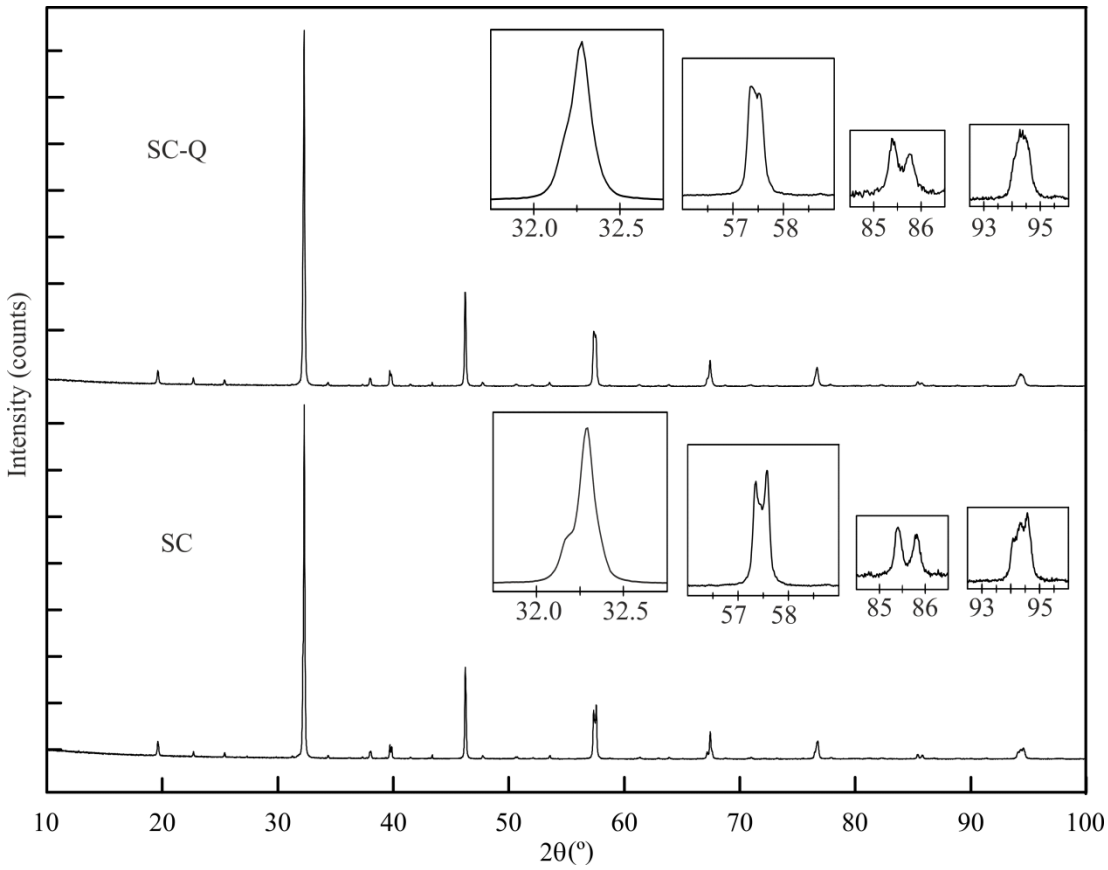


Figure 3.7. Comparison of X-ray diffraction patterns of the slow-cooled subsequently quenched sample (top) and the original slow-cooled sample (bottom). Insets show expanded regions 32 < 2θ(º) < 33, 56 < 2θ(º) < 59, 84 < 2θ(º) < 86, 93 < 2θ(º) < 96.

The fit to the $P2_1/n$ monoclinic model refined against the data collected from the SC-Q sample is shown in Figure 3.8. No change was observed in the lattice parameters of the quenched sample compared to the original slow-cooled sample, and the TGA data shown in Figure 3.5 (Table 3.2) revealed identical compositions for the two samples. Refinement

of the Ni/Ru order led to 8.3(4)% antisite disorder (Table 3.3), suggesting that the cation order is preserved over the B-sites.

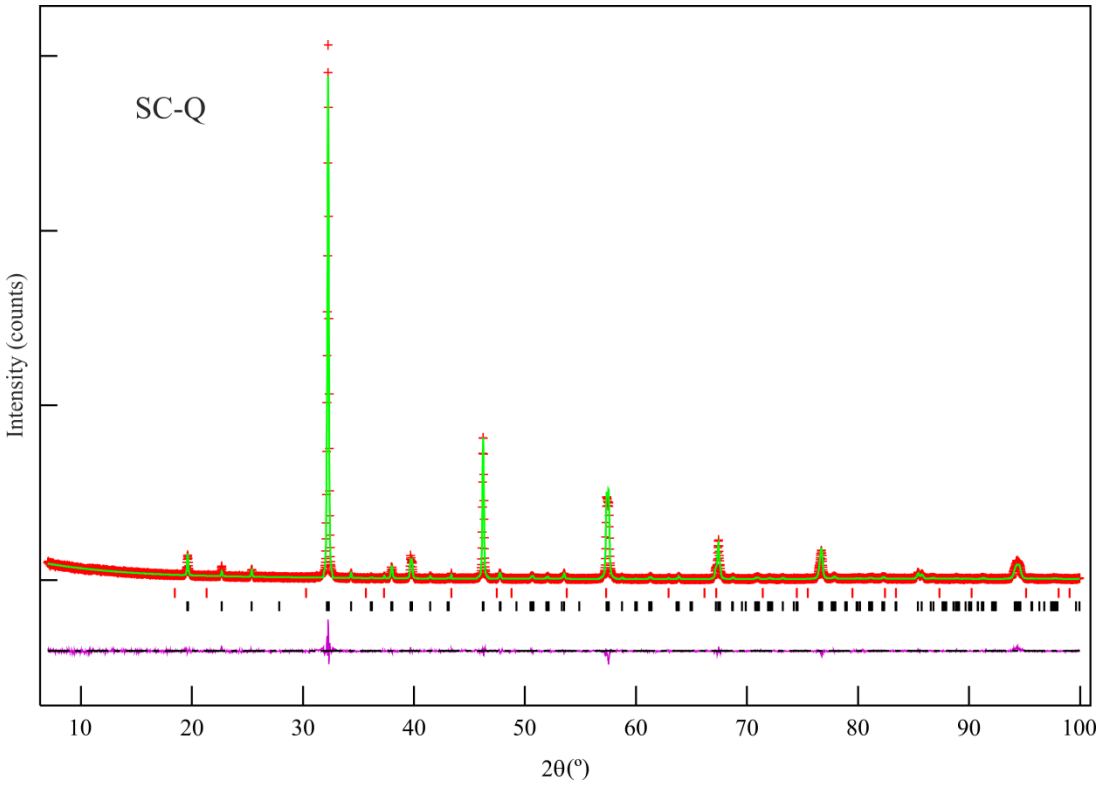


Figure 3.8. Observed, calculated, and difference plots from refinement of the structural model of the 'SC-Q' $LaSrNiRuO_6$ sample in space group $P2_1/n$ against X-ray powder diffraction data. The upper set of tick marks corresponds to NiO (1.15% by weight).

Table 3.3. Ni/Ru atomic fractions in the structural model of $LaSrNiRuO_6$ refined against X-ray powder diffraction data of the 'SC-Q' sample.

atom	Wyck.	*x*	*y*	*z*	fraction	U_{iso} (Å^2)
Ni(1)/Ru(1)	*2c*	1/2	0	1/2	0.917(4)/0.083(4)	0.0380(5)
Ru(2)/Ni(2)	*2d*	1/2	0	0	0.083(4)/0.971(4)	0.0380(5)
$LaSrNiRuO_6$: space group $P2_1/n$; a = 5.575(1) Å, b = 5.543(2) Å, c = 7.853(1) Å, β = 89.99(1)°; V = 242.7(1) Å^3. χ^2 = 1.587; wR_p = 10.45%, R_p = 7.29%.						

Table 3.4. Comparison of the refined lattice parameters of the structural model of $LaSrNiRuO_6$ in space group $P2_1/n$ against X-ray powder diffraction data collected from the slow cooled and quenched samples.

Sample	*a* (Å)	*b* (Å)	*c* (Å)	*β* (º)	*V* (Å^3)
SC	5.575(1)	5.545(1)	7.853(1)	89.99(1)	242.8(1)
Q	5.574(1)	5.543(2)	7.851(2)	89.99(1)	242.6(2)
SC-Q	5.575(1)	5.543(2)	7.853(1)	89.99(1)	242.7(1)

The observed changes in the broadness of peaks were found to be 'reversible'. The sample denoted as SC-Q-SC in the comparison shown in Figure 3.9, resulted from heating the SC-Q sample again at 1200 ºC in air for 2 h, and subsequently slow-cooling. This process 'sharpened' the peaks, and yielded a peak profile comparable to that observed for the original SC sample.

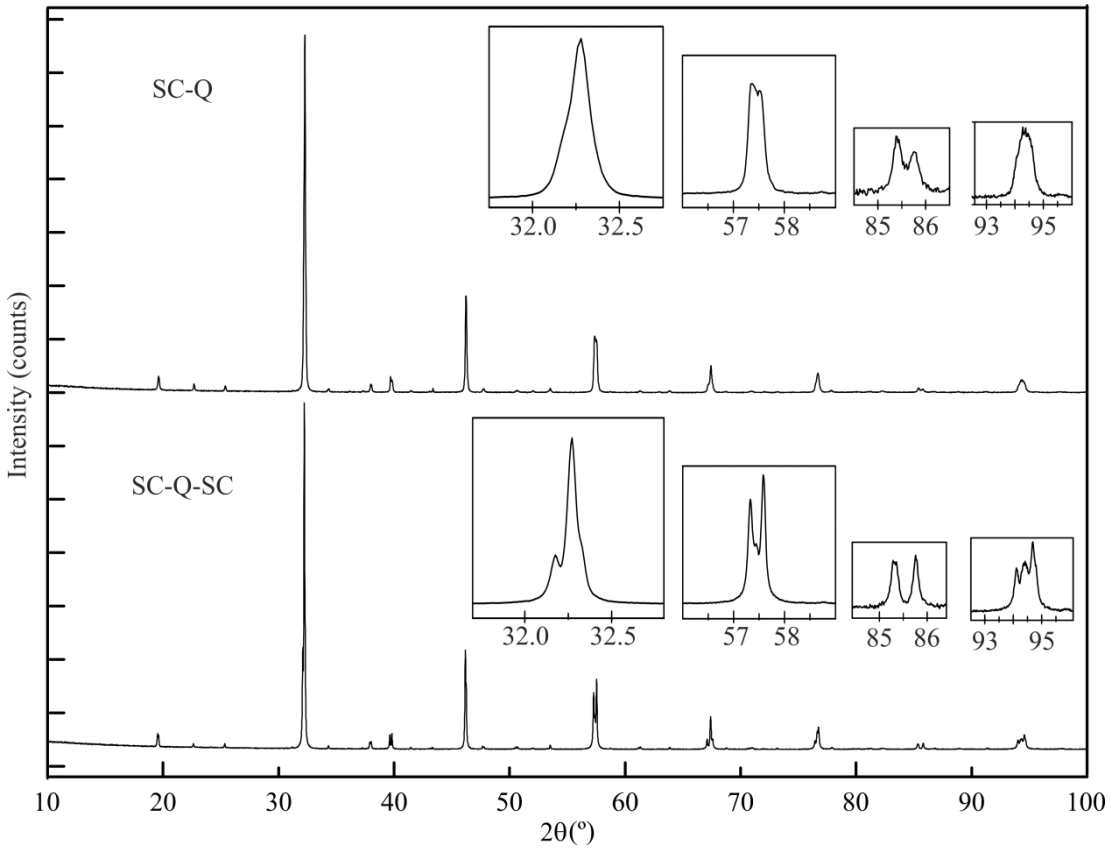


Figure 3.9. Comparison of X-ray diffraction patterns of the slow-cooled subsequently quenched sample (top) and the result of slow-cooling again (bottom). Insets show expanded regions 32 < 2θ(º) < 33, 56 < 2θ(º) < 59, 84 < 2θ(º) < 86, 93 < 2θ(º) < 96.

3.3.4 Comparison of the Broadness of Peaks of Slow-Cooled and Quenched $LaSrNiRuO_6$ Samples

As detailed in Section 2.5, the software used for Rietveld refinements uses a pseudo-Voigt type function to describe the peak profile shape.[64] The Gaussian components GU, GV, GW were considered instrumental terms, while the Lorentzian coefficients, LX and LY, were considered to describe the peak broadening due to the size of crystalline domains (*i.e.* coherently scattering domains) and microstructural strain, respectively. The crystalline domain size and isotropic lattice strain for each $LaSrNiRuO_6$ sample were calculated from the refined profile parameters LX and LY (Section 2.5.1). The results are summarised in Table 3.5. As noted in Section 2.5.1, the as calculated values represent good parameters for comparison but are not absolute values as the instrumental contribution to the broadness of peaks was not taken into account. During the refinements for the samples for which the X-ray diffraction experiments were carried out using the same diffractometer and identical conditions (*e.g.* samples SC and SC-Q), the profile parameters GU, GV and GW were fixed to be the same (values were fixed to be those refined for the slow-cooled sample).

Table 3.5. Calculated size and microstructural isotropic strain for slow-cooled and quenched $LaSrNiRuO_6$ samples.

Sample	Refined profile parameters		Size (Å)	Isotropic strain (%)
	LX (×0.01°)	LY (×0.01°)		
Slow-cooled (SC)	1.3(1)	8.6(2)	6790(35)	0.15(2)
SC-Q-SC	1.6(1)	8.7(3)	5516(44)	0.15(3)
SC-Q	2.15(2)	9.5(4)	4105(29)	0.17(4)
Quenched	2.54(2)	9.7(4)	3475(34)	0.17(4)

The smaller crystalline domains size along with greater isotropic microstructural strain for quenched $LaSrNiRuO_6$ samples are consistent with the broader peaks observed for the as prepared materials (Figure 3.6, Figure 3.7, Figure 3.9). These results suggest that the size of the crystalline domains is the main contribution to the broadness of peaks.

3.4 Discussion

3.4.1 Slow-cooled and Quenched $LaSrNiRuO_6$ Samples

The structures extracted from refinement of the monoclinic $P2_1/n$ model against X-ray powder diffraction data collected from slow-cooled and quenched $LaSrNiRuO_6$ samples demonstrate that the difference between the two sets of samples is not in their crystal structures. Consistent with this observation, thermogravimetric data demonstrate that the composition of all the samples measured is the same. The difference between slow-cooled and quenched samples was found to be microstructural: the cooling rate used in the synthesis of the materials affects the growth of crystalline domains. Materials that were rapidly cooled, exhibit smaller crystalline domains compared to slow-cooled samples (Table 3.5). This observation could be explained by the phase transition reported in literature for $LaSrNiRuO_6$,[92] which involves the change from the monoclinic crystal system of space group $P2_1/n$ to a trigonal system of space group R-3 upon heating above the transition temperature of 670 K (396.85 ºC). The two structures are shown in Figure 3.10.

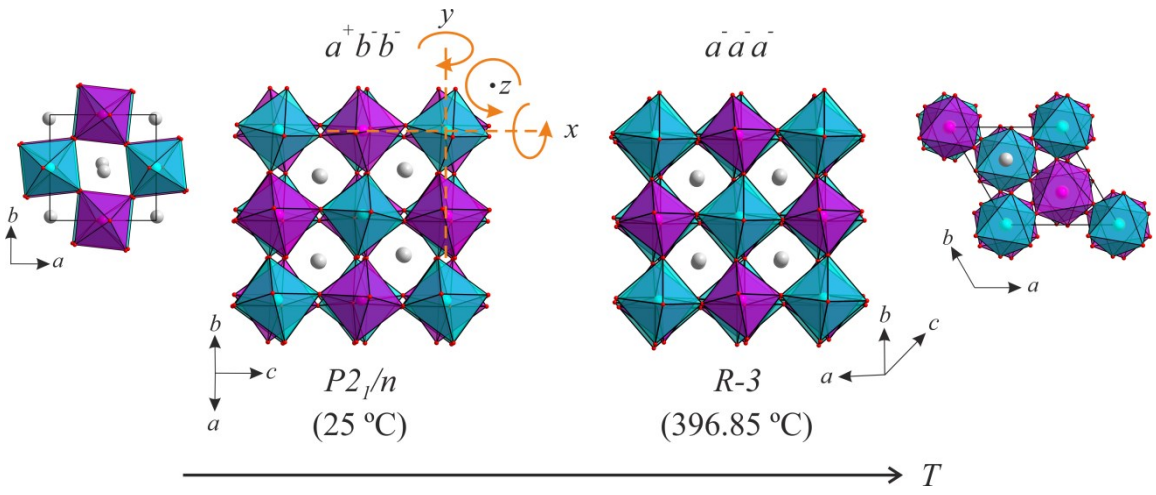


Figure 3.10. The monoclinic $P2_1/n$ (left) and trigonal R-3 (right) structures of $LaSrNiRuO_6$. Curved, arrows describe the rotation of the BO_6 (B = Ni, Ru) octahedra about each Cartesian axis, in the Glazer notation.

The high-temperature trigonal structure (R-3) corresponds to the 1:1 B-site cation ordered $a^-a^-a^-$ tilt system, and the room temperature monoclinic structure ($P2_1/n$) to the $a^+b^-b^-$ tilt system.[14] Cooling from the transition temperature to room temperature involves a

symmetry break by the twist of the BO_6 octahedra, rotating clockwise or anticlockwise, about the three Cartesian axes *x*, *y* and *z*. Thus, upon cooling from the synthesis temperature of 1200 ºC to room temperature, there are six possible ways in which the symmetry can be broken. It can be expected that each possible 'symmetry-breaking combination' (*i.e.* clockwise or anticlockwise twisting of the BO_6 octahedra along *x*, *y* or *z*), gives way to the formation of different crystalline domains. The growth of these crystalline domains minimises the free energy by reducing the boundary surface area between them. Therefore, when samples are cooled below the phase transition as schematised in Figure 3.11, two processes take place: (1) monoclinic crystalline domains form as a consequence of the symmetry breaking by any of the six possible combinations of BO_6 octahedra twists and (2) the crystalline domains grow to minimise the surface of domain walls and hence the free energy.

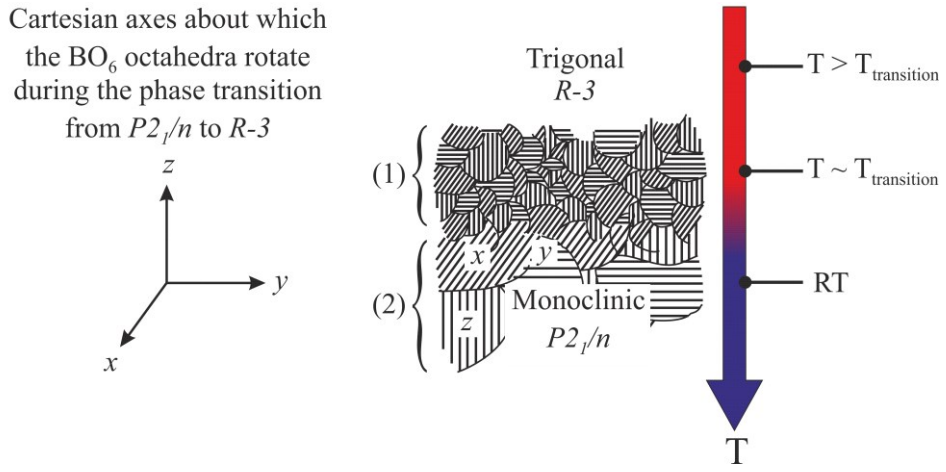


Figure 3.11. Representation of the processes involved when cooling $LaSrNiRuO_6$ below the phase transition temperature. Region (1) schematises the formation of the monoclinic crystalline domains and region (2) their growth. The different patterns are parallel to the Cartesian axes *x*, *y* or *z* about which rotation can take place clockwise or anticlockwise.

The growth of crystalline domains in this case requires a reorientation, which in turn costs energy (i.e. an activation energy) and takes time. By slow cooling, enough time and thermal energy is expected to be available for growth of large monoclinic crystalline domains. On the other hand, by quenching, smaller domains that could not fully grow are 'trapped'.

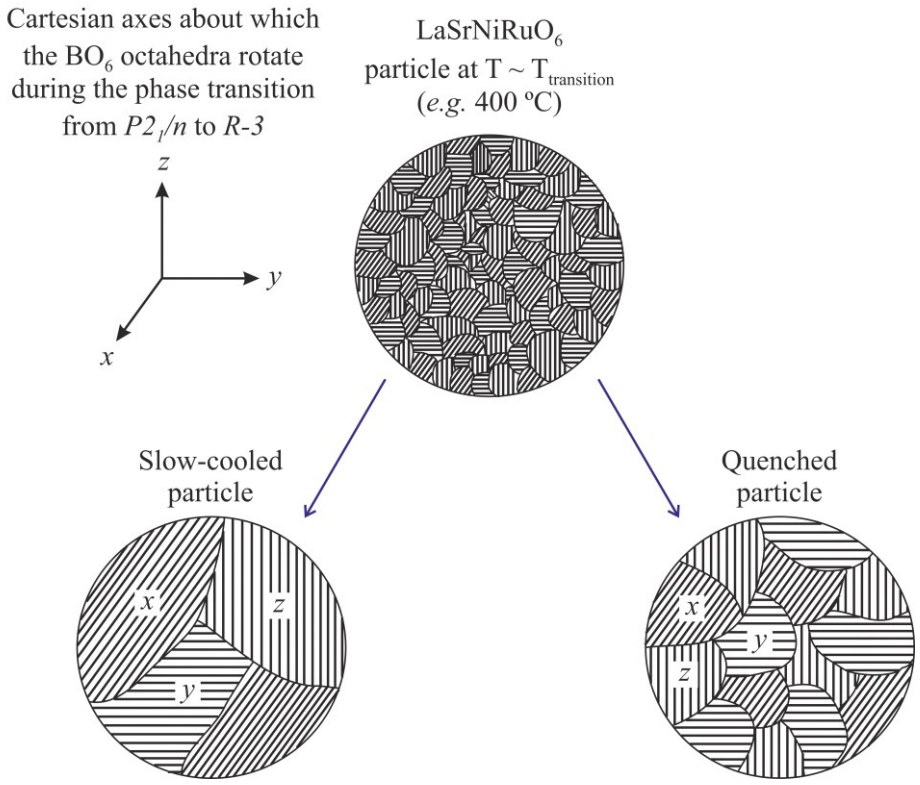


Figure 3.12. Schematic representation of the crystalline domains in slow-cooled and quenched $LaSrNiRuO_6$ samples. The different patterns are parallel to the Cartesian axes *x*, *y* or *z* about which rotation can take place clockwise or anticlockwise.

The structural phase transition of $LaSrNiRuO_6$ from trigonal to monoclinic upon cooling is reported to be reversible. This is consistent with the reproducibility observed for the changes in the peak shape in the diffraction patterns of samples that were slow-cooled, subsequently quenched and then slow-cooled again (Figure 3.7, Figure 3.9).

3.4.2 The Topochemical Reduction of Slow-cooled and Quenched $LaSrNiRuO_6$ Samples

As will be described in Chapter 4, inconsistencies in the reactivity of different $LaSrNiRuO_6$ samples were observed. Comparison of reductions under identical reaction conditions (as summarised in Figure 3.13) showed that slow-cooled samples undergo incomplete reduction, while quenched samples readily convert into the product $LaSrNiRuO_4$ (Chapter 5).

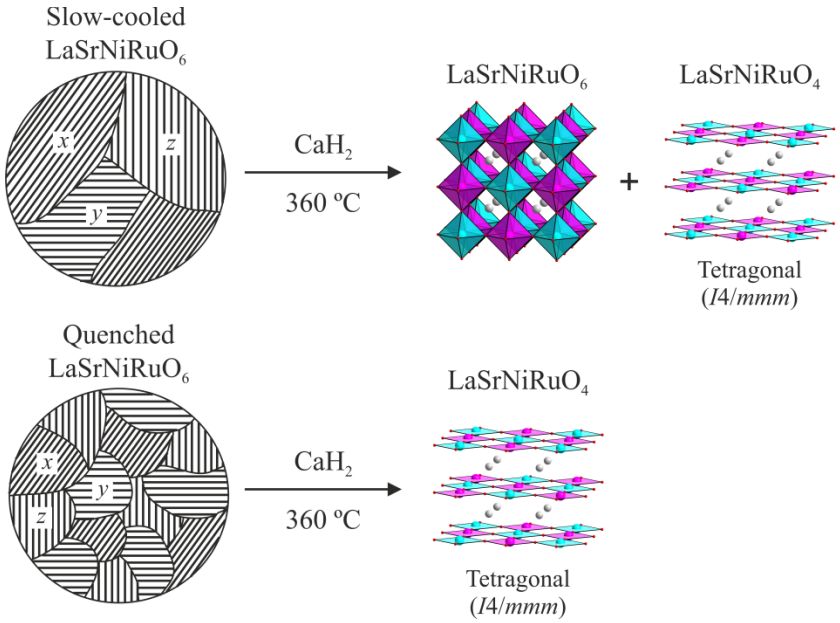


Figure 3.13. Schematic representation of the reduction reactions carried out with slow-cooled and quenched $LaSrNiRuO_6$ samples.

The observed limited reactivity towards reduction of the slow-cooled $LaSrNiRuO_6$ samples with respect to the quenched samples can be explained on the basis of the differences in the microstructure. During the reduction via topochemical anion deintercalation, the removal of oxygen will initially take place at the surface of particles. The transformation of $LaSrNiRuO_6$ into $LaSrNiRuO_4$ involves a structural change in which the lattice parameter perpendicular to the sheets of oxygen anions that are removed, changes (it contracts as will be detailed in Sections 4.3 and 4.4), and as the reaction progresses, lattice strain builds up. Across the reaction interface, schematised in Figure 3.14, the formation of the anion deficient phase $LaSrNiRuO_4$ produces a compression strain (arrows pointing towards each other) along the direction parallel to the *c* lattice parameter, whilst shear strain (arrows pointing in opposite directions) is exerted along the same direction by the unreacted starting material.

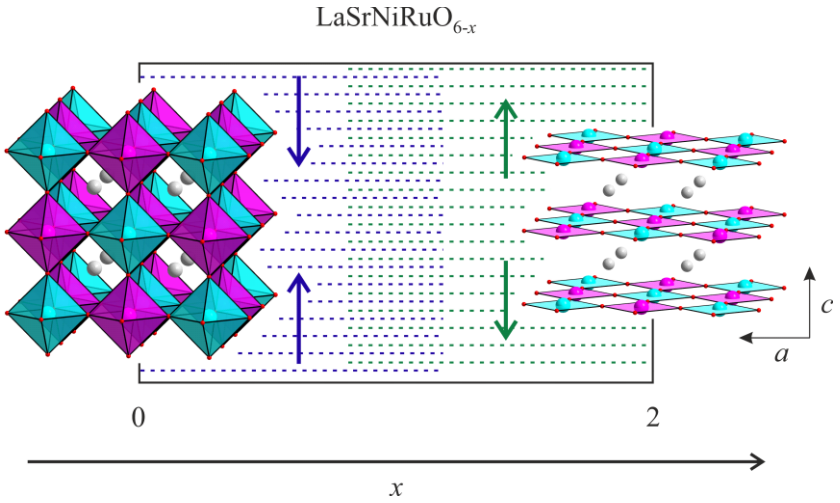


Figure 3.14. Representation of the strain 'regions' at the reaction interface during reduction of $LaSrNiRuO_6$ to form $LaSrNiRuO_4$. Coloured arrows represent the two types of strain generated at each end composition and dotted lines of the corresponding colour represent the regions affected by each type of strain.

The build-up of strain, represented as the overlap of the two strain regions in Figure 3.14, adds up to the energy barrier for the reaction. This could explain why incomplete reduction is observed for slow-cooled samples. As demonstrated in Section 3.3.4 from refinement of the microstructure, slow-cooled samples exhibit crystalline domains of greater size with respect to the quenched samples. The energy penalty for the lattice strain to build up (and disrupt the microstructure) is therefore expected to be greater for slow-cooled samples. This results in a lift of the energy barrier of the reaction (Section 4.4.3). In this context, the comparatively less stable microstructural configuration of quenched particles makes them more 'flexible' with respect to the slow-cooled samples. The strain build-up during the reaction could be partly removed by raising the temperature (the stress component due to the temperature variation vanishes at the annealing temperature).[93] However, as discussed in Section 4.4.3, raising the temperature fulfils the energy requirements for the competing decomposition reaction to take place.

3.5 Conclusions

The cooling method used in the final heating step during the synthesis of $LaSrNiRuO_6$ affects the size of the crystalline domains in the resulting materials. This is a consequence of the phase transition from the *R*-3 trigonal structure to the $P2_1/n$ monoclinic structure upon cooling from the synthesis temperature to room temperature ($T_{transition}$ = 670 K).

The slow-cooled and quenched $LaSrNiRuO_6$ samples are chemically identical. However, slow-cooling results in the growth of the monoclinic crystalline domains that form upon cooling, and are trapped before they are allowed to grow in the quenched samples.

As the topochemical reduction of $LaSrNiRuO_6$ progresses, there is a build-up in the lattice strain from the mismatch in the *c* lattice parameter between the product $LaSrNiRuO_4$ and the starting material. This strain seems likely to be the cause of the increase in the energy barrier for the reaction. In terms of this flexibility of particles, the smaller crystalline domains in quenched samples make the particles more 'plastic' and the reaction proceeds to completion for the as prepared samples under the conditions studied. On the other hand, the reduction of slow-cooled samples requires higher temperatures that, as will be discussed in Section 4.4.3, overcome the energy needed for the competing decomposition reaction.

Chapter 4

The Topochemical Reduction of $LaSrNiRuO_6$

4.1 Introduction

As noted previously in Section 3.1, the interest in reducing the mixed transition-metal double perovskite phase $LaSrNiRuO_6$ (as described in Figure 3.2, 3.1) lies in the possibility of further exploring the complex interactions between electrons in 3*d* and 4*d* orbitals in a cation-ordered extended oxide, as a parallel to the disordered $SrFe_{0.5}Ru_{0.5}O_2$ phase.[38]

The attempted reduction of $LaSrNiRuO_6$ slow-cooled and quenched samples, exhibiting the different microstructures described in Section 3.4.1, revealed the relevance of this structural aspect in the reactivity of the substrate oxides towards reduction via topochemical anion deintercalation.

4.2 Experimental

4.2.1 Reduction of Slow-Cooled and Quenched $LaSrNiRuO_6$ Samples

The slow-cooled and quenched $LaSrNiRuO_6$ samples characterised in Section 3.3 were reacted with 4 mole equivalents of CaH_2 (Alfa Aesar, 98%) in the venting apparatus described in Section 2.2.2. The reaction mixtures were heated at 360 ºC for periods of 48 hours (which will be referred to as heating cycles), with intermediate regrinding. Reaction progress was monitored via X-ray powder diffraction. The reduction reaction is proposed as follows (Section 1.3.1):

$$LaSrNiRuO_6 + x\ CaH_2 \xrightarrow[\text{48 h}\\ \text{heating cycles}]{\text{360 ºC}} LaSrNiRuO_{6-x} + x\ CaO + x\ H_2 \qquad (4.1)$$

Upon reaction completion, samples were washed with a 0.05 M solution of NH_4Cl in methanol to remove the calcium containing phases as described in Section 2.2.3.

4.2.2 Thermogravimetric Measurements

The composition of the $LaSrNiRuO_{6-x}$ products was determined from both reductive and oxidative thermogravimetric measurements. The reductive thermogravimetric measurements were performed as described in Section 3.2.3 for the starting materials (Reaction 3.1), by heating powder samples under a 10% H_2 in N_2 flow at 5 ºC min^{-1} to 900 ºC. For reoxidative measurements, samples were heated under an O_2 flow using the same heating rate of 5 ºC min^{-1}. The following oxidation reaction was considered:

$$LaSrNiRuO_{6-x} + 1/2\ x\ O_2 \longrightarrow LaSrNiRuO_6 \qquad (4.2)$$

The products of reductive decomposition and oxidation were confirmed by powder X-ray diffraction.

Corrections were made for the small amount of Ni produced during reduction of the NiO present as a secondary phase in the starting materials (Section 3.3.2).

4.3 Results

4.3.1 Reactivity of $LaSrNiRuO_6$ Starting Materials

4.3.1.1 The Reduction Product $LaSrNiRuO_{6-x}$

X-ray powder diffraction data collected from the progress of reaction between $LaSrNiRuO_6$ and CaH_2 (both for slow-cooled and quenched samples), revealed the formation of a tetragonal phase that could be indexed using an *I*4/*mmm* tetragonal cell with lattice parameters a = 5.65(1) Å and c = 6.92(1) Å based on the cation ordered structure of the starting material (Figure 4.1).

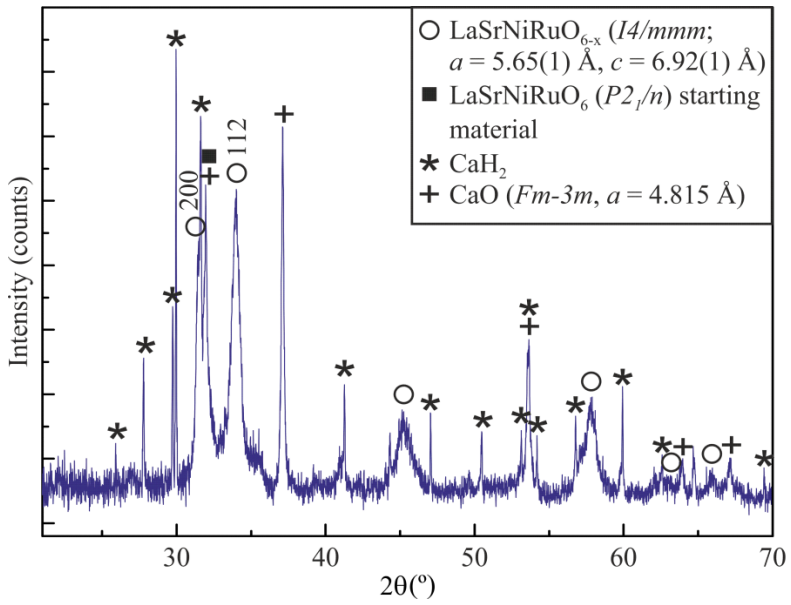


Figure 4.1. X-ray powder diffraction data collected from the reaction between $LaSrNiRuO_6$ and CaH_2 in the venting apparatus. A tetragonal phase could be indexed (○) using a tetragonal model of space group *I*4/*mmm* (*a* = 5.65(1) Å, *c* = 6.92(1) Å).

The formation of this tetragonal phase is accompanied by the formation of CaO in agreement with Reaction 4.1 therefore this tetragonal phase was identified as the reduction product $LaSrNiRuO_{6-x}$. The progress of reduction of the $LaSrNiRuO_6$ starting materials was evaluated by observing the splitting of the 200 and 112 reflections of the tetragonal product, the increase of the by-product CaO (*Fm*-3*m*, *a* = 4.815 Å) and the decrease in intensity of the main reflections of the starting materials at 2θ ≈ 32.3º.

4.3.1.2 Comparison of the Reactivity of Slow-Cooled and Quenched $LaSrNiRuO_6$ Samples

Comparison of the X-ray powder diffraction data collected from the reduction of a slow-cooled 'SC-R' and a quenched 'Q-R' $LaSrNiRuO_6$ sample, after 3 heating cycles using identical experimental setups (360 ºC in the venting apparatus) revealed important differences in the progress of reduction as shown in Figure 4.2. The estimated fractions of reduced product and unreacted starting material for each sample are shown in Table 4.2. These fractions were calculated using the relative intensity of the most intense peak of the tetragonal phase (112 reflection at 2θ = 34.25º), with respect to those of the main peaks of

the starting materials (at 2θ = 32.25º). The intensities were calculated using the STOE WinXPOW suite of programs.[94]

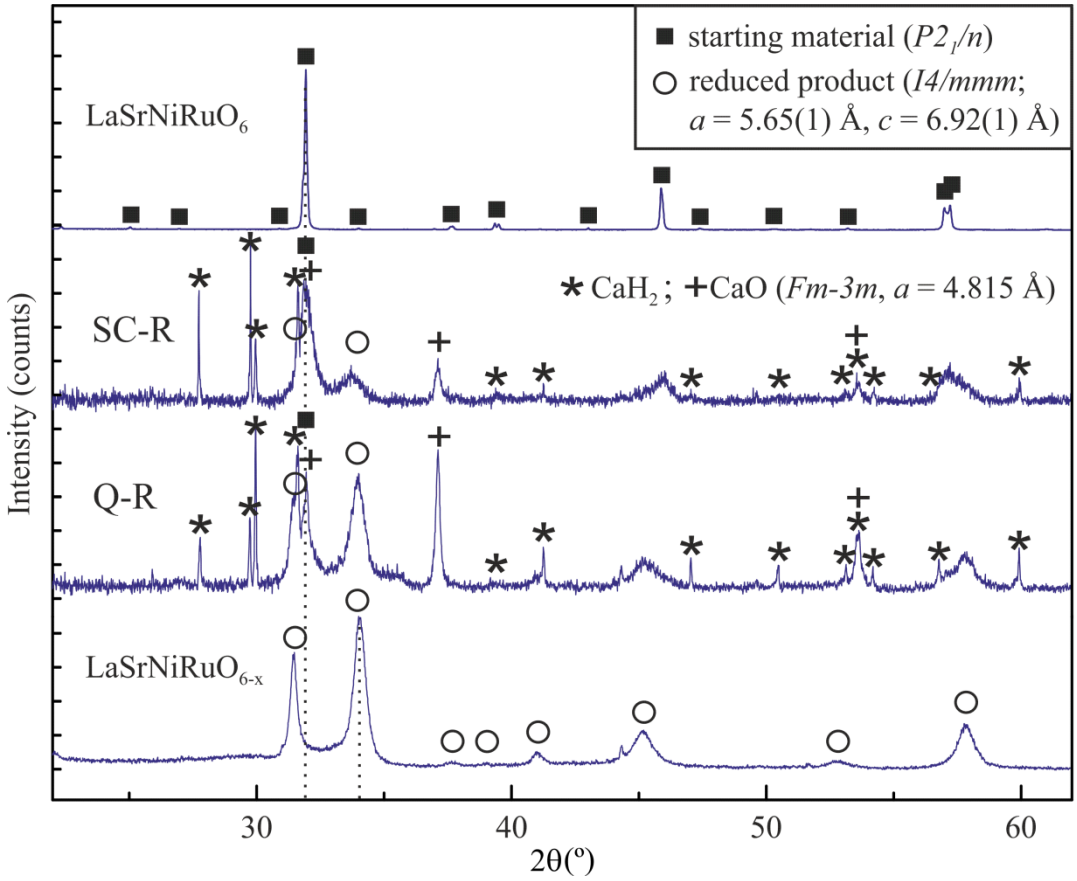


Figure 4.2. X-ray powder diffraction data collected from the reaction of a $LaSrNiRuO_6$ slow-cooled (top) and a quenched (bottom) sample, with CaH_2 after 3 heating cycles at 360ºC in the venting apparatus. The dotted lines mark the position of the peaks used as reference.

Table 4.1. Estimated fractions of reduced product and unreacted starting material in SC-R and Q-R calculated from the relative intensity of the main peaks of each phase.

Sample	Majority phase	Fraction of starting material (%)	Fraction of reduced phase (%)
SC-R	starting material	74.8	25.2
Q-R	reduced phase	29.3	70.7

It can be observed that, after the same period of time, the quenched starting material had almost fully converted into the tetragonal product while the slow-cooled starting material had only partially reduced (25.2% vs 74.8%). Further extended heating of the slow-

cooled starting materials exhibiting this behaviour resulted in a mixture of the tetragonal product, and decomposition products of reduction as shown in Figure 4.3.

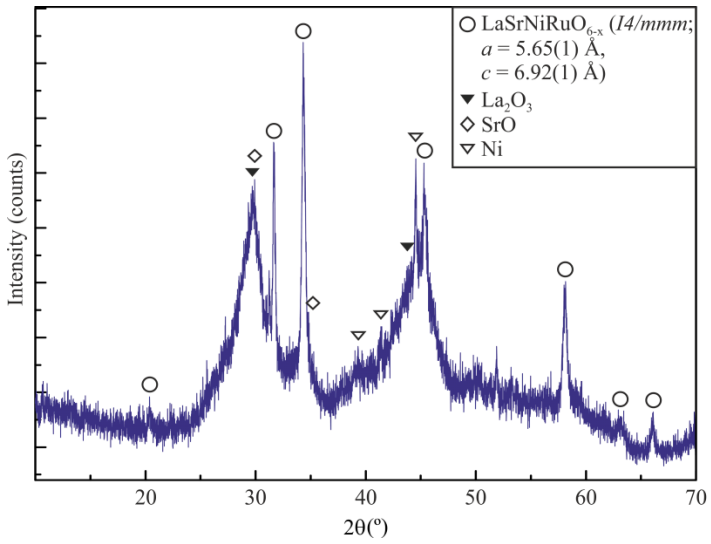


Figure 4.3. X-ray powder diffraction data collected from the washed product of reduction a $LaSrNiRuO_6$ slow-cooled starting material after 10 heating cycles at 360 ºC.

One of the possibilities for explaining the observed difference in the reactivity of slow-cooled samples was that the experimental conditions were dissimilar with respect to that for the quenched samples. In particular, it was possible that the partial pressure of oxygen was higher in the venting system used for the reduction of slow-cooled samples. The venting system was therefore modified by adding an oxygen getter between the reaction mixture and the connection to the argon flow, as schematised in Figure 4.4. The reagent chosen as the oxygen getter was CaH_2. Prior to reaction, the venting system was thoroughly purged with argon. In order to favour the renewal of the inert atmosphere in the reaction vessel, the 'T' connection to the argon flow was also modified (Figure 4.4 inset).

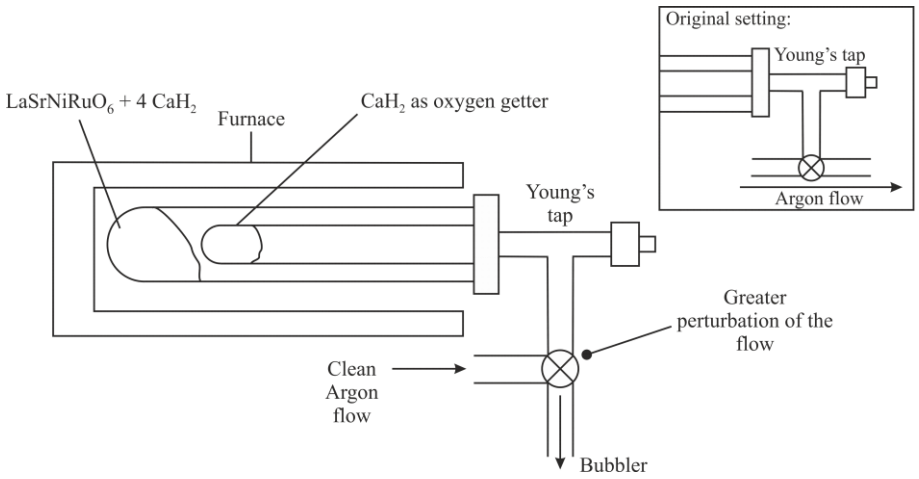


Figure 4.4. The modified venting apparatus.

Figure 4.5 shows the X-ray powder diffraction data collected from the reaction of a new sample of a slow-cooled $LaSrNiRuO_6$ starting material after 3 heating cycles, using the modified venting apparatus. Comparison of these data with the diffraction pattern in Figure 4.2 for the SC-R sample shows that the reaction progress in the modified venting apparatus and the original setup is very similar (~25% of the reduced product is formed). This suggested that the experimental setup was not the origin of the difference in reactivity observed from slow-cooled $LaSrNiRuO_6$ samples.

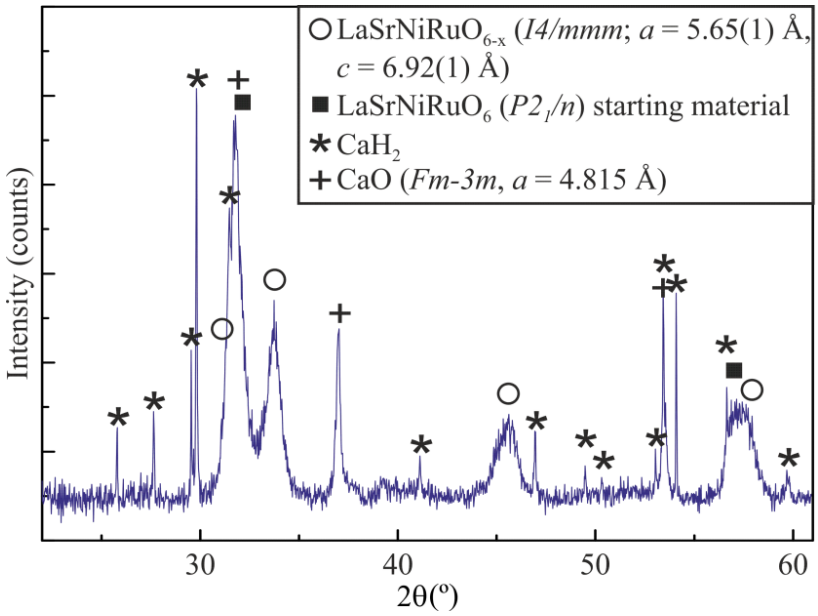


Figure 4.5. X-ray powder diffraction data collected from the reaction between a $LaSrNiRuO_6$ slow-cooled sample and CaH_2 after 3 heating cycles at 360 ºC, in the modified venting apparatus.

Slow-cooled starting materials were only observed to fully reduce when higher reaction temperatures were employed. The reduction of a 4 g sample of the slow-cooled $LaSrNiRuO_6$ starting material shown in Figure 4.2 (SC-R), was achieved by increasing the temperature of reaction from 360 ºC to 375 ºC taking steps of 5 ºC for each heating cycle. Figure 4.6 shows the X-ray powder diffraction data collected from the reaction after heating at 375 ºC. As will be shown in Section 4.4.2 however, a secondary phase was formed at this temperature. This secondary phase was indicative of decomposition.

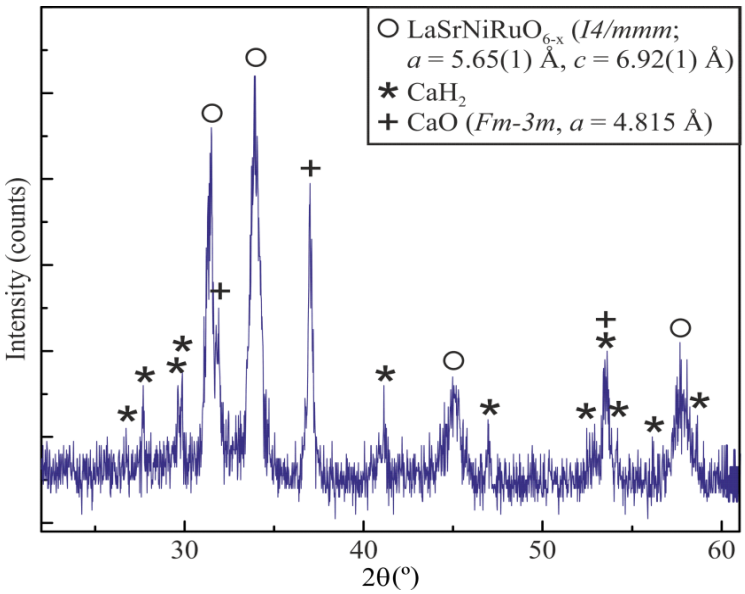


Figure 4.6. X-ray powder diffraction data collected from the reaction between a $LaSrNiRuO_6$ slow-cooled sample and CaH_2 after heating at the increased temperature of 375 ºC.

4.3.2 The Reduction Product $LaSrNiRuO_4$

4.3.2.1 X-ray Powder Diffraction and Thermogravimetric Data

Figure 4.7 shows the X-ray powder diffraction patterns of the washed reduction products SC-R and Q-R (shown previously in Figure 4.2), after 5 heating cycles. As shown in Section 4.3.1, the product SC-R required a final reaction temperature of 375 ºC while the Q-R product formed at 360 ºC. A thorough analysis of the structure of the Q-R sample is presented in Chapter 5. The data for both the SC-R and Q-R samples could be indexed using an *I*4/*mmm* tetragonal model with lattice parameters a = 5.65(1) Å and c = 6.92(1) Å. However, a reflection that could not be accounted for at 2θ = 10.60º (marked with a

dotted line), was observed for the SC-R sample. This additional reflection was further investigated using neutron powder diffraction data as will be described in Section 4.3.2.2

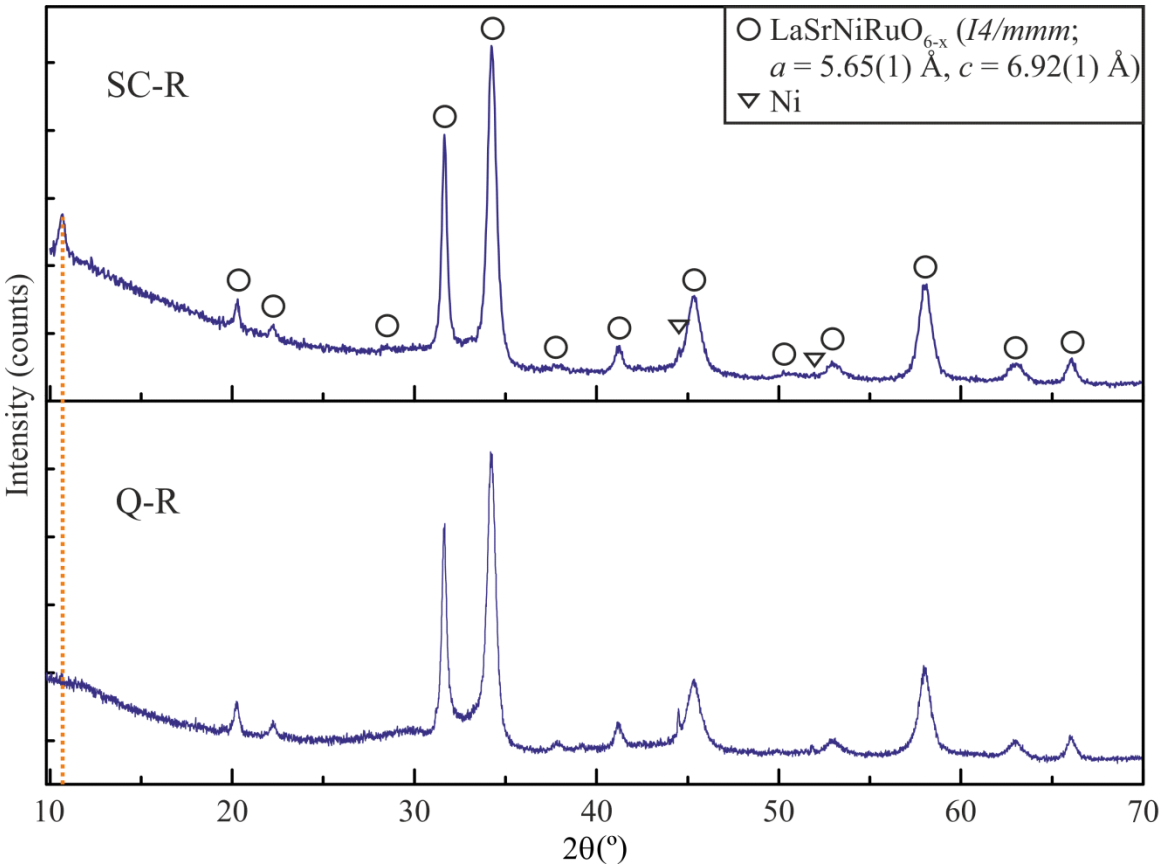


Figure 4.7. X-ray diffraction data collected from the washed reduction products of a slow-cooled (SC-R) and a quenched (Q-R) $LaSrNiRuO_6$ sample. The dotted line (2θ = 10.60°) marks the position of the extra peak observed in the SC-R data.

Figure 4.8 shows the thermogravimetric data collected during the reductive decomposition of the SC-R and Q-R products, and the data collected during reoxidation are shown in Figure 4.9. The initial compositions calculated from the mass changes are summarised in Table 4.2. The reported error for the oxygen content of the samples was calculated as the propagated error of the measurement of the mass from the TGA balance.

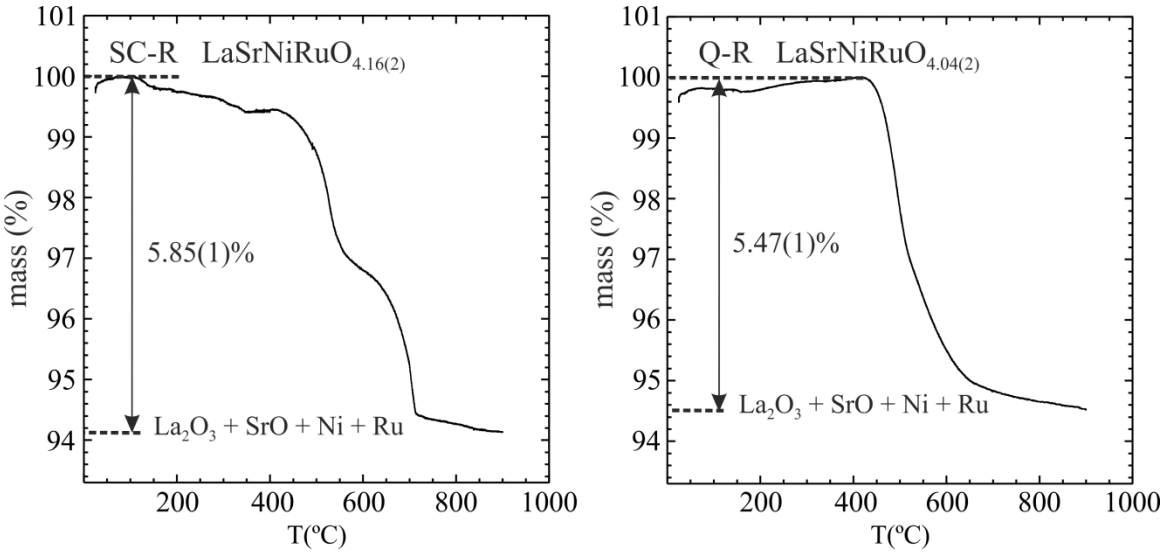


Figure 4.8. Thermogravimetric data collected during reductive decomposition of the SC-R and Q-R $LaSrNiRuO_{6-x}$ products.

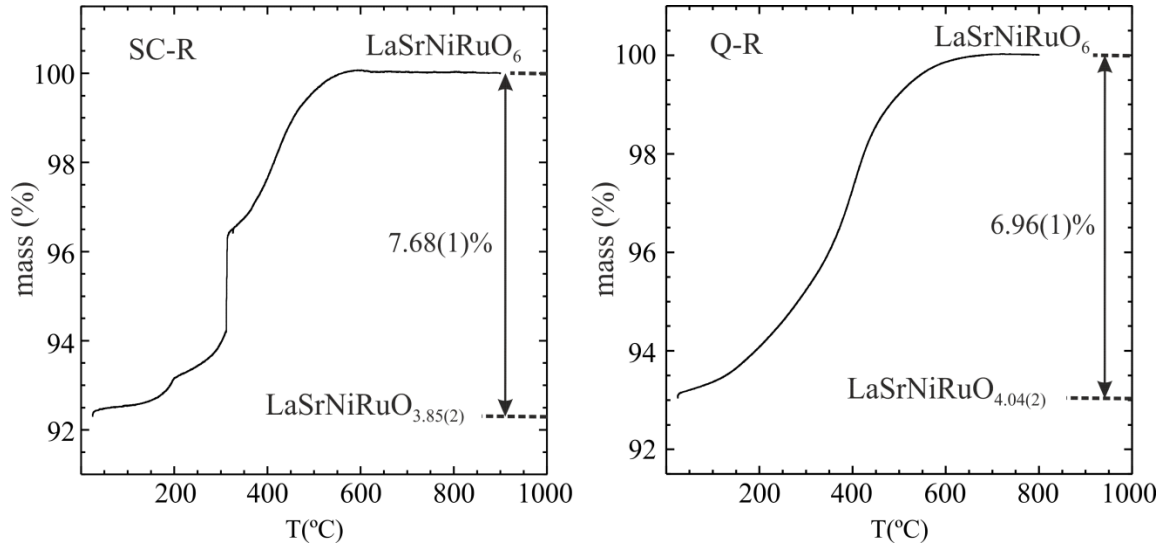


Figure 4.9. Thermogravimetric data collected during oxidation of the SC-R and Q-R products.

Table 4.2. Summary of the thermogravimetric data collected during reduction and oxidation of the SC-R and Q-R $LaSrNiRuO_{6-x}$ products.

Reductive Decomposition			
Sample	**Mass loss (%)**	**RMM***	**Oxygen content**
SC-R	5.85(1)	452.83	4.16(2)
Q-R	5.47(1)	450.93	4.04(2)
* A mass loss of 5.33% corresponds to an initial RMM of 450.29 consistent with the composition $LaSrNiRuO_4$.			

Oxidation			
Sample	**Mass gain (%)**	**RMM****	**Oxygen content**
SC-R	7.68(1)	447.87	3.85(2)
Q-R	6.96(1)	450.93	4.04(2)
** A mass gain of 7.11% corresponds to the initial composition $LaSrNiRuO_4$ (RMM 450.29)			

From the reduction experiments, the mass loss for both the SC-R and Q-R samples suggested an initial content of oxygen of x = 4.0(1) in the $LaSrNiRuO_{6-x}$ products, henceforth referred to as $LaSrNiRuO_4$. The mass loss shown by the Q-R sample corresponds, within error, to the value expected of 5.33% for the proposed initial composition (Table 4.2). However, the mass loss of the SC-R sample was observed to be smaller with respect to the Q-R sample. In addition, inflection points are observed in the change in mass as a function of temperature for the SC-R sample in contrast with the smooth change in mass displayed by the Q-R sample. The same observation can be made from the oxidative thermogravimetric data in Figure 4.9. The mass gain from reoxidation of the Q-R sample is consistent with the reductive thermogravimetric data giving an initial composition of $LaSrNiRuO_{4.04(2)}$. The mass gain observed from the SC-R sample on the other hand, deviates more significantly with respect to the Q-R sample from the expected value of 7.11% for an initial composition of $LaSrNiRuO_4$.

The X-ray powder diffraction data collected from the resulting oxidised phases of the SC-R and Q-R samples are shown in Figure 4.10. Both sets could be indexed using a $P2_1/n$ monoclinic cell based on the structure of the $LaSrNiRuO_6$ starting materials, as described in Section 3.3.1.

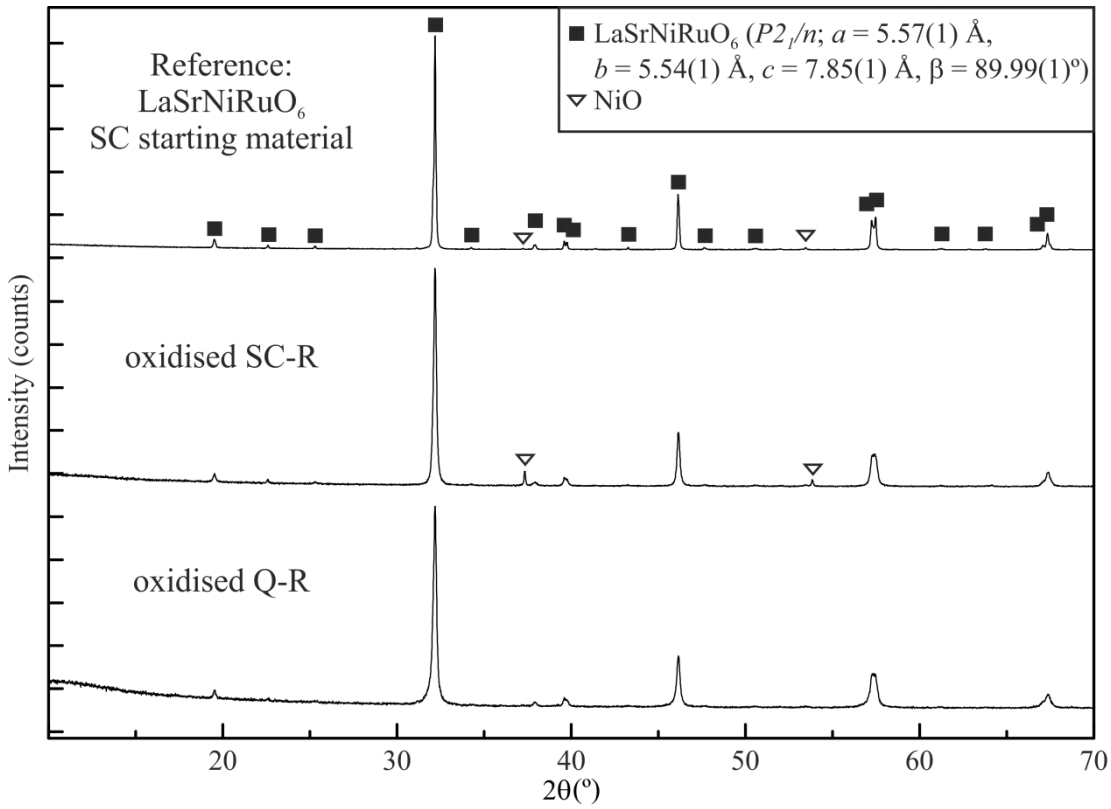


Figure 4.10. Comparison of the X-ray powder diffraction data collected from the products from oxidation of the SC-R and Q-R samples. The X-ray diffraction pattern of a $LaSrNiRuO_6$ starting material is included at the top as a reference.

The X-ray diffraction pattern of the starting material of the SC-R sample is included as a reference. A greater amount of NiO was observed as a secondary phase in the X-ray diffraction pattern of the SC-R oxidised product compared to the $LaSrNiRuO_6$ starting material and the Q-R oxidised product.

4.3.2.2 Neutron Powder Diffraction Data

Neutron powder diffraction data were collected from the SC-R product using the D2B instrument at ILL, and from the Q-R product using the Polaris instrument at ISIS. Full structural details of the refined structure of the $LaSrNiRuO_4$ Q-R sample are given in Chapter 5. The observed, calculated, and difference plots from refinement of a body-centred *I*4/*mmm* tetragonal model against the data collected at room temperature from the SC-R sample are shown in Figure 4.11. The full range in 2θ is presented for the purpose of highlighting the unaccounted-for peak at low angle (d = 8.378(2) Å, 2θ = 10.97º),

consistent with the observations from X-ray diffraction (Figure 4.7). Exclusion of this peak yields discrepancy values which indicate a reasonable fit of the tetragonal model to the rest of the data (χ^2 = 4.612, *wRP* = 1.63%, *Rp* = 1.19%). As will be discussed in Section 4.4.2, the hydride $LaRu_2H_4$, which exhibits an *Fd*-3*m* cubic structure (*a* = 8.38 Å), has been reported in the literature.[95] The allowed peaks for such lattice can account for the observed low angle reflection at *d* = 8.378(2) Å (100 reflection at 2θ = 10.97º in Figure 4.11). However, a structural model based on $LaRu_2H_4$ did not fit the data as the first reflection of the latter phase is the 111 reflection at *d* = 4.838 Å. The high background intensity is consistent with the presence of a hydride secondary phase. A secondary phase of composition $La(Ru_{1-x}Ni_x)_2H_4$ could explain these observations, however, a complete model for such secondary phase could not be proposed.

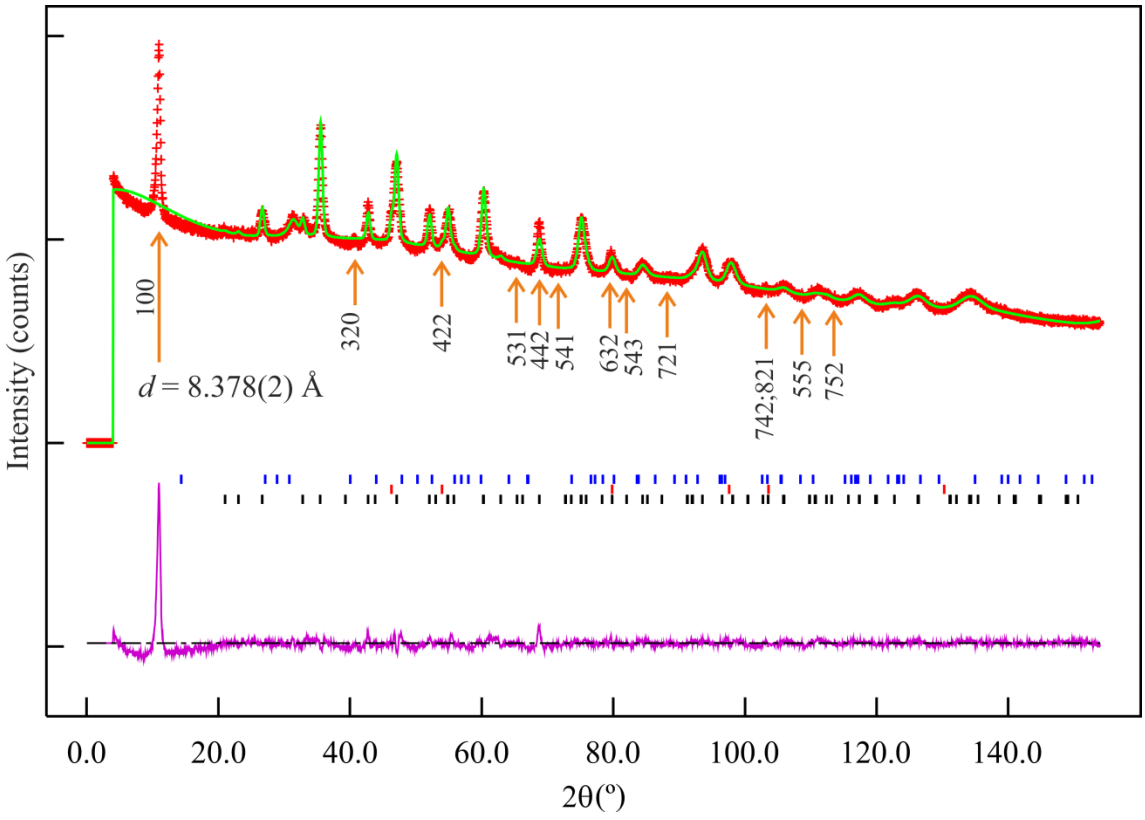


Figure 4.11. Observed, calculated and difference plots from the refinement of the *I*4/*mmm* structural model of $LaSrNiRuO_4$ against neutron powder diffraction data collected from the SC-R sample at 298 K using the D2B instrument. Black tick marks indicate the peak positions for the majority tetragonal phase; red elemental Ni (1.74(5)% by weight) and blue La_2O_3 (1.39(2)% by weight). The position of peaks of an *Fd*-3*m* cubic model (*a* = 8.378(2) Å) is indicated with arrows.

4.4 Discussion

4.4.1 The Topochemical Reduction of $LaSrNiRuO_6$

Reaction of $LaSrNiRuO_6$ with CaH_2 results in the formation of a reduced phase that can be indexed using a tetragonal cell (space group *I*4/*mmm*) and lattice parameters a = 5.65(1) Å, c = 6.92(1) Å. The average composition of a set of products obtained from reduction of a slow-cooled and a quenched starting material was $LaSrNiRuO_{4.0(1)}$. In analogy to the topochemical anion deintercalation of the disordered perovskite phase $Sr(Ru_{0.5}Fe_{0.5})O_3$ to form $Sr(Ru_{0.5}Fe_{0.5})O_2$ (using CaH_2 at 400 ºC),[38] the reduction reaction of $LaSrNiRuO_6$ was proposed as depicted in Figure 4.12b.

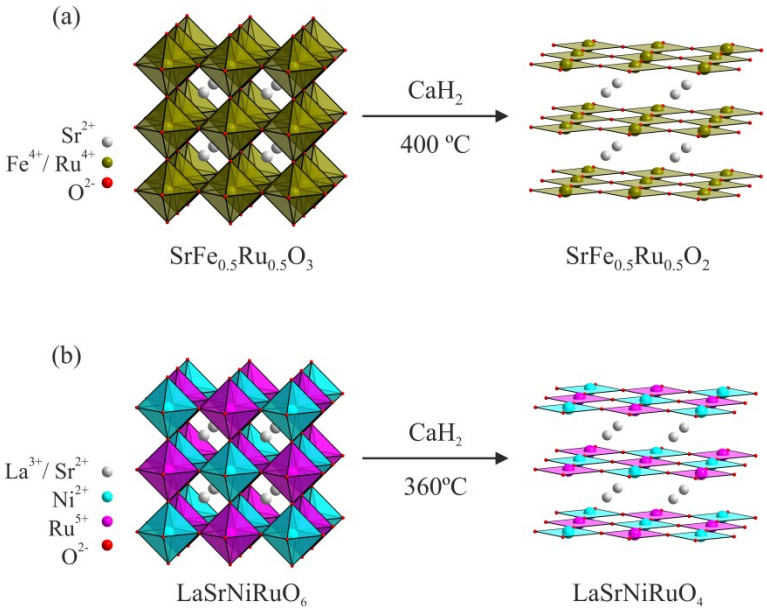


Figure 4.12. The reduction of (a) $SrFe_{0.5}Ru_{0.5}O_3$ and (b) $LaSrNiRuO_6$ via topochemical anion deintercalation using CaH_2.

The structure of the disordered phase $SrFe_{0.5}Ru_{0.5}O_2$ can be described using a primitive tetragonal unit cell (*P*4/*mmm*) with a = 3.99(1) Å, c = 3.49(1) Å. The $LaSrNiRuO_4$ structural model was based on a √2 by √2 by 2 cell expansion from the *P*4/*mmm* model. The resulting body centred *I*4/*mmm* tetragonal cell accounts for the reflection observed at 2θ = 20.26º (101) for $LaSrNiRuO_4$ and confirms that the Ni/Ru cation order of the $LaSrNiRuO_6$ parent phase is preserved. The formation of $LaSrNiRuO_4$ via the reduction of $LaSrNiRuO_6$ demonstrates that, like the Sr-Fe-O lattice in $SrFe_{0.5}Fe_{0.5}O_2$ or the Na-La-

Ti-O lattice in $Na_2La_2Ti_2RuO_8$,[38,91] the La-Sr-Ni-O lattice in $LaSrNiRuO_4$ is sufficiently robust to resist decomposition into the metals Ru and Ni, and oxides La_2O_3 and SrO.

Notably, no intermediate compositions $LaSrNiRuO_{6-x}$ with x in the range $0 < x < 2$ seems to be observed. This is evident from the fact that no continuous change in the lattice parameters is observed during the transformation of $LaSrNiRuO_6$ into the tetragonal product. Instead, $LaSrNiRuO_4$ is observed to form as a separate phase and grow at the expense of the starting material (Figures 4.1and 4.2).

4.4.2 Reduction behaviour of Slow-Cooled and Quenched $LaSrNiRuO_6$ Starting Materials

The comparison of X-ray diffraction data collected from the reaction of the slow-cooled and quenched $LaSrNiRuO_6$ starting materials after identical periods of time and under the same conditions (Figure 4.2) revealed a clear difference in the progress of reduction of the two sets of samples. While the quenched starting material almost fully transformed into the tetragonal reduced product after 3 heating cycles, all reactions with slow-cooled samples resulted in a mixture of $LaSrNiRuO_4$ and either unreacted starting material (Figure 4.2 and Figure 4.5) or decomposition products (Figure 4.3). $LaSrNiRuO_4$ could not be isolated as a single phase from slow-cooled $LaSrNiRuO_6$ samples at the reaction temperature of 365 ºC. Using higher reaction temperatures for the reduction of a slow-cooled $LaSrNiRuO_6$ sample yielded a product (SC-R) that could be indexed using the proposed structural model for $LaSrNiRuO_4$, however unaccounted-for peaks were observed in the X-ray and neutron powder diffraction data. The changes in mass for this SC-R sample during reduction and oxidation diverged from the expected values for an initial composition of $LaSrNiRuO_4$ as shown in Table 4.3. A noticeably smaller mass loss was observed during the reductive decomposition while a greater mass gain was measured during reoxidation.

Table 4.3. Comparison of the thermogravimetric data collected from the SC-R sample against the calculated values for $LaSrNiRuO_4$.

Reductive Decomposition			
	Mass loss (%)	**RMM**	**Oxygen content**
SC-R sample	5.85(1)	452.83	4.16(2)
$LaSrNiRuO_4$	5.33	450.29	4.00
Oxidation			
Sample	**Mass gain (%)**	**RMM****	**Oxygen content**
SC-R	7.68(1)	447.87	3.85(2)
$LaSrNiRuO_4$	7.11	450.29	4.00

Additionally, in contrast to the smooth changes in mass observed for the Q-R sample (resulting from reduction of a quenched $LaSrNiRuO_6$ starting material), both the reduction and the oxidation thermogravimetric data collected from the SC-R sample exhibited points of inflection which suggest that both processes take place in stages (Figure 4.8 and Figure 4.9). A small amount of an over-reduced phase similar to the $LaRu_2H_4$ phase reported in the literature could explain these observations.[95] Further reduction of the $LaSrNiRuO_4$ product to form a hydride phase of the form $LaRu_2H_4$ or $La(Ru_{1-x}Ni_x)_2H_4$, would explain a smaller mass loss during reductive decomposition to form La_2O_3, SrO, Ru and Ni. A reaction for this further reduction is proposed below.

$$2\ LaSrNiRuO_4 + 2\ CaH_2 \longrightarrow La(Ru_{1-x}Ni_x)_2H_4 + 1/2\ La_2O_3 + 2\ SrO + 2(1-x)\ Ni + 2\ CaO + 5/4\ O_2 \quad (4.3)$$

The greater gain in mass observed during oxidation is also consistent with the presence of an over-reduced hydride secondary phase. Additionally, the oxidation of a hydride analogous with $La(Ru_{1-x}Ni_x)_2H_4$ into the final $LaSrNiRuO_6$ phase (confirmed as the product of the TGA experiments from the X-ray diffraction data shown in Figure 4.10), would be expected to occur stepwise. The binary oxides La_2O_3, RuO_2 and NiO would form, and then react together with the SrO present to incorporate into the final $LaSrNiRuO_6$ phase. The X-ray powder diffraction pattern of $LaSrNiRuO_6$ included as a reference in Figure 4.10 is the slow-cooled starting material of the SC-R sample. The greater amount of the NiO secondary phase observed in the diffraction pattern of the SC-

R oxidised product compared to that of the Q-R analogue, and the SC starting material, is consistent with the 'staged' reoxidation process of the SC-R sample.

Both the X-ray and neutron powder diffraction data collected from the SC-R sample are consistent with the presence of a hydride secondary phase. The reported structure of the hydride $LaRu_2H_4$ is cubic with space group *Fd*-3*m*, a = 8.38 Å.[95] The first reflection of a model based on this structure is the 111 reflection at d = 4.838 Å which does not account for the extra peak observed in the X-ray and neutron powder diffraction data at d = 8.378(2) Å (Figure 4.7 and Figure 4.11). However, this reflection is allowed and corresponds to the 100 reflection of an *Fd*-3*m* cubic unit cell with a = 8.38 Å. This suggests that the atoms in the hydride formed (with proposed composition $La(Ru_{1-x}Ni_x)_2H_4$) might not be in the same disposition than in the reported hydride $LaRu_2H_4$. Proposing a model for a secondary hydride phase is challenging given that very few unaccounted-for peaks are observed in the X-ray and neutron diffraction data. Nonetheless, the high background intensity observed in the neutron diffraction data, is consistent with incoherent scattering from a hydride phase such as the one proposed. It is reasonable to believe that the formation of this secondary phase is the result of a competing reaction for which enough energy is provided when the temperature for the reduction is raised.

4.4.3 The Reactivity of Slow-Cooled and Quenched $LaSrNiRuO_6$ Starting Materials

A summary of the different outcomes observed from reduction of the slow-cooled and quenched $LaSrNiRuO_6$ starting materials is presented in Figure 4.13 (an extended scheme of Figure 3.13, Section 3.4.2). The observation that implementations to the experimental setup, such as lowering the partial pressure of oxygen (by using an oxygen getter), did not improve the progress of reduction of slow-cooled samples, can only be explained by a difference in the reactivity between the slow-cooled and the quenched $LaSrNiRuO_6$ starting materials.

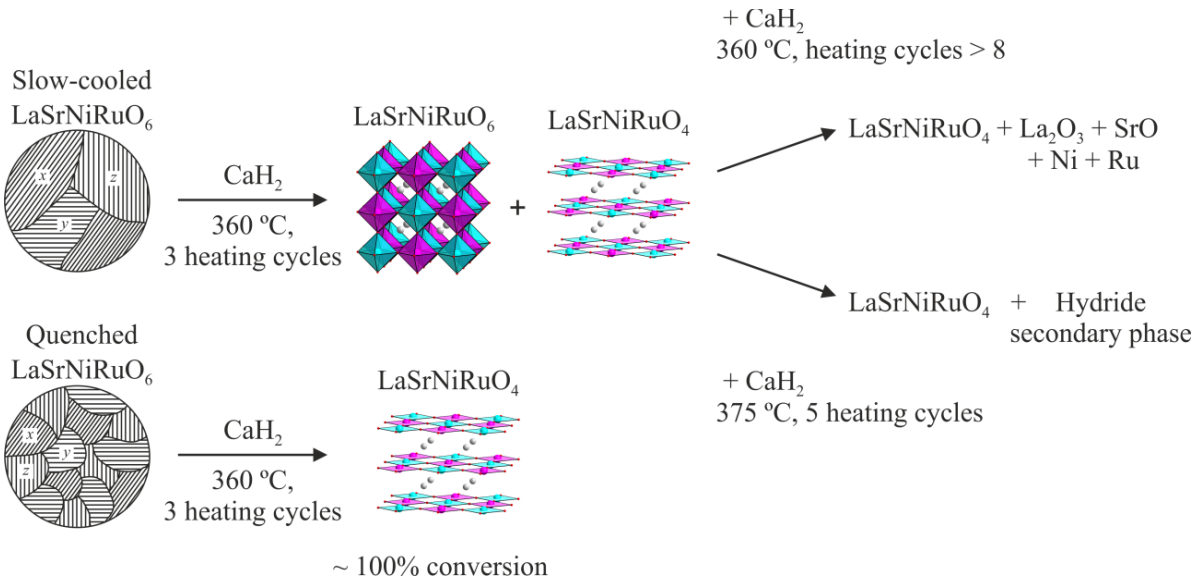


Figure 4.13. Summary of the different outcomes observed from reduction of the slow-cooled and quenched $LaSrNiRuO_6$ starting materials.

As shown in Sections 3.3.1 and 3.3.2, both the slow-cooled and quenched $LaSrNiRuO_6$ starting materials are chemically similar however, microstructurally they exhibit important differences. A phase transition from the *R*-3 trigonal structure to the $P2_1/n$ monoclinic structure takes place upon cooling from the synthesis temperature (1200 ºC) to room temperature ($T_{transition}$ = 397 ºC).[92] The mechanism by which the symmetry is broken during the phase transition (Section 3.4.1) means that the cooling method used in the final heating step during the synthesis affects the size of the crystalline domains in the resulting materials. Slow-cooling allows the growth of the monoclinic crystalline domains throughout the particles of the material, while quenching traps configurations consisting of smaller domains. The topochemical anion deintercalation of $LaSrNiRuO_6$ causes a contraction along the *c*-axis from 7.85(1) Å in the starting material to 6.92(1) Å in the reduced product. As a consequence, as the reduction progresses, lattice strain builds up at the interface between the anion deficient product and the starting material, as was schematised in Figure 4.14. The energy penalty of this lattice strain build-up across the crystalline domains can be expected to contribute to the energy barrier for the reaction. As discussed in Section 3.4.1, the $LaSrNiRuO_6$ quenched samples are comprised of particles with configurations of comparatively smaller crystalline domains with respect to the slow-cooled analogues. The reduction of quenched starting materials proceeds

completely to the formation of the $LaSrNiRuO_4$ product at 360 ºC. This suggests that such microstructure of smaller crystalline domains sets the energy barrier to a value that is met under the reaction conditions studied, which is consistent with the particles being 'plastic' towards topochemical anion deintercalation. In contrast, the phase separation (into the $LaSrNiRuO_4$ product and unreacted starting material) observed during reduction of slow-cooled samples, suggests that the energy penalty for disrupting the more stable configuration of larger crystalline domains lifts the energy barrier for the reaction. An energy profile for the reduction of $LaSrNiRuO_6$ is proposed in Figure 4.14.

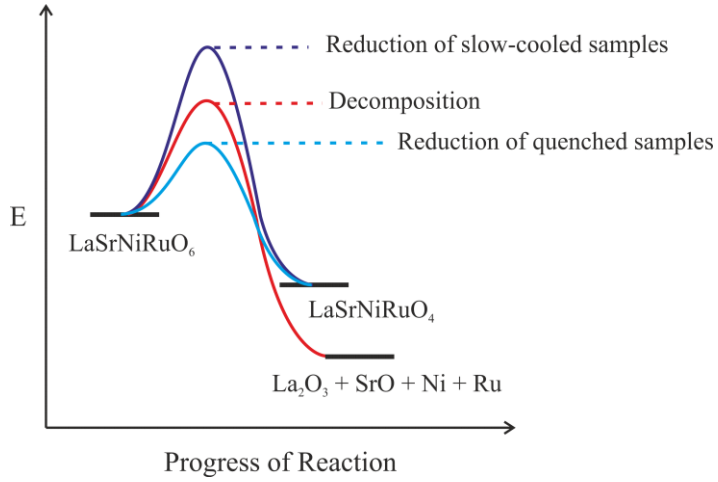


Figure 4.14. Proposed reaction profile for the topochemical reduction of $LaSrNiRuO_6$. The path in red represents the extreme case of complete reductive decomposition.

The proposed diagram in Figure 4.14 is an attempt to schematise the observation that, the reduction of slow-cooled starting materials (dark blue path in the reaction profile) proceeds to the formation of $LaSrNiRuO_4$ until the build-up lattice strain overcomes the energy being supplied at the reaction temperature, at which point the reaction stops. The strain build-up can be partly removed by raising the reaction temperature. However, the formation of the secondary hydride phase, indicative of partial decomposition is observed at only 15 ºC above the original reaction temperature. This suggests that as well as overcoming the energy barrier for further reduction of the slow-cooled samples, raising the temperature fulfils the energy requirements for the competing decomposition reaction to take place. The observation that prolonged heating at 360 ºC results both in the reduced product $LaSrNiRuO_4$ and the decomposition products La_2O_3, SrO, Ru and Ni (as shown

in the X-ray diffraction pattern in Figure 4.10), suggests that the energy barrier for the formation of $LaSrNiRuO_4$ (light blue path in Figure 4.14) is very close to the energy barrier for the decomposition (path in red). This is consistent with $LaSrNiRuO_4$ being a kinetic product during the reduction of $LaSrNiRuO_6$. The decomposition path depicted in the reaction profile of Figure 4.14 (red) is the extreme case of complete reductive decomposition. As noted earlier, the observed hydride secondary phase can be considered a product of partial decomposition.

The reactivity of slow-cooled and quenched $LaSrNiRuO_6$ samples to form $LaSrNiRuO_4$ via topochemical anion deintercalation can be understood as a phase separation (of unreacted starting material and reduced material) which is a consequence of the accumulated strain. This is a markedly different case than other reported phase separations upon topochemical reduction of complex transition metal oxides. For example, reaction of the Ruddlesden-Popper phases $Sr_2Fe_{0.5}Ru_{0.5}O_4$ and $Sr_3(Fe_{0.5}Ru_{0.5})_2O_7$ results in the formation of two-phase mixtures of reduced phases (in both cases) with subtly different oxygen contents.[96] For these two cases, the phase separation can be explained on the basis of short-range inhomogeneous distribution of iron and ruthenium in the starting materials. Similarly, topochemical reduction of $Y_2Ti_2O_7$ yields mixtures of the two reduced phases, $Y_2Ti_2O_{6.5}$ and $Y_2Ti_2O_{5.9}$.[97] This phase separation is associated with a phase gap in the composition range $Y_2Ti_2O_{7-x}$, $0.5 < x < 1.1$ due to an electronic instability. The observed products of reduction bound that region of unstable composition.

4.5 Conclusions

The topochemical reduction of $LaSrNiRuO_6$ with CaH_2 was carried out to produce a novel extended oxide phase with composition $LaSrNiRuO_4$.

The reactivity of quenched $LaSrNiRuO_6$ starting materials demonstrates that a microstructure comprised of small crystalline domains is required for the topochemical anion deintercalation to form the product $LaSrNiRuO_4$ under the conditions studied.

The inability to reduce slow-cooled starting materials can be explained from the lattice strain lifting the reaction energy barrier. The anion deintercalation causes a contraction of

the *c*-lattice parameter from 7.85(1) Å in the starting material to 6.92(1) Å in the reduced product. As discussed in Section 3.4.2, lattice strain builds up as the reduction progresses. The energy needed to overcome the barrier for the reduction of $LaSrNiRuO_6$ slow-cooled samples to form $LaSrNiRuO_4$ fulfils the requirements for the competing reaction of over-reduction/decomposition.

Encompassing this case in a broader context, we believe that this is the first example in which accessibility of the reduced product via topochemical reduction of a complex transition metal oxide is observed to be limited by the microstructural features of the starting material. This is in contrast to the reduction of the Ruddlesden-Popper phases $Sr_2Fe_{0.5}Ru_{0.5}O_4$ and $Sr_3(Fe_{0.5}Ru_{0.5})_2O_7$ as well as $Y_2Ti_2O_7$, for which chemical or electronic features, limit the reactivity of the parent phases towards topochemical reduction.

Chapter 5

Synthesis and Characterisation of $LaSrNiRuO_4$

5.1 Introduction

As discussed previously in Chapters 3 and 4, the topochemical reduction of $LaSrNiRuO_6$ with CaH_2, yields the reduced product $LaSrNiRuO_4$ in which the cation-order is retained. This phase can be understood as a parallel to the disordered $SrFe_{0.5}Ru_{0.5}O_2$ phase, the first reported example of Ru^{2+} in an extended oxide.[38] In the latter phase, the disordered arrangement of the Fe^{2+} and Ru^{2+} centres results in frustration of the magnetic couplings and spin glass behaviour, preventing a detailed exploration of the interactions between the 3*d* and 4*d* electronic states. The ordered arrangement adopted by the nickel and ruthenium cations in $LaSrNiRuO_4$ allowed such electronic couplings to be studied for the first time in an extended oxide phase as will be described in this chapter.

5.2 Experimental

5.2.1 Synthesis of $LaSrNiRuO_4$

The starting materials of $LaSrNiRuO_6$ were prepared as described in Section 3.2.1 via a citrate gel method. In order to prepare materials that could be topochemically reduced (Section 6.4.3), samples were quenched after the final heating period during the synthesis by removal from the furnace at 1200 ºC (the synthesis temperature), and allowed to equilibrate rapidly to room temperature.

The $LaSrNiRuO_{6-x}$ samples were prepared by reacting $LaSrNiRuO_6$ with 4 mole equivalents of CaH_2 at 360 ºC in the venting apparatus (Section 2.2.2). After the reaction,

calcium-containing phases were washed out of the samples with a 0.05 M solution of NH_4Cl in methanol as (Section 2.2.3).

5.3 Results

5.3.1 Thermogravimetric Analysis

The composition of the $LaSrNiRuO_{6-x}$ samples was determined from both reductive and oxidative thermogravimetric measurements (Sections 3.2.3 and 4.2.2). A summary of the data collected from the 'Q-R' sample discussed in Section 4.3.2.1, (prepared as described in Section 5.2.1) is presented in Figure 5.1 (Figures 4.8 and 4.9). The experiments confirmed an initial composition of $LaSrNiRuO_{4.04(2)}$ (Table 5.1).

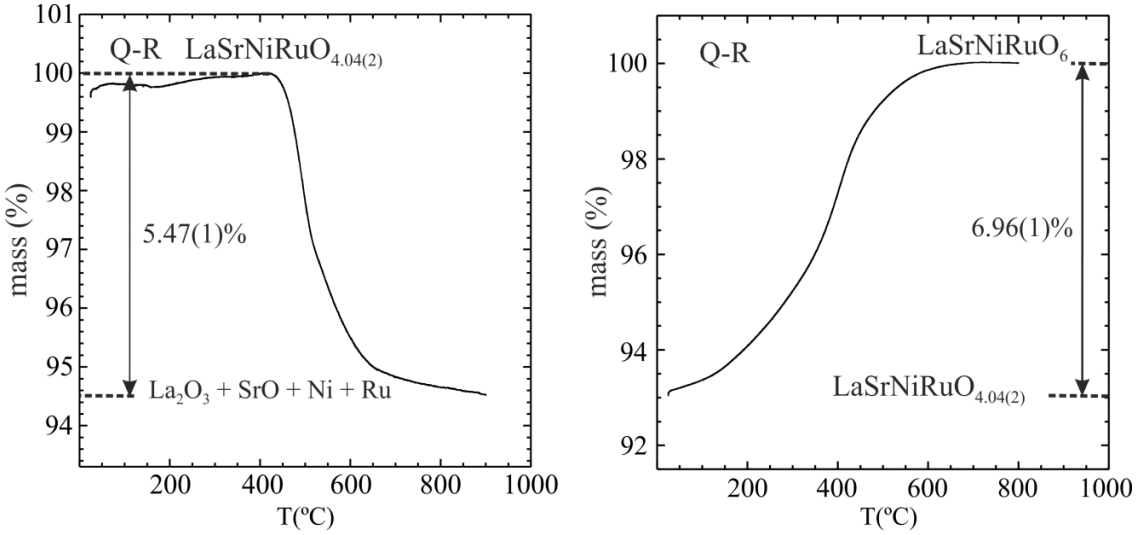


Figure 5.1. Thermogravimetric data collected during reductive decomposition (left) and reoxidation (right) of the $LaSrNiRuO_{6-x}$ Q-R product.

Table 5.1. Summary of the thermogravimetric data collected during reduction and oxidation of the Q-R $LaSrNiRuO_{6-x}$ product.

Reductive Decomposition			
Experiment	**Mass loss (%)**	**RMM***	**Oxygen content**
Reduction	5.47(1)	450.93	4.04(2)
Oxidation	6.96(1)	450.93	4.04(2)

* The theoretical RMM for $LaSrNiRuO_4$ was considered as 450.29. The expected mass loss from reduction was 5.33% and the mass gain during oxidation 7.11%.

5.3.2 X-ray Powder Diffraction

A model based on an *I*4/*mmm* tetragonal structure with lattice parameters a = 5.65(1) Å and c = 6.92(1) Å described in Section 4.3.2, was initially refined against the X-ray powder diffraction data collected from $LaSrNiRuO_4$. Small amounts of elemental nickel (2.5(4)%) and La_2O_3 (0.5(3)%) were observed. These secondary phases were therefore added to the model. As can be noted from the observed and calculated XRD plots shown in Figure 5.2, the tetragonal model yielded a poor fit to the intensity and the width of the diffraction peaks (χ^2 = 2.637, *wRP* = 9.83%, *Rp* = 7.28%). This is particularly clear for the most intense peaks at 2θ ≈ 30.5º and 34.2º (reflections 200 and 112).

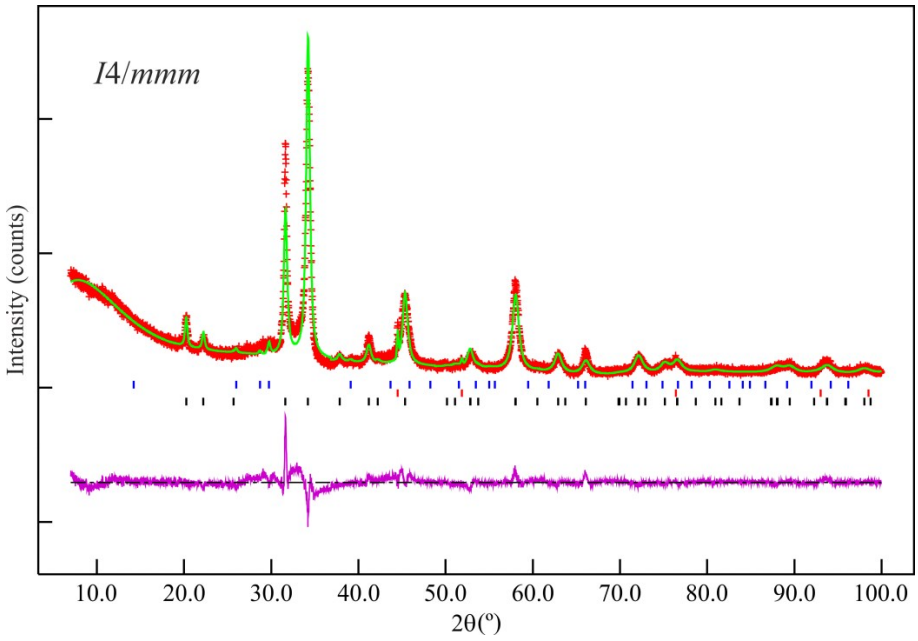


Figure 5.2. Observed, calculated and difference plots from refinement of an *I*4/*mmm* structural model of $LaSrNiRuO_4$ against X-ray powder diffraction data. Black tick marks indicate the peak positions for the majority tetragonal phase; red, elemental Ni (2.5(4)% by weight) and blue, La_2O_3 (0.5(3)% by weight).

A closer inspection of the data revealed that a model of lower symmetry could better describe the structure. An *I*2/*m* monoclinic model based on the *I*4/*mmm* tetragonal cell was constructed. A refinement of the monoclinic model converged to give a better statistical fit (χ^2 = 1.785, *wRP* = 8.91%, *Rp* = 6.48%, Table 5.2). Figure 5.3 shows the plots of the observed and calculated diffraction data. A more detailed structural

characterisation was carried out using neutron powder diffraction data as described in Section 5.3.3.

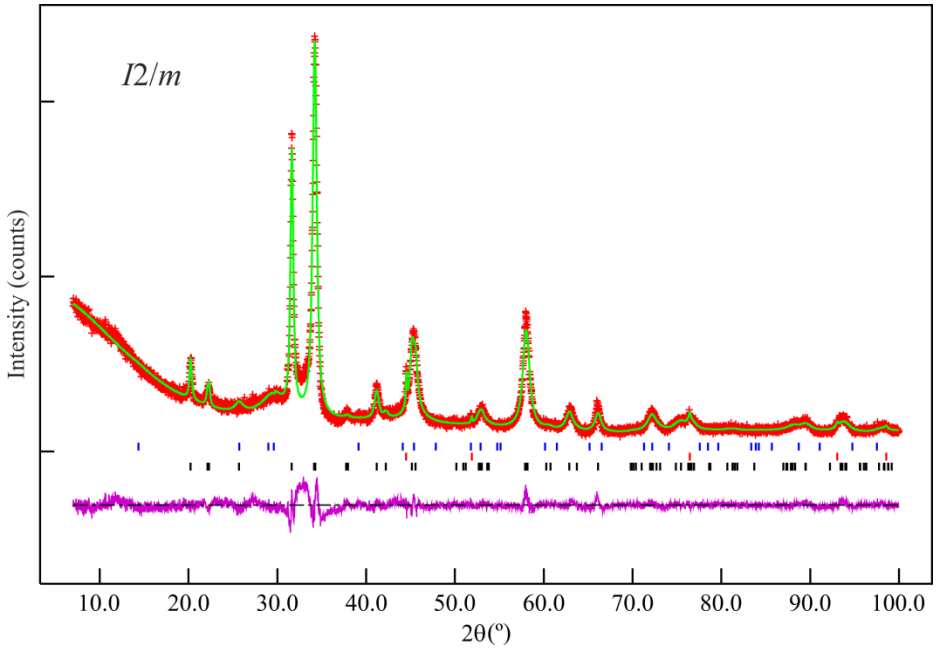


Figure 5.3. Observed, calculated and difference plots from refinement of an *I*2/*m* monoclinic structural model of $LaSrNiRuO_4$ against X-ray powder diffraction data. Black tick marks indicate the peak positions for the majority phase; red, elemental Ni (2.7(3)% by weight) and blue, La_2O_3 (0.5(2)% by weight).

Table 5.2. The *I*2/*m* structural model of $LaSrNiRuO_4$ refined against X-ray powder diffraction data.

atom	Wyck.	*x*	*y*	*z*	fraction	U_{iso} (Å^2)
La/Sr	*4h*	0	½	0.246(2)	0.5/0.5	0.022(1)
Ni	*2a*	0	0	0	1	0.039(1)
Ru	*2b*	½	½	0	1	0.039(1)
O(1)	*4i*	0.246(2)	0.253(2)	0	1	0.037(2)
O(2)	*4i*	0.233(2)	0.739(2)	0	1	0.037(2)
Lattice parameters:						
a **(Å)**		***b*** **(Å)**		***c*** **(Å)**	***γ*** **(°)**	***V*** **(Å^3)**
5.646(2)		5.647(2)		6.925(1)	90.46(1)	220.83(5)
Ni: space group *Fm*-3*m*; *a* = 3.52(1) Å, weight fraction = 2.7(3)%						
La_2O_3: space group *P*-3*m*; *a* = 3.93(1) Å, *c* = 6.21(2) Å weight fraction = 0.5(2)%						
$\chi^2 = 1.785$; $wR_p = 8.91\%$, $R_p = 6.48\%$						

5.3.3 Neutron Powder Diffraction Data Collected at Room Temperature

Neutron powder diffraction data were collected from $LaSrNiRuO_4$ at 300 K using the POLARIS instrument at ISIS (Section 2.4.3.2). The *I*2/*m* monoclinic model (previously described in Section 5.3.2), was refined against the data. During the refinement all the atomic positions were allowed to vary freely and all atoms were described using anisotropic displacement parameters; the refinement converged readily to give a good statistical fit ($\chi^2 = 5.478$; $wR_p = 2.13\%$, $R_p = 2.19\%$, Table 5.3). The observed, calculated, and difference plots are shown in Figure 5.5. Full details of the structural parameters are given in Table 5.3, and selected bond lengths are given in Table 5.5 where they are compared with the results from refinement of the 5 K data set. The refined structure for $LaSrNiRuO_4$ confirms a structure consisting of sheets of square-planar nickel and ruthenium centres, linked by the apexes in a checkerboard arrangement as depicted in Figure 5.4.

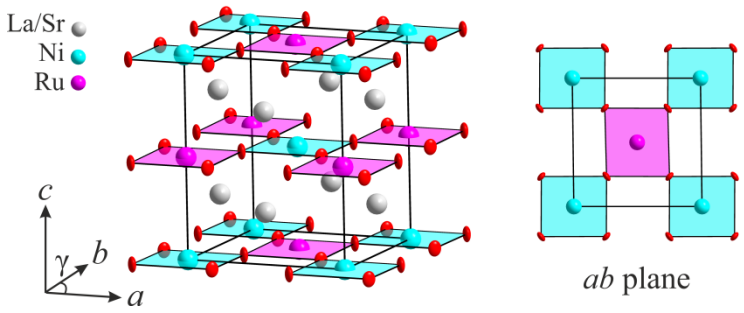


Figure 5.4. Representation of the crystal structure of $LaSrNiRuO_4$ at 300 K. Red ellipsoids represent the oxygen positions.

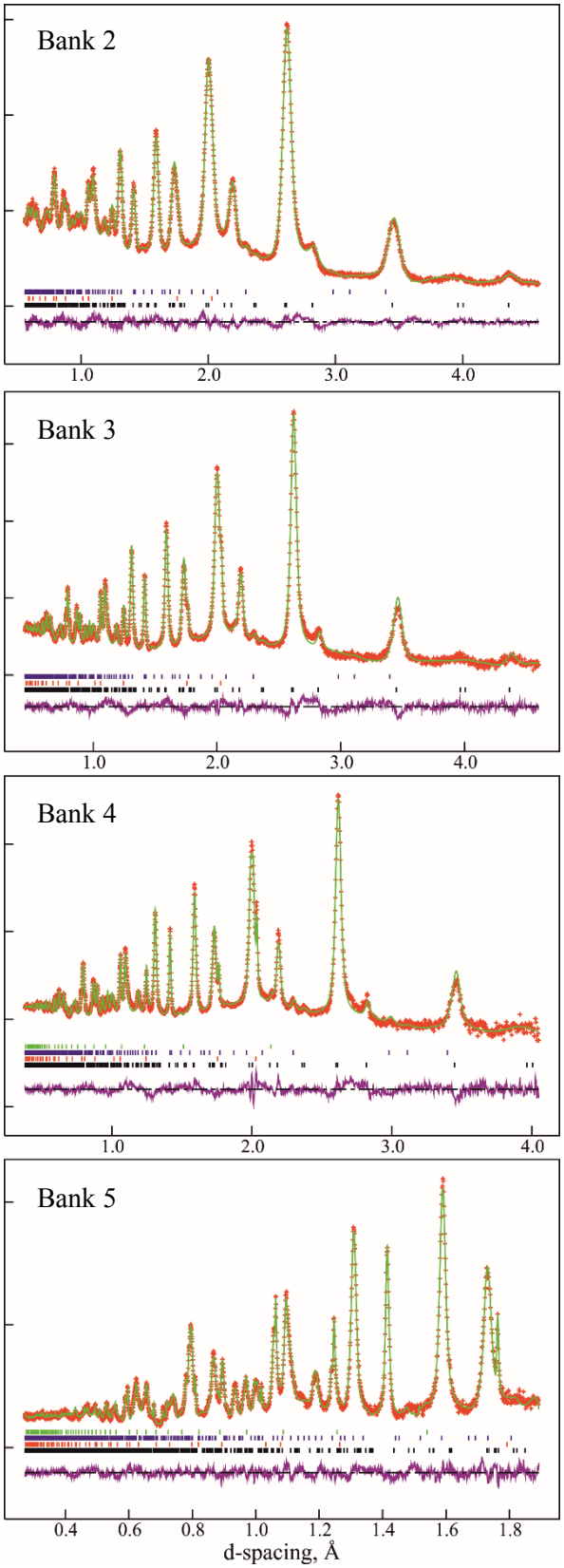


Figure 5.5. Observed, calculated and difference plots of the structural refinement of $LaSrNiRuO_4$ against neutron powder diffraction data collected at 300 K. Black tick marks indicate the peak positions for the monoclinic majority phase; red, elemental Ni (2.3(3)% by weight); blue, La_2O_3 (0.3(1)% by weight); and green, vanadium from the sample holder.

Table 5.3. Structural parameters of $LaSrNiRuO_4$ refined against neutron powder diffraction data collected at 300 K.

atom	Wyck.	*x*	*y*	*z*	fraction
La/Sr	*4h*	0	½	0.2464(7)	0.5/0.5
Ni	*2a*	0	0	0	1
Ru	*2b*	½	½	0	1
O(1)	*4i*	0.251(1)	0.236(1)	0	1
O(2)	*4i*	0.245(1)	0.768(1)	0	1
		U_{11} (Å^2)	U_{22} (Å^2)	U_{33} (Å^2)	U_{12} (Å^2)
La/Sr		0.0048(2)	0.0059(2)	0.0023(1)	0.0016(4)
Ni		0.0112(3)	0.0105(2)	0.0098(4)	0.0009(3)
Ru		0.0135(3)	0.0148(2)	0.0095(8)	0.0010(4)
O(1)		0.0051(1)	0.0068(2)	0.0116(2)	-0.0032(1)
O(2)		0.0052(1)	0.0057(1)	0.0118(2)	0.0031(1)
$\chi^2 = 5.478$; $wR_p = 2.13\%$, $R_p = 2.19\%$					
$LaSrNiRuO_4$: space group *I*2/*m*; $a = 5.652(3)$ Å, $b = 5.652(3)$ Å, $c = 6.9151(4)$ Å, $\gamma = 90.54(1)^o$; $V = 220.89(17)$ Å^3; weight fraction = 97.4(2)% **Ni**: space group *Fm*-3*m*; $a = 3.523(1)$ Å; weight fraction = 2.3(3)% **La_2O_3**: space group *P*-3*m*; $a = 3.933(1)$ Å, $c = 6.238(2)$ Å; weight fraction = 0.3(1)%					

5.3.4 Magnetisation Measurements

Magnetisation data were collected from $LaSrNiRuO_4$ by performing the ferromagnetic subtraction experiment as described in Section 2.6.1. Details of the experiment are given in Appendix 1 and the data are shown in Figure 5.6.

The paramagnetic susceptibility of $LaSrNiRuO_4$ can be fitted by the Curie-Weiss law (Section 2.6.2) in the temperature range 250 < T (K) < 300 to yield values of C = 1.395(2) cm^3 K mol^{-1} and θ = + 192.7(2) K. The observed Curie constant is in good agreement with that expected for a combination of a d^9, S = ½ Ni^{1+} centre and a d^6 Ru^{2+} centre with two unpaired electrons (S =1) as previously observed in $SrFe_{0.5}Ru_{0.5}O_2$.[38]

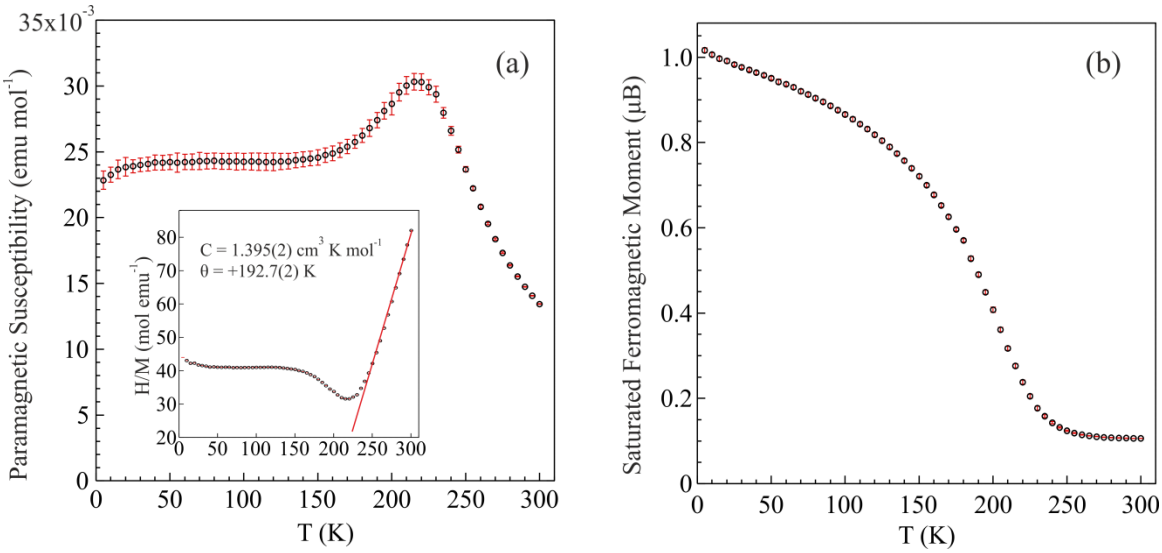


Figure 5.6. The paramagnetic susceptibility (a) and saturated ferromagnetic moment (b) of $LaSrNiRuO_4$ collected as a function of temperature. Inset in the left panel shows the fit to the Curie-Weiss law in the temperature range 250 < T(K) < 300.

On cooling below T ~ 250 K the magnetic susceptibility of $LaSrNiRuO_4$ goes through a local maximum before becoming essentially temperature independent. This change is accompanied by a large increase in the saturated ferromagnetic moment of the sample, consistent with a transition to a magnetically ordered state with a net spontaneous magnetic moment.

5.3.5 Neutron Powder Diffraction at Low Temperature

A comparison of the neutron powder diffraction data collected from $LaSrNiRuO_4$ at 5 K and 300 K is shown in Figure 5.7. A subtle enhancement in the intensity of some of the diffraction peaks can be observed in the low temperature data set. This is consistent with magnetic scattering from the ordered state observed from the magnetisation measurements (Figure 5.6).

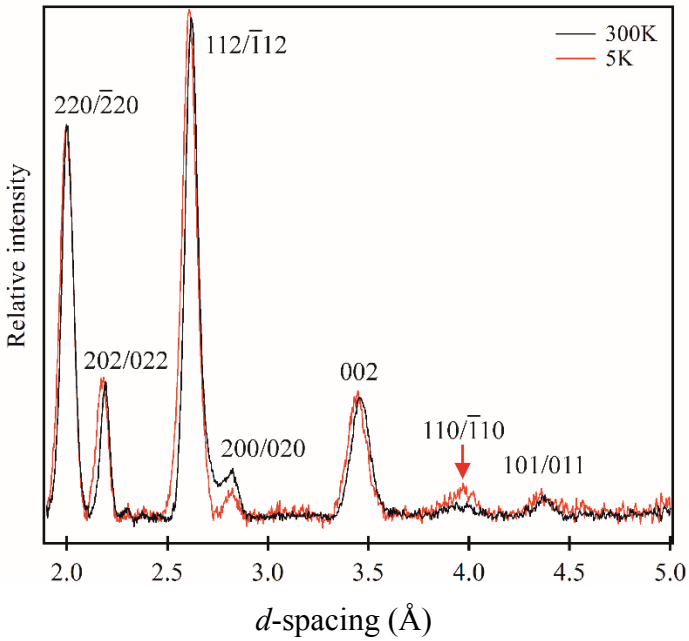


Figure 5.7. Neutron powder diffraction data collected from $LaSrNiRuO_4$ at 5 K exhibit enchanced intensity of the 110/-110 diffraction peak, compared to analogous data collected at 300 K, consistent with a magnetically ordered state at low temperature.

It was observed that the magnetic peaks can be indexed using the body-centred crystallographic structure. This suggested that the ordered magnetic lattice is also body centred. Therefore, a magnetic model was constructed in a way that all the nickel centres had the same ordered magnetic moment with respect to each other, and the ruthenium centres had the same ordered moment in analogous fashion. Antiferromagnetic models of this kind, in which the magnetic moments on the nickel and the ruthenium centres align antiparallel to each other (either within the MO_2 planes and/or between metal centres in adjacent MO_2 planes), yield magnetic scattering peaks that are not observed in the experimental data. Therefore, the magnetic model schematised in Figure 5.8 was used as a starting point.

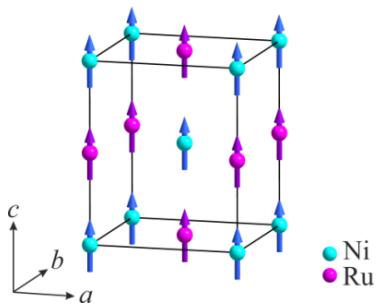


Figure 5.8. Base model for refinement of the magnetic structure of $LaSrNiRuO_4$. Arrows represent the magnetic moments on nickel and ruthenium centres.

The model in Figure 5.8 was refined against the low-temperature diffraction data, in combination with the structural model previously described for the room temperature diffraction data (Table 5.4). The magnetic moments on the nickel and ruthenium centres were allowed to vary independently, and the best fit to the data was achieved by aligning both the nickel and ruthenium moments parallel to the *c*-axis. Applying this constraint, the refined magnetic moments were 1.03(8) μ_B on the nickel site and 0.05(9) μ_B on the ruthenium site. The two moments were refined to be in parallel alignment with each other. The net moment of 1.08(17) μ_B is in good agreement with the saturated ferromagnetic moment of $LaSrNiRuO_4$ measured at 5 K (Figure 5.6b). A scheme of the refined magnetic model is shown in Figure 5.9.

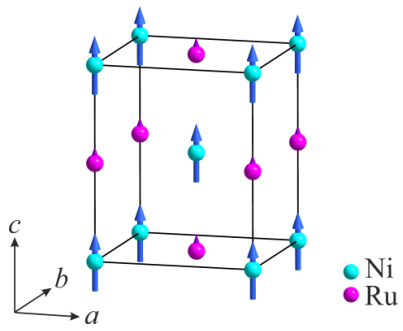


Figure 5.9. Representation of the refined magnetic structure of $LaSrNiRuO_4$.

A net moment of ~ 1 μ_B per formula unit could also result from the ferrimagnetic ordering of 1 μ_B on the nickel centres anti-aligned with 2 μ_B on the ruthenium centres. However, refinement of this model yields a very poor fit to the data and rapidly converts to the ferromagnetic nickel model (described in Figure 5.9) when the magnitude of the ordered moments is refined. Full details of the magnetic structure of $LaSrNiRuO_4$ refined against the neutron powder diffraction data collected at 5 K are given in Table 5.6. The observed and calculated diffraction data are shown in Table 5.4. Details of the crystallographic structure are presented in Figure 5.10 with selected bond lengths and angles in Table 5.5. A comparison with the results from refinement against the 300 K data set is presented.

Table 5.4. The magnetic structure of $LaSrNiRuO_4$ refined from neutron powder diffraction data collected at 5 K.

Atom	*x*	*y*	*z*	Mz (μ_B)
Ni(1)	0	0	0	1.03(8)
Ni(2)	½	½	½	1.03(8)
Ru(1)	½	½	0	0.05(9)
Ru(2)	0	0	½	0.05(9)

Table 5.5. Selected bond lengths and angles from the refined structures of $LaSrNiRuO_4$ at 300 K and 5 K.

Cation	Anion	Bond Lengths (Å)	
		300 K	5 K
Ni	O(1)	1.916(11) × 2	1.959(11) × 2
	O(2)	1.938(11) × 2	1.950(11) × 2
Ru	O(1)	2.041(12) × 2	2.023(12) × 2
	O(2)	2.101(12) × 2	2.078(12) × 2
Bond		**Bond Angles (°)**	
Ni-O(1)-Ru		176.5(3)	174.4(3)
Ni-O(2)-Ru		177.0(3)	176.3(3)

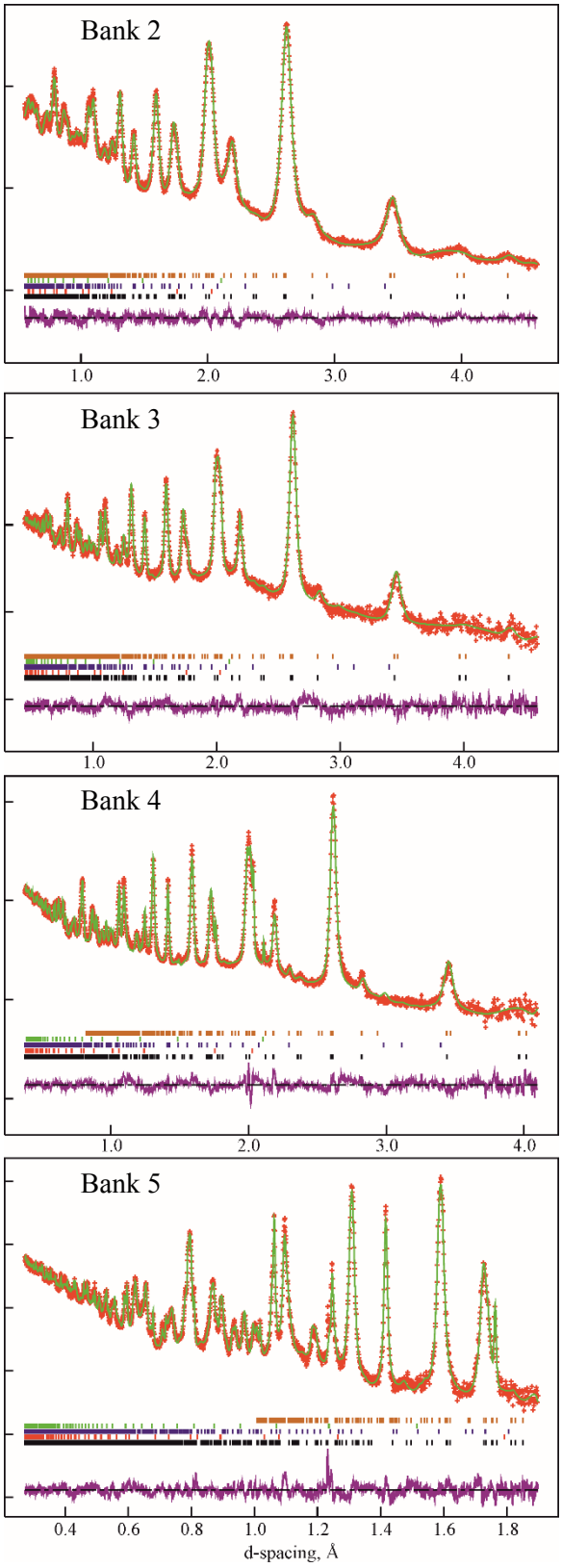


Figure 5.10. Observed, calculated and difference plots of the structural refinement of $LaSrNiRuO_4$ against neutron powder diffraction data collected at 5 K. Black tick marks indicate the peak positions for the monoclinic majority phase; red, elemental Ni (2.3% by weight); blue, La_2O_3 (0.3% by weight); green, vanadium from the sample holder; and orange, the magnetic cell of $LaSrNiRuO_4$.

Table 5.6. Structural parameters of $LaSrNiRuO_4$ refined against neutron powder diffraction data collected at 5 K.

atom	Wyck.	*x*	*y*	*z*	fraction
La/Sr	*4h*	0	½	0.2450(5)	0.5/0.5
Ni	*2a*	0	0	0	1
Ru	*2b*	½	½	0	1
O(1)	*4i*	0.258(1)	0.234(1)	0	1
O(2)	*4i*	0.250(1)	0.766(1)	0	1
		U_{11} (Å^2)	U_{22} (Å^2)	U_{33} (Å^2)	U_{12} (Å^2)
La/Sr		0.0032(2)	0.0047(2)	0.0020(1)	0.0018(3)
Ni		0.0114(2)	0.0101(1)	0.0081(4)	0.0007(3)
Ru		0.0142(3)	0.0140(3)	0.0084(4)	0.0012(4)
O(1)		0.0049(1)	0.0048(1)	0.0125(2)	0.0042(1)
O(2)		0.0058(1)	0.0057(1)	0.0127(2)	-0.0047(1)
$\chi^2 = 3.199$; $wR_p = 1.31\%$, $R_p = 1.51\%$					
$LaSrNiRuO_4$: space group *I*2/*m*; $a = 5.660(3)$ Å, $b = 5.658(3)$ Å, $c = 6.9007(4)$ Å, $\gamma = 90.70(1)^o$; $V = 220.97(17)$ Å^3; weight fraction = 97.4% **Ni**: space group *Fm*-3*m*; $a = 3.520(1)$ Å; weight fraction = 2.3% **La_2O_3**: space group *P*-3*m*; $a = 3.928(1)$ Å, $c = 6.235(1)$ Å; weight fraction = 0.3%					

5.3.6 Density Functional Theory Calculations

In order to explore the nature of the magnetic coupling in $LaSrNiRuO_4$, Density Functional Theory (DFT) calculations were performed. First-principles methods using DFT calculations with a plane-wave basis set can provide details about the atomic-scale structure of a periodic unit (*e.g.* a crystal cell), and therefore allow the investigation of structural, magnetic and electronic properties in many-electron systems. Low-energy structures can be relaxed from starting guesses, which yields calculated symmetry, bond-lengths and coordination environments for atomic positions previously derived from available crystallographic data. The DFT calculations were performed by Prof. John McGrady and his DPhil student Dihao Zeng (Department of Chemistry, Physical and Theoretical Chemistry Laboratory, University of Oxford).

5.3.6.1 Computational Methodology for the DFT Calculations

The calculations were performed using the VASP software package (VASP 5.3),[98] with the PBE density functional[99] and the PAW pseudopotentials.[100] A plane-wave cut off energy of 600 eV was used, along with a 9 by 9 by 9 gamma-centred grid for sampling of the Brillouin zone. The strong correlations effect was introduced by the addition of the effective Hubbard U(U_{eff}) value to the Hamiltonian (DFT+U). The choice of U_{eff} has been discussed extensively, and is typically larger for the compact *3d* orbitals with respect to the more diffuse *4d* orbitals. Typical values in the literature are U_{eff} = 6.0 eV for Ni and 3.0 eV for Ru, therefore such values were chosen for the calculations. However, given the rather unusual state prevalent in this low-valent $LaSrNi^{I}Ru^{I\,I}O_4$ system, the dependence of the results on U_{eff} was tested across a broad range of values. The lattice parameters, M-O bond lengths and spin densities prove to be largely independent of the choice of U_{eff} for Ni, up to 8.0 eV. In contrast, increasing the value of U_{eff} for Ru is observed to increase the spin density from values of ~1.50 for U_{eff} = 0 eV to ~1.80 for U_{eff} = 5 eV. A dependence of the lattice parameters and M-O bond lengths is also observed with the choice of U_{eff} for Ru as will be discussed in Section 5.3.6.2.

The energy computations were performed for the three spin configurations shown in Figure 5.11. Geometry optimisations were performed with the unit cell volume constraint released, and all ions were allowed to move freely.

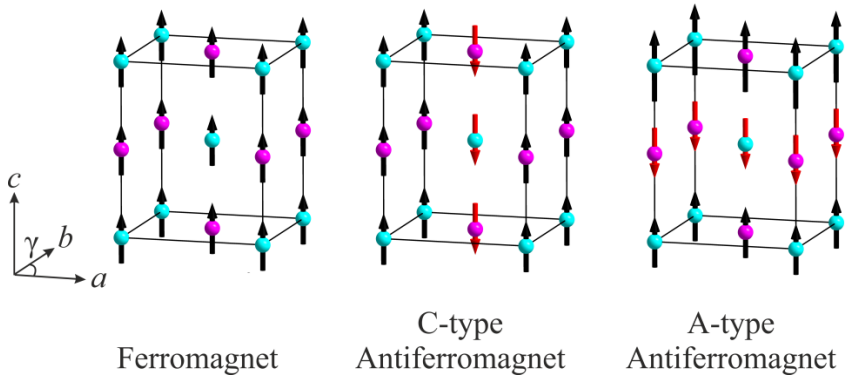


Figure 5.11. Three distinct spin configurations of $LaSrNiRuO_4$ system. Spheres represent the nickel and ruthenium centres. The unit cells are monoclinic *I*2/*m*.

5.3.6.2 Results from the DFT Calculations

The energies calculated for the models of Figure 5.11, are shown in Table 5.7.

Table 5.7. Energies computed for the ferromagnetic, and C-type and A-type antiferromagnetic spin models of $LaSrNiRuO_4$.

Spin Configuration	Energy (eV)
Ferromagnetic	-101.187
C-type Antiferromagnetic	-101.040
A-type Antiferromagnetic	-101.181

The configurations with ferromagnetic coupling in the Ni/Ru planes (F and A-type configurations) are observed to be substantially more stable than the C-type antiferromagnetic configuration. The ferromagnetic configuration is the most stable of the three. The energies mapped onto the diagonal elements of the Heisenberg spin Hamiltonian in Equation 5.1 yielded exchange coupling constants of J_1 = 1184 cm^{-1}; J_2 = 46 cm^{-1} depicted in Figure 5.12.

$$\hat{H} = -\sum_{i>j} 2\boldsymbol{J}_{ij}\hat{S}_i\hat{S}_j \qquad (5.1)$$

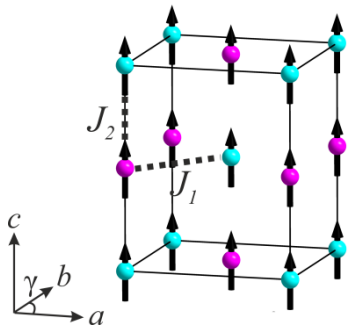


Figure 5.12. Representation of the most stable spin configuration. Dashed lines represent the exchange coupling interactions from which J_1 and J_2 are calculated.

A projection down the *c*-axis of the optimised lattice is presented in Figure 5.13. The computed lattice parameters *a* = 5.724 Å, *b* = 5.716 Å and *c* = 6.881 Å are in good agreement with the refined crystallographic model against powder diffraction data. However, the optimised angle γ = 92.41° is larger than the refined value of γ = 90.70(1)°

(Table 5.6). The degree of asymmetry in the Ni-O and Ru-O bond lengths is therefore overestimated in the optimised lattice (computed Ni-O bond lengths: 2.01/2.06 Å, refined: 1.959(11)/1.950(11) Å; computed Ru-O bond lengths: 1.95/2.06 Å, refined: 2.023(12)/2.078(12) Å). The value of γ and therefore the degree of asymmetry was observed to be strongly dependent on the chosen value of U_{eff} for Ru. Values of U_{eff} = 5.0 eV or higher give way to an almost tetragonal lattice. This shift towards a more tetragonal structures is commensurate with an increase in the spin-density at Ru (1.80 for U_{eff} = 5.0 eV), which suggests that the lower covalency of the Ru-O bond plays an important role in the magnitude of the distortion of the lattice.

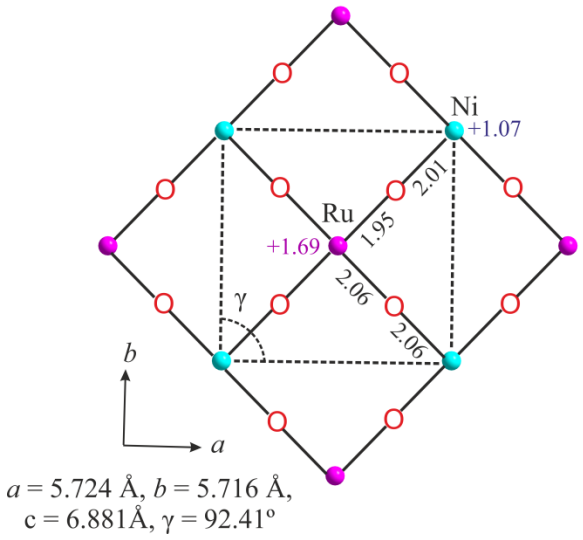


Figure 5.13. Representation of the optimised bond lengths and net spin densities for the computed monoclinic unit cell (dotted line).

The density of states, projected onto the individual components of the *d* orbitals of both Ni and Ru, are shown in Figure 5.14. The axes are defined such that *x* and *y* bisect the O-M-O angles in Figure 5.13.

Only the spin-*β* component of the d_{xy} orbital of Ni lies above the Fermi level, while the d_{z^2} orbital is doubly occupied, which gives a local configuration of $(d_{z^2})^2(d_{xy/yz})^4(d_{x^2-y^2})^2(d_{xy})^1$ that corresponds to a S = ½ spin state. In contrast, for Ru both components of the d_{xy} orbital, the spin-*β* components of $d_{x^2-y^2}$ and one linear combination of $d_{xz/yz}$, lie above the Fermi level. This results in a local configuration of $(d_{z^2})^2(d_{xy/yz})^3(d_{x^2-y^2})^1(d_{xy})^0$, as is expected by analogy to the electronic configuration of ruthenium in $SrFe_{0.5}Ru_{0.5}O_2$.[38]

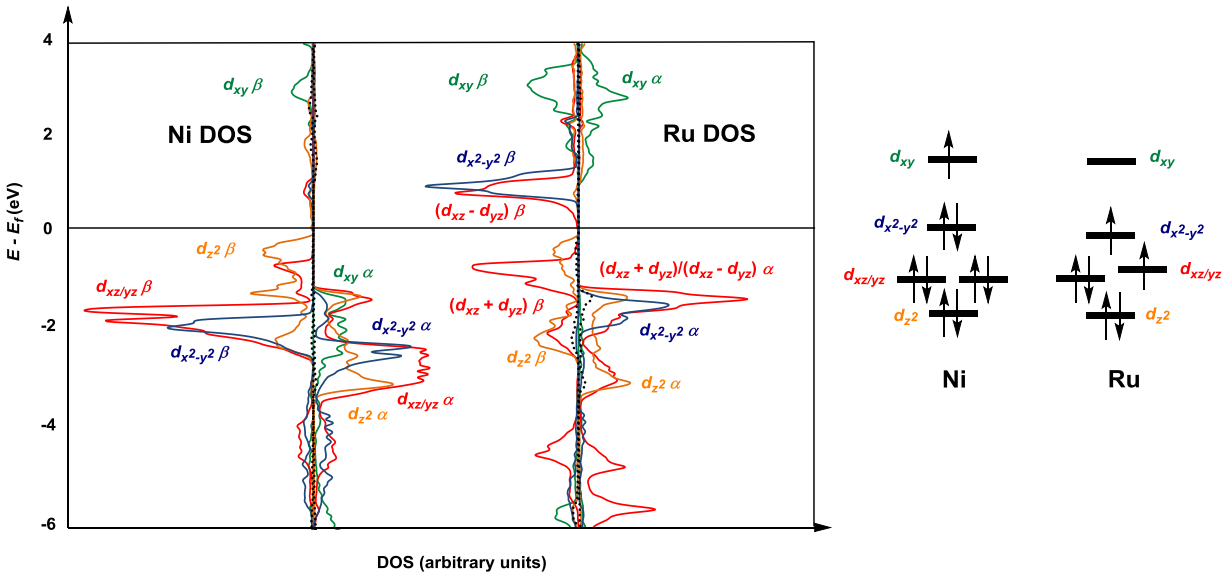


Figure 5.14. Spin-polarised projected density of states for nickel and ruthenium in $LaSrNiRuO_4$ (U_{eff}(Ni) = 6.0 eV, U_{eff}(Ru) = 3.0 eV.

The dashed black line in Figure 5.14 corresponds to the *s* orbital components for Ni and Ru. The DOS for Ru was observed to have a significant *5s* character coincident with the prominent d_z^2 features (also observed in the electronic structure of $SrFe_{0.5}Ru_{0.5}O_2$).[38] This is suggestive of a strong s/d_z^2 hybridisation, which is in agreement with previous reports in the literature ($Ca_{1-x}Sr_xFeO_2$, $SrFe_{0.5}Ru_{0.5}O_2$).[38,101,102] Canadell *et al.* showed that such s/d_z^2 orbital hybridisation allows the majority- and minority-spin components to differ spatially, which reduces the repulsion between the formally paired electrons.[103]

5.4 Discussion

The topochemical reduction of suitably prepared $LaSrNiRuO_6$ (Chapters 3 and 4) with CaH_2 yields $LaSrNiRuO_4$. The refined structural model confirms that $LaSrNiRuO_4$ adopts an infinite layer structure formed by sheets of corner sharing square-planar ruthenium and nickel centres. The cation order is preserved and the NiO_4 and RuO_4 squares adopt a checkerboard arrangement (Figure 5.4).

5.4.1 High Temperature Structural and Magnetsiation Data

The room-temperature structure and magnetic behaviour of $LaSrNiRuO_4$ are both consistent with a transition-metal oxidation state combination of Ni^{1+} and Ru^{2+}. A direct comparison of the Ru-O lengths in $LaSrNiRuO_4$ with those in $SrFe_{0.5}Ru_{0.5}O_2$ is not possible given that the former is B-cation ordered in contrast with the latter. However, the average M-O bond lengths in the two phases are almost identical as shown in Table 5.8.

Table 5.8. Average M-O bond lengths in $LaSrNiRuO_4$ and $SrFe_{0.5}Ru_{0.5}O_2$ at 300 K.[38]

	Average Bond Lengths (Å)
Ni/Ru-O	1.999(13)*
Fe/Ru-O	1.998(1)

* Calculated from data in Table 5.5.

On the other hand, the Ni-O bond lengths in $LaSrNiRuO_4$ (1.916(11) Å and 1.938(11) Å (Figure 5.5), are shorter than those in $LaNiO_2$ (1.979 Å).[35] This observation suggests that the $NiRuO_4$ plane is under significant compression. As will be discussed later, such a structural feature seems to drive the changes observed from the data collected at a low temperature.

The Curie constant obtained from the high-temperature magnetisation data (T > 250 K) is consistent with the value predicted for a combination of d^9, S = ½ Ni^{1+} centres, and d^6, S = 1 Ru^{2+} centres ($C_{expected}$ = 1.375 cm^3 K mol^{-1}, $C_{observed}$ = 1.395(2) cm^3 K mol^{-1}). The S = 1 spin state for ruthenium agrees with the previous observation in $SrFe_{0.5}Ru_{0.5}O_2$ (Ru^{2+}:$(d_z^2)^2(d_{xz}, d_{yz})^3(d_{xy})^1(d_{x^2-y^2})^0$).[38,91]

5.4.2 Low Temperature Structure and Magnetic Behaviour of $LaSrNiRuO_4$

The magnetic behaviour of $LaSrNiRuO_4$ at low temperature is highly unusual. On cooling below 250 K the phase adopts an ordered magnetic state with a net saturated magnetic moment of ~1 μ_B per formula unit (Figure 5.6b), which seems to come entirely from the nickel centres. The latter is suggested by the refined magnetic model against the neutron

diffraction data collected at 5 K, in which the moment is 1.03(8) μ_B on nickel and 0.05(9) μ_B on ruthenium. The magnetisation data shows a practically temperature-independent magnetic susceptibility for $LaSrNiRuO_4$ below T ~ 200K (Figure 5.6a). This supports the observation that the ruthenium centres exhibit an almost diamagnetic behaviour in the low-temperature regime. The low-temperature crystal structure of $LaSrNiRuO_4$ also exhibits rather unexpected features that can give insight to the phase transition observed from the magnetic data. The volume of the unit cell at 5 K is larger than that at 300 K (V_{5K} = 220.97(17) Å^3 vs V_{300K} = 220.89(17) Å^3, Tables 5.3 and 5.6), which is a consequence of an expansion in the *xy*-plane that counteracts a contraction parallel to the *z*-axis upon cooling. In addition, the bond lengths in Table 5.5 show that there is a shortening of the Ru-O bonds and a lengthening of Ni-O bonds from the structure at 300 K to the structure at 5 K. These changes 'equalise' the M-O bond lengths in the low temperature structure in which a change in the oxygen displacement parameters is observed. A comparison of the structure of $LaSrNiRuO_4$ with the displacement ellipsoids of the oxide ions at 300 K and 5 K is shown in Figure 5.15.

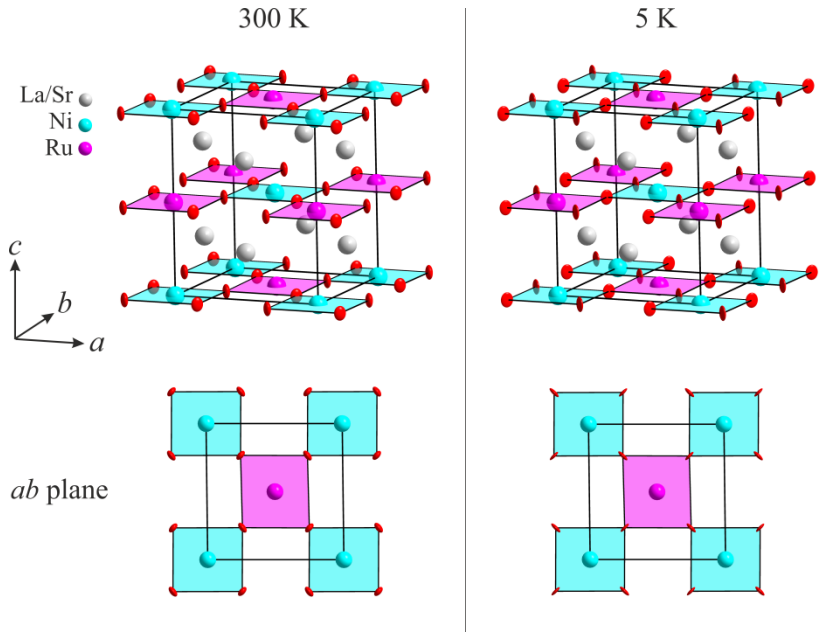


Figure 5.15. Comparison of the crystal structure of $LaSrNiRuO_4$ at 300 K and 5 K. Red ellipsoids represent the oxygen positions

The displacement ellipsoids of both the crystallographically distinct oxide ions in the 300 K structure have their largest values perpendicular to the Ni-O-Ru bond vector. This is a feature which is consistent with the lowest energy vibrational displacement also being perpendicular to the bond vector. In contrast the largest displacement of the oxide ions in the 5 K structure is approximately parallel to the Ni-O-Ru bond vector. This behaviour is inconsistent with a vibrational displacement and is more indicative of static disorder in the positions of the oxide ions.

The magnetisation data and neutron diffraction data indicate that $LaSrNiRuO_4$ appears to exist in two different electronic states. At temperatures above ~250 K, the data are consistent with a paramagnetic state with localised S = ½, Ni^{2+} and S = 1, Ru^{2+}, but upon cooling the system appears to undergo a cooperative ordering transition that leads to a ferromagnetic alignment of the nickel spins and concomitant loss of spin moment at ruthenium. The DFT calculations were important for the exploration of the origins of these structural and magnetic features in more detail (Section 5.4.3).

5.4.3 The Electronic Structure of $LaSrNiRuO_4$

The electronic structure presented in Figure 5.14 for $LaSrNiRuO_4$ is consistent with the high temperature powder diffraction and magnetisation data, and confirms the electronic configurations of $(d_{z^2})^2(d_{xy/yz})^4(d_{x^2-y^2})^2(d_{xy})^1$ for S = ½, Ni^{1+} and $(d_{z^2})^2(d_{xy/yz})^3(d_{x^2-y^2})^1(d_{xy})^0$ for S = 1, Ru^{2+}. The combination of a singly occupied d_{xy} orbital on Ni^{1+} and a vacant d_{xy} orbital on Ru^{2+} provides a superexchange coupling pathway which is in agreement with the ferromagnetic structure proposed for $LaSrNiRuO_4$ upon cooling. The partial occupation of the $d_{xy/yz}$ manifold on Ru presents a clear driving force for the distortion from a perfect tetragonal symmetry, which is consistent with the refined monoclinic structural model. However, in the magnetisation and neutron diffraction data at a low-temperature the apparent absence of paramagnetic moment at the ruthenium centres (that in fact seem to exhibit a diamagnetic behaviour), is rather unexpected. One of the possible explanations was a large spin-orbit coupling for the ruthenium that resulted in reduction of the observed moment. However, the inclusion of spin-orbit coupling was observed to have a minor impact on the computed moment on ruthenium, consistent with earlier observations by Lee *et al.* on the double perovskite phase Sr_2CrRuO_6.[104] The electronic

configuration of Ru^{2+} ($(d_{z^2})^2(d_{xz/yz})^3(d_{xy})^1(d_{x^2-y^2})^0$) is unstable with respect to a symmetry breaking, Jahn-Teller like, structural distortion that lifts the degeneracy of the local ruthenium electronic state. Building on this idea, another possible explanation for the unexpected diamagnetic moment observed at the ruthenium centres at low temperature is a pronounced FOJT (Section 1.1.1) distortion in $LaSrNiRuO_4$ that would split the $d_{xy/yz}$ manifold to an even greater degree, and induce spin pairing at the Ru^{2+} centres and yield a $(d_{z^2})^2(d_{xz+yz})^2(d_{x^2-y^2})^2(d_{xz-yz})^0(d_{xy})^0$ configuration as schematised in Figure 5.16. A stable minimum corresponding to such a state was attempted by initialising the DFT calculations from a range of highly distorted structures, however the system invariably returns to the monoclinic moderately distorted structure with two unpaired electrons on the ruthenium. Hence, no evidence was found for this type of extreme Jahn-Teller distortion. In principle, an ordered arrangement of the local Jahn-Teller distortions of the Ru^{2+} centres analogous to the orbital order observed in $LaMnO_3$,[105] could stabilise a sufficiently large structural distortion and support a transition to a diamagnetic state. However, the average structure observed by neutron powder diffraction provides no information about the presence or nature of such orbital ordering. Furthermore, such ordering is intrinsically beyond the limits of the small unit cell used for the DFT calculations.

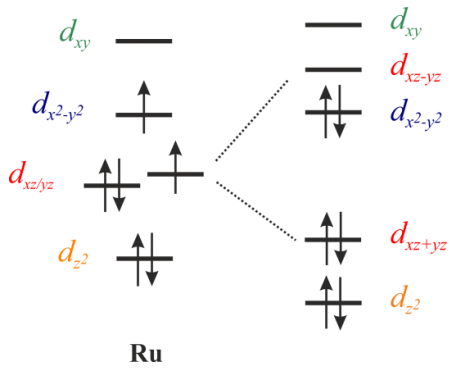


Figure 5.16. Schematisation of the proposed FOJT effect for the ruthenium centres in the low temperature structure of $LaSrNiRuO_4$. The relative position of the d_{z^2}, $d_{x^2-y^2}$ and d_{xy} orbitals has been adjusted for simplicity in showing the splitting of the $d_{xy/yz}$ manifold.

5.5 Conclusions

Reaction of the double perovskite, $LaSrNiRuO_6$, with CaH_2 at 360 ºC yields the novel phase $LaSrNiRuO_4$ via topochemical anion deintercalation. The structure of this new material is body-centred monoclinic *I*2/*m* with lattice parameters a = 5.652(3) Å, b = 5.652(3) Å, c = 6.9151(4) Å, γ = 90.54(1)°.

The formation of $LaSrNiRuO_4$ via the reduction of $LaSrNiRuO_6$ demonstrates that the La-Sr-Ni-O lattice in $LaSrNiRuO_4$ is sufficiently robust to resist decomposition, and can thus stabilize the formation of Ru^{2+} centres in an extended oxide phase. This allows for the preparation of what is, to the best of our knowledge, the first example of a B-cation ordered infinite-layer oxide phase.

The room-temperature structure and magnetic behaviour of $LaSrNiRuO_4$ are consistent with a combination of transition metal oxidation states of Ni^{1+} and Ru^{2+}. DFT calculations support these oxidation states and predict a triplet configuration at ruthenium with a Jahn-Teller distortion driven by an orbitally degenerate state $(d_z^2)^2(d_{xy/yz})^3(d_x^2\text{-}_y^2)^1(d_{xy})^0$.

On cooling below 250 K the magnetic susceptibility goes through a local maximum indicative of the onset of ferromagnetic order. The saturated moment of the sample of $1\mu_B$ (observed at low temperature) is localised entirely on the nickel centres, with the ruthenium ions becoming diamagnetic. An extreme Jahn-Teller distortion offers one potential explanation for this observation. However, the powder diffraction data provides no information about the presence or nature of such structure and computationally locating such a structure using DFT calculations has not been possible.

Chapter 6

The Topochemical Reduction of $SrV_{0.95}Ti_{0.05}O_3$

6.1 Introduction

The reaction of complex transition metal oxides with binary metal hydrides is not limited to the topochemical deintercalation of oxide anions but can also lead to the exchange of oxide anions for hydride to form transition metal oxyhydrides. For example, reaction of $LaSrCoO_4$ with CaH_2 initially forms the reduced phase $LaSrCoO_{3.35}$ and further heating leads to an anion exchange reaction to form the first reported transition metal oxyhydride phase $LaSrCoO_3H_{0.7}$.[44] Similarly, the strontium vanadium oxyhydride phases $SrVO_2H$, Sr_2VO_3H and $Sr_3V_2O_5H_2$ were prepared via oxide-for-hydride exchange reduction of $SrVO_3$, Sr_2VO_4 and $Sr_3V_2O_7$, respectively.[48] These strontium vanadium oxyhydrides, shown in Figure 6.1, consist of sheets or chains of apex-linked $V^{3+}O_4$ squares stacked with SrH layers (or chains) and are the first materials reported to exhibit both stoichiometric exchange of oxide for hydride, and a rigorous oxide/hydride anion order.

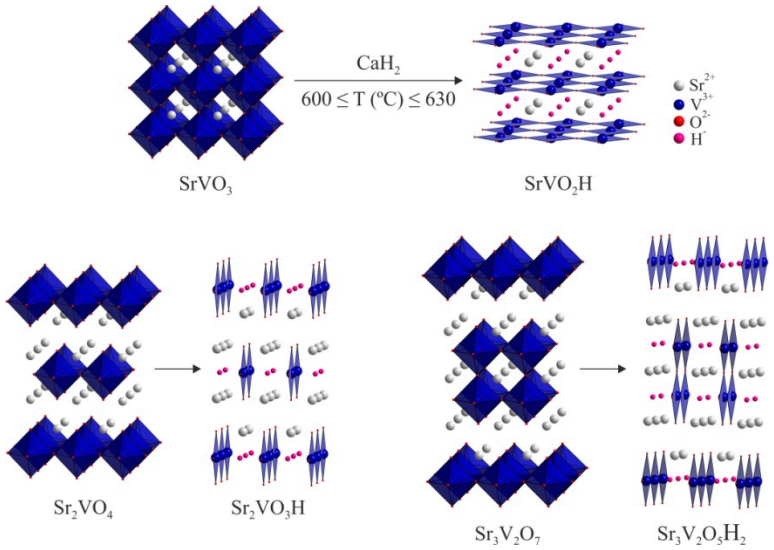


Figure 6.1. Reaction of the $SrO(SrVO_3)n$ (n = 1, 2, ∞) phases with CaH_2 to form the $Sr_{n+1}V_nO_{2n+1}H_n$ phases.

The electronic structure of the vanadium centres in the $Sr_{n+1}V_nO_{2n+1}H_n$ phases is depicted in Figure 6.2. Despite the formal 6-fold coordination of the vanadium centres in these VO_4H_2 units, the VO_2 infinite sheets in $SrVO_2H$ can be compared to the CuO_2 planes observed in $Sr_{1-x}Ca_xCuO_2$ phases, among which the parent phase of the high-T_c cuprate superconductors is found.[48,106] In contrast to $Sr_{1-x}Ca_xCuO_2$ and other infinite layer phases such as $LaNiO_2$ or $SrFeO_2$, the (d^2) VO_2 planes in $SrVO_2H$ are connected by hydride ions. The 1*s* valence orbitals of the hydride ions have strict σ-type symmetry and are thus orthogonal to the π-symmetry low-lying d_{xz}, d_{yz}, and d_{xy} orbitals of vanadium. The latter set of orbitals host the electrons of the d^2,V^{3+} centres, and interact with the oxygen 2*p* orbitals, which yields a degenerate $(d_{xz}, d_{yz})^2$ pair of orbitals that comprises the HOMO, and a destabilised d_{xy} empty orbital from which the LUMO is derived. Since the σ-type vanadium *d*-orbitals that interact with the hydride 1*s* orbitals are empty and energetically remote from the filled orbitals, the environment for the vanadium centres resembles that of V-O infinite layer framework.

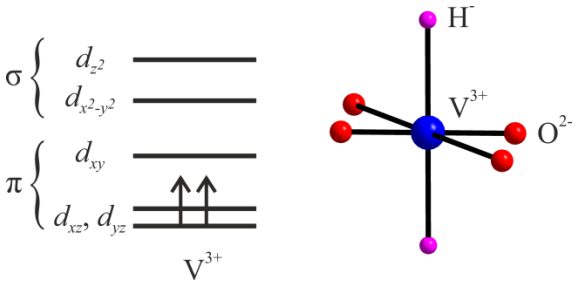


Figure 6.2. Local electronic structure (left) of the VO_4H_2 units (right).

Hence, there is a direct structural and electronic analogy between $SrVO_2H$ and the infinite-layer ABO_2 phases where B is a transition metal in square-planar coordination (Figure 6.3).

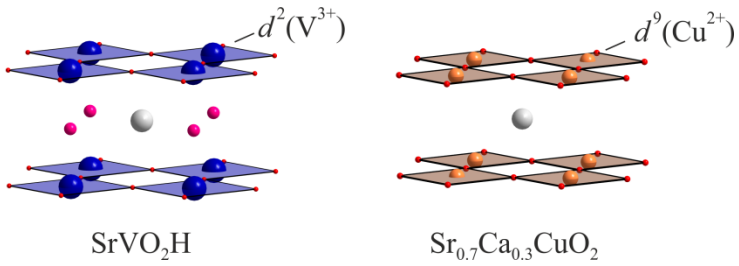


Figure 6.3. An analogous coordination environment for the transition-metal centres can be observed by comparison of the $SrVO_2H$ and $Sr_{0.7}Ca_{0.3}CuO_2$ structures.

In contrast to the growing diversity of such materials where the B cation has configurations of d^6 to d^9, $SrVO_2H$ is an electron-poor phase with d^2, V^{3+} centres.[38,39,107] Therefore, this phase represents an important extension for the investigation of strongly interacting *d*-electrons in a low electron-count regime. Most of the ABO_2 phases with occupied σ-symmetry metal *d*-orbitals (as is the case in the *d*-electron-rich phases), are observed to exhibit the behaviour of a Mott–Hubbard insulator with a strong tendency for antiferromagnetic order. Despite the empty σ-symmetry metal *d*-orbitals in $SrVO_2H$, this phase is similarly an insulator and exhibits long-range antiferromagnetic order with T_N > 300 K.[48] This high magnetic transition temperature is unexpected given that the magnetic order arises from interactions between electrons in π-symmetry *d*-orbitals (Figure 6.2). The magnetic structure derived from neutron powder diffraction data (and confirmed via μ^+SR spectroscopy) is shown in Figure 6.4.

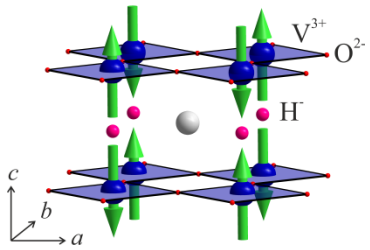


Figure 6.4. Magnetic structure of $SrVO_2H$.

A common approach to investigate the electronic interactions in materials with square-planar transition-metal centres in the low-electron count regime is to try to introduce electron holes by doping the A sites. In this work, a different approach was taken by investigating the effect of substitution of titanium onto the B-sites of $SrVO_2H$. Thus, phases of composition $SrV_{1-x}Ti_xO_3$ were prepared to be topochemically reduced with CaH_2.

$SrV_{1-x}Ti_xO_3$ (x = 0.05) starting materials were synthesised via two different methods, the ceramic method and the arc-melt technique. Despite the chemical and structural similarities of the samples obtained via the two synthesis methods, a markedly different behaviour upon reduction was observed from the two materials. The differences between the reduction products from the $SrV_{1-x}Ti_xO_3$ (x = 0.05) starting materials prepared via the ceramic and arc-melt methods are investigated in this chapter while Chapter 7 concerns the characterisation of the $SrV_{1-x}Ti_xO_3$ starting materials.

6.2 Experimental

6.2.1 Synthesis of the $SrV_{1-x}Ti_xO_3$ (x = 0.05) starting materials

Two $SrV_{1-x}Ti_xO_3$ (x = 0.05) samples were prepared: Sample C was prepared via the ceramic method previously described by Rey *et al.* for the synthesis of $SrO(SrVO_3)_n$ phases,[108] and sample A using an arc-melt furnace (Section 2.1.3). The details of each synthesis method are given in Section 7.2. The resulting diffractograms of the C and A starting materials are shown in Figure 6.5.

6.2.2 Reduction of the $SrV_{1-x}Ti_xO_3$ (x = 0.05) Samples Prepared via the Ceramic and Arc-Melt Methods

The $SrV_{1-x}Ti_xO_3$ (x = 0.05) samples prepared via the ceramic and arc-melt methods, were reduced with CaH_2 (Section 2.2) and the reaction progress was followed by X-ray powder diffraction.

After reaction, calcium-containing phases were removed from samples by washing with a 0.05 M solution of NH_4Cl in methanol as described in Section 2.2.3.

6.3 Results

6.3.1 X-ray Powder Diffraction Data of the $SrV_{1-x}Ti_xO_3$ (x = 0.05) Starting Materials

The X-ray powder diffraction data collected from the samples prepared via the ceramic method (sample 'C'), and the arc-melt furnace method (sample 'A') are compared in Figure 6.5. Two cubic phases (of space group *Pm*-3*m*) with lattice parameters comparable to those of $SrVO_3$ (a = 3.843(1) Å)[108] and $SrTiO_3$ (a = 3.901(1) Å)[109] were observed in both samples. Therefore, a model based on a mixture of the two extreme compositions, $SrVO_3$ and $SrTiO_3$, was refined against the data collected from the C and A samples (as shown in Figure 6.5). The fit of the model to both sets of data is statistically reasonable.

The refined lattice parameters for the two cubic phases in the C sample are remarkably similar to those of $SrVO_3$ and $SrTiO_3$, while the lattice parameters of the cubic phases in the A sample deviate more significantly. Nevertheless, the error bars on these parameters are likely to be underestimated in the refinements and to a first approximation, both the C sample and the A sample appear to be mixtures of $SrVO_3$ and $SrTiO_3$ rather than $SrV_{1-x}Ti_xO_3$ solid-solutions. This observation is supported by the refined weight fraction of the minority phase (w_2), which for both samples is in relatively good agreement with the value of 5.0%. However, topochemical reduction of the samples revealed that the two materials are not equivalent (Section 6.3.2).

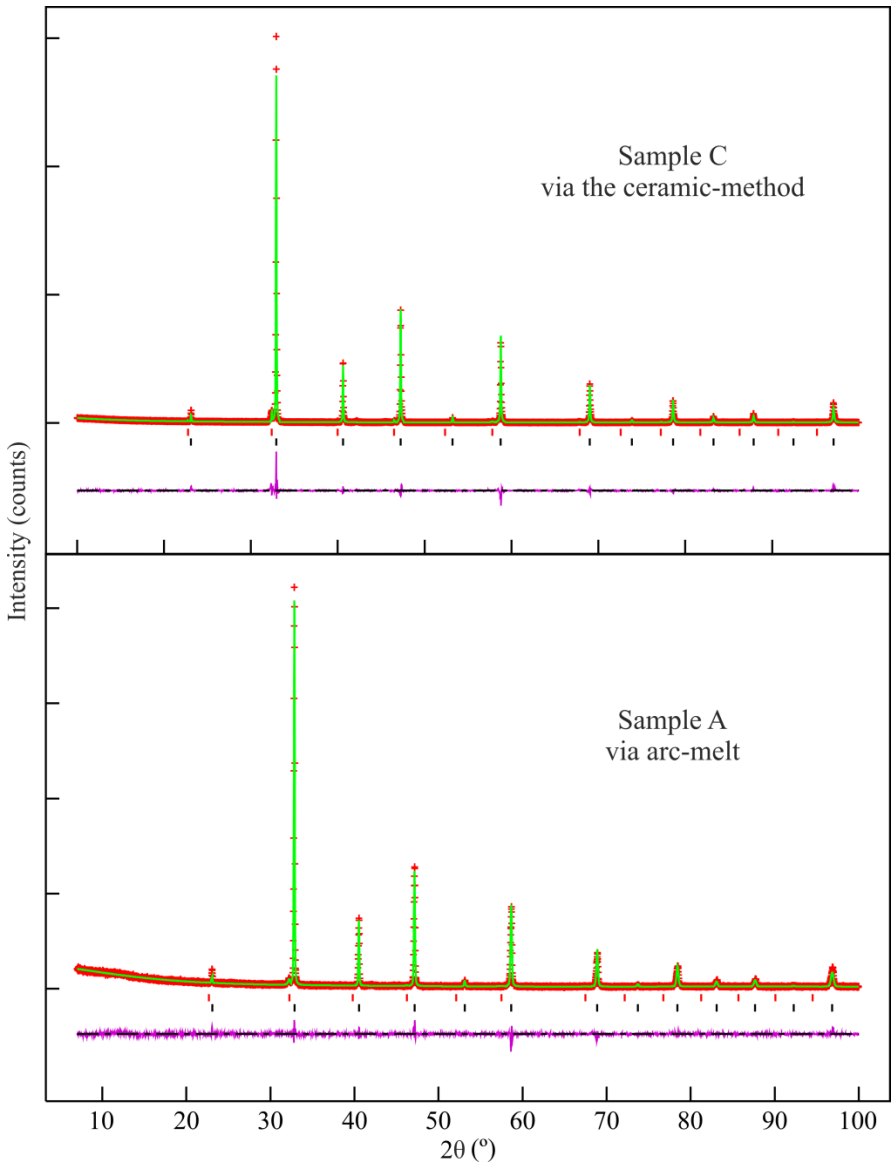


Figure 6.5. Observed, calculated, and difference plots from refinement of the structural model based on a mixture of cubic phases with space group *Pm*-3*m* against X-ray diffraction data collected from the $SrV_{0.95}Ti_{0.05}O_3$ C and A samples. The bottom tick marks (black) correspond to the majority cubic phase in each case.

Table 6.1. Lattice parameters and weight fractions of the two cubic phases of a model based on $SrVO_3$ and $SrTiO_3$ refined against laboratory X-ray powder diffraction data collected from the $SrV_{0.95}Ti_{0.05}O_3$ C and A samples. The label '1' corresponds to the majority phase.

Sample	Lattice parameters (Å)		Weight fractions (%)		Fit statistics		
	a_1	a_2	w_1	w_2	χ^2	*wRp* (%)	*Rp* (%)
C	3.846(1)	3.904(1)	95.43(1)	4.57(3)	3.944	15.76	10.93
A	3.854(1)	3.926(4)	96.66(1)	3.34(3)	1.282	10.19	7.56
Reference lattices: $SrVO_3$ (a = 3.843(1) Å), $SrTiO_3$ (a = 3.901(1) Å)							

6.3.2 Reduction of the $SrV_{0.95}Ti_{0.05}O_3$ Samples Prepared via the Ceramic and Arc-Melt Methods

The X-ray powder diffraction data collected during reduction of the C and A samples are shown in Figure 6.6. The diffraction pattern of a $SrVO_2H$ sample is included as a reference. The formation of a tetragonal phase with lattice parameters consistent with those of $SrVO_2H$ is observed as both the C sample and the A sample react with CaH_2. Multiple heating cycles at 610 ºC of the C sample, result in an almost complete conversion of the starting material to the tetragonal phase. This reduction product from the C sample will be referred to as C-R (bottom left, Figure 6.6).

The reduction of the A sample is markedly different. Initially, the cubic material is converted into the tetragonal phase (heating cycles 2-6 in Figure 6.6); however, on further heating under the same reduction conditions than sample C, a cubic phase re-emerges (heating cycles 8-11). This reduction product will be referred to as A-R.

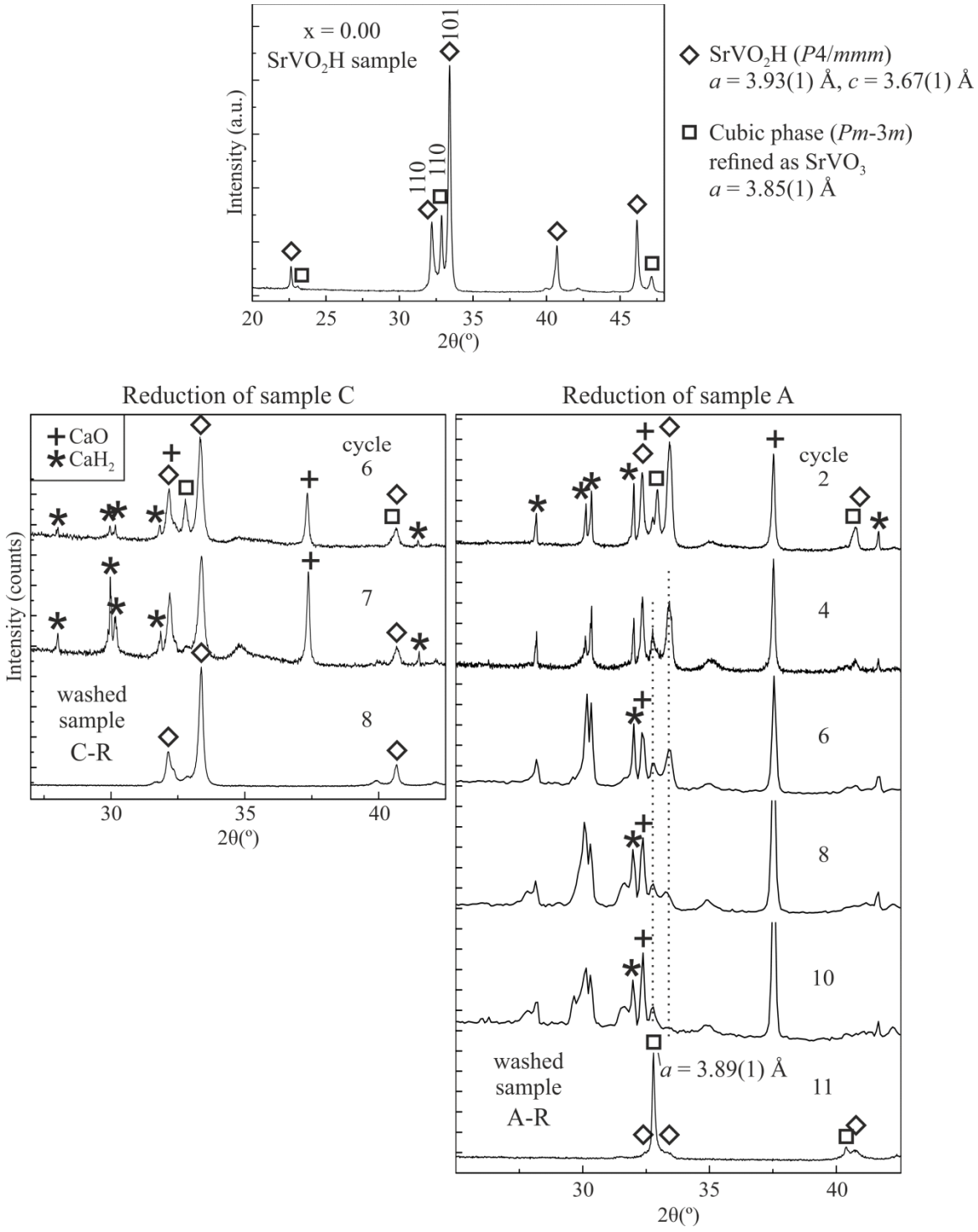


Figure 6.6. X-ray powder diffraction data collected during the reduction of the $SrV_{0.95}Ti_{0.05}O_3$ samples prepared via the ceramic (C, left panel), and arc-melt (A, right panel) methods. The diffraction pattern of a $SrVO_2H$ sample is shown (at the top) for comparison. The growth of the cubic phase at the expense of the tetragonal phase as the reaction progresses for the A sample is highlighted with the dotted lines (110 and 101 reflections respectively).

6.3.3 Structural Characterisation of the C-R and A-R Reduction Products

X-ray powder diffraction data using synchrotron radiation (Section 2.4.1.2) were collected from the C-R and A-R products.

The data collected from the C-R sample could be readily indexed using a tetragonal model based on $SrVO_2H$ (a = 3.9331(4) Å, c = 3.6671(3) Å) and a fraction of $SrVO_{3-y}$ (a = 3.8556(4) Å).[48] Close inspection of the data revealed a small amount of vanadium metal, and a further cubic phase which was indexed as $SrTiO_{3-y}$ (a = 3.911(1) Å, weight fraction 4.8(2)%). The fraction of this titanium phase is consistent with the fraction of $SrTiO_3$ observed in the C starting material.

Upon reduction of the C material, the lattice parameter of the $SrTiO_3$ phase changes from a = 3.904(1) Å to a = 3.911(1) Å in the reduction product. This is consistent with the formation of the oxyhydride $SrTiO_{2.88}H_{0.12}$ (a = 3.91119(4) Å), which is reported to result from reaction of $SrTiO_3$ with CaH_2 at T = 530 ºC.[47] Thus, this additional cubic phase in the C-R sample is assumed to be $SrTiO_{2.88}H_{0.12}$.

The weight fraction of approximately 5% of $SrTiO_{2.88}H_{0.12}$ suggests that the content of titanium in the tetragonal phase in the C-R sample (which could be written as $SrV_{1-x}Ti_xO_2H$), is small ($x < 0.05$).

The observed, calculated and difference plots from the refinement of the C-R sample are shown in Figure 6.7. The structural parameters of the phases refined are given in Table 6.2. The visual fit of the model to the data is reasonable, and the values of the R-factors resulting from the refinement suggest a good statistical fit. However, as detailed in Section 2.4.1.2, an unexpectedly high value for χ^2 can result from refinements against synchrotron X-ray diffraction data as a consequence of the large number of data points and the large ratio of signal to noise.

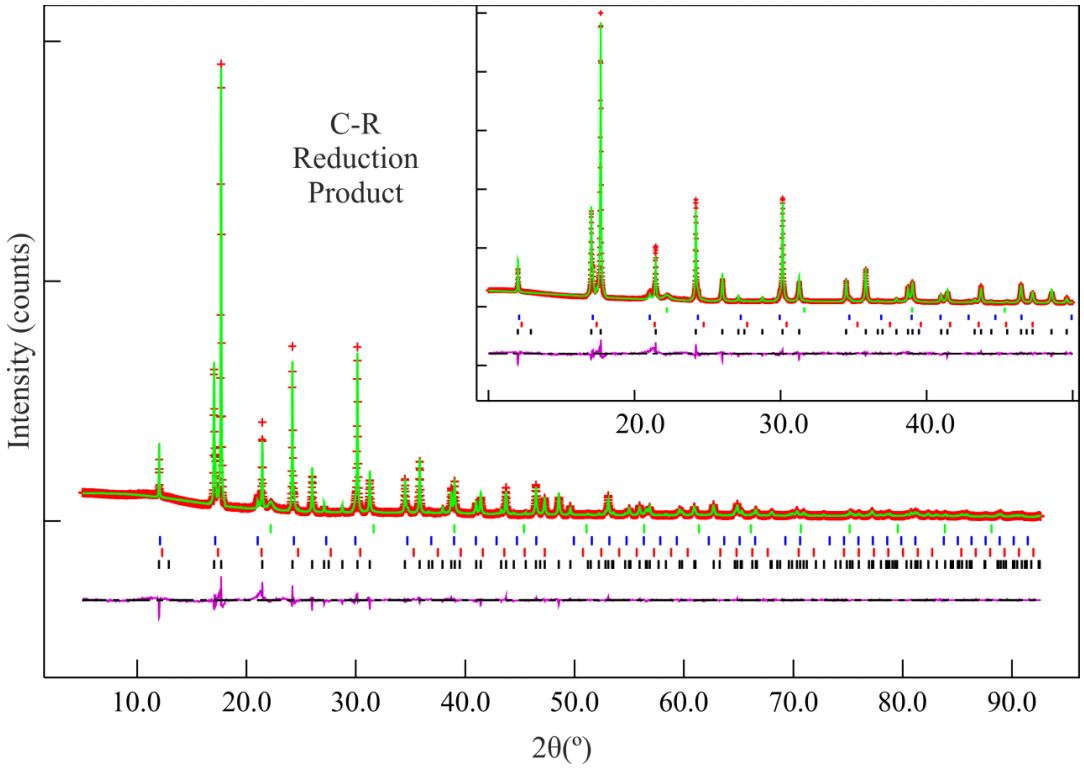


Figure 6.7. Observed, calculated and difference plots from refinement against synchrotron X-ray powder diffraction data collected from the C-R reduction product of the C starting material (prepared via the ceramic method). Bottom tick marks (black) correspond to peak positions for the tetragonal majority phase, bottom middle tick marks (red) to the vanadium secondary phase $SrVO_{3-y}$, top middle tick marks (blue) to the titanium secondary phase $SrTiO_{3-y}$, and top tick marks (green) to vanadium metal.

Table 6.2. Structural parameters refined against synchrotron X-ray powder diffraction data collected from the C-R reduction product.

$SrV_{1-x}Ti_xO_2H$						
Atom	**Wyck.**	***x***	***y***	***z***	**Fraction**	**U_{iso} (Å^2)**
Sr	*1d*	1/2	1/2	1/2	1	0.0040(2)
V / Ti	*1a*	0	0	0	1	0.0033(1)
O	*2f*	1/2	0	0	1	0.0028(5)
Space group: *P*4/*mmm*, *a* = 3.935(1) Å, *c* = 3.665(1) Å; weight fraction = 81.3(1)% Reported lattice parameters for $SrVO_2H$: *a* = 3.9331(4) Å, *c* = 3.6671(3) Å						

$SrVO_{3-y}$						
Atom	**Wyck.**	***x***	***y***	***z***	**Fraction**	**U_{iso} (Å^2)**
Sr	*1b*	1/2	1/2	1/2	1	0.0040(2)
V	*1a*	0	0	0	1	0.0033(1)
O	*3d*	1/2	0	0	0.92*	0.0028(5)
Space group: *Pm*-3*m*, *a* = 3.852(1) Å; weight fraction = 6.8(1)% Reference lattices: $SrVO_{3-y}$, *a* = 3.8556(4) Å; $SrVO_3$, *a* = 3.843(1) Å						
$SrTiO_{2.88}$						
Atom	**Wyck.**	***x***	***y***	***z***	**Fraction**	**U_{iso} (Å^2)**
Sr	*1b*	1/2	1/2	1/2	1	0.0040(2)
Ti	*1a*	0	0	0	1	0.0033(1)
O	*3d*	1/2	0	0	0.96	0.0028(5)
Space group: *Pm*-3*m*, *a* = 3.911(1) Å; weight fraction = 4.8(2)% $SrTiO_3$ reference lattice *a* = 3.901(1) Å						
Vanadium metal						
Space group: *Im*-3*m*, *a* = 3.026(1) Å; weight fraction = 7.1(1)% χ^2 = 105.8, wR_p = 6.49%, R_p = 4.32%						

* This parameter was taken to be the same as that for the $SrVO_{3-y}$ secondary phase in the $SrVO_2H$ sample reported by Denis Romero *et al*.[48]

In contrast with the C-R reduction product, the majority phase in the data collected from the A-R sample could be indexed using a cubic cell of space group *Pm-3m* and lattice parameter *a* = 3.888(1) Å. This lattice parameter is different from those of the phases observed in the A starting material (a_1 = 3.854(1) Å, a_2 = 3.926(4) Å, Table 6.1) and $SrVO_3$ or $SrTiO_3$ (Table 6.1).

The secondary phase in the A-R sample can be indexed using a model based on $SrVO_2H$ with a slightly larger *c* lattice parameter. The results from refinement of a model based on $SrVO_{3-y}$ and $SrVO_2H$ are shown in Figure 6.8 and summarised in Table 6.3. A greater fraction of vanadium metal was observed as a secondary phase in this A-R reduction product.

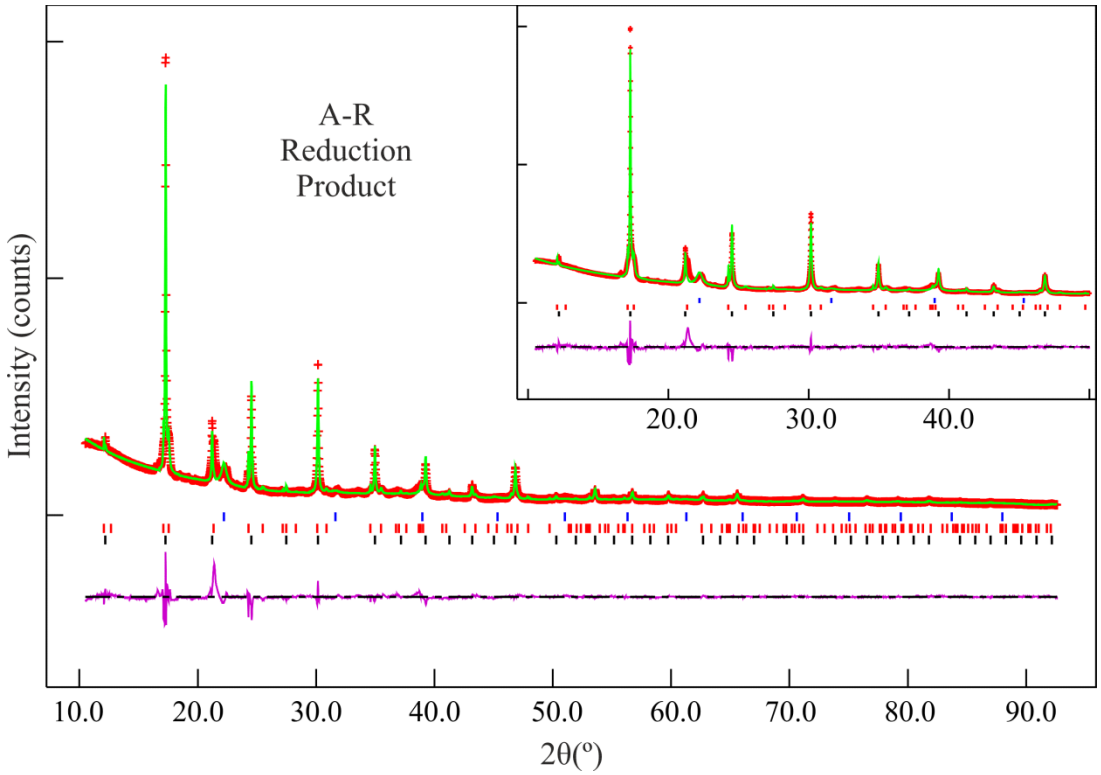


Figure 6.8. Observed, calculated and difference plots from refinement against synchrotron X-ray powder diffraction data collected from the A-R reduction product of the A starting material (prepared via the arc-melt method). Bottom tick marks (black) correspond to peak positions for the cubic majority phase, middle tick marks (red) to the tetragonal phase SrV_2OH, top tick marks (blue) to vanadium metal.

Table 6.3. Structural parameters refined against synchrotron X-ray powder diffraction data collected from the A-R reduction product.

$SrV_{1-x}Ti_xO_{3-y}$						
Atom	**Wyck.**	***x***	***y***	***z***	**Fraction**	**U_{iso} (Å^2)**
Sr	*1b*	1/2	1/2	1/2	1	0.0038(2)
V / Ti	*1a*	0	0	0	1	0.0024(1)
O	*3d*	1/2	0	0	1	0.0017(2)
Space group: *Pm*-3*m*, a = 3.888(1) Å; weight fraction = 65.0(1)% Reference lattices: $SrVO_{3-y}$, a = 3.8556(4) Å;[2] $SrVO_3$, a = 3.843(1) Å; $SrTiO_3$, a = 3.901(1) Å; starting material: a_1 = 3.854(1) Å, a_2 = 3.926(4) Å						

$SrVO_2H$						
Atom	**Wyck.**	***x***	***y***	***z***	**Fraction**	**U_{iso} (Å^2)**
Sr	*1d*	1/2	1/2	1/2	1	0.0038(2)
V	*1a*	0	0	0	1	0.0024(1)
O	*2f*	1/2	0	0	1	0.0017(2)
Space group: *P*4/*mmm*, *a* = 3.929(1) Å, *c* = 3.738(4) Å; weight fraction = 17.5(3)% Reported lattice parameters for $SrVO_2H$: *a* = 3.9331(4) Å, *c* = 3.6671(3) Å						
Vanadium metal						
Space group: *Im*-3*m*, *a* = 3.032(4) Å; weight fraction = 17.5(4)%						
χ^2 = 195.5, wR_p = 6.30%, R_p = 3.90%						

As is the case for the C and A starting materials, the error bars on the lattice parameters of the phases observed in the C-R and A-R reduction products are likely to be underestimated from the refinements. Since the differences between the lattice parameters of the cubic phases in the reduction products are relatively small with respect to those observed in the starting materials, it is not possible to unequivocally identify these products as reduced phases solely from the X-ray diffraction data. Further characterisation of the C-R and A-R reduction products was carried out via thermogravimetric analysis and oxidative titrations.

6.3.4 Chemical Characterisation of the C-R and A-R Reduction Products

6.3.4.1 Thermogravimetric Analysis

Oxidative decompositions of the C-R and A-R samples were performed in the TGA (Section 2.7) by heating powder samples at 5 ºC min^{-1} to 600-700 ºC under an O_2 flow. The SrO, V_2O_5 and TiO_2 products of decomposition were confirmed by powder X-ray diffraction. The mass change as a function of temperature during oxidation of the C-R and A-R samples is shown in Figure 6.9. The results from analogous data collected from $SrVO_2H$ are shown as a reference (top panel, sample shown in Figure 6.9).

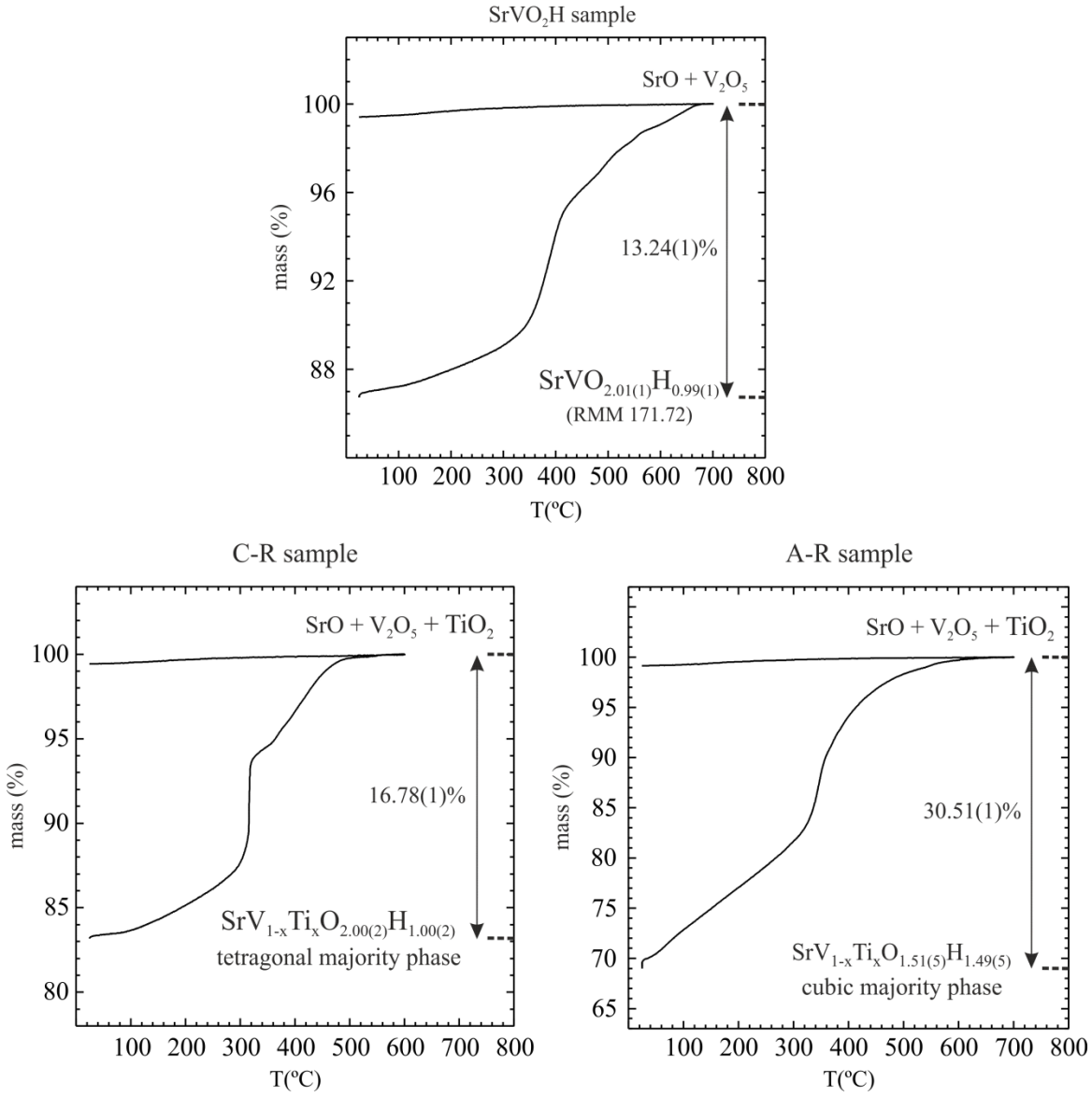


Figure 6.9. Thermogravimetric data collected during oxidative decomposition of the $SrVO_2H$ sample of Figure 6.6 (top panel), the C-R reduction product (bottom left), and the A-R reduction product (bottom right). The theoretical mass gain for the exact stoichiometric composition of $SrVO_2H$ (RMM 171.57) is 13.40%.

The mass gain observed from both the C-R sample and A-R sample are significantly larger than that observed from $SrVO_2H$. Consideration of the refined weight fractions of the secondary phases (Tables 6.2 and 6.3) allows for the mass gain corresponding to the majority phases in each sample to be determined. The results are summarised in Table 6.4, where the errors reported (calculated as propagated errors) come from the measurement of the mass from the TGA balance (Section 2.7).

Table 6.4. Summary of the thermogravimetric data collected during oxidation of the C-R and A-R reduction products in combination with the results from X-ray powder diffraction of Figure 6.7 and Figure 6.8.

C-R sample			
(a) Refined weight fractions of secondary phases in the C-R sample (%):	**$SrTiO_{2.88}H_{0.12}$** 4.8(2)	**$SrVO_3$** 6.8(1)	**V** 7.1(1)
(b) Mass gain during oxidation of the secondary phases (%):	0.99 ($SrO + TiO_2$)	4.29 ($SrO + V_2O_5$)	78.52 (V_2O_5)
Contribution to the mass gain from oxidation of the secondary phases ((a)/100)x(b) (%):	0.05(2)	0.29(1)	5.58(1)
Contribution of secondary phases to the total mass gain observed (%):	5.92(2)		
Total mass gain observed (%):	16.78(1)		
Mass gain from the 81.3% weight fraction of majority phase (%):	16.78(1) - 5.92(2) = 10.86(2) 10.86(2) / (81.3(1)/100) = <u>13.36(2)</u>		
Estimated RMM of majority phase from mass gain (considering decomposition into only SrO and V_2O_5):	171.63		
Proposed formula of majority phase in the C-R product:	$SrV_{1-x}Ti_xO_{2.00(2)}H_{1.00(2)}$ ($x < 0.05$)		
A-R sample			
Refined weight fractions of secondary phases (%):	**$SrVO_2H$** 17.5(3)	**V** 17.5(4)	
Mass gain during oxidation of the secondary phases (%):	13.40 ($SrO + V_2O_5$)	78.52 (V_2O_5)	
Contribution to the mass gain from oxidation of the secondary phases ((a)/100)x(b) (%):	2.35(3)	13.74(4)	

Contribution of secondary phases to the total mass gain observed (%):	16.09(5)
Total mass gain observed (%):	30.51(1)
Mass gain from the 65.0(1)% weight fraction of majority phase (%):	30.51(1) – 16.09(5) = 14.42(5) 14.42(5) / (65.0(1)/100) = <u>22.19(2)</u>
Estimated RMM of majority phase from mass gain (considering decomposition into only SrO and V_2O_5):	159.23
Proposed formula of majority phase in the A-R product:	$SrV_{1-x}Ti_xO_{1.51(5)}H_{1.49(5)}$ ($x < 0.05$)

An initial composition of $SrV_{1-x}Ti_xO_{2.00(2)}H_{1.00(2)}$ can be proposed for the tetragonal material in the C-R product from the mass gain calculated from the main phase (13.36(2)%). This mass gain is very close to that expected from $SrVO_2H$ (13.40%) and greater than that expected from $SrV_{0.95}Ti_{0.05}O_2H$ (13.18%). This supports the observations that $x < 0.05$, and suggests that the composition of the $SrV_{1-x}Ti_xO_2H$ tetragonal phase is very close to that of $SrVO_2H$.

For the A-R product on the other hand, the notably larger mass gain from the main phase in the sample (30.51(1)%) confirms that the cubic material, which is observed to re-emerge during reduction (Figure 6.6), is a reduced phase. Furthermore, after taking into account the secondary phases (there is a greater vanadium metal content in this A-R sample) and from comparison of the calculated mass gain of the main cubic phase (22.19(2)%) with that expected from $SrVO_2H$, a composition of hydride significantly greater than 1 is found. The proposed formula for this cubic reduction product is $SrV_{1-x}Ti_xO_{1.51(5)}H_{1.49(5)}$.

Thermogravimetric data confirms that oxygen has been removed. However, it is not possible to confirm the hydride content in the proposed formulas for the C-R and A-R products from thermogravimetric analysis.

6.3.4.2 Manganometric Titrations

In order to determine the average oxidation state of the vanadium cations present in the C-R and A-R samples, and hence confirm the hydride content in the reduced phases, titrations using $KMnO_4$ were carried out (Section 2.8). The results are summarised in Table 6.5.

The average oxidation state of the vanadium is consistent with the expected value from the refined phases (and their weight fractions) from X-ray powder diffraction data for both the C-R and A-R products. The oxidation state for the vanadium centres found for the tetragonal and cubic products are consistent with the hydride composition in the proposed formulas $SrV_{1-x}Ti_xO_2H$ and $SrV_{1-x}Ti_xO_{1.5}H_{1.5}$ respectively.

Table 6.5. Average vanadium oxidation state in the C-R and A-R reduction products from manganometric titration.

Sample	Average Vanadium Oxidation State from Titration[(i)]	Sample Composition by Weight (from X-ray Powder Diffraction Data)	Calculated Vanadium Oxidation State in the Main Phase
$SrVO_2H$	+3.20(1)	80.3(1)% $SrVO_2H$ + 19.7(2)% $SrVO_3$ [(ii)]	+3.00(2)
C-R	+2.90(4)	81.3(1)% $SrV_{1-x}Ti_xO_2H$ + 4.8(2)% $SrTiO_{2.88}H_{0.12}$ + 6.8(1)% $SrVO_3$ + 7.1(1)% V	+3.00(2)
A-R	+2.13(3)	65.0(1)% $SrV_{1-x}Ti_xO_{1.5}H_{1.5}$ + 17.5(3)% $SrVO_3$ + 17.5(4)% V	+2.47(4)

(i) The error bars correspond to the standard deviation in the volume of titre spent in three titration trials.
(ii) These weight fractions were refined from the X-ray powder diffraction data shown in Figure 6.6.

6.3.5 Magnetic Characterisation of the C-R and A-R Reduction Products

6.3.5.1 Magnetisation Measurements

Zero-field cooled and field cooled magnetisation data as a function of temperature (Section 2.6) were collected for the C-R and A-R products in the range $5 \leq T\ (K) \leq 350$. The results are shown in Figure 6.10. Analogous data collected from $SrVO_2H$ in the range $5 \leq T\ (K) \leq 300$ are shown for comparison.

Consistent with previous observations from the magnetisation data collected from $SrVO_2H$, the zero-field cooled and field cooled plots collected from the C-R and A-R samples diverge over the whole temperature range measured and exhibit no observable magnetic events.[48] With respect to the divergence between the zero-field cooled and field-cooled plots, it is worth noting that, given the small magnitude of the magnetic moment of the samples, any small amount of a magnetic impurity (such as nickel from the spatula or V_2O_3 formed during reduction) can contribute significantly to the separation of the curves.

The C-R sample and $SrVO_2H$ yield remarkably similar Curie constants of $C = 0.0174(1)$ $cm^3\ K\ mol^{-1}$ and $C = 0.0176(1)$ $cm^3\ K\ mol^{-1}$, respectively. These Curie constants, extracted from the fit to the Curie-Weiss law of the zero-field cooled data, are significantly lower than expected for a sample containing one d^2,V^{3+} centre per formula unit ($C = 1$ $cm^3\ K\ mol^{-1}$). The secondary phases present in each sample can explain the discrepancy: $SrVO_{3-y}$ containing d^1,V^{4+} centres and $SrTi_{2.88}H_{0.12}$ with d^1,Ti^{3+} centres.

The Curie constant ($C = 0.0200(1)$ $cm^3\ K\ mol^{-1}$) extracted for the A-R sample is slightly greater than those for $SrVO_2H$ and $SrV_{1-x}Ti_xO_2H$. This supports the observation that the A-R product is further reduced with respect to the C-R product (there are ~0.5 extra electrons per mole in $SrV_{1-x}Ti_xO_{1.5}H_{1.5}$ with respect to $SrV_{1-x}Ti_xO_2H$). However, the value of the Curie constant for the A-R sample is much smaller than the value expected of $C = 1.4062$ $cm^3\ K\ mol^{-1}$ for a $SrVO_{1.5}H_{1.5}$ composition. In addition to the presence of the $SrVO_2H$ and vanadium secondary phases in the A-R sample, the small value of C in this case could be partly attributed to the substitution of a fraction of the d^2,V^{3+} centres in $SrVO_{1.5}H_{1.5}$, for the electron-poorer d^1,Ti^{3+} centres in $SrV_{1-x}Ti_xO_{1.5}H_{1.5}$.

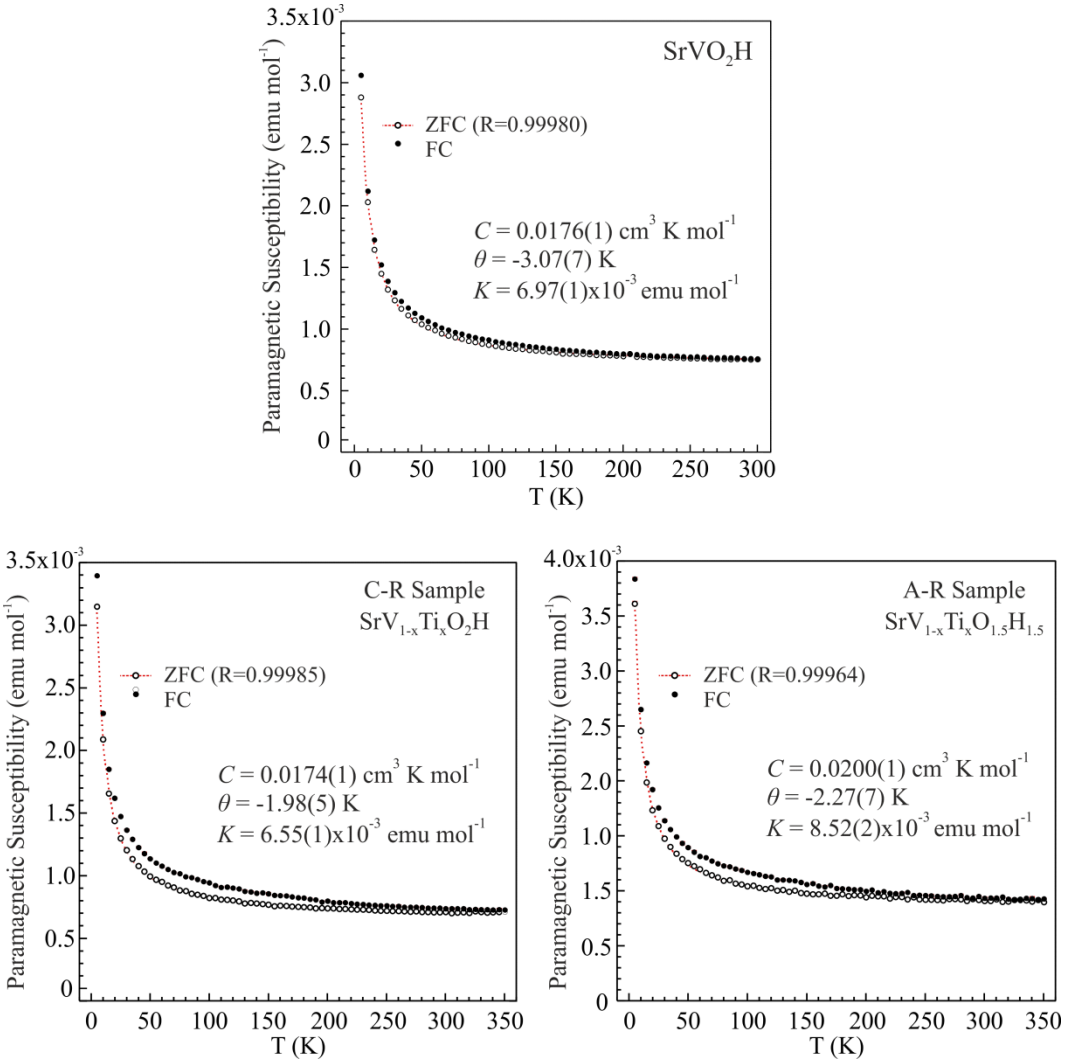


Figure 6.10. Zero-field cooled and field cooled susceptibility data as a function of temperature collected from $SrVO_2H$ (top panel), the C-R reduction product (bottom left) and the A-R reduction product (bottom right). The *C* and *θ* values result from the fit of the zero-field cooled data to the Curie-Weiss law over the whole range of T measured.

As highlighted in Section 6.1, $SrVO_2H$ exhibits antiferromagnetic order at room temperature. However, such magnetic behaviour shows no signature in the magnetisation data.[48] Therefore, in order to investigate the magnetic order in the C-R and A-R reduction products, neutron powder diffraction data and μ+SR data (Section 2.10) were collected.

6.3.5.2 Neutron Powder Diffraction of the C-R Sample

Neutron powder diffraction data were collected from the C-R sample using the POLARIS diffractometer at ISIS neutron source (Section 2.4.2.2). A comparison of the data

collected from the C-R sample at 298 K, with analogous data collected from the $SrVO_2H$ sample of Figure 6.6 is shown in Figure 6.11.

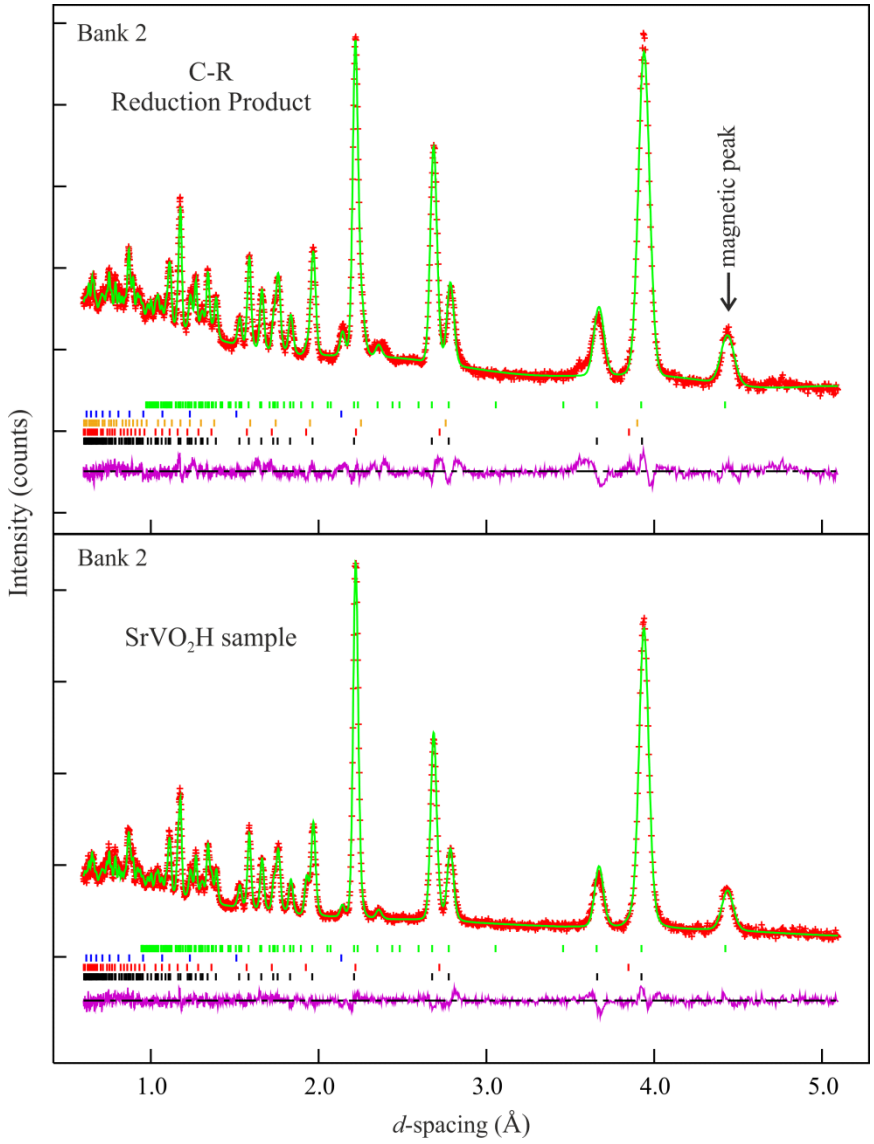


Figure 6.11. Observed, calculated and difference plots from refinement of the C-R reduction product (top) and $SrVO_2H$ (bottom) against neutron powder diffraction data collected at 298 K. Black tick marks correspond to the peak positions of the majority phase, red to $SrVO_{3-y}$, yellow to $SrTiO_{2.88}H_{0.12}$, blue to the contribution from vanadium (both from the sample holder and the secondary phase), and green to the magnetic models.

Additional features at high *d*-spacing are observed in the data collected from the C-R sample, which can be indexed using a model based on the magnetic structure of $SrVO_2H$. This magnetic structure is a G-type antiferromagnetic lattice with the moments aligned parallel to the *z*-axis ($a_{mag} = \sqrt{2}a_{cryst}$, $b_{mag} = \sqrt{2}b_{cryst}$, $c_{mag} = 2c_{cryst}$, Figure 6.12).[48] Consistent with the Curie constant of the C-R sample and $SrVO_2H$, which are very close

in value, the refined magnetic moment for the magnetic phase in the C-R sample is equal within experimental uncertainty to that refined for $SrVO_2H$ (1.46(2) μ_B compared to 1.50(3) μ_B, see Tables 6.6 and 6.7).

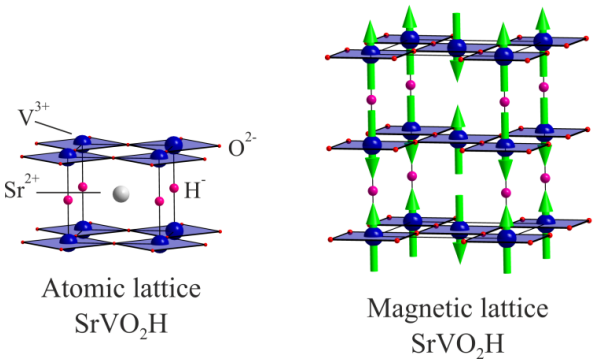


Figure 6.12. The refined atomic and magnetic structures of $SrVO_2H$ at 298 K.

Table 6.6. Structural parameters from the refinement of the C-R reduction product against neutron powder diffraction data collected at 298 K.

C-R reduction product						
$SrV_{1-x}Ti_xO_2H$						
Atom	**Wyck.**	***x***	***y***	***z***	**Fraction**	**U_{iso} (Å^2)**
Sr	*1d*	1/2	1/2	1/2	1	0.0031(1)
V / Ti	*1a*	0	0	0	1	0.002*
O	*2f*	1/2	0	0	1	0.0054(2)
H	*1b*	0	0	1/2	1	0.0075(3)
Space group: *P*4/*mmm*, *a* = 3.9365(1) Å, *c* = 3.6680(1) Å; weight fraction = 88.41(1)%						
G-type antiferromagnetic order: 1.46(2) μ_B per vanadium centre, align parallel to *z*-axis						
$SrVO_{3-y}$						
Atom	**Wyck.**	***x***	***y***	***z***	**Fraction**	**U_{iso} (Å^2)**
Sr	*1b*	1/2	1/2	1/2	1	0.0031(2)
V	*1a*	0	0	0	1	0.002*
O	*3d*	1/2	0	0	0.92**	0.0054(2)
Space group: *Pm*-3*m*, *a* = 3.8579(6) Å; weight fraction = 6.74(2)%						

$SrTiO_{2.88}H_{0.12}$						
Atom	**Wyck.**	***x***	***y***	***z***	**Fraction**	U_{iso} **(Å^2)**
Sr	*1a*	0	0	0	1	0.0031(2)
Ti	*1b*	1/2	1/2	1/2	1	0.0066(2)
O	*3c*	1/2	0	1/2	0.96	0.0054(2)
H	*3c*	1/2	0	1/2	0.04	0.0075(3)
Space group: *Pm*-3*m*, *a* = 3.9094(3) Å; weight fraction = 4.85(2)% Reference lattice: $SrTiO_{2.88}H_{0.12}$, *a* = 3.91119(4) Å						
χ^2 = 1.951, wR_p = 1.38%, R_p = 1.79%						

* The low neutron scattering cross section of vanadium led repeatedly to negative thermal displacements for this atom, therefore the parameter was fixed to a reasonable value for all phases.

** This parameter was taken to be the same as that for the $SrVO_{3-y}$ secondary phase in the $SrVO_2H$ sample reported by Denis Romero *et al*.[48]

Table 6.7. Structural parameters from the refinement of the $SrVO_2H$ sample against neutron powder diffraction data collected at 298 K.

$SrVO_2H$ sample						
$SrVO_2H$						
Atom	**Wyck.**	***x***	***y***	***z***	**Fraction**	U_{iso} **(Å^2)**
Sr	*1d*	1/2	1/2	1/2	1	0.0045(2)
V	*1a*	0	0	0	1	0.002*
O	*2f*	1/2	0	0	1	0.0058(1)
H	*1b*	0	0	1/2	1	0.0074(5)
Space group: *P*4/*mmm*, *a* = 3.9352(1) Å, *c* = 3.6679(1) Å; weight fraction = 80.23(1)%						
G-type antiferromagnetic order: 1.50(3) μ_B per vanadium centre, align parallel to *z*-axis						
$SrVO_{3-y}$						
Atom	**Wyck.**	***x***	***y***	***z***	**Fraction**	U_{iso} **(Å^2)**
Sr	*1b*	1/2	1/2	1/2	1	0.0045(2)
V	*1a*	0	0	0	1	0.002
O	*3d*	1/2	0	0	0.92*	0.0058(1)

$SrVO_{3-y}$: pace group *Pm*-3*m*, *a* = 3.8579(6) Å; weight fraction = 19.77(3)%
χ^2 = 1.136, wR_p = 1.30%, R_p = 1.84%

* See notes for Table 6.6

In addition to confirming the magnetic order in the C-R sample, the neutron powder diffraction data confirms the presence of the $SrTiO_{2.88}H_{0.12}$ secondary phase. A comparison of the data from bank 5 collected at 298 K from the C-R and the $SrVO_2H$ samples is shown in Figure 6.13 (on the next page). The additional 111 reflection from $SrTiO_{2.88}H_{0.22}$ can be clearly observed.

Since for the neutron powder diffraction data there is a contribution from vanadium metal from the cans, the fraction of vanadium was not taken into account for the calculation of the weight fractions in the C-R sample. Therefore, from these data the weight fraction of $SrV_{1-x}Ti_xO_2H$ is higher than that found from X-ray powder diffraction. The refined weight fractions of the $SrVO_{3-y}$ and $SrTiO_{2.88}H_{0.12}$ secondary phases from synchrotron X-ray powder diffraction data are confirmed from the refinement against neutron powder diffraction data.

6.3.6 Muon Spin Relaxation (μSR) Spectroscopy of $SrV_{1-x}Ti_xO_{1.5}H_{1.5}$

μSR spectroscopy data were collected from the A-R sample contained within a silver foil envelope (thickness 25 cm) using the GPS instrument at the Swiss Muon Source, Paul Scherrer Institut, Switzerland (Section 2.10).

No oscillations in the asymmetry between forward (F) and backwards (B) detectors were observed even at 5 K. Therefore, in contrast with the C-R sample, there is no indication of long-range magnetic order through the bulk of the A-R sample.

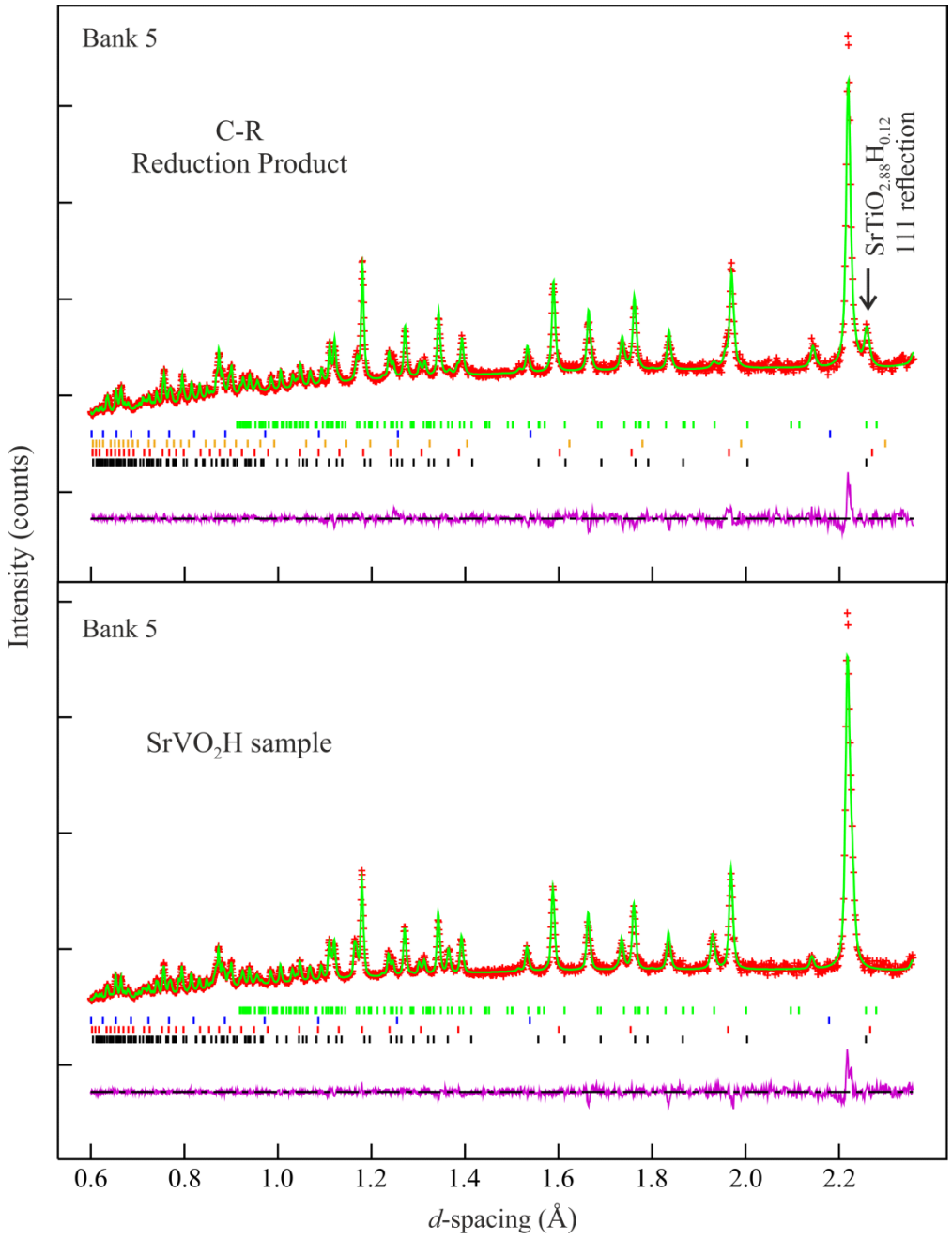


Figure 6.13. Observed, calculated and difference plots from refinement of the C-R reduction product (top) and $SrVO_2H$ (bottom) against neutron powder diffraction data collected at 298 K. Black tick marks correspond to the peak positions of the majority phase, red to $SrVO_{3-y}$, yellow to $SrTiO_{2.88}H_{0.12}$, blue to the contribution from vanadium (both from the sample holder and the secondary phase), green to the magnetic models.

6.4 Discussion

6.4.1 Reduction Behaviour of the $SrV_{0.95}Ti_{0.05}O_3$ Starting Materials Prepared via the Ceramic and Arc-Melt Methods

The $SrV_{0.95}Ti_{0.05}O_3$ starting materials prepared via the ceramic and the arc-melt methods (C and A samples respectively), seem to be equivalent from the X-ray powder diffraction data shown in Figure 6.5. Both in the C sample and in the A sample, two cubic phases with lattice parameters close to those of $SrVO_3$ (a = 3.843(1) Å) and $SrTiO_3$ (a = 3.901(1) Å) are observed (Table 6.1). In addition, for both the C and A samples, the minority cubic phase, labelled as '2', is that of greater lattice parameter and thus was identified as $SrTiO_3$. The weight fraction of these phases (w_2) is relatively close to 5.0% in both the C and the A sample, which suggests that the solution of titanium in $SrVO_3$ is incomplete. Therefore, the C and A $SrV_{0.95}Ti_{0.05}O_3$ samples consist of $SrV_{1-x}Ti_xO_3$ phases in which the fraction x is unknown.

The reduction of the C and A $SrV_{0.95}Ti_{0.05}O_3$ samples with CaH_2 was expected to proceed analogous to that of $SrVO_3$. Although the formation of a tetragonal phase which can be indexed as $SrVO_2H$ is observed in the reduction products of both the C and A samples (heating cycles 2 to 6 in Figure 6.6), upon further reaction of the A sample, a cubic phase re-emerges at the expense of the tetragonal $SrV_{1-x}Ti_xO_2H$ material. This differing reduction behaviour exhibited by the C and the A $SrV_{0.95}Ti_{0.05}O_3$ samples revealed that the two starting materials are not equivalent, with the most likely difference being the content of titanium. A summary of the observed reduction behaviour of the C and A samples is schematised in Figure 6.14.

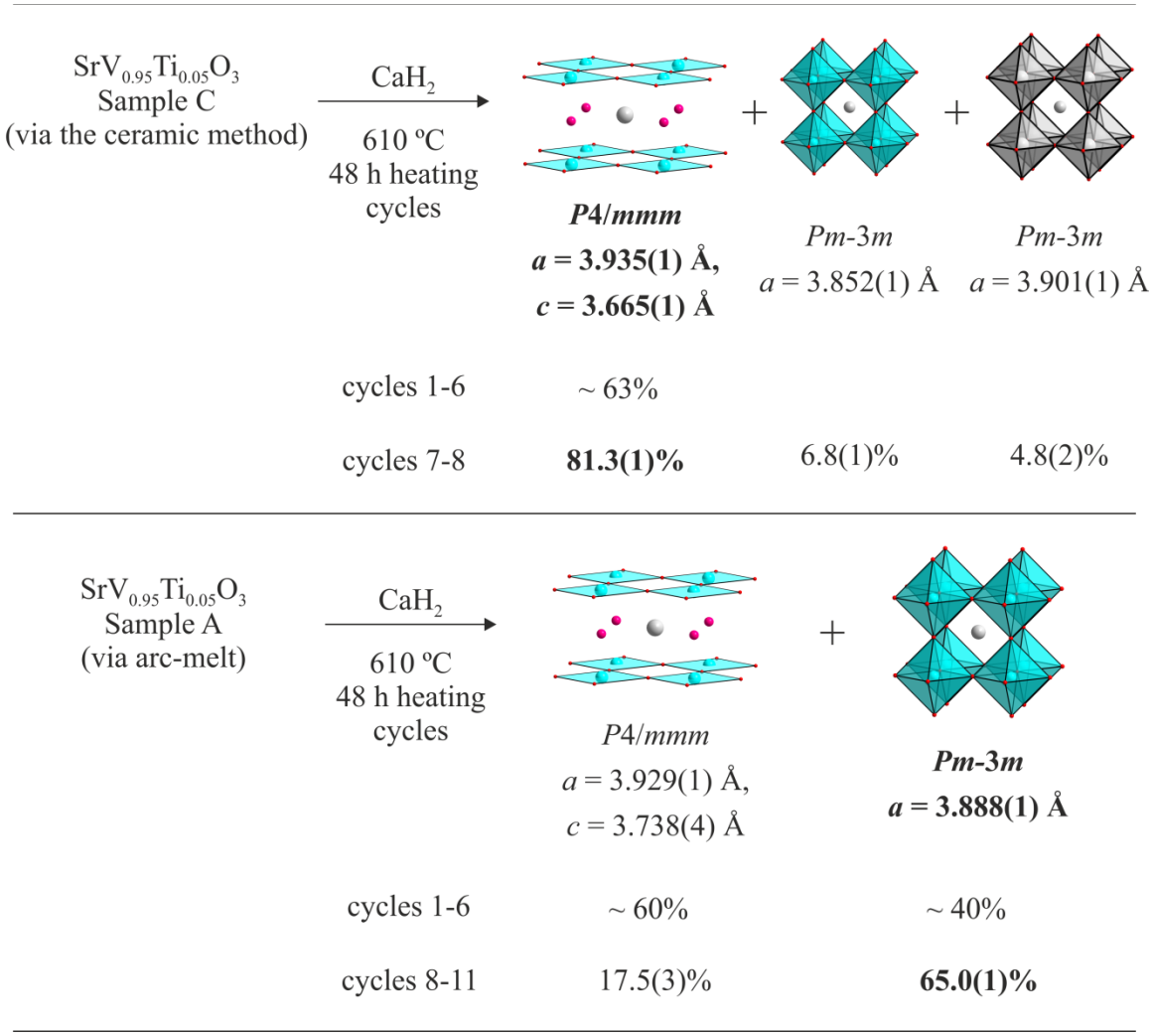


Figure 6.14. Schematised reactivity of the $SrV_{0.95}Ti_{0.05}O_3$ samples prepared via the ceramic (C, top) and arc-melt (A, bottom) methods.

Given that the lattice parameter (a = 3.888(1) Å) of the cubic phase in the A-R reduction product is almost exactly the average of the lattice parameters a_1 and a_2 refined for the A starting material ($a_{average}$ = 3.890(1) Å, Table 6.1), at a first approach, this re-emerging cubic product was interpreted as a reoxidised phase. The reoxidation could be explained from the fact that, during the reductions, the silica ampoules that contain the reactions are opened after every heating cycle in order to follow the progress of the reductions. This means that there is a limit to the H_2 pressure that can build up during the reactions. If the H_2 pressure was not sufficiently high in order for the $SrV_{1-x}Ti_xO_2H$ tetragonal phase initially formed to remain stable, subsequent heating cycles could lead to the oxidation of

this hydride back into the starting material. However, the chemical characterisation via thermogravimetric analysis and oxidative titrations confirms that this is not the case, and that the cubic phase in the A-R reduction product is a reduced phase rather than starting material.

Meanwhile, the C-R tetragonal product is almost identical to $SrVO_2H$. This is confirmed by the structural and magnetic characterisation from neutron powder diffraction data (Table 6.6). The stoichiometric $SrV_{1-x}Ti_xO_2H$ composition can be proposed for this sample from the formula mass determined via thermogravimetric analysis (Table 6.4) and from the average oxidation state of +3.00(2) determined for the vanadium centres via oxidative titrations (Table 6.5). The content of titanium in $SrV_{1-x}Ti_xO_2H$ is expected to represent a maximum of ~0.2% from the refined fraction of the $SrTiO_{2.88}H_{0.12}$ secondary phase (both from X-ray and neutron powder diffraction data).

6.4.2 Disorder in the Vanadium-Titanium Oxyhydrides

The mass gain during oxidation of the A-R product, suggests a greater content of hydride with respect to that in the C-R product. While for the C-R sample a formula mass almost identical to that of $SrVO_2H$ was found (171.48(2) g mol^{-1}, Table 6.4), for the A-R cubic product a formula mass consistent with an oxygen-deficient phase by ~0.5 mols with respect to $SrVO_2H$ can be extracted from the data (164.23(5) g mol^{-1}, Table 6.4). The proposed formula for this cubic product is $SrV_{1-x}Ti_xO_{1.5}H_{1.5}$ in which the content of hydride is confirmed from the average oxidation state of +2.47(4) for the vanadium centres (Table 6.5).

The cubic structure observed for this A-R product can be explained from the position that the hydride ions take in the coordination environment of the transition-metal cations in $SrV_{1-x}Ti_xO_{1.5}H_{1.5}$. As can be observed in Figure 6.15, in $SrVO_2H$ the hydride ions take the apical positions around the vanadium six-fold coordination environment, to yield VO_4H_2 units (*trans* configuration), which form a stoichiometric tetragonal anion-ordered phase.

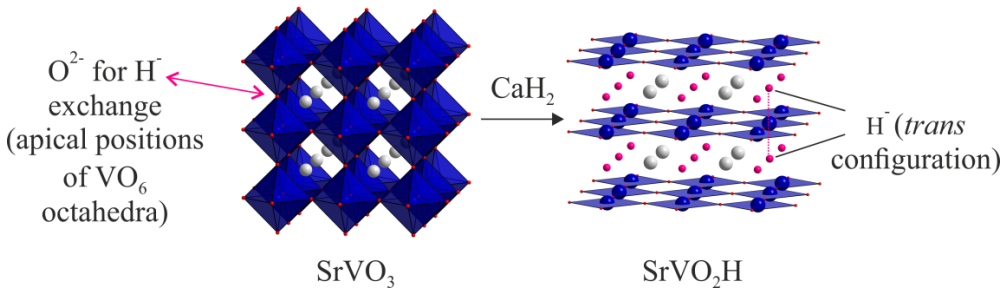


Figure 6.15. Schematic representation of the topochemical reduction of $SrVO_3$ via exchange of O^{2-} for H^-. Exchange takes place preferably on the apical positions of the original VO_6 octahedra to yield infinite VO_2 sheets connected by hydride ions which take the *trans* configuration around the vanadium centres.

Stoichiometric anion-ordered phases are not common among other known perovskite-derived binary oxyhydrides. For example, the $ATiO_{3-y}H_y$ (A = Ba, Sr, Ca) phases are all non-stoichiometric and disordered, while the $SrCrO_2H$ phase is stoichiometric but disordered.

The preferred substitution of the hydride ions to yield a *trans* configuration in the VO_4H_2 units in $SrVO_2H$ is unexpected when considering an isolated metal ion in an octohedral coordination environement. In an octahedral metal complex, the effect of a first substitution from a strong σ-donor ligand (such as the hydride ions) over the rate of further substitution of ligands of the same nature is expected to lead to a *cis* configuration as a consequence of the *trans effect*. A *cis* arrangement of the hydride ions around the vanadium centres however, would yield a disordered oxyhydride phase contrary to the anion-order observed in $SrVO_2H$.

The anion-order in $SrVO_2H$ can be explained from the energy gain for a square-planar array of the *p*-donor oxide ions around the d^2,V^{3+} centres. As schematised in Figure 6.16, such array of the oxide ions leads to a net stabilisation by splitting the octahedral t_{2g} orbitals into a doubly degenerate $(d_{xz}, d_{yz})^2$ pair (which comprises the HOMO), and a destabilised d_{xy} orbital (from which the LUMO derives). This destabilisation of the ground state for the vanadium centres seems to override the preference for the hydride ions to be mutually *cis*.

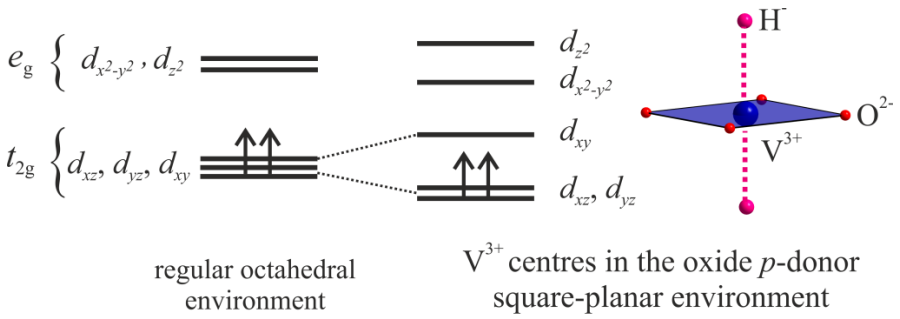


Figure 6.16. Schematisation of the stabilisation via splitting of the octahedral t_{2g} orbitals which takes place for a square-planar array of the oxide anions around the vanadium centres in $SrVO_2H$.

In contrast with $SrVO_2H$, in $SrCrO_2H$ the three degenerate t_{2g} orbitals are singly occupied in the d^3,Cr^{3+} centres. Therefore, an array of the *p*-donor ligands on the equatorial plane around the chromium does not lead to a net stabilisation in this case, and the *cis* and *trans* isomers (Figure 6.17) are equally preferred resulting in a disordered cubic structure.

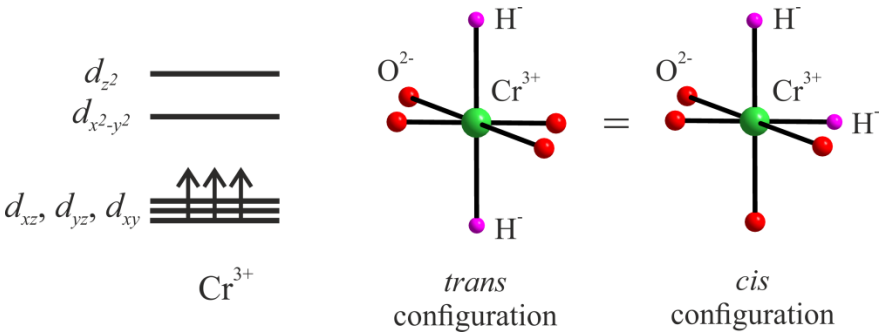


Figure 6.17. Electronic configuration for the d^3,Cr^{3+} centres in $SrCrO_2H$. There is no preference for a *trans* or *cis* configuration of the hydride ions around the chromium centres.

Upon substituting a fraction of the d^2,V^{3+} centres in $SrVO_2H$, by d^1,Ti^{3+} cations in $SrV_{1-x}Ti_xO_2H$, a similar situation with that of the d^3,Cr^{3+} centres can be expected. For the d^1,Ti^{3+} centres, the configuration with only one electron in the degenerate t_{2g} set means that the stabilisation gained by the hydride ions being inserted *trans* or the *cis* with respect to each other, is equivalent. Thus the *lift* of an electronic constraint can be proposed in the titanium doped $SrV_{1-x}Ti_xO_2H$ phase which allows further reduction by substitution of additional oxide for hydride ions in the equatorial plane, as schematised in

Figure 6.18. This further hydride insertion introduces anion-disorder and the $SrV_{1-x}Ti_xO_{2-y}H_{1+y}$ phases become cubic as observed for $SrV_{1-x}Ti_xO_{1.5}H_{1.5}$.

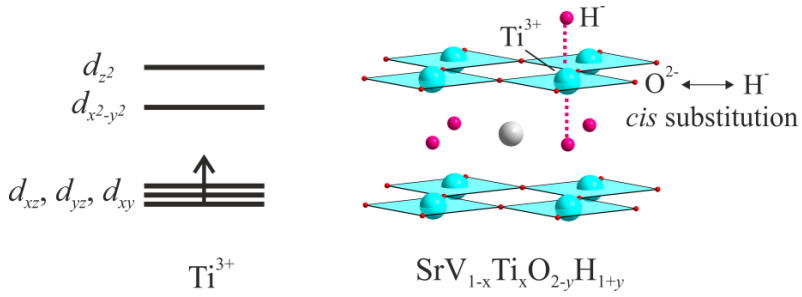


Figure 6.18. On the left, the electronic configuration for the d^1,Ti^{3+} is shown. There is no stabilisation energy gain from a *trans* configuration and thus further substitution of O^{2-} for H^- can take place in the equatorial positions of the $V_{1-x}Ti_xO_4H_2$ units (as schematised on the right hand side diagram).

The magnetic characterisation of the samples summarised in Figure 6.10 supports the electronic configurations that would result from the proposed structure and composition of the C-R and A-R reduction products. The magnetic order at room temperature observed in the C-R sample is consistent with the tetragonal, stoichiometric, anion-ordered phase $SrV_{1-x}Ti_xO_2H$ analogous with $SrVO_2H$ in which strong coupling π to π interactions take place. Meanwhile, the Curie constant of the A-R sample is consistent with a further reduced phase, $SrV_{1-x}Ti_xO_{1.5}H_{1.5}$, and the absence of magnetic order confirmed from μ^+SR consistent with this reduction product being anion-disordered.

6.4.3 The Kinetic Trap in the Formation of $SrVO_2H$

Cubic disordered hydride-rich phases are not observed during topochemical reduction of $SrVO_3$. As discussed in Section 6.4.2, the formation of $SrVO_2H$ occurs via stoichiometric oxide for hydride exchange. On the one hand, attempts to further reduce $SrVO_2H$ result in decomposition to SrO, vanadium, V_2O_3 and lower vanadium oxides (VO_2, VO). On the other hand, heating $SrVO_2H$ samples above T ≈ 650 ºC in evacuated sealed ampoules, results in decomposition to SrO, $Sr(OH)_2$, V, VO, V_2O_3.[48] These observations confirm that $SrVO_2H$ is a metastable phase.

A proposed energy profile for the reduction of $SrVO_3$ to form $SrVO_2H$ is schematised in Figure 6.19 (dark blue pathway).

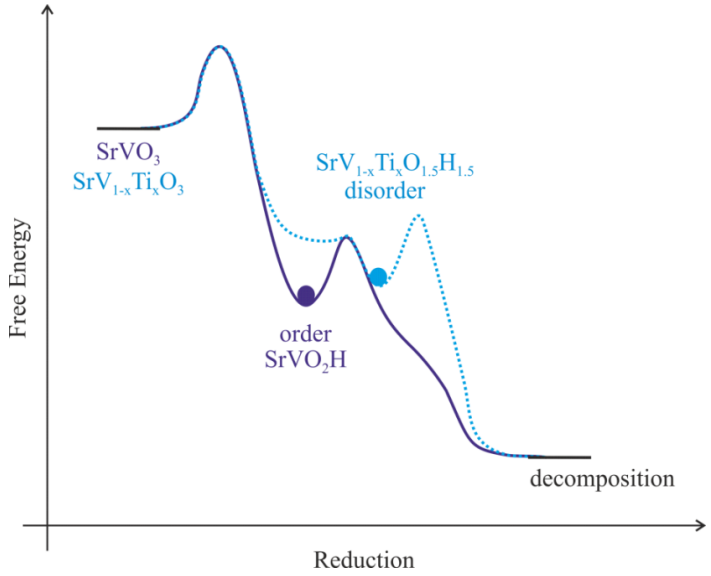


Figure 6.19. Proposed reaction profile for the topochemical reduction of $SrVO_3$ (pathway in dark blue) and $SrV_{1-x}Ti_xO_3$ (pathway in light blue).

The $SrVO_2H$ metastable material is accessible via kinetic control because, as discussed in Section 6.4.2, there is preference towards the substitution of hydride that yields the *trans* configuration around the six-fold coordinated d^2,V^{3+} centres. This configuration stabilises the ordered structure and it can be thought as a local minimum in the energy profile as shown in Figure 6.19. If the barrier towards decomposition is overcome when enough energy is supplied, the reaction proceeds all the way to the decomposition of the oxyhydride phase.

Conversely, upon doping $SrVO_2H$ with d^1,Ti^{3+} cations, the energy gain from ordering becomes less significant as the titanium cations show no preference for the position of substitution of hydride within their six-fold coordination sphere. As a result, the potential well in which an ordered $SrV_{1-x}Ti_xO_2H$ phase would be trapped becomes less shallow with respect to the all-vanadium case (light blue pathway in Figure 6.19), and the reduction proceeds to the formation of hydride-richer disordered phases.

The presence of reduction decomposition products such as vanadium metal in the prepared $SrV_{1-x}Ti_xO_{1.5}H_{1.5}$ phase suggests that the energy 'window' at which this oxyhydride is found might be close to the decomposition.

6.4.4 Titanium Content in the $SrV_{1-x}Ti_xO_3$ Starting Materials

From the discussion in Sections 6.4.1 to 6.4.3, it is clear that the differences between the C-R and A-R reduction products can be explained from the content of titanium. The tetragonal C-R product has a very small content of titanium and thus is almost identical with $SrVO_2H$. In contrast, the A-R cubic reduction product has a greater content of titanium such that more hydride can be exchanged, and the resulting hydride-rich phase is anion-disordered.

The structural and chemical properties of the C-R and A-R reduction products can only be explained from a difference in composition of $SrV_{0.95}Ti_{0.05}O_3$ C and A starting materials. These compositional differences between the $SrV_{1-x}Ti_xO_3$ phases prepared via the ceramic and the arc-melt methods will be further discussed in Chapter 7.

6.5 Conclusions

Two $SrV_{0.95}Ti_{0.05}O_3$ starting materials were synthesised for the preparation of $SrV_{0.95}Ti_{0.05}O_2H$ via topochemical reduction with CaH_2. The starting materials were synthesised via two different methods: the ceramic method and the arc-melt technique.

Although the as-prepared $SrV_{0.95}Ti_{0.05}O_3$ starting materials are equivalent from X-ray powder diffraction data, upon reduction these materials yielded markedly different products. This distinct reactivity revealed that the two starting materials, obtained via the two different synthesis methods, are not equivalent.

The $SrV_{1-x}Ti_xO_2H$ reduction product which results from the $SrV_{0.95}Ti_{0.05}O_3$ starting material prepared via the ceramic method is almost identical with $SrVO_2H$. In contrast, the reduction of the $SrV_{0.95}Ti_{0.05}O_3$ starting material prepared via the arc-melt method yields a hydride-rich anion disordered phase of formula $SrV_{1-x}Ti_xO_{1.5}H_{1.5}$.

The structural and chemical difference between the two observed reduction products, $SrV_{1-x}Ti_xO_2H$ and $SrV_{1-x}Ti_xO_{1.5}H_{1.5}$, can be explained from a difference in the content of titanium.

Chapter 7

The Synthesis of $SrV_{0.95}Ti_{0.05}O_3$

7.1 Introduction

Chapter 6 discussed the characterisation of the products which result from the topochemical reduction of $SrV_{0.95}Ti_{0.05}O_3$ samples prepared via the ceramic method and the arc-melt technique. Each synthesis method yielded a material from which the reduction product upon reaction with CaH_2 is markedly different. The reduction of the $SrV_{0.95}Ti_{0.05}O_3$ sample synthesised via the ceramic method resulted in a material analogous to $SrVO_2H$ (a tetragonal anion-ordered phase). On the other hand, the $SrV_{0.95}Ti_{0.05}O_3$ sample prepared via arc-melt technique can be reduced further, and yields a hydride-rich anion-disordered cubic material.

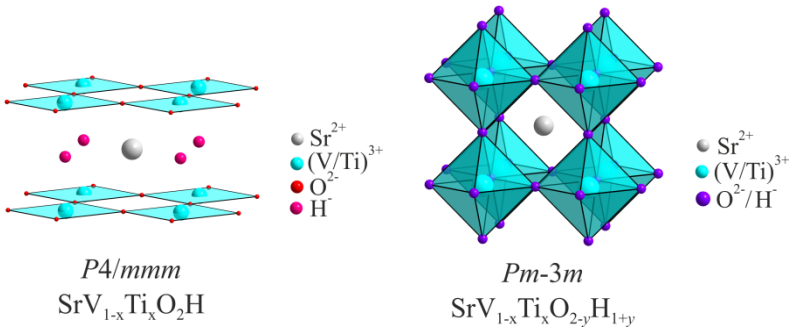


Figure 7.1. The structure and composition of the characterised reduction products from $SrV_{0.95}Ti_{0.05}O_3$ samples synthesised via the ceramic method (C-R, left) and the arc-melt technique (A-R, right).

The differences between the C-R and A-R products shown in Figure 7.1 can be explained from a difference in titanium content. Such compositional differences are likely to arise from the C and A $SrV_{0.95}Ti_{0.05}O_3$ starting materials prepared via the two synthesis methods attempted (the ceramic and the arc-melt methods). This observation in combination with the fact that the C and the A $SrV_{0.95}Ti_{0.05}O_3$ samples are a mixture of phases (as shown in Section 7.3.1), suggests inhomogeneous formation of the $SrV_{1-x}Ti_xO_3$

solid-solutions. This is rather unexpected given the structural and chemical similarities of the extreme compositions $SrVO_3$ and $SrTiO_3$.

To investigate the synthesis of more homogeneous $SrV_{0.95}Ti_{0.05}O_3$ starting materials for the preparation of novel $SrV_{0.95}Ti_{0.05}O_{2-y}H_{1+y}$ phases, synthesis of $SrV_{1-x}Ti_xO_3$ solid-solutions with different titanium contents was performed. Contrary to what has been previously reported in the literature,[110,111] the results in this work suggest that the $SrTiO_3$ and $SrVO_3$ phases are only marginally miscible.

7.2 Experimental

As described in Section 6.2.1, $SrV_{0.95}Ti_{0.05}O_3$ samples were prepared via the ceramic method reported by Rey *et al.*,[108] and the arc-melt technique (Section 2.1.3).

7.2.1 Synthesis of $SrV_{0.95}Ti_{0.05}O_3$ via the Ceramic Method – Sample C

Suitable stoichiometric amounts of $SrCO_3$ (Alfa Aesar, 99.99%), V_2O_5 (Alfa Aesar, 99.99%) and TiO_2 (Alfa Aesar, 99.995% previously dried at 900 ºC) were ground together using an agate mortar and pestle. The resulting powders were then placed in an alumina crucible and heated to 900 ºC for 12 hours to decompose the carbonate. At this point, the V^{5+} precursor phase $Sr_2V_2O_7$ was observed (in the X-ray powder diffraction data) in agreement with previous reports in the literature.[108,112] The powders were then heated in a clamshell furnace at 1075 °C, under flowing H_2 (100%), for periods of 12 hours with intermediate grinding. After each heating cycle, samples were cooled down in the furnace at 2 ºC min^{-1}. Reaction progress was monitored via X-ray powder diffraction. Heating cycles were performed until the cubic $SrV_{1-x}Ti_xO_3$ phases were completely formed.

7.2.2 Synthesis of $SrV_{0.95}Ti_{0.05}O_3$ Using the Arc-Melt Furnace – Sample A

For this method, SrO was prepared from $SrCO_3$ by heating at 900 ºC for 24 hours in air, followed by heating treatments at 1000 ºC and 1100 ºC under dynamic vacuum for 24 hours at each temperature. Suitable stoichiometric amounts of the as-prepared SrO, V_2O_3

(Alfa Aesar 99.7%), and TiO_2 were thoroughly mixed inside an argon filled glovebox, using an agate mortar and pestle. The resulting powders were pressed into a pellet and transferred to the arc-melt furnace without being exposed to air. The pellets were melted a total of four times, and flipped between each firing to expose potentially unreacted material. As described in Section 2.1.3 (Figure 2.1), the stage of the arc-melt furnace is continuously cooled with a water flow. After the final firing, the samples were allowed to cool for 15 minutes inside the furnace under the argon flow, and then immediately transferred to an argon filled glovebox.

7.3 Results

7.3.1 X-Ray Powder Diffraction Data

The C and A $SrV_{0.95}Ti_{0.05}O_3$ samples seem to be equivalent from laboratory X-ray powder diffraction data, as shown in 6.2.1, Figure 6.5. Two cubic phases with lattice parameters comparable to those of the extreme compositions, $SrVO_3$ (a = 3.843(1) Å) and $SrTiO_3$ (a = 3.901(1) Å), are present in both the C sample and the A sample. The results from refinement of a model based on $SrVO_3$ and $SrTiO_3$ are summarised in Table 6.1, where the label '1' denotes the majority cubic phase in each sample.

Table 7.1. Lattice parameters and weight fractions of the two cubic phases of a model based on $SrVO_3$ and $SrTiO_3$ refined against laboratory X-ray powder diffraction data collected from the $SrV_{0.95}Ti_{0.05}O_3$ C and A samples. The label '1' corresponds to the majority phase.

Sample	Lattice parameters (Å)		Weight fractions (%)		Fit statistics		
	a_1	a_2	w_1	w_2	χ^2	*wRp* (%)	*Rp* (%)
C	3.846(1)	3.904(1)	95.43(1)	4.57(3)	3.944	15.76	10.93
A	3.854(1)	3.926(4)	96.66(1)	3.34(3)	1.282	10.19	7.56
Reference lattices: $SrVO_3$ (a = 3.843(1) Å), $SrTiO_3$ (a = 3.901(1) Å)							

Although the refined lattice parameters for the cubic phases present in the A sample exhibit a larger deviation from those of $SrVO_3$ and $SrTiO_3$, the error bars are likely to be underestimated in the refinements as observed in Section 6.2.1. Therefore both the C and A samples were considered to be mixtures of $SrVO_3$ and $SrTiO_3$ rather than $SrV_{1-x}Ti_xO_3$ solid-solutions at a first approach. Topochemically reducing these materials revealed that this is not the case as the two samples exhibit markedly different reactivity (Section 6.2.2, Figure 6.6). The characterisation of the C-R and A-R reduction products suggest that the main cubic phases observed in the C and A starting materials have a composition $SrV_{1-x}Ti_xO_3$ where the titanium content x is different for each sample.

High-quality X-ray diffraction data collected from the C and A samples using synchrotron radiation (Section 2.4.1.2) are shown in Figure 7.2 and the results from refinement are given in Table 7.2. The larger lattice parameters of the cubic phases observed in the A sample were confirmed from the refinement against the synchrotron data. The refined phase fractions are also in good agreement with those refined using the laboratory X-ray data. For the C sample, the refined fractions of the cubic phases 1 and 2 are almost identical from both refinements, while for the A sample the refined fractions against synchrotron data confirm that the secondary phase is present in a smaller proportion for this sample. These observations support that more titanium is incorporated in the $SrV_{1-x}Ti_xO_3$ phase for A with respect to the C.

The C sample was synthesised via the ceramic method reported for $SrVO_3$ by incorporating TiO_2 as a reagent (Section 7.2.1).[108] The $SrV_{0.95}Ti_{0.05}O_3$ phase is not reported in the literature; however, $SrV_{1-x}Ti_xO_3$ ($0.00 \leq x \leq 0.90$) solid-solutions are reported to form single phases at a higher temperature than that used for the synthesis of the C sample (T = 1075 ºC). The synthesis of $SrV_{0.95}Ti_{0.05}O_3$ was carried out using the reported ceramic method for $SrV_{1-x}Ti_xO_3$ ($0.00 \leq x \leq 0.90$) solid-solutions (Section 7.3.2).

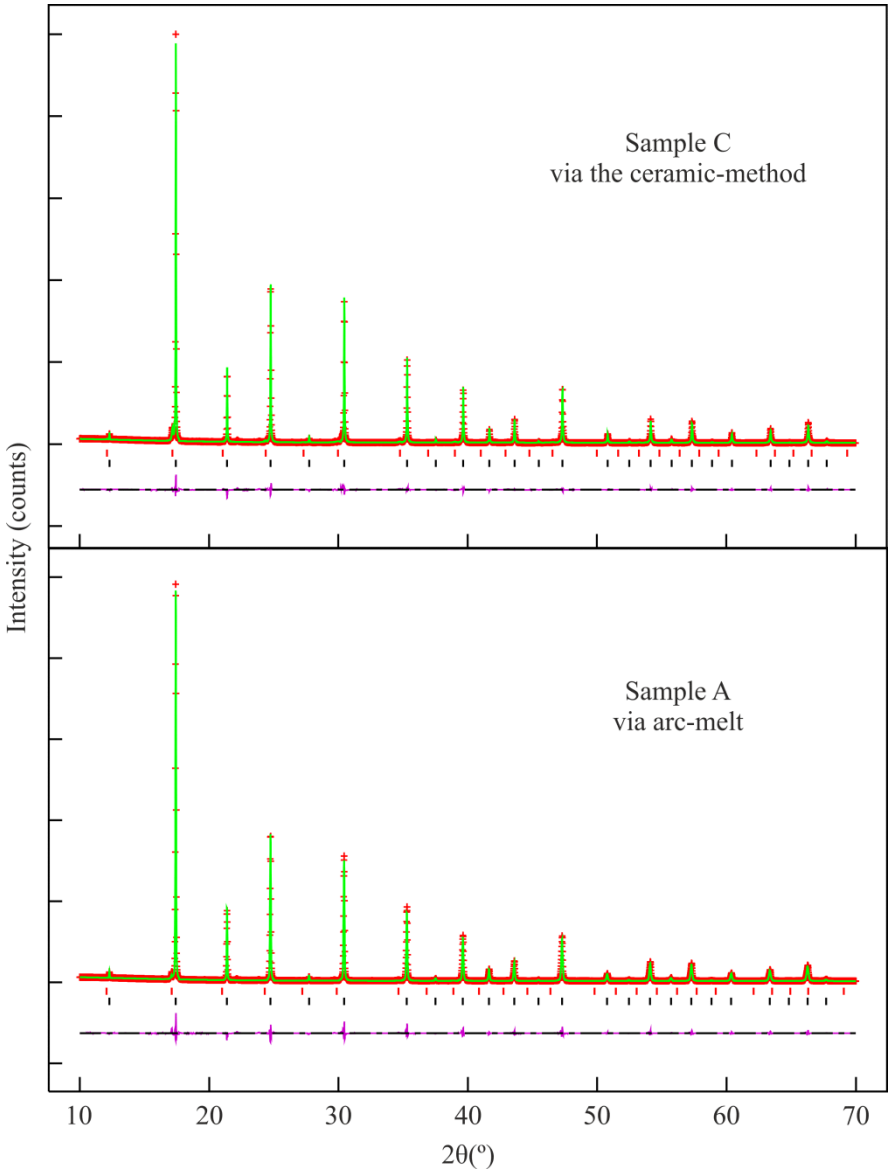


Figure 7.2. Observed, calculated, and difference plots from refinement of the structural model based on a mixture of cubic phases with space group *Pm*-3*m* against synchrotron X-ray diffraction data (λ = 0.8259 Å) collected from the $SrV_{0.95}Ti_{0.05}O_3$ C and A samples. The bottom tick marks (black) corresponds to the majority cubic phase in each case.

Table 7.2. Lattice parameters and weight fractions of the two cubic phases of a model based on $SrVO_3$ and $SrTiO_3$ refined against synchrotron X-ray powder diffraction data (λ = 0.8259 Å) collected from the $SrV_{0.95}Ti_{0.05}O_3$ C and A samples. The label '1' corresponds to the majority phase.

Sample	Lattice parameters (Å)		Weight fractions (%)		Fit statistics		
	a_1	a_2	w_1	w_2	χ^2	*wRp* (%)	*Rp* (%)
C	3.847(1)	3.906(1)	95.7 (1)	4.3(1)	51.52	8.20	5.33
A	3.851(1)	3.921(3)	97.4(1)	2.6(1)	39.16	6.92	4.73

7.3.2 $SrV_{0.95}Ti_{0.05}O_3$ Samples Prepared via the Ceramic Method at Higher Temperatures

To the best of our knowledge, only two ceramic methods have been reported for the synthesis of $SrV_{1-x}Ti_xO_3$ powder phases (references concerning the $SrTiO_3$-$SrVO_3$ solid solution system are largely focused on epitaxial films and superlattices). The first ceramic method for $SrV_{1-x}Ti_xO_3$ ($0.00 \leq x \leq 0.81$, steps of 0.1) solid-solutions utilises high pressure (1983, Tsuiki *et al*.).[110] The most recently reported method is very similar to that of $SrVO_3$ but utilises higher synthesis temperatures (2002, Hong *et al*.).[111] Both ceramic methods are reported to yield single phases. Therefore, the synthesis of $SrV_{0.95}Ti_{0.05}O_3$ was carried out via the most recently reported method.

7.3.2.1 Experimental Details

Suitable stoichiometric amounts of $SrCO_3$, V_2O_5 and TiO_2, were ground together in an agate mortar and pestle. The resulting powders were pressed into a pellet and heated to 1550 ºC at 4 ºC min^{-1} under a 10% H_2/Ar flow, for 12 hours. Samples were cooled down inside the furnace at 2 ºC min^{-1} (under the H_2/Ar flow) after completion of the 12 hour dwell.

7.3.2.2 X-ray Powder Diffraction Data from the $SrV_{0.95}Ti_{0.05}O_3$ Samples Prepared via the Ceramic Method at T = 1550 ºC, 1525 ºC

Figure 7.3 shows the X-ray powder diffraction data collected from the $SrV_{0.95}Ti_{0.05}O_3$ sample prepared as described in Section 7.3.2.1 (Sample C-1550, top panel (a)). Analogous to the C and A samples, two cubic phases are clearly observed in the C-1550 sample. The lattice parameters of these phases are also consistent with $SrVO_3$ and $SrTiO_3$ (Table 6.1). Additional reflections in the C-1550 sample (which grow upon further heating cycles as shown in panel (b)), could be indexed as the strontium-deficient phase $SrV_{10}O_{15}$ (*Ccmb*; a = 9.91(1) Å, b = 11.57(2) Å, c = 9.32(1) Å).[113] The results from refinement of a model based on $SrVO_3$, $SrTiO_3$ and $SrV_{10}O_{15}$ against the data collected from the C-1550 sample are summarised in Table 7.3. Asymmetric peak shapes for all the reflections of the main cubic phase in the sample yield a relatively poor statistical fit of the model to the data as shown in the inset of Figure 7.3(a).

Syntheses carried out at the same temperature (T = 1550 ºC), but using a lower concentration of H_2 in the reductive gas flow (5% H_2 in N_2), led to multiple-phase samples analogous to C-1550, with greater fractions of the strontium-deficient $SrV_{10}O_{15}$ phase. A sample with the minimum observed weight fraction of the latter phase was achieved at the lower synthesis temperature of 1525 ºC under a 10% H_2/Ar flow. The data collected from this sample (C-1525) are shown in Figure 7.4, with the results from refinement of a model based on $SrVO_3$, $SrTiO_3$ and $SrV_{10}O_{15}$ summarised in Table 7.4. An asymmetric peak shape for all the reflections is also observed in this case (inset of Figure 7.4).

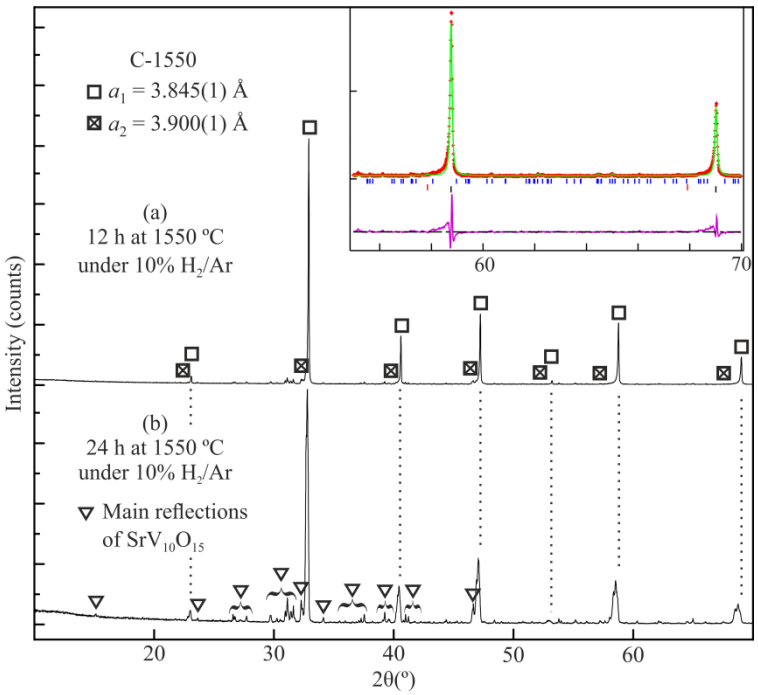


Figure 7.3. X-ray data collected from a $SrV_{0.95}Ti_{0.05}O_3$ sample prepared under a 10% H_2/Ar flow at 1550 ºC after (a) one 12-hour heating cycle (C-1550) and (b) two 12-hour heating cycles. Inset in (a) shows the observed, calculated, and difference plots from the refinement of C-1550. The black set of tick marks (bottom) corresponds to the majority cubic phase (a_1 = 3.845(1) Å), red (middle) to the minority cubic phase (a_2 = 3.900(1) Å) and blue to the secondary phase $SrV_{10}O_{15}$.

Table 7.3. Summary of results from refinement of the $SrV_{0.95}Ti_{0.05}O_3$ C-1550 sample.

Main cubic phases			
Lattice parameters (Å)		Weight fraction (%)	
a_1	a_2	w_1	w_2
3.845(1)	3.900(1)	81.40(1)	4.56(3)

Secondary phase $SrV_{10}O_{15}$ in sample C-1550
space group: *Ccmb*; a = 9.903(1) Å, b = 11.553(2) Å, c = 9.316(1) Å; weight fraction 14.04(9)%
χ^2 = 16.04, *wRp* = 22.70%, *Rp* = 14.80%
Reference lattices: $SrVO_3$ (a = 3.843(1) Å), $SrTiO_3$ (a = 3.901(1) Å)

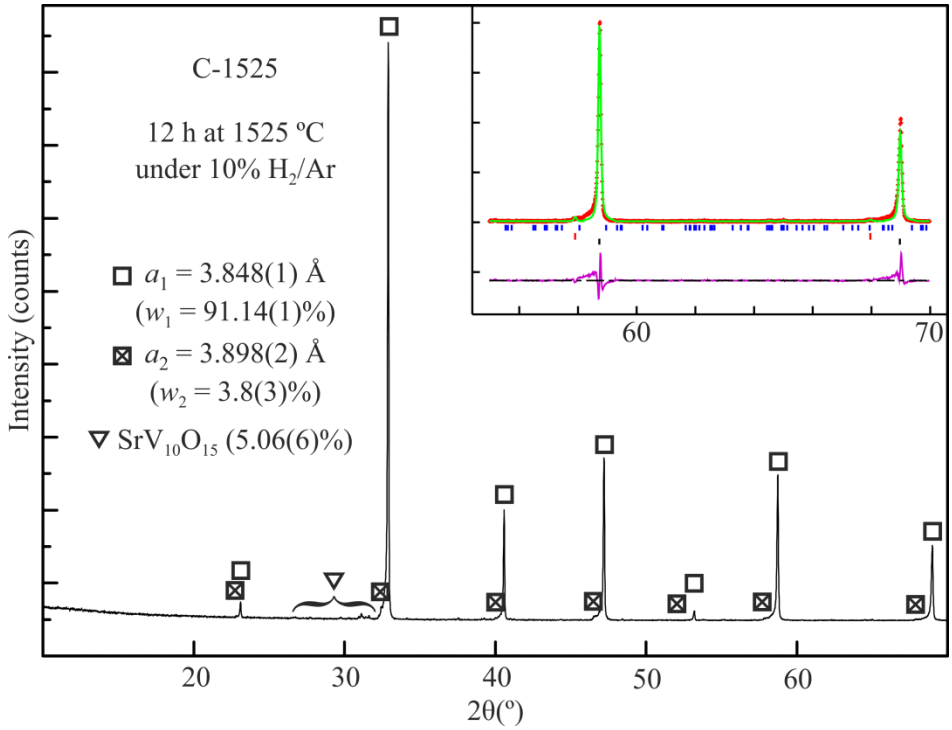


Figure 7.4. X-ray powder diffraction data collected from the $SrV_{0.95}Ti_{0.05}O_3$ C-1525 sample prepared under a 10% H_2/Ar flow at 1525 ºC after one 12-hour heating cycle. Inset shows the observed, calculated, and difference plots from the refinement of a model based on a mixture of $SrVO_3$ and $SrTiO_3$. The black set of tick marks (bottom) corresponds to the majority cubic phase (a_1 = 3.848(1) Å), red (middle) to the minority cubic phase (a_2 = 3.898(2) Å) and blue to the secondary phase $SrV_{10}O_{15}$.

Table 7.4. Summary of results from refinement of the $SrV_{0.95}Ti_{0.05}O_3$ C-1525 sample.

Main cubic phases			
Lattice parameters (Å)		**Weight fraction (%)**	
a_1	a_2	w_1	w_2
3.848(1)	3.898(2)	91.14(1)	3.8(3)

Secondary phase $SrV_{10}O_{15}$ in sample C-1525
space group: *Ccmb*; a = 9.909(2) Å, b = 11.546(2) Å, c = 9.316(2) Å; weight fraction 5.06(6)%
χ^2 = 6.854, *wRp* = 18.70%, *Rp* = 12.66%
Reference lattices: $SrVO_3$ (a = 3.843(1) Å), $SrTiO_3$ (a = 3.901(1) Å)

An inverse relation is observed between the fraction of the secondary cubic phases and the lattice parameter of the majority phases in all the $SrV_{0.95}Ti_{0.05}O_3$ samples prepared. Within the $SrV_{0.95}Ti_{0.05}O_3$ samples prepared via the ceramic method, the C-1525 sample contains the smallest fraction of the secondary cubic phase (w_2 = 3.8(3)%) and also contains the main cubic phase for which the greater lattice parameter was observed in the set (a_1 = 3.848(1) Å). These observations agree with the phases refined in the arc-melt sample (w_2 = 2.6(1)%, Table 7.2) for which the main cubic phase exhibits a lattice parameter (a_1 = 3.851(1) Å) consistent with the values reported for the $SrV_{1-x}Ti_xO_3$ ($0.10 \leq x \leq 0.90$) phases.[110,111]

The comparison of the X-ray powder diffraction data collected from the $SrV_{0.95}Ti_{0.05}O_3$ samples prepared via the ceramic and arc-melt methods, suggest that the latter method yields $SrV_{1-x}Ti_xO_3$ solid-solutions with a greater content of titanium. This observation supports the hypothesis that the differing reactivity between the A and C samples of $SrV_{0.95}Ti_{0.05}O_3$, arises from the different concentration of titanium in the two samples. In order to confirm this hypothesis, $SrV_{1-x}Ti_xO_3$ samples with higher titanium contents were prepared via the ceramic and arc-melt methods, and the results compared.

7.3.3 $SrV_{1-x}Ti_xO_3$ Samples with x = 0.40, 0.50

$SrV_{0.60}Ti_{0.40}O_3$ and $SrV_{0.50}Ti_{0.50}O_3$ samples were prepared via the ceramic method described in Section 7.3.2.1 (at T = 1525 ºC), and via the arc-melt technique (Section 7.2.2). The X-ray powder diffraction data collected from the as prepared samples are shown in Figure 7.5 and Figure 7.6. The lattice parameters and weight fractions presented result from refinement of a model based on the mixture of $SrVO_3$ and $SrTiO_3$. The phase labelled as '1' is the majority cubic phase in each sample.

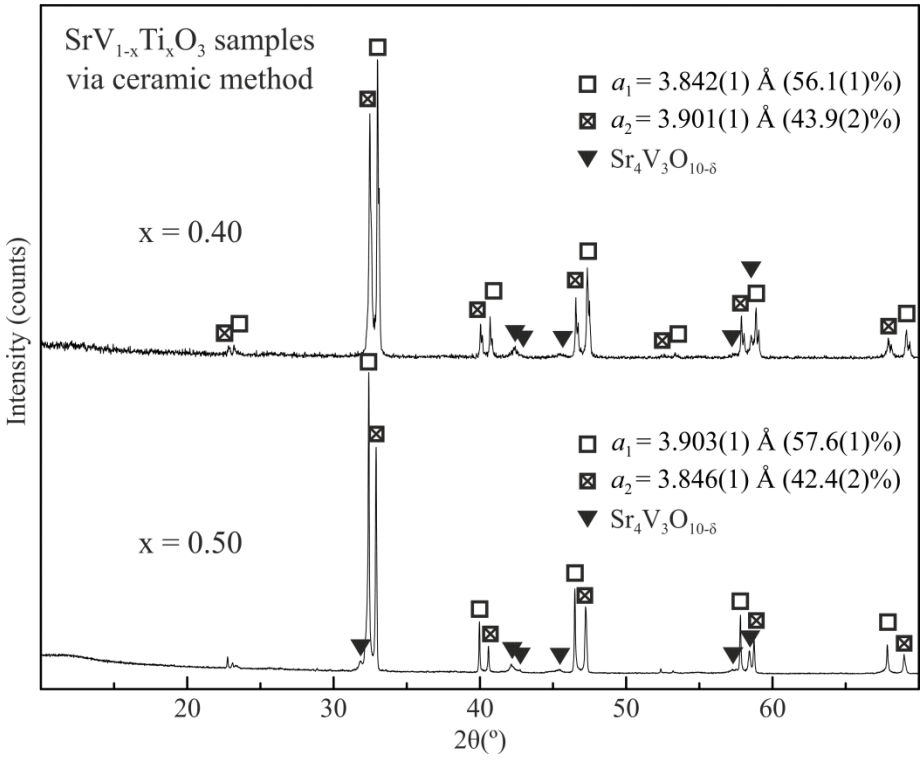


Figure 7.5. X-ray powder diffraction data collected from $SrV_{1-x}Ti_xO_3$ samples with x = 0.40 (top) and x = 0.50 (bottom) prepared under a 10% H_2/Ar flow at 1525 ºC for 12 hours.

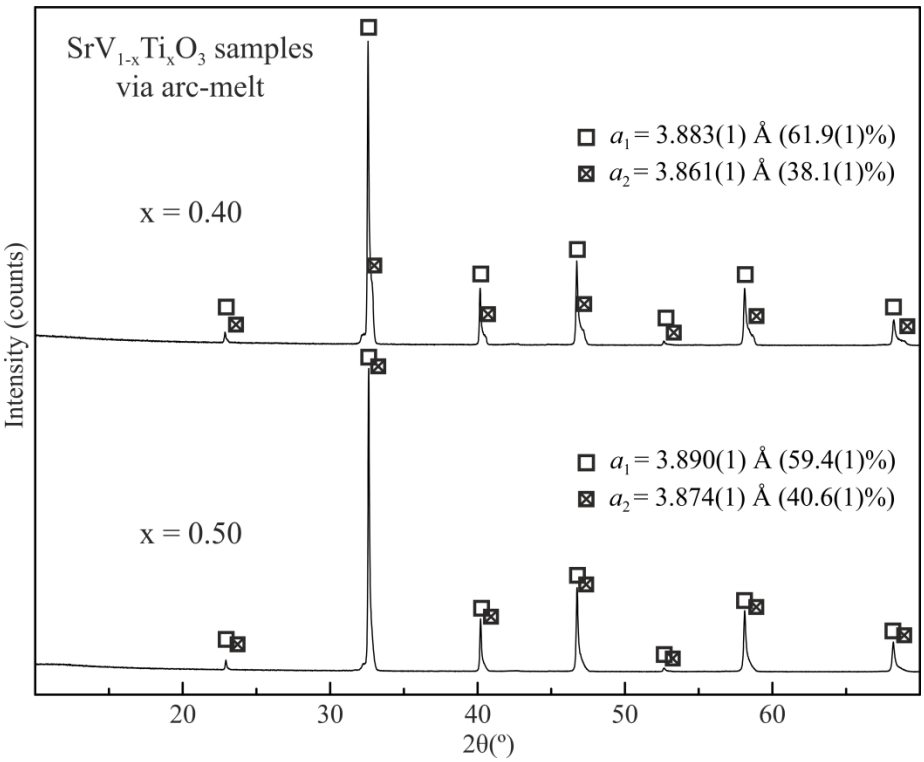


Figure 7.6. X-ray powder diffraction data collected from $SrV_{1-x}Ti_xO_3$ samples with x = 0.40 (top) and x = 0.50 (bottom) prepared via arc-melt.

As can be observed from comparison of Figure 7.5 and Figure 7.6, in contrast with the arc-melt method, the ceramic method yields $SrV_{0.60}Ti_{0.40}O_3$ and $SrV_{0.50}Ti_{0.50}O_3$ samples comprised of cubic phases which are very evidently segregated. This suggests that the samples prepared via the arc-melt technique are more homogeneous.

Consistent with the observations for the $SrV_{0.95}Ti_{0.05}O_3$ C and A samples, the refined lattice parameters for the cubic phases observed in the $SrV_{0.60}Ti_{0.40}O_3$ and $SrV_{0.50}Ti_{0.50}O_3$ samples prepared via the ceramic method are in very good agreement with those of $SrVO_3$ (a = 3.843(1) Å) and $SrTiO_3$ (a = 3.901(1) Å). However, those of the phases observed in the samples prepared via arc-melt deviate more significantly from $SrVO_3$ and $SrTiO_3$.

Notably, the weight fractions of the majority and minority cubic phases in the samples (in both sets of data) deviate from the values expected from the composition of the samples (40% and 50% titanium). This is particularly clear for the $SrV_{0.50}Ti_{0.50}O_3$ samples. Additionally, while the cubic phase of greater lattice parameter (thus proposed to be a titanium-rich phase) represents the minority phase in the $SrV_{0.60}Ti_{0.40}O_3$ samples, this larger lattice phase becomes the majority phase for the $SrV_{0.50}Ti_{0.50}O_3$ samples. These observations suggest that $SrTiO_3$ and $SrVO_3$ are not extensively miscible.

Finally, both sets of data collected from the $SrV_{0.60}Ti_{0.40}O_3$ and $SrV_{0.50}Ti_{0.50}O_3$ samples exhibit features which suggest that, in addition to the refined cubic phases 1 and 2, further cubic phases are also formed via the two synthesis methods. In the data collected from the samples prepared via the ceramic method, additional reflections which can be indexed using cubic phases with lattice parameters a_4 = 3.825(1) Å and a_5 = 3.885(1) Å are observed (as shown in Figure 7.7). Meanwhile, the asymmetric peak profile observed for all the reflections in the data collected from the arc-melt samples (Figure 7.8) suggest that a range of $SrV_{1-x}Ti_xO_3$ compositions (either vanadium or titanium rich, or with subtly different oxygen content) are present in the samples.

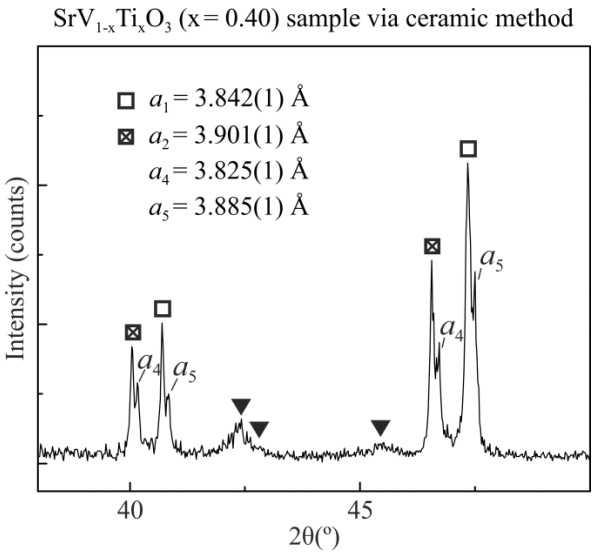


Figure 7.7. Reflections observed from additional cubic phases revealed upon closer inspection of the X-ray powder diffraction data collected from $SrV_{0.60}Ti_{0.40}O_3$ sample prepared under a 10% H_2/Ar flow at 1525 ºC for 12 hours.

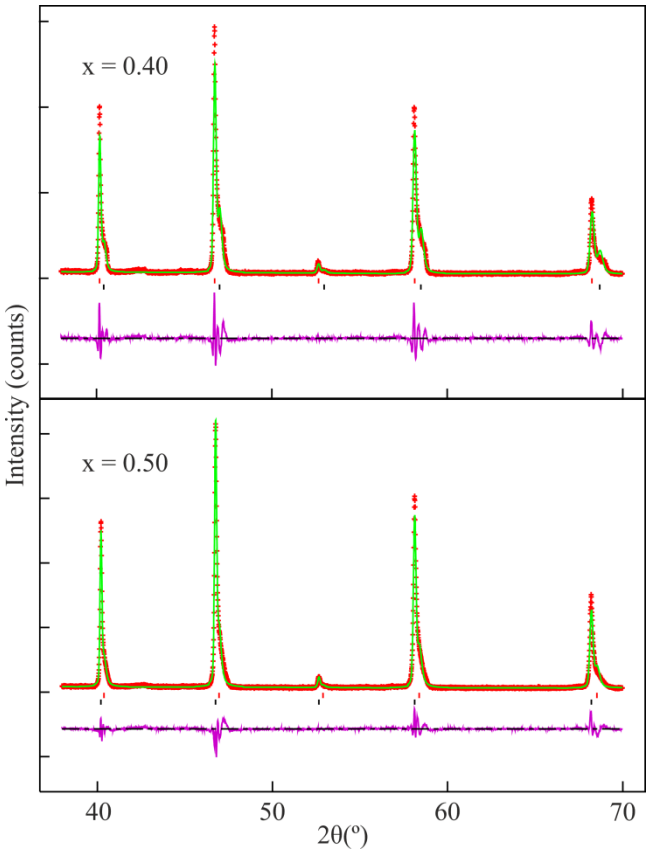


Figure 7.8. Observed, calculated, and difference plots (in the range 38 ≤ 2θ (º) ≤ 70) from refinement of the model based on two cubic phases against the data collected from the $SrV_{1-x}Ti_xO_3$ (x = 0.40, 0.50) arc-melt samples. The black set of tick marks corresponds to the majority cubic phases (a_1) and red to the minority cubic phases (a_2).

7.3.4 $SrV_{1-x}Ti_xO_3$ Solid-Solutions

The refined lattice parameters of the majority phases for a series of $SrV_{1-x}Ti_xO_3$ samples with x in the range $0.10 \leq x \leq 0.30$ (steps of 0.05), prepared via the arc-melt technique (as described in Section 7.2.2), are plotted as a function of x in Figure 7.9. The lattice parameters found for the majority phases in the x = 0.05, 0.40 and 0.50 samples prepared via the ceramic and arc-melt methods are also included in the plot. The reported values for $SrVO_3$ and $SrTiO_3$ are included as a reference.

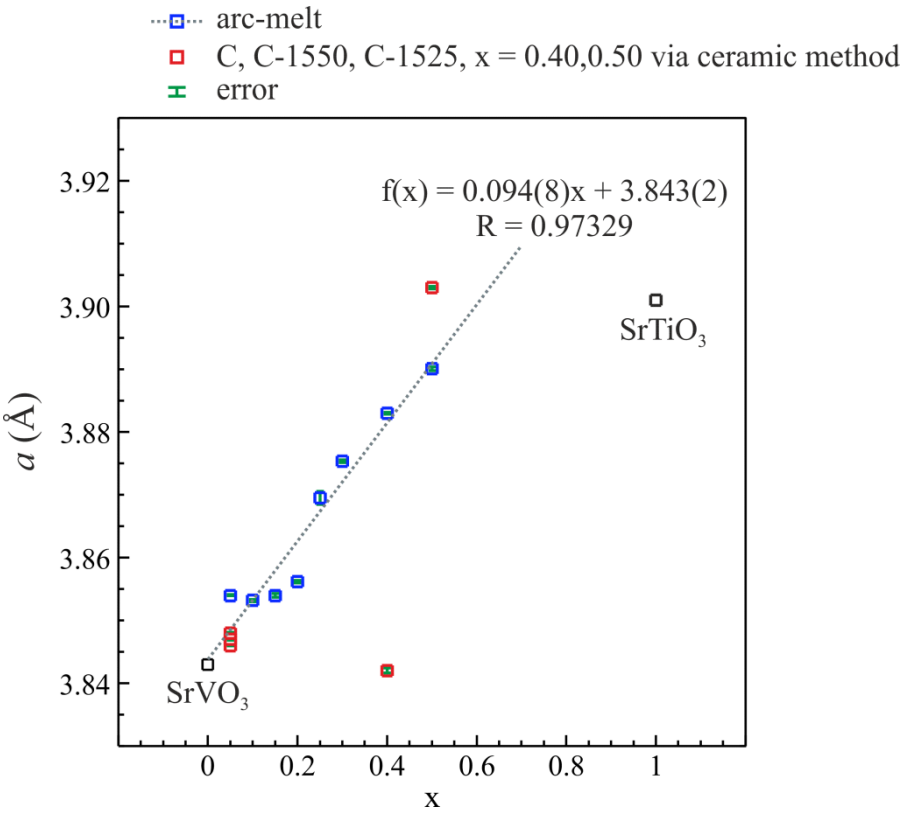


Figure 7.9. Refined lattice parameters of the majority cubic phases observed in the $SrV_{1-x}Ti_xO_3$ ($0.10 \leq x \leq 0.30$) samples prepared via arc-melt. The lattice parameters of the extreme compositions $SrVO_3$, $SrTiO_3$ and the x = 0.05, 0.40, 0.50 samples previously discussed have been included in the plot.

From the plot of Figure 7.9, the lattice parameters of the majority phases in the samples prepared via arc-melt are observed to be a function of the nominal composition of the samples x, with a linear model for the observed trend (as predicted from Vegard's law) yielding a reasonable fit (R = 97.3%). The increase in the lattice parameters with the

increase of x confirms that titanium is incorporated in the $SrV_{1-x}Ti_xO_3$ solid-solutions prepared via the arc-melt method.

On the other hand, the trend for the lattice parameters in the samples prepared via the ceramic method is less clear. Although it is reasonable to propose that a fraction of titanium is also incorporated in the $SrV_{1-x}Ti_xO_3$ solid-solutions prepared via the ceramic method, it is not possible to relate this fraction to the nominal composition of the samples from the data collected.

The X-ray powder diffraction data collected from the $SrV_{1-x}Ti_xO_3$ (range) samples prepared via arc-melt are shown in Figure 7.10.

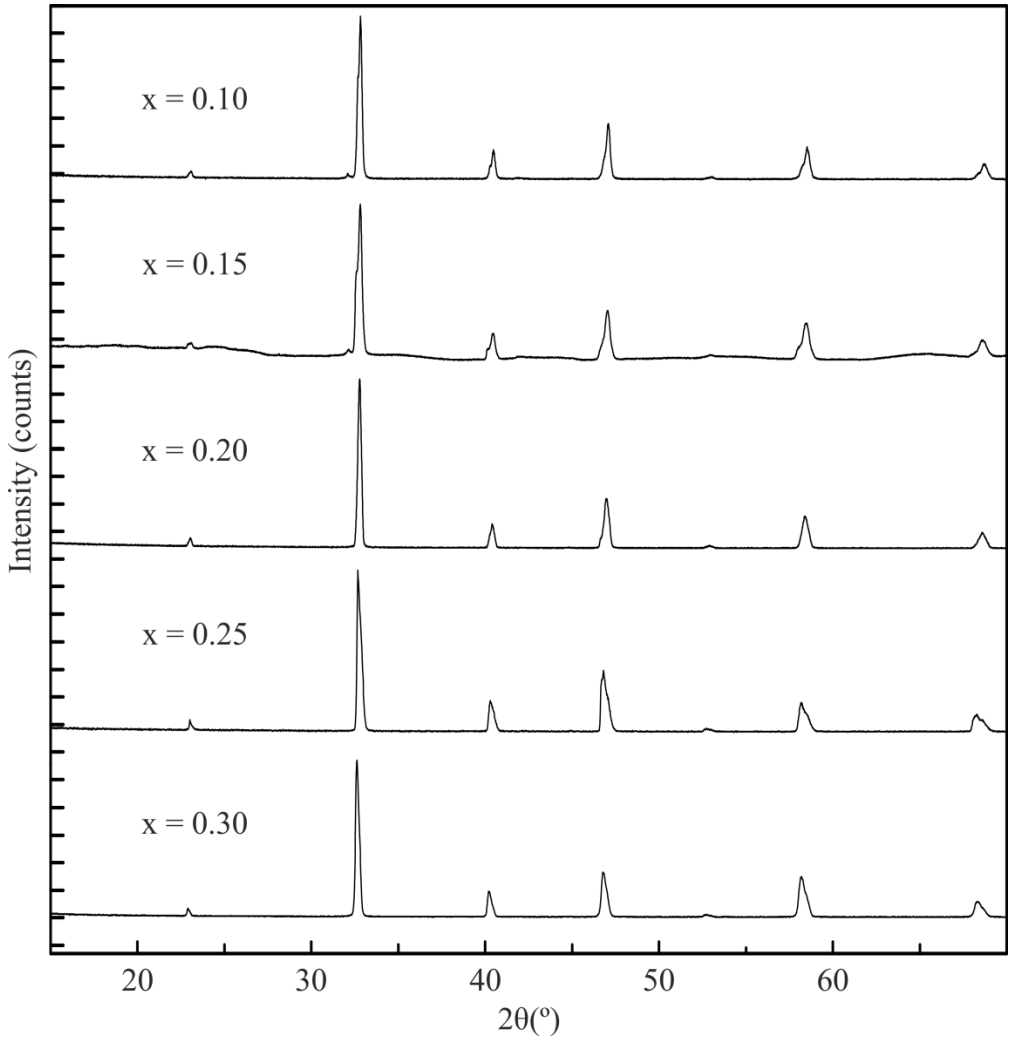


Figure 7.10. X-ray powder diffraction data collected from $SrV_{1-x}Ti_xO_3$ ($0.10 \leq x \leq 0.30$) samples prepared via arc-melt.

Consistent with the observations in the X-ray diffraction patterns of the $SrV_{1-x}Ti_xO_3$ samples with x = 0.05 (C and A), and x = 0.40, 0.50 prepared via the two synthesis methods, the reflections from two cubic phases are evident in the data shown in Figure 7.10. As the value of x increases, the reflections overlap more significantly however, the two-phase models were found to fit the data collected from all samples significantly better than single-phase cubic models. The presence of multiple phases is also supported by an asymmetric peak profile observed for all the samples across the range studied. This asymmetry of the peaks is observed in the X-ray diffraction data reported by Hong *et al.* (and no diffraction data is reported by Tsuiki *et al.*).[110,111] These observations support the hypothesis that there is limited miscibility between $SrTiO_3$ and $SrVO_3$, and thus the incorporation of titanium in the $SrV_{1-x}Ti_xO_3$ solid-solutions is also limited.

7.3.5 Phase Segregation in a $SrV_{0.95}Ti_{0.05}O_3$ Sample Prepared via Arc-Melt

The most important difference between the two syntheses methods attempted for the preparation of the $SrV_{1-x}Ti_xO_3$ solid-solutions is the cooling rate used in each method. During the arc-melt method, the stage of the furnace was rapidly cooled from temperatures in the range $1000 \leq T\ (^{o}C) \leq 3000$ (the actual temperature is unknown, Section 2.1.3) to room temperature in approximately 120 seconds. Contrastingly, during the ceramic method samples were cooled from temperatures in the range $1075 \leq T\ (^{o}C) \leq 1550$ to room temperature, at 2 ºC min^{-1}. A fraction of the x = 0.05 arc-melt material shown in Figure 7.11(a) (A_1) was annealed at 1100 °C in an evacuated sealed silica ampoule, and slow-cooled at 2 ºC min^{-1}. The resulting sample, A_1-SC is shown in Figure 7.11(b).

The refinements of the model based on $SrVO_3$ and $SrTiO_3$ against the two sets of data show that the cubic phases in the A_1-SC have different lattice parameters with respect to those in the original A_1 sample. The values refined in the A_1-SC sample are closer to those of $SrVO_3$ and $SrTiO_3$. Furthermore, the weight fraction of the phase with lattice parameter closer to $SrTiO_3$ is significantly greater in the A_1-SC sample (and in agreement with the value of x = 0.05). These observations are consistent with those from the data collected from $SrV_{0.95}Ti_{0.05}O_3$ samples prepared via the ceramic method (C, C-1550 and

C-1525) and suggest that in these samples the components of the $SrV_{1-x}Ti_xO_3$ are more segregated compared to the arc-melt analogues.

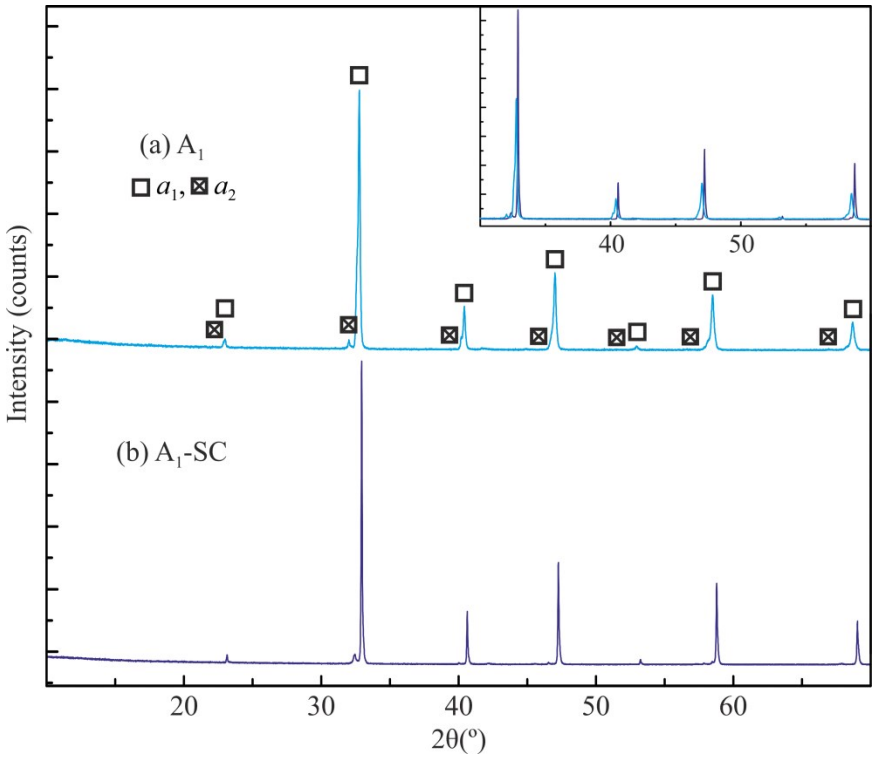


Figure 7.11. X-ray diffraction patterns collected from an arc-melt $SrV_{0.95}Ti_{0.05}O_3$ sample (a) before heating at 1100 ºC and slow-cooling (A_1), and (b) after this annealing process (A_1-SC). The overlaid diffraction patterns in the range $30 \leq 2\theta\ (º) \leq 60$ are shown in the inset of (a).

Table 7.5. Lattice parameters and weight fractions of the cubic phases refined for the arc-melt $SrV_{0.95}Ti_{0.05}O_3$ A_1 and A_1-SC samples. The label '1' corresponds to the majority phase.

Sample	Lattice parameters (Å)		Weight fractions (%)		Fit statistics		
	a_1	a_2	w_1	w_2	χ^2	*wRp* (%)	*Rp* (%)
A_1	3.853(1)	3.923(1)	97.8 (1)	2.2(1)	2.352	11.86	8.62
A_1-SC	3.844(1)	3.900(2)	94.7(1)	5.3(2)	3.201	15.31	10.38
Reference lattices: $SrVO_3$ (a = 3.843(1) Å), $SrTiO_3$ (a = 3.901(1) Å)							

7.3.5.1 Stability of the $SrV_{1-x}Ti_xO_3$ Samples Prepared via Arc-Melt at T = 610 ºC

The differing reactivity between the C and A samples of $SrV_{0.95}Ti_{0.05}O_3$ can be explained on the basis of the different composition in titanium, only if at the reduction temperatures the solid-solutions are stable (*i.e.* remain chemically unchanged).

The stability of the $SrV_{0.50}Ti_{0.50}O_3$ solid solution prepared via the arc-melt method was tested under the reduction conditions. The $SrV_{0.50}Ti_{0.50}O_3$ sample shown in Figure 7.6 was annealed for 72 hours at 610 ºC in an evacuated sealed silica ampoule. The X-ray diffraction data collected before and after the annealing process are shown in Figure 7.12. No indication of segregation is observed from the refined lattice parameters and weight fractions.

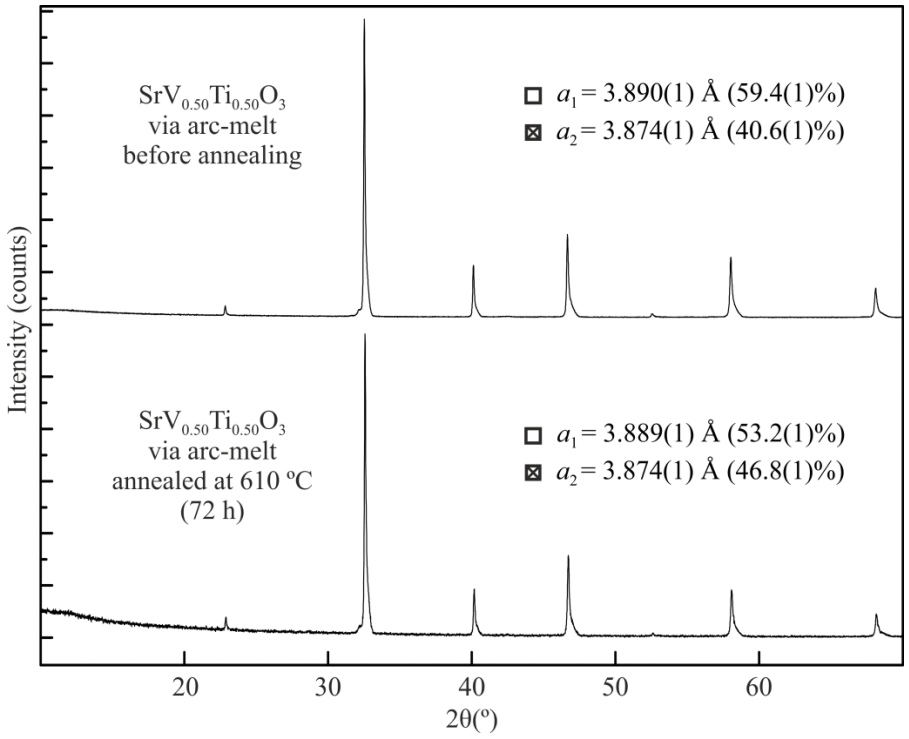


Figure 7.12. X-ray diffraction patterns of the $SrV_{0.50}Ti_{0.50}O_3$ sample prepared via the arc-melt method, before (top) and after (bottom) annealing at 610 ºC for 72 hours.

7.3.5.2 Reactivity of Slow-cooled and Quenched $SrV_{0.95}Ti_{0.05}O_3$ Samples

The X-ray powder diffraction data collected from the reduction of the $SrV_{0.95}Ti_{0.05}O_3$ A_1 sample prepared via arc-melt (Section 7.3.5), and the fraction of the same sample which was slow-cooled A_1-SC, are shown in Figure 7.13. The A_1-SC fraction shows analogous

reduction behaviour to the C starting material (Section 6.2.2, Figure 6.6), and in contrast to the original arc-melt A_1 sample, no cubic phase is observed in the reduction product A_1-SC-R after equivalent periods of reaction.

The diffraction pattern collected after the second cycle from the A_1-R product is dominated by the CaO by-product of reaction. At this stage all the CaH_2 had reacted with the A_1 sample. Consistent with the observations for the A starting material, continuation of the reduction of the A_1-R sample yields the growth of a cubic phase at the expense of the tetragonal material (Figure 7.13, bottom left). The lattice parameter of the cubic phase observed in the A_1-R product is different from those in A_1, and is consistent with the refined lattice parameter for the A-R product (Figure 7.8, Table 7.3).

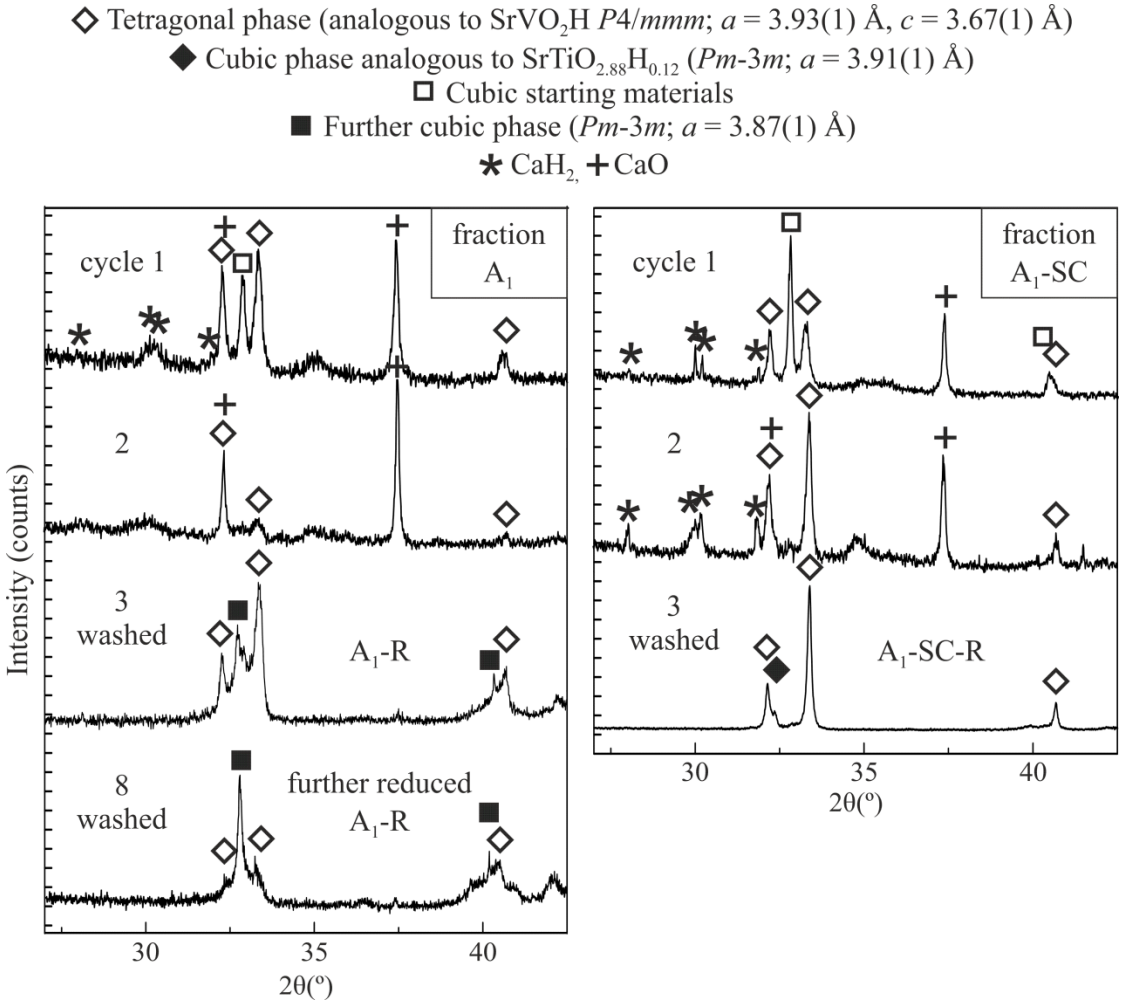


Figure 7.13. X-ray diffraction data collected from the reduction of the arc-melt A1 sample and the annealed (1100 °C) slow-cooled fraction A_1-SC. Continuing the reduction of the A1 sample yields a cubic material consistent with that observed in the A-R reduction product characterised in Section 6.3.

7.4 Discussion

In contrast to what has been reported in the literature, attempts to synthesise $SrV_{1-x}Ti_xO_3$ ($0.05 \leq x \leq 0.50$) homogeneous solid-solutions via the ceramic and arc-melt methods are not observed to result in single-phase samples. This is surprising given that the end-members, $SrVO_3$ and $SrTiO_3$, have the same structure (cubic perovskite structure, *Pm*-3*m*) with the cations being substituted (in the B-sites) having the same charge. Additionally, the $V^{4+}(d^1)$ and $Ti^{4+}(d^0)$ cations have very similar ionic radii in an octahedral environment (58.0 pm and 60.5 pm respectively) as expected from their electronic configuration.[114] Therefore, structurally, all the conditions for the formation of extensive solid-solutions between $SrVO_3$ and $SrTiO_3$ are met. However, multiple phases (very close to the separate components) are observed to be consistently preferred in all the syntheses attempted rather than $SrV_{1-x}Ti_xO_3$ solid solutions.

The formation of the separate components $SrVO_3$ and $SrTiO_3$ rather than the $SrV_{1-x}Ti_xO_3$ solid solution seems to be thermodynamically favoured. This is confirmed by the effect that a slow-cooling process has over the $SrV_{1-x}Ti_xO_3$ samples prepared via the arc-melt method. Slow-cooling a $SrV_{0.95}Ti_{0.05}O_3$ sample prepared via arc-melt (A_1, Figure 7.11a) results in a mixture of cubic phases which are more similar to $SrVO_3$ and $SrTiO_3$, than the initial phases prior to slow-cooling (Table 7.5). The weight fractions of the resulting mixture of cubic phases are in good agreement with the composition expected from the segregated components: ~95% $SrVO_3$ and ~5% $SrTiO_3$. Furthermore, the reduction of this slow-cooled fraction yields products analogous to $SrVO_2H$ and $SrTi_{2.88}H_{0.12}$, consistent with the characterised products of reduction of the $SrV_{0.95}Ti_{0.05}O_3$ C sample (Section 6.3).

The observation that slow cooling the $SrV_{1-x}Ti_xO_3$ samples leads to the separation into the components $SrTiO_3$ and $SrVO_3$ can be explained from the free energy associated with the formation of a mixture ($\Delta G = \Delta H - T\Delta S$). At high temperatures (where the term $-T\Delta S$ is dominant) the dispersion between the components of a mixture is thermodynamically favoured. However, if the formation of the mixture requires energy such that $\Delta H > 0$ and if the components of the mixture are immiscible, the segregation into separate components is thermodynamically favoured upon cooling. This seems to be the case in the $SrTiO_3$-$SrVO_3$ solid-solution system. Thus, by slow-cooling enough energy is available for the diffusion of the ions to form the separate phases $SrVO_3$ and $SrTiO_3$. In contrast, by quenching, the $SrV_{1-x}Ti_xO_3$ solid-solutions reach rapidly temperatures at

which not enough energy is available for the diffusion of ions (e.g. the room temperature), and the high temperature dispersions are 'frozen'. This effect of the cooling method on the $SrV_{1-x}Ti_xO_3$ samples is schematised in Figure 7.14 and can be understood as being analogous to a dispersion of oil in water.

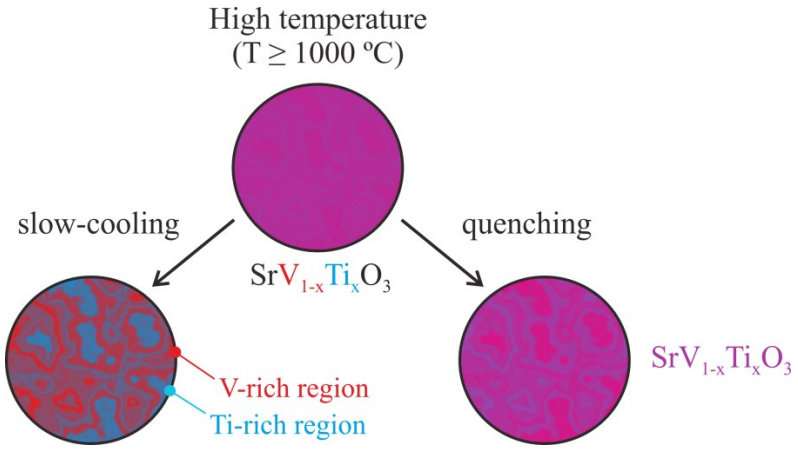


Figure 7.14. Schematisation of the effect of the cooling rate on the $SrV_{1-x}Ti_xO_3$ samples. The circles represent particles of the samples, where the dispersion of $SrTiO_3$ (blue) in $SrVO_3$ (red) leads to $SrV_{1-x}Ti_xO_3$ phases in purple.

The reduction of the A_1 $SrV_{1-x}Ti_xO_3$ sample prepared via arc-melt and the slow-cooled fraction A_1-SC, confirms that the difference in the reactivity between the $SrV_{0.95}Ti_{0.05}O_3$ C and A samples is a consequence of the composition of titanium in each sample. The sample A contains more titanium with respect to the sample C, and thus the reduction can proceed further as discussed in Section 6.4.2.

The reason why the $SrTiO_3$ and $SrVO_3$ phases are not extensively miscible is a non-trivial question however an interesting observation is that, although structurally similar, the two phases (in bulk) display markedly different optical and electric properties. $SrTiO_3$ is white and insulating, while $SrVO_3$ is black and a correlated metal.[115-117] It is reasonable to believe that the electronic structures of $SrTiO_3$ and $SrVO_3$ drive the preferred formation for the separate phases.

Interestingly, not many reports are found about substitutional solid-solutions in the B-sites of $SrVO_3$. Further work in this respect could shed some light on the intriguing correlated electronic structure of $SrVO_3$.

Finally, it is worth noting that the topochemical nature of the reductions carried out on the $SrV_{1-x}Ti_xO_3$ solid-solutions reveals the fine chemical and structural differences between the samples which are otherwise fairly challenging to explore. This case adds to the list of phases for which the topochemical reduction highlights key aspects about the chemical and structural characteristics of the materials. For example, phase separation is observed as a consequence of an electronic instability during the reduction of $Y_2Ti_2O_7$; dissimilar extents of reaction from different parts of the samples is observed as a consequence of local chemical inhomogeneity (undetectable by powder diffraction techniques) during the reduction of $Sr_{n+1}(Fe_{0.5}Ru_{0.5})_nO_{3n+1}$. Furthermore, a phase separation (of unreacted starting material and reduced material) is observed as a consequence of the accumulated strain during the reduction of $LaSrNiRuO_6$ (Chapters 3-5).

7.5 Conclusions

Attempts of preparing the $SrV_{1-x}Ti_xO_3$ solid-solutions with x in the range $0.05 \leq x \leq 0.30$ via the ceramic and arc-melt methods are not observed to yield single-phase samples. The results suggest that the $SrTiO_3$-$SrVO_3$ system does not form extensive solid-solutions, in contrast to what has been reported in the literature. These results are rather unexpected from the structural similarity of the components $SrTiO_3$ and $SrVO_3$. The preference for the formation of the separate phases is proposed to be a consequence of the markedly different electronic structure of $SrTiO_3$ and $SrVO_3$.

The differing reactivity between the $SrV_{0.95}Ti_{0.05}O_3$ samples prepared via the ceramic and arc-melt methods was confirmed to arise from a different content of titanium in the $SrV_{1-x}Ti_xO_3$ solid-solutions formed by each method. Additionally, given that the temperature is not accurately controlled during the arc-melt technique described in Section 7.2.2 the different samples obtained are likely to have different chemical compositions.

Finally, the reduction of the $SrV_{1-x}Ti_xO_3$ phases represents another example in which the topochemical nature of the reaction highlights chemical and structural characteristics which are relevant for the understanding of the materials.

Chapter 8

Cation Exchanges in $NaTaO_3$ and $NaNbO_3$

8.1 Introduction

Magnetoelectric multiferroic materials are phases in which the properties of ferroelectricity and ferromagnetism are combined and coupled. The search for these materials is driven by the prospect of tuning the magnetic polarization with an electric field or the electric polarization with a magnetic field, giving an extra degree of freedom which is then available for information storage and/or the construction of multifunctional devices.[5,118,119] Magnetoelectric multiferroic materials however, remain a synthetic challenge because in the majority of systems the requirements for having one or the other constituent property appear to be mutually exclusive.[5] In order for a material to exhibit ferroelectricity, it must have a non-centrosymmetric structure. However, the vast majority of inorganic solids possess centrosymmetric structures due to the high energetic favourability of symmetric packing schemes.

Metallic cations with d^0configurations, or ns^2 "lone-pair" configurations (by means of a Second-Order Jahn-Teller (SOJT) distortion, discussed in Section 1.1.1) can break the symmetry of the coordination polyhedra by removing the centre of inversion in these localities; leading, in principle, to non-centrosymmetric structures. However, these species do not have unpaired electrons (and therefore do not contribute with a net magnetic moment), and crystallizing non-centrosymmetric structural units in a way that they align to yield a ferroelectric polarization rather than antialigning to eliminate it, requires further structural constraints. Antialigning any distortion present to recover the inversion symmetry of the extended lattice seems to be energetically favoured in a solid.

The conventional approach to prepare magnetoelectric multiferroic ABO_3 perovskite materials uses a 'composite' strategy in which non-spherical cations (*e.g.* ns^2 post-

transition metal cations) occupy the A-sites of a magnetic lattice formed by strongly interacting magnetic cations on the B-sites. The majority of interesting magnetoelectric multiferroic candidates has been prepared through this approach, an example is $BiFeO_3$.[120-123] In contrast, the alternative case where magnetic cations are located on the A-sites of the perovskite structure and symmetry-breaking non-spherical cations are located on the B-sites has not been extensively studied. The lack of suitably large, paramagnetic monovalent or divalent cations, suggests that any perovskite phase in this class would not be thermodynamically stable. Thus, the aim of this work is to explore a synthetic strategy to prepare this class of magnetoelectric multiferroic materials. The strategy consists in introducing d^n magnetic cations via topochemical cation exchange in the A-sites of the perovskite phases $NaNbO_3$ and $NaTaO_3$ in which the d^0 cations Nb^{5+} and Ta^{5+} shift off-centre within their coordination octahedra.

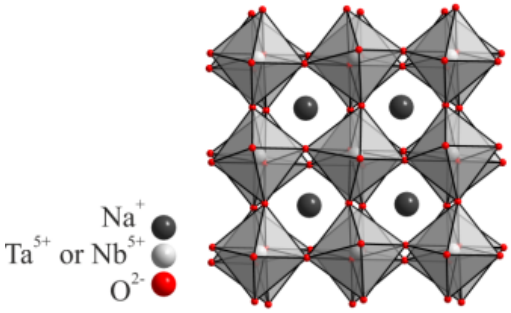


Figure 8.1. The structure of the perovskites $NaBO_3$ (B = Nb^{5+}, Ta^{5+}).

As highlighted in Section 1.3.2, cations tend to be tightly bound within their oxide coordination polyhedra in complex-oxide phases so that they are normally effectively immobile under the 'soft' reaction conditions required to access thermodynamically metastable phases. However, under suitable conditions, large monovalent cations can participate in exchange reactions in which they are replaced by other, smaller ions. This has been reported for Ruddlesden-Popper phases such as $Na_2La_2Ti_3O_{10}$ in which smaller divalent Co^{2+} cations can be inserted within the perovskite layers with retention of the Ruddlesden-Popper framework as shown in Figure 8.1.[49]

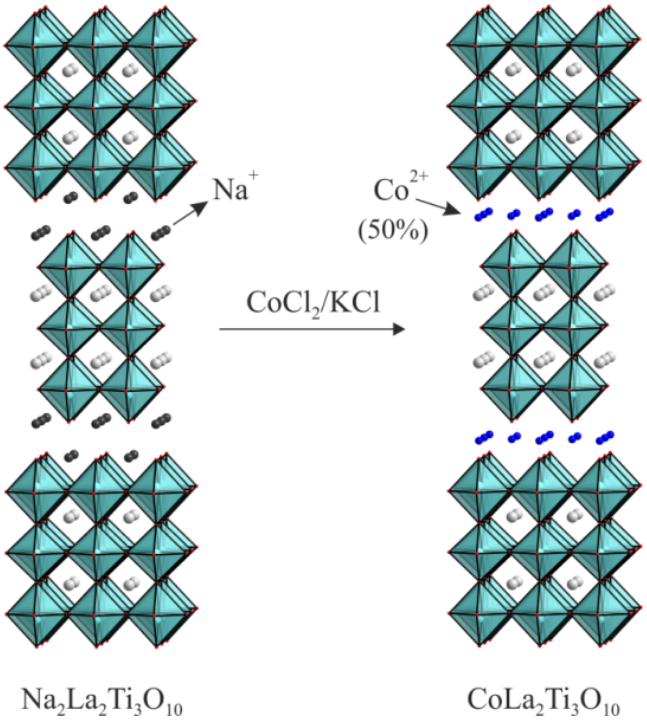


Figure 8.2. Reaction of the Ruddlesden-Popper phase $Na_2La_2Ti_3O_{10}$ with $CoCl_2$. The Co^{2+} substitutes in half the tetrahedral interlayer Na^+ sites.[49]

Similar with the example of Figure 8.2, in the $NaNbO_3$ and $NaTaO_3$ perovskite structures, the motion of the Na^+ cations in the A-sites is expected to take place before that of the smaller highly charged d^0 cations Nb^{5+} and Ta^{5+} which constitute the BO_n framework. Therefore exchanges with divalent transition-metal cations such as Ni^{2+} and Cu^{2+} were attempted. Such cation exchange reactions yielded phases $Na_{1-2x}M_xBO3$ (M = Ni^{2+}, Cu^{2+}; B = Ta^{5+}, Nb^{5+}), however, the formation of these phases requires extended reaction times, of the order of weeks. This large timescale is not surprising as cation exchange reactions in complex transition metal oxides are kinetically controlled, and are limited by the mobility of the ingoing and outgoing cations to be exchanged as well as the displacements that the host phase can allow in order to favour the mobile ions to diffuse.[124] While expansion of the separation between layers is possible in layered compounds such as the Ruddlesden-Popper phase $Na_2La_2Ti_3O_{10}$, the $NaNbO_3$ and $NaTaO_3$ perovskite structures contain three-dimensional networks in which lattice strain is not easily relieved. In addition, the lengths over which the species have to diffuse (several microns) make the cation exchange process particularly slow.

8.2 Experimental

8.2.1 Synthesis of $NaNbO_3$ and $NaTaO_3$

The host materials $NaNbO_3$ and $NaTaO_3$ were prepared via the ceramic method previously described by Mitchell *et al.*[125] Suitable stoichiometric ratios of Na_2CO_3 (99.997%) and Nb_2O_5 (99.999%, dried at 900 ºC) or Ta_2O_5 (99.993 %), were thoroughly mixed in an agate pestle and mortar. The mixtures were heated in air at 900 °C to decompose the carbonate and then reground and pressed into 13 mm pellets and heated for 2 periods of 24 h at 1000 °C in air, with intermediate regrinding. The resulting materials were observed to be single phases by X-ray powder diffraction, with lattice parameters that are in good agreement with literature values ($NaNbO_3$, space group *Pbcm*, a = 5.504(1) Å, b = 5.568(1) Å, c = 15.517(1) Å; $NaTaO_3$, space group *Pbnm*, a = 5.480(1) Å, b = 5.525(1) Å, c = 7.794(1) Å).[125,126]

8.2.2 Preparation of Anhydrous $NiCl_2$ and $CuCl_2$

Anhydrous $NiCl_2$ and $CuCl_2$ were obtained from the hydrated chlorides ($NiCl_2{\cdot}6H_2O$ Alfa Aesar, 99.95% and $CuCl_2{\cdot}xH_2O$ (x ≈ 2) Alfa Aesar, 99.999%) through a slow drying process under an argon flow. As described in Section 2.3.1, the hydrated materials were heated at temperatures found from thermogravimetric analysis 280 ºC and 180 ºC (for $NiCl_2$ and $CuCl_2$ respectively). The anhydrous chloride was then transferred and stored in an argon filled glove box without exposure to air, and X-ray powder diffraction along with TGA data collected to confirm the efficacy of the drying procedure.

8.2.3 Synthesis of $Ni_{0.5}TaO_3$ and $Cu_{0.5}TaO_3$ Phases

$Ni_{0.5}TaO_3$ phases were prepared via cation exchange reactions. To investigate the reactivity of the system, 10:1 molar ratios of $NiCl_2/NaTaO_3$ with a total mass of ~2g were ground together in an argon-filled glovebox, sealed in evacuated silica ampoules, and then heated at temperatures between 400 and 500 °C, with intermediate regrinding and resealing as required. After reaction, the NaCl produced in the reaction and excess $NiCl_2$ were removed from samples by washing in 1.2 M HCl and then distilled water. Products

were then filtered and dried in air at 75 °C. Caution: heating of incompletely dried $NiCl_2$ in sealed ampoules is an explosion hazard.

Samples for analysis by neutron powder diffraction were prepared by heating 10:1 molar ratios of $NiCl_2/NaTaO_3$ or $CuCl_2/NaTaO_3$ (based on a mass of 5 g $NaTaO_3$) at 450 °C for 6 periods of 7 days. All the samples were then washed and dried as described above.

8.2.4 Cation Exchanges in $NaNbO_3$

The 10:1 molar ratio of chloride to host used for the cation exchanges in $NaTaO_3$ was also used for the reactions with $NaNbO_3$. Reactions with the latter host were heated in the range $300 \leq T\ (ºC) \leq 450$ (using a 50 ºC step) to explore the reactivity. Progress of reaction was monitored via X-ray powder diffraction and samples were then washed and dried as described in Section 8.2.3.

8.3 Results

The X-ray powder diffraction data collected from the reaction mixtures between $NaTaO_3$ and the $NiCl_2$ and $CuCl_2$ suggest that the cation exchanges take place in this host phase, and are presented in Sections 8.3.1 and 8.3.2. Contrastingly however, the data collected from reaction mixtures between the host $NaNbO_3$ and $NiCl_2$ or $CuCl_2$ showed no evidence of reaction when heated at temperatures in the range $300 \leq T\ (ºC) \leq 350$. Washed products of reaction at these temperatures could be readily indexed using a model based on $NaNbO_3$. Meanwhile, data collected from mixtures heated at temperatures in the range $400 \leq T\ (ºC) \leq 450$ yielded products of reaction which could be readily indexed using a model based on Nb_2O_5, and the reported structure for the thermodynamic phase $NiNb_2O_6$ (when reactions were carried out with $NiCl_2$) or $CuNb_2O_6$ (when reactions were carried out with $CuCl_2$).

8.3.1 $Ni_{0.5}TaO_3$

8.3.1.1 Reaction chemistry of $Ni_{0.5}TaO_3$

X-ray powder diffraction data collected from the washed products of reaction between $NaTaO_3$ with $NiCl_2$ as a function of time, reveal a slow transformation from the orthorhombic $NaTaO_3$ to materials which could be indexed using the rhombohedral and cubic cells (space group *R*-3*c*; a = 5.48(2) Å, α = 55.73(3)º Figure 8.3). Prior to washing, weak, broad diffraction peaks attributed to NaCl were observed in the X-ray powder diffraction patterns collected from both reaction mixtures, consistent with the cation exchange described in the following reaction scheme:

$$NaBO_3\ (B = Ta^{5+}, Nb^{5+}) + x\ MCl_2\ (M = Ni^{2+}, Cu^{2+}) \xrightarrow[\text{7 days heating cycles}]{400 < T\ /\ ºC < 500} Na_{1-2x}M_xBO_3 + 2x\ NaCl \quad (8.1)$$

Reaction mixtures heated at 500 °C rapidly yielded $NiTa_2O_6$, a cation ordered rutile-type phase previously prepared via high temperature synthesis routes and presumed to be the thermodynamically most stable $Ni_xTa_{2x}O_{6x}$ phase.

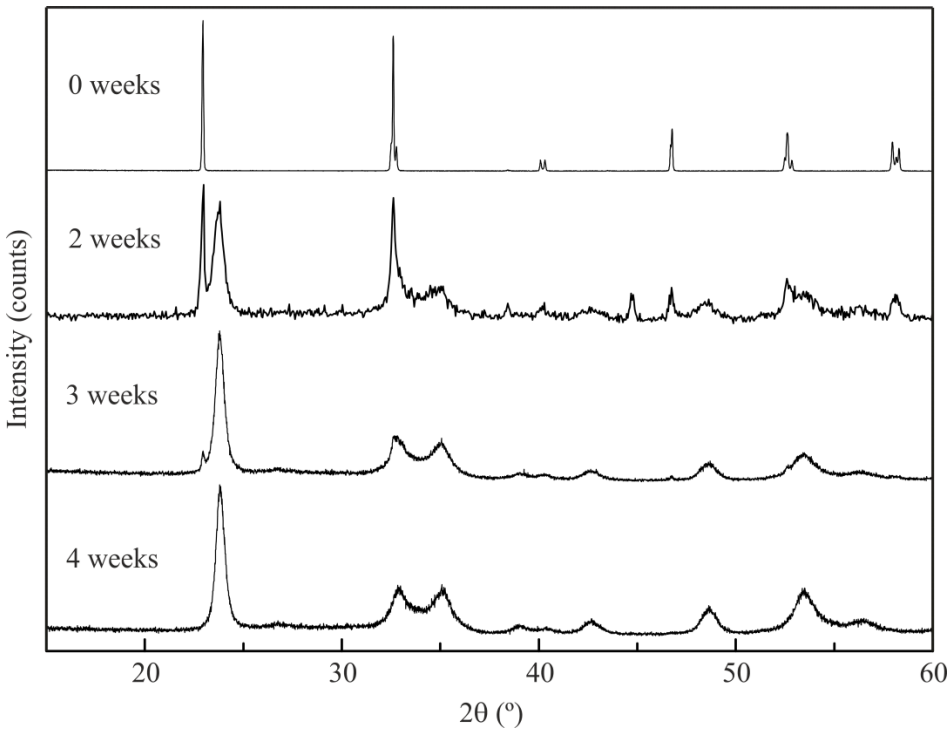


Figure 8.3. X-ray powder diffraction patterns collected from the washed products of reaction between $NaTaO_3$ and $NiCl_2$ at 450 °C, as a function of time.

8.3.1.2 Structural Characterization of $Ni_{0.5}TaO_3$

X-ray and neutron powder diffraction data collected from $Ni_{0.5}TaO_3$ (product after 4 weeks of reaction with intermediate regrinding, and then washed in dilute acid) could be readily indexed into a rhombohedral cell with a = 5.48(2) Å, α = 55.73 (3)º, similar to that reported for the high-temperature paraelectric phase of $LiTaO_3$. Therefore, the *R-3c* model adopted by $LiTaO_3$ was constructed with each lithium atom replaced by 0.5 Ni atoms, and then refined against the neutron diffraction data collected from $Ni_{0.5}TaO_3$ at 298 K. The refinement proceeded smoothly; however, the fit between the model and the data was very poor (χ^2 = 9.12). Close inspection of the data indicated there are some weak diffraction peaks that cannot be indexed into a unit cell with a rhombohedral symmetry. The crystallographic symmetry was in fact triclinic (Figure 8.4, bottom). A new model was thus constructed by transposing the atoms from the rhombohedral model into a triclinic cell of the same volume but with space group *P-1*. A significantly better fit to the data was achieved by using the new model (χ^2 = 4.088). In the end of the refinement, the occupancies of the nickel site were set to be refined freely, which did not lead to significant deviations from 25% occupation, consistent with the stated $Ni_{0.5}TaO_3$ composition. Observed, calculated and difference plots from the final refinement are shown in Figure 8.4 (bottom) with details of the refined model in Table 8.1 and selected bond lengths, angles and the bond valence sums (BVS) in Table 8.2.

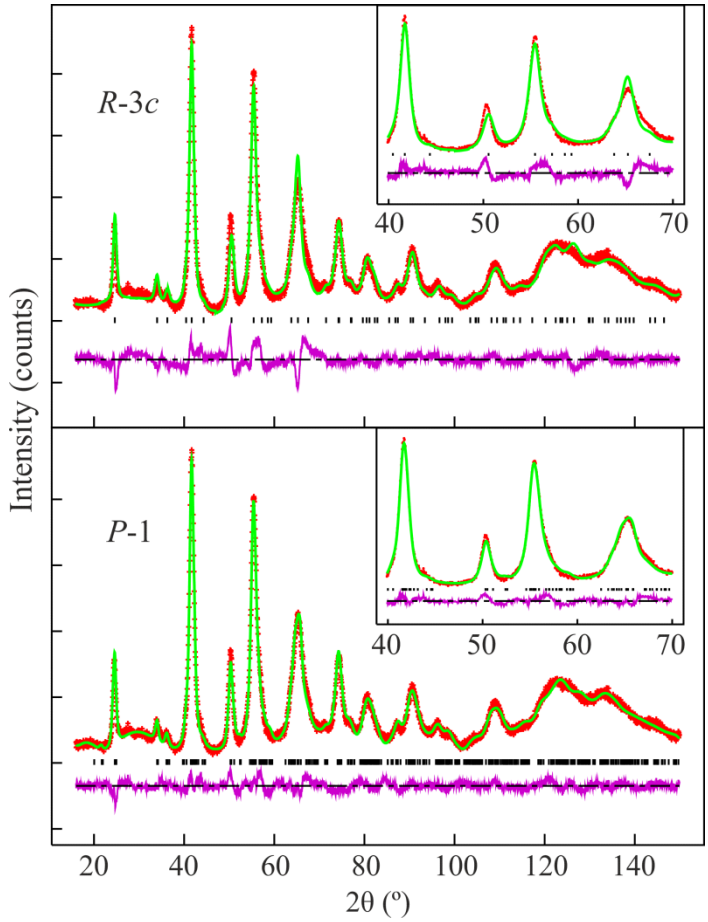


Figure 8.4. Observed, calculated, and difference plots for refinement of structural models in space group *R*-3*c* (top; $\chi^2 = 9.12$) and *P*-1 (bottom; $\chi^2 = 4.088$) against neutron powder diffraction data collected from $Ni_{0.5}TaO_3$ at 298 K using the D2B instrument, ILL neutron source.

Table 8.1. Structure of $Ni_{0.5}TaO_3$ refined against neutron powder diffraction data collected at 298 K using the D2B instrument, ILL neutron source.

Atom	Wyck.	*x*	*y*	*z*	Fraction	U_{iso} (Å^2)
Ta(1)	*1a*	0	0	0	1	0.019(1)
Ta(2)	*1h*	½	½	½	1	0.019(1)
Ni(1)	*2i*	0.352(4)	0.289(5)	0.288(3)	0.26(1)	0.0056(2)
Ni(2)	*2i*	0.146(5)	0.231(4)	0.170(5)	0.25(1)	0.0056(2)
O(1)	*2i*	0.862(2)	0.628(2)	0.284(2)	1	0.0018(6)
O(2)	*2i*	0.625(2)	0.253(3)	0.867(2)	1	0.0018(6)
O(3)	*2i*	0.241(2)	0.871(2)	0.624(3)	1	0.0018(6)
$Ni_{0.5}TaO_3$: space group *P-1*; $a = 5.470(1)$ Å, $b = 5.498(1)$ Å, $c = 5.507(1)$ Å, $\alpha = 55.69(1)$ °, $\beta = 56.19(1)$ °, $\gamma = 55.31(1)$ °, $V = 105.5(9)$ Å^3. $\chi^2 = 4.088$; $wR_p = 3.38\%$, $R_p = 2.63\%$.						

Table 8.2. Selected bond lengths, angles and bond valence parameters (Section 2.9) from the refined structure of $Ni_{0.5}TaO_3$ at 298 K.

Cation	Anion	Bond length (Å)	BVS
Ta(1)	O(1)x2	2.009(19)	Ta+4.75
	O(2)x2	2.020(19)	
	O(3)x2	1.989(18)	
Ta(2)	O(1)	1.963(17)	Ta+5.44
	O(2)	1.959(20)	
	O(3)	1.945(18)	
Ni(1)	O(1)	2.161(27)	Ni+1.63
	O(1)	2.234(26)	
	O(2)	2.111(29)	
	O(2)	2.149(31)	
	O(3)	2.214(32)	
	O(3)	1.993(24)	
Ni(2)	O(1)	2.042(29)	Ni+1.56
	O(1)	2.180(33)	
	O(2)	2.266(31)	
	O(2)	2.011(33)	
	O(3)	2.221(30)	
	O(3)	2.286(29)	
Bond angles:			
Ta(1)-O(1)-Ta(2)	143.9(5) º		
Ta(1)-O(2)-Ta(2)	142.6(6) º		
Ta(1)-O(3)-Ta(2)	142.9(5) º		

8.3.1.3 Magnetic Characterisation of $Ni_{0.5}TaO_3$

Both the Ni^{2+} and the Cu^{2+} exchanged samples became paramagnetic with magnetic susceptibilities that increased as the cation exchange reactions progressed. The magnetisation data collected from $Cu_{0.5}TaO_3$ is discussed in Section 8.3.2.3.

8.3.1.3.1 Magnetisation Data of $Ni_{0.5}TaO_3$

Magnetization data collected as a function of temperature from $Ni_{0.5}TaO_3$ (Figure 8.5) could be fitted to the Curie−Weiss law in the temperature range $15 \leq T\ (K) \leq 300$. The extracted Curie constants (C = 0.567(1) $cm^3\ K\ mol^{-1}$) is consistent with the maximum expected value of 0.5 × S = 1 Ni^{2+} centres per formula unit, confirming the stated $Ni_{0.5}TaO_3$ composition.

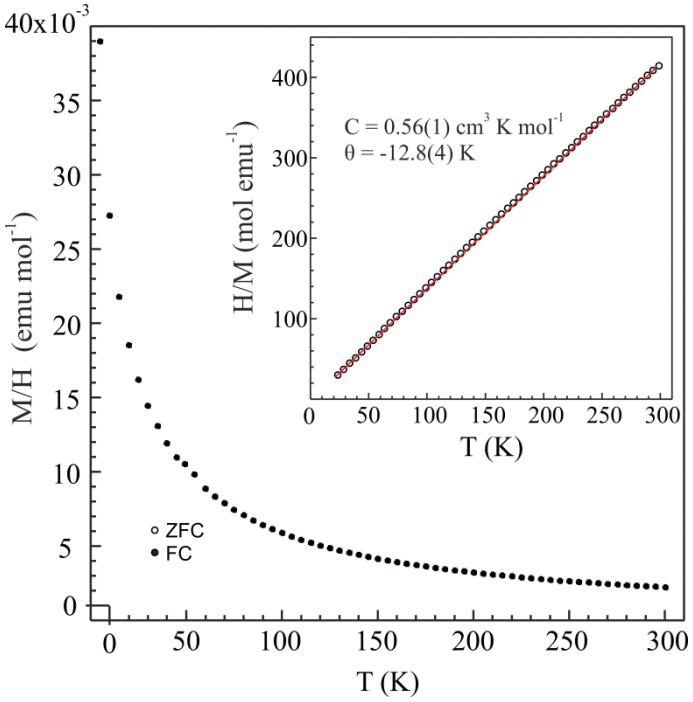


Figure 8.5. Magnetization data collected from $Ni_{0.5}TaO_3$ in an applied field of 100 Oe. The fit to the Curie-Weiss law is shown in the inset.

8.3.1.3.2 Neutron Powder Diffraction collected at 5 K

Neutron powder diffraction data collected from $Ni_{0.5}TaO_3$ at 5 K could be refined using an identical triclinic *P-1* structural model to that used for the refinement of data collected at 298 K as shown in Figure 8.6. The unfitted peaks in the range $40 \leq 2\theta\ (^o) \leq 50$ are contributions from the cryostat. No obvious magnetic scattering peaks were observed, indicating the absence of long range magnetic order.

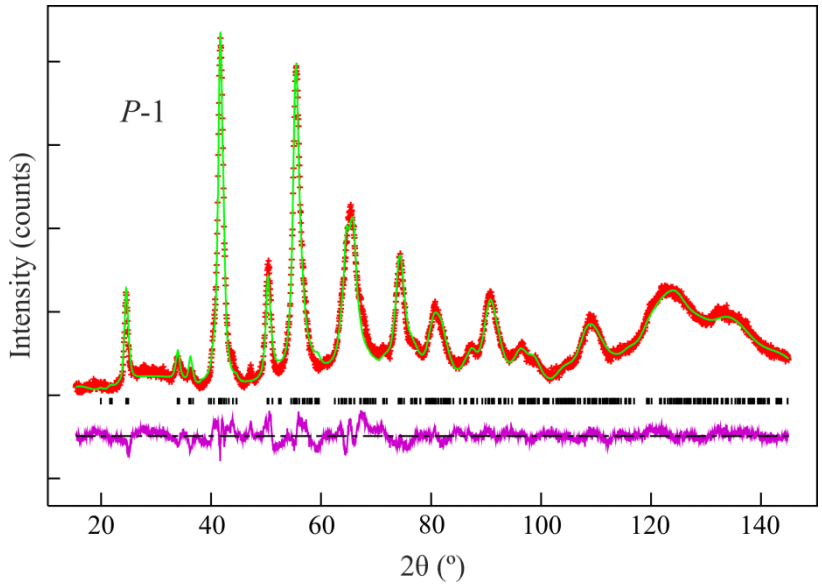


Figure 8.6. Observed, calculated, and difference plots for refinement of the structural model in space group *P-1* (a = 5.468(1) Å, b = 5.481(1) Å, c = 5.501(1) Å, α = 55.68(1)°, β = 56.17(1)°, γ = 55.29(1)°) against neutron powder diffraction data collected from $Ni_{0.5}TaO_3$ at 5 K using the D2B instrument, ILL neutron source. The features at 2θ = 47.2°, 71.2° correspond to reflections from the cryostat. χ^2 = 4.035, *wRp* = 3.43%, *Rp* = 2.61%.

8.3.2 $Cu_{0.5}TaO_3$

8.3.2.1 Reaction chemistry of $Cu_{0.5}TaO_3$

Similarly, X-ray powder diffraction data collected from the washed products of reaction between $NaTaO_3$ with $CuCl_2$ as a function of time reveal a slow transformation from the orthorhombic $NaTaO_3$ to materials which could be indexed using a cubic unit cell with a = 7.55(2) Å (Figure 8.7). This suggests a cation exchange reaction similar to that between $NaTaO_3$ with $NiCl_2$ (Section 8.3.1.1). Reaction mixtures heated at 500 °C rapidly yielded the thermodynamically most stable $CuTa_2O_6$ phase.

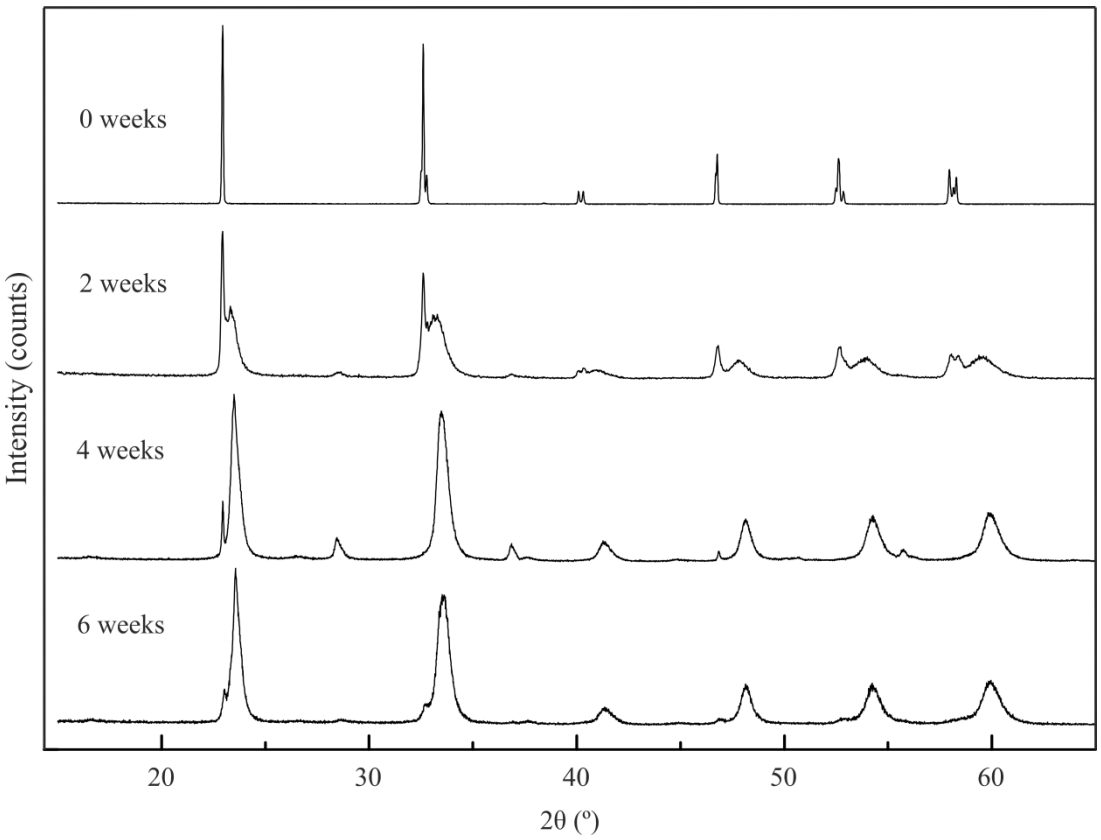


Figure 8.7. X-ray powder diffraction patterns collected from the washed products of reaction between $NaTaO_3$ and $CuCl_2$ at 450 °C, as a function of time.

8.3.2.2 Structural Characterisation of $Cu_{0.5}TaO_3$

The X-ray powder diffraction data collected from $Cu_{0.5}TaO_3$ (produced after 6 weeks of reaction with intermediate regrinding, and then washed in dilute acid) could be indexed into a cubic unit cell in space group *Pm*-3. However, neutron powder diffraction data collected at 298 K revealed that the structure of $Cu_{0.5}TaO_3$ adopts a lower symmetry since some diffraction features cannot be described in *Pm*-3 (as marked with the arrows in Figure 8.8). An orthorhombic model in space group *Pmmm* (a = 7.545(4) Å, b = 7.561(3) Å, c = 5.527(2) Å) was thus constructed and refined against the data. This *Pmmm* model leads to a better fit (χ^2 = 6.465) with respect to the cubic *Pm-3* model (χ^2 = 5.120). Similarly, the occupancies of the copper site were set to be refined freely in the end of the refinement, which did not lead to significant deviations from 25% occupation, consistent with the stated $Cu_{0.5}TaO_3$ composition. Observed, calculated and difference plots from the final refinement are shown in Figure 8.8 with details of the refined model in Table 8.3 and elected bond lengths, angles and the bond valence sums (BVS) in Table 8.4.

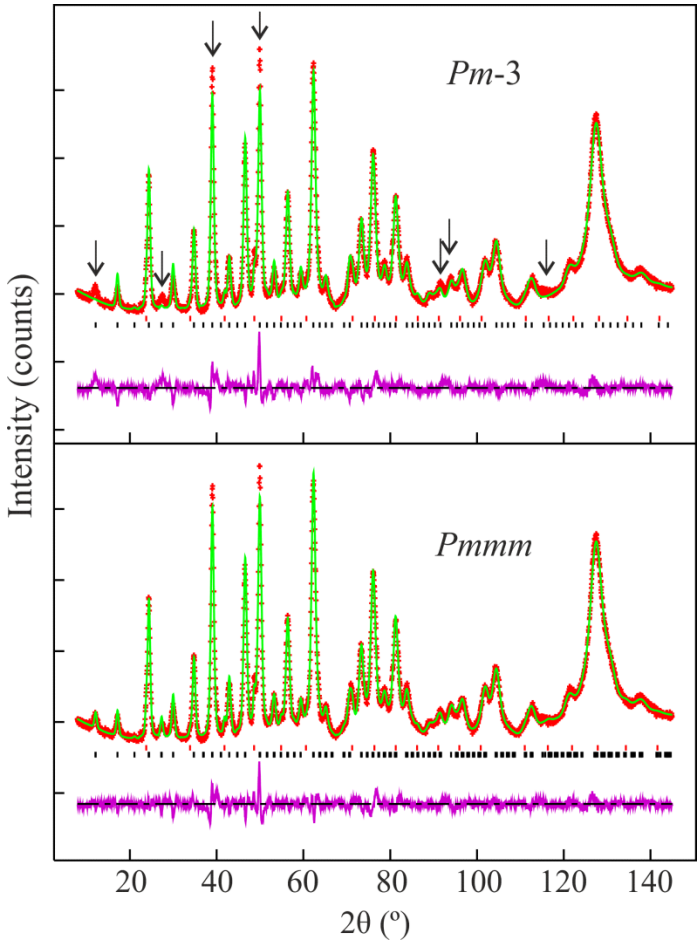


Figure 8.8. Observed, calculated, and difference plots for refinement of structural models in space group *Pm-3* (top; χ^2 = 6.465) and *Pmmm* (bottom; χ^2 = 5.120) against neutron powder diffraction data collected from $Cu_{0.5}TaO_3$ at 298 K using the D2B instrument, ILL neutron source. Red tick marks correspond to a 6.17(3) % by weight of starting material $NaTaO_3$.

Table 8.3. Structure of $Cu_{0.5}TaO_3$ refined against neutron powder diffraction data collected at 298 K using the D2B instrument, ILL neutron source.

Atom	Wyck.	*x*	*y*	*z*	Fraction*	U_{iso}(Å^2)
Ta(1)	*8@*	0.250(2)	0.248(2)	0.250(1)	1	0.018(1)
Cu(1)	*1b*	½	0	0	0.72(1)	0.0023(5)
Cu(2)	*1e*	0	½	0	0.70(1)	0.0023(5)
Cu(3)	*1c*	0	0	½	0.71(1)	0.0023(5)
Cu(4)	*1f*	½	½	0	0.36(2)	0.0023(5)
Cu(5)	*1d*	½	0	½	0.32(2)	0.0023(5)
Cu(6)	*1g*	0	½	½	0.33(2)	0.0023(5)
O(1)	*4u*	0	0.295(1)	0.188(3)	1	0.0029(3)

O(2)	*4w*	0.186(3)	0	0.310(3)	1	0.0029(3)
O(3)	*4y*	0.298(3)	0.205(2)	0	1	0.0029(3)
O(4)	*4v*	0.5	0.196(2)	0.318(4)	1	0.0029(3)
O(5)	*4x*	0.304(3)	0.5	0.190(4)	1	0.0029(3)
O(6)	*4z*	0.189(5)	0.318(3)	0.5	1	0.0029(3)
$Cu_{0.5}TaO_3$: space group *Pmmm*; a = 7.545(1) Å, b = 7.561(1) Å, c = 5.527(2) Å; V = 429.5(5) Å^3. weight fraction: 93.83(2)%						
$NaTaO_3$: space group *Pbnm*; a = 5.484(3) Å, b = 5.525(3) Å, c = 7.795(2) Å; weight fraction: 6.17(3)%						
χ^2 = 5.120; wR_p = 4.42%, R_p = 3.40%						

Table 8.4. Selected bond lengths, angles and bond valence sums (Section 2.9) from the refined structure of $Cu_{0.5}TaO_3$ at 298 K.

Cation	Anion	Bond length (Å)	BVS
Ta(1)	O(1)	1.954(21)	Ta+5.10
	O(2)	1.997(24)	
	O(3)	1.943(15)	
	O(4)	1.990(22)	
	O(5)	1.991(24)	
	O(6)	2.008(17)	
Cu(1)	O(3) x 4	1.955(25)	Cu+1.90
Cu(2)	O(1) x 4	1.954(22)	Cu+1.90
Cu(3)	O(2) x 4	1.957(25)	Cu+1.87
Cu(4)	O(5) x 4	1.992(30)	Cu+1.72
Cu(5)	O(4) x 4	1.977(29)	Cu+1.79
Cu(6)	O(6) x 4	1.975(32)	Cu+1.80
Bond angles:			
$Cu_{0.5}TaO_3$			
Ta(1)-O(1)-Ta(1)	151.5(14) º		
Ta(1)-O(2)-Ta(1)	141.1(13) º		
Ta(1)-O(3)-Ta(1)	151.2(11) º		
Ta(1)-O(4)-Ta(1)	141.2(20) º		

Ta(1)-O(5)-Ta(1)	141.1(13) º
Ta(1)-O(6)-Ta(1)	140.9(19) º
$NaTaO_3$	
Ta(1)-O(1)-Ta(1)	159.3(15) º
Ta(1)-O(2)-Ta(1)	160.8(16) º

8.3.2.3 Magnetic Characterisation of $Cu_{0.5}TaO_3$

8.3.2.3.1 Magnetisation Data

Figure 8.9 shows the magnetization data collected from $Na_{1-2x}Cu_xTaO_3$ as a function of temperature. The data could be fitted to the Curie−Weiss law in the temperature range $20 \leq T\ (K) \leq 300$. The extracted Curie constant in this case is $C = 0.188(1)$ cm^3 K mol^{-1} which corresponds to 0.502, S = 1/2, Cu^{2+} centres per formula unit. Thus the proposed formula for this material can be $Cu_{0.5}TaO_3$.

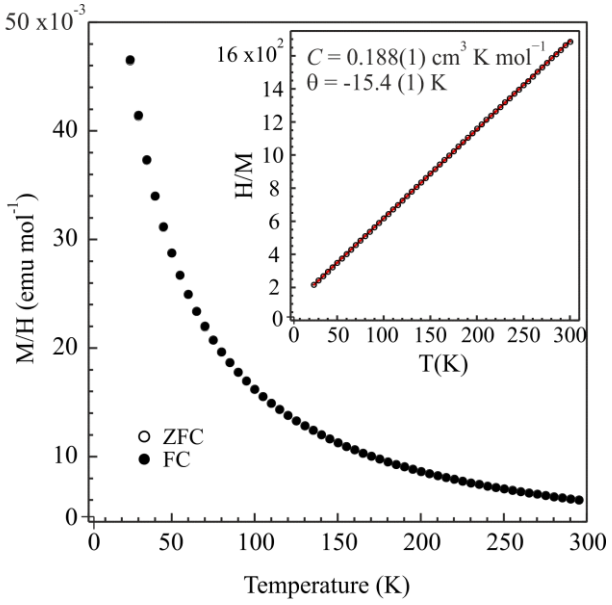


Figure 8.9. Magnetization data collected from $Cu_{0.5}TaO_3$ in an applied field of 100 Oe. The fit to the Curie-Weiss law is shown in the inset.

A small divergence between the zero-field-cooled field-cooled plots for $Cu_{0.5}TaO_3$ was observed in the low temperature range $5 \leq T\ (K) \leq 20$. This divergence results in a deviation from the Curie-Weiss law in this temperature region and is consistent with

weak hysteresis observed in the isotherm collected at 5 K as shown in Figure 8.10. Zero-field-cooled (ZFC) and field-cooled (FC) magnetisation measurements, carried out in small temperature steps in range $8 \leq T\ (K) \leq 25$, reveals a small deviation between the ZFC and FC data in this temperature range (Figure 8.11).

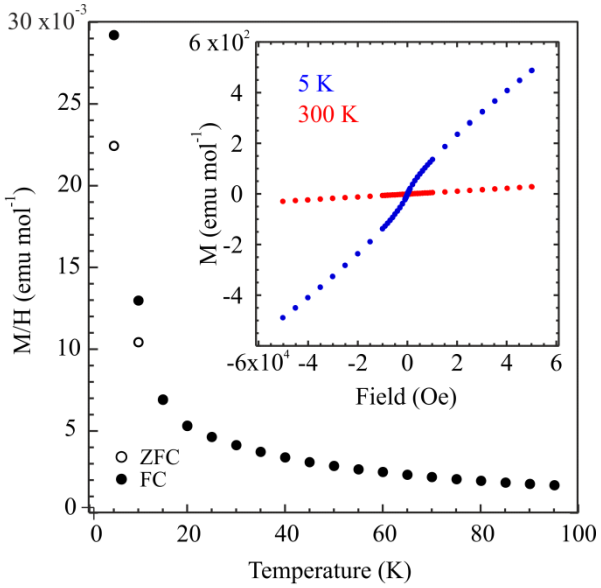


Figure 8.10. Extended range in the low temperature region of the magnetisation data collected from $Cu_{0.5}TaO_3$ in an applied field of 100 Oe. The isotherms collected at 300 K and 5 K are shown in the inset.

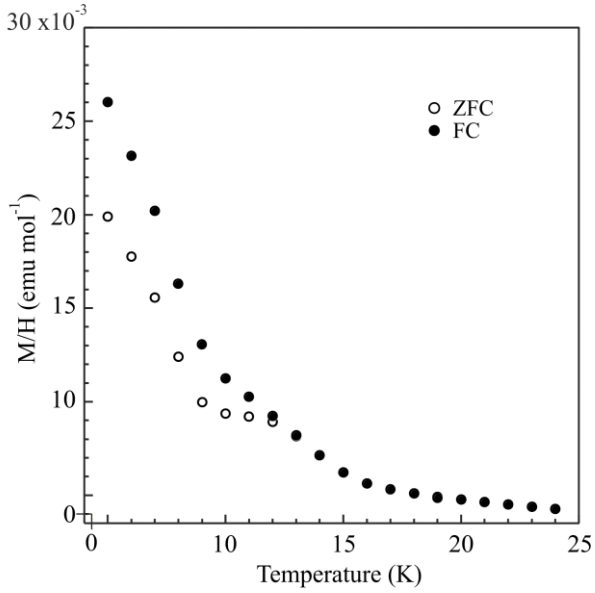


Figure 8.11. Expanded region ($5 \leq T\ (K) \leq 25$) of the magnetization data collected from $Cu_{0.5}TaO_3$ during a high resolution zfc-fc experiment in an applied field of 100 Oe.

8.3.2.3.2 Neutron Powder Diffraction Collected at 5 K

Neutron powder diffraction data collected from $Cu_{0.5}TaO_3$ at 5 K showed no clear additional diffraction features relative to analogous data collected at 298 K (Figure 8.12), indicating the absence of long range magnetic order.

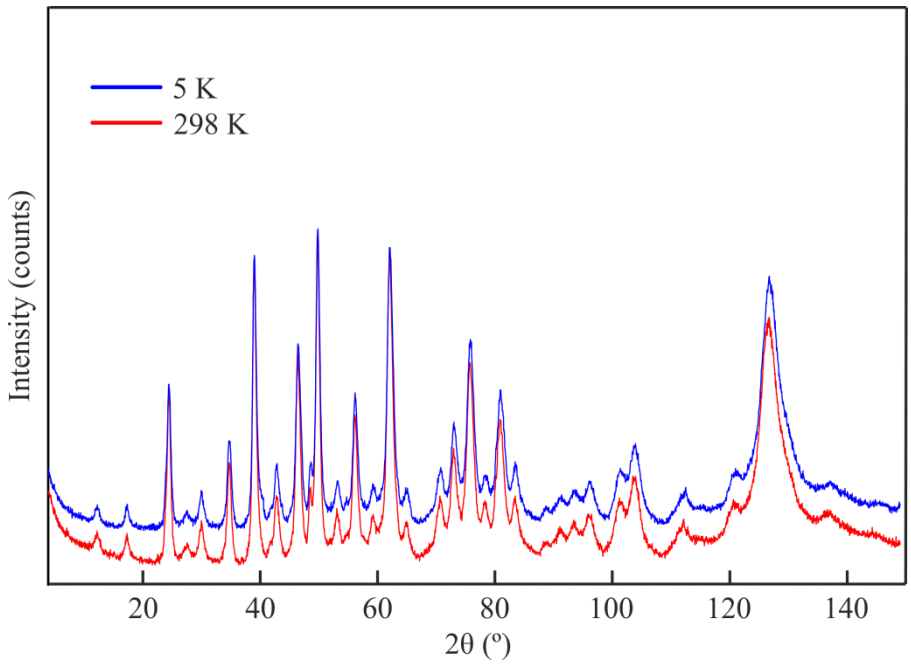


Figure 8.12. Neutron powder diffraction data collected from $Cu_{0.5}TaO_3$ at 298 K (bottom) and 5 K (top).

8.4 Discussion

8.4.1 Topochemical Cation Exchange Reactions

The X-ray and neutron powder diffraction data show that reaction between $NaTaO_3$ and $NiCl_2$ leads to the formation of the metastable phase $Ni_{0.5}TaO_3$ via a very slow topochemical cation-exchange process in which two Na^+ cations are replaced by a single Ni^{2+} cation, while the apex-linked network of TaO_6 octahedra present in $NaTaO_3$ is conserved. The topochemical cation exchange reaction between $NaTaO_3$ and $CuCl_2$ behaves in a similar way. Raising the reaction temperature above 500 °C or annealing washed samples at this temperature, results in the rapid formation of $NiTa_2O_6$, the trirutile, thermodynamically stable form of "$Ni_{0.5}TaO_3$". This suggests that this is the

temperature above which the Ta−O framework breaks down and is likely to be the temperature limit for all topochemical reactions involving $ATaO_3$ perovskite frameworks.

The cation exchange reaction conditions which lead to the formation of $Ni_{0.5}TaO_3$ and $Cu_{0.5}TaO_3$ in $NaTaO_3$ lead to a rearrangement of the $NaNbO_3$ host phase to form mixtures of Nb_2O_5 and the reported thermodynamically stable phases MNb_2O_6 (M = Ni or Cu depending on the chloride used). This suggests that the Nb-O framework in $NaNbO_3$ is mobile at the reaction conditions studied. This result is consistent with the oxygen *2p* orbitals overlapping more efficiently with the tantalum *5d* orbitals compared to the niobium *4d* orbitals. The Ta-O bonds in $NaTaO_3$ are expected to be stronger with respect to the Nb-O bonds in $NaNbO_3$. Thus, while the $NaTaO_3$ host is more robust and can yield cation exchanges under accessible reaction conditions, for $NaNbO_3$ the displacements needed for accommodating Ni^{2+} or Cu^{2+} cations compete with a reorganization of the atoms to form thermodynamically stable products at the temperatures studied.

8.4.2 The Structural Change on Cation Exchange Reaction from $NaTaO_3$ to $Ni_{0.5}TaO_3$

The smaller ionic radius of Ni^{2+} compared to Na^+ (Ni^{2+} radius = 0.69 Å; Na^+ radius = 1.02 Å) leads to a large distortion in the Ta−O−Ta framework on cation exchange, in which the rigid TaO_6 octahedra rotate in a cooperative manner to convert the 12-coordinate sodium site present in $NaTaO_3$ into two pseudo-octahedral sites analogous to those observed in the ReO_3 lattice upon lithiation (Section 1.3.2, Figure 1.15). The distorted A-sites in $Ni_{0.5}TaO_3$ are shown in Figure 8.13.

The cation exchange reaction leads to a contraction in the lattice volume of 10.5%, a tightening of the Ta−O−Ta bond angles from an average of 159.2° in $NaTaO_3$ to an average of 143.1° in $Ni_{0.5}TaO_3$, as well as a lowering of the lattice symmetry to triclinic. However, despite the large deformation of the tantalum-oxide lattice in the transformation from $NaTaO_3$ to $Ni_{0.5}TaO_3$, the nickel cations appear to be "under bonded" with bond valence sums (Table 8.2) of Ni+1.63 and Ni+1.56 for the two nickel sites. It should be noted however, that the A-site cations in the paraelectric phases $LiTaO_3$ (BVS = Li+0.793)[127] and $AgTaO_3$ (BVS = Ag+0.911)[128] are also under bonded.

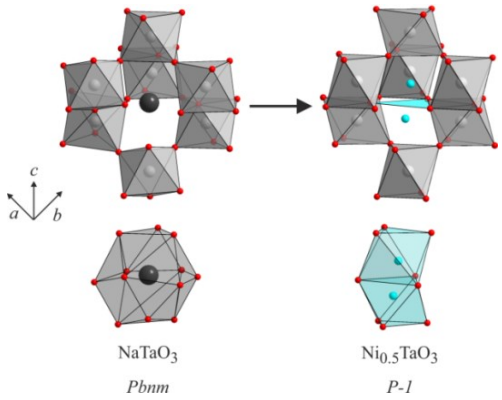


Figure 8.13. Schematic representation of the distortion of the A-sites in $NaTaO_3$ into the product $Ni_{0.5}TaO_3$.

8.4.3 Comparison Between $Ni_{0.5}TaO_3$ and $LiTaO_3$

The resulting tantalum-oxide framework in $Ni_{0.5}TaO_3$ is analogous to that observed for the paraelectric phase of $LiTaO_3$ (space group *R-3c*, Figure 8.4, top), consistent with the more similar ionic radii of Li^+ and Ni^{2+} (Li^+ radius = 0.76 Å). The major difference between the structure of paraelectric $LiTaO_3$ and $Ni_{0.5}TaO_3$ is that in the former phase the two "octahedral" sites derived from the perovskite A-site are 50% occupied by lithium, whereas in the latter phase, they are 25% occupied by nickel.

$LiTaO_3$ undergoes a structural transition to a polar ferroelectric structure (space group *R3c*) in which the lithium cations occupy only one of the two face-sharing "octahedral" A-cation sites (Figure 8.14). The displacement of the lithium cations in the A-sites in combination with the off-centring of the d^0 tantalum cations in the TaO_6 octahedral B-sites drives the net spontaneous electrical polarization observed in the material.

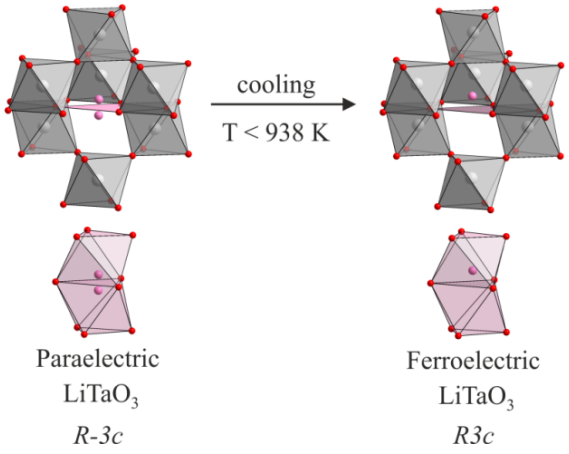


Figure 8.14. The paraelectric and ferroelectric structures of $LiTaO_3$.

In order to investigate whether $Ni_{0.5}TaO_3$ undergoes a symmetry-lowering structural transition from the refined structure *P-1* to a *P1* structure, in analogy to the structural transition of $LiTaO_3$ from *R-3c* to *R3c*, the neutron powder diffraction data collected at 5 K were refined using the non-centrosymmetric structural model *P1*. However, this refinement does not yield a better fit (χ^2 = 6.522) with respect to the centrosymmetric model in space group *P-1* (χ^2 = 4.025) used in the refinement of the data collected at room temperature. Therefore, no evidence was found for a structural transition in $Ni_{0.5}TaO_3$ to a ferroelectric polar phase upon cooling, and the centrosymmetric structure of the material at room temperature is consistent with the absence of any observable SHG activity.

This outcome is surprising given the similarity of the structure of $Ni_{0.5}TaO_3$ with that of $LiTaO_3$. In the ferroelectric $LiTaO_3$ phase, the displacement of the tantalum cations off centre in the octahedra TaO_6 yields lithium-oxygen separations that are shorter than the sum of the Li-O ionic radii.[129] One of the driving mechanisms for the combined displacements that yield the observed polarisation is the coupled motion of the lithium and oxygen ions moving away from each other. A comparison between the ferroelectric phases $LiTaO_3$, $KTaO_3$ and $Li_xK_{1-x}TaO_3$, shows that the magnitude of this coupled motion in which the cations in the A-sites move away from the oxygen anions, depends significantly on the size of the A-site cations. The smaller the A-site cations are, the greater the amplitude of their displacement with concomitant increased contribution to the resulting polarisation. It is possible that the absence of a structural transition in $Ni_{0.5}TaO_3$ is a consequence of the difference in the ionic radius between Ni^{2+} and Li^+ (Ni^{2+} radius = 0.69 Å; Li^+ radius = 0.60 Å).[114] More importantly, it is expected for the motion of a d^n cation to occur through significantly different mechanisms with respect to more "spherical" cations such as Li^+ or K^+.

Finally, in $Ni_{0.5}TaO_3$, the two "octahedral" sites derived from the perovskite A-sites are 25 % occupied by nickel (Table 8.1) as opposed to 50 % occupied in $LiTaO_3$ by lithium. This "dilution" of Ni^{2+} magnetic centres in the structure is consistent with the absence of observable magnetic order and could also mean that moderate displacements of the nickel centres are not possible to detect.

8.4.4 The structure of $Cu_{0.5}TaO_3$

The structure of $Cu_{0.5}TaO_3$ refined against neutron powder diffraction data is presented in Figure 8.15. This orthorhombic structure of space group *Pmmm* results from the tilt system $a^+b^+c^-$ of the octahedra TaO_6 in $NaTaO_3$. The results from SHG activity measurements are consistent with this centrosymmetric structural model (there was no observable measurable effect).

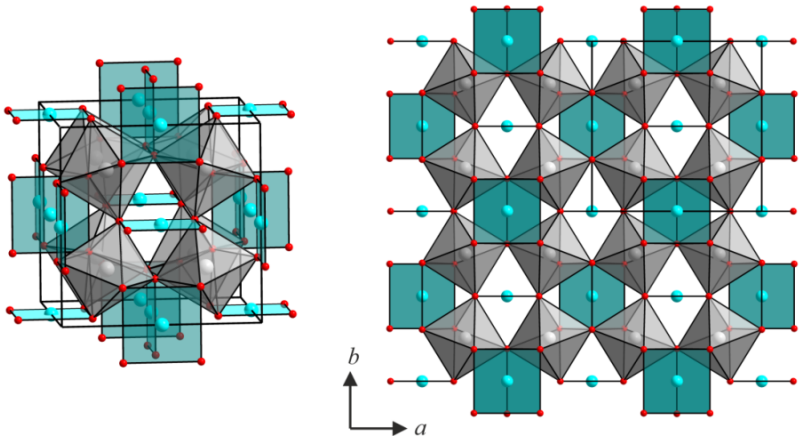


Figure 8.15. The structure of $Cu_{0.5}TaO_3$ (space group *Pmmm*) refined against neutron powder diffraction data.

Rather than taking the A-sites, the Cu^{2+} cations occupy 4-coordinate square planar sites located at the centre of the faces and edges of the new unit cell as schematised in Figure 8.15, (the atomic positions are outlined in Table 8.3); the channels formed by the A-sites along which the Cu^{2+} centres distribute, are depicted on the right. This structure is analogous to that of $Li_{0.75}WO_3$ which is the result from lithiation of WO_3 (Section 1.3.2, Figure 1.15).

The copper cations appear to be "under bonded" analogous to the case of nickel in $Ni_{0.5}TaO_3$ in this case with bond valence sums of a minimum value of Cu^+ 1.04 and a maximum value of Cu^+ 1.76 (Table 8.4). The Ta−O−Ta bond angles change from an average of 163.1° in the starting material $NaTaO_3$ to an average of 144.9° in the product $Cu_{0.5}TaO_3$ (Table 8.4).

Orthorhombic structures of space group *Pmmm* like the one refined for $Cu_{0.5}TaO_3$ has been reported for phases of composition $Cu_{1+x}Ta_2O_6$.[130] Thus, it is not clear from the final

product $Cu_{0.5}TaO_3$ that the cation exchange reaction carried out in this work takes place topochemically. However, the temperature found for the exchange reaction (T = 450 °C) is significantly lower with respect to those reported for the synthesis of phases $Cu_{1+x}Ta_2O_6$ (T ≥ 1000 ºC).[130-132] This observation suggests that temperature at which the cation exchange reaction takes place is well below the temperature necessary for the formation of $Cu_{0.5}TaO_3$ via reconstruction and rearrangement of the tantalum-oxide lattice. It is likely that the cation exchange reaction found in this work plays a mechanistic role in the formation of $Cu_{1-x}Ta_2O_6$ phases.

Although the cation exchange reaction was not complete, the refined weight fraction of the product was 93.83(2)% (Table 8.3). This is surprising given the aforementioned syntheses of $Cu_{1+x}Ta_2O_6$ phases are also reported to be technically challenging.

A detailed analysis of the low-temperature magnetic structure of $Cu_{0.5}TaO_3$ could not be performed but it is surprising that, in order for the phase to be magnetically ordered, interaction between the copper centres would be required. It is not straightforward how this interaction could take place via 2*p* orbitals of the oxygen anions and the distance from which they sit from each other in the structure seems too great for direct magnetic interaction (approximately 3.786 Å calculated from a crystallographic model of the refined structure).

8.4.5 Exchanges with Other Divalent Cations in $NaTaO_3$

In light of the success in the preparation of the phases $Ni_{0.5}TaO_3$ and $Cu_{0.5}TaO_3$, exchanges with other d^n metal cations were studied in this host. Using the established optimum reaction conditions exchanges with the cations Mn^{2+}, Fe^{2+} and Co^{2+} were carried out.

A series of reactions were performed using the corresponding anhydrous chloride in a 1:10 molar ratio $NaTaO_3$ to chloride and after 1 period of 7 days at 450°C, the corresponding thermodynamic products (MTa_2O_6, M = Mn^{2+}, Fe^{2+}, Co^{2+}) formed in all the reaction mixtures.

Exploratory reactions to determine the particular optimum temperatures for mobility of these other cations in $NaTaO_3$, were carried out in the range 300 ≤ T (ºC) ≤ 450 using

steps of 10 °C and periods of reaction of 7 days. X-ray powder diffraction data collected from reaction mixtures heated at temperatures in the range 300 ≤ T (ºC) ≤ 360 showed no observable changes in the lattice parameters of the original pseudo cubic unit cell of $NaTaO_3$ (space group *Pm-3m*; a_p = 3.89(3) Å). However from T = 370 ºC sharp peaks corresponding to phases MTa_2O_6, where M = Mn^{2+}, Fe^{2+} and Co^{2+}, were observed to appear.[133,134] Figure 8.17 shows the X-ray powder diffraction data collected from the washed product of reaction between $NaTaO_3$ with $CoCl_2$ during 1 period of 7 days. It can be observed that, while heating at 370 °C results in no observable changes in the host, an increment of 10 °C results in the clear reorganization to formation the thermodynamic product $CoTa_2O_6$ (Figure 8.16).

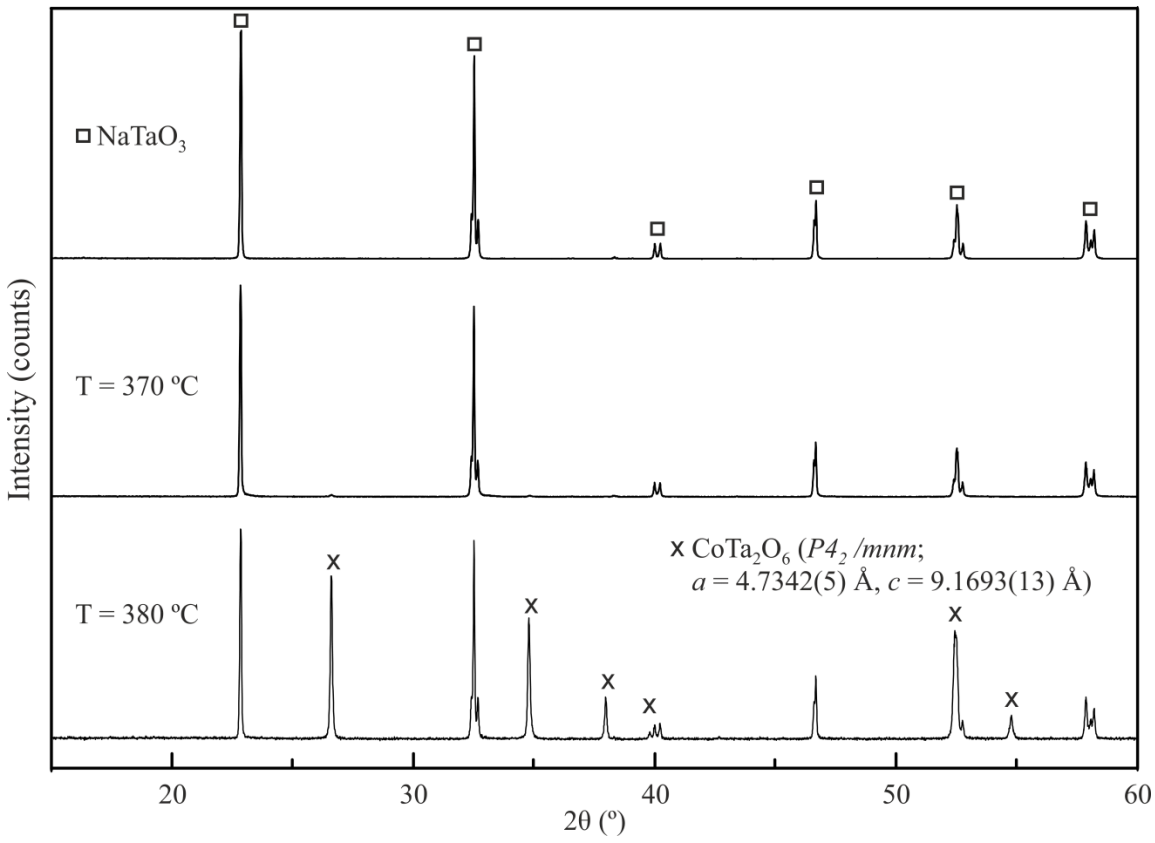


Figure 8.16. X-ray powder diffraction data collected from the washed product of reaction between $NaTaO_3$ and $CoCl_2$ carried out at 370 ºC and 380 ºC during 1 period of 7 days.

In particular, at 350°C after 3 periods of 7 days, the exchange with Co^{2+} gives way to a phase that could be approximately indexed as cubic with lattice parameter a = 7.63 Å (Figure 8.17).

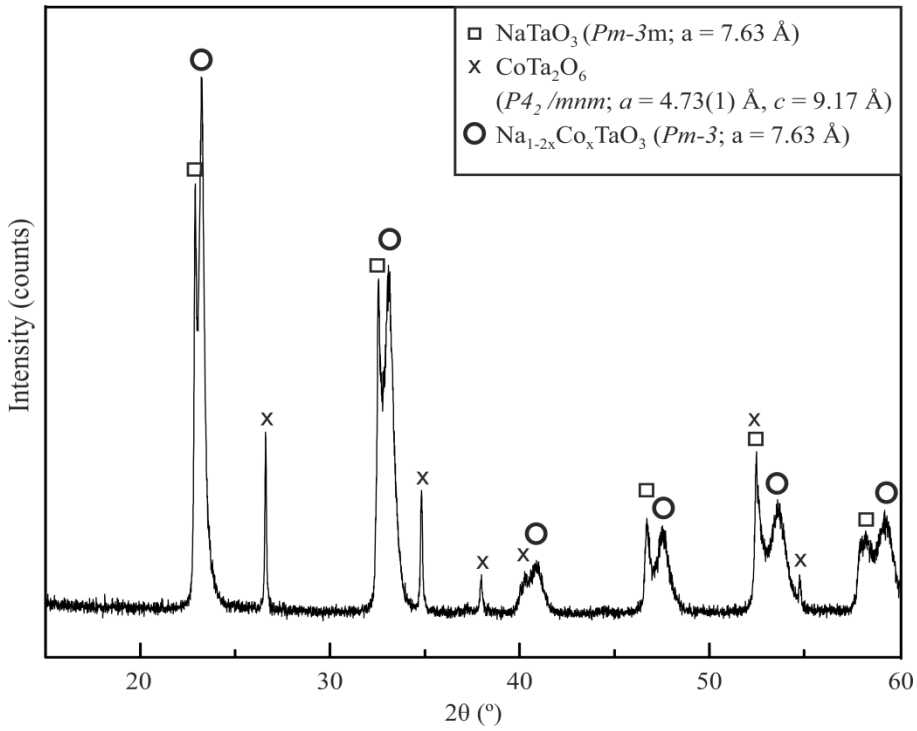


Figure 8.17. X-ray powder diffraction data collected from the reaction mixture of $NaTaO_3$ and $CoCl_2$ after 3 periods of 7 days at 350 ºC.

Longer times of reaction, however, also favoured the transformation of the observed cubic phase (potentially a topochemical phase $Na_{1-2x}Co_xNbO_3$) into the thermodynamic product $CoTa_2O_6$ (space group $P4_2/mnm$).[134] Furthermore, at higher temperatures of reaction the cubic product is not observed at all. This suggests that topochemical exchanges with Mn^{2+} and Fe^{2+} might also take place even when it has not been possible to observe them in the temperature and reaction windows explored. Observation of the metastable phases might be possible by using smaller and more precise temperature and time windows, however, if the formation of such kinetic products and the thermodynamically stable products are competing reactions (with comparable activation energies), kinetic control for these cation exchange reactions would not be possible.

8.4.6 Cation Exchange in Three Dimensional Perovskite Structures

It is worth noting that the cation exchange reactions studied in this work are normally expected to take place in layered or 'tunnel like' structures rather than in three dimensional perovskite structures. To the best of our knowledge, this is the first time that redox-neutral, topochemical cation-exchange reactions are used to insert paramagnetic cations into three-dimensional perovskite structures.[135]

The cation exchanges carried out in this work in the host $NaTaO_3$ show that host perovskite structures comprised of "flexible" networks that can allow significant displacements or distortions without destabilizing are good candidates for these topochemical processes.

The thermodynamics of exchange typically favour exchange between ions of comparable size, unless the hosts are readily expandable.[124] For the case of the three dimensional perovskite host phases studied in this work, the exchanged ions are of significantly different sizes and the displacements that the structures can take are limited by the B-O bond strength (as discussed for $NaNbO_3$), so substitution is not expected to be energetically viable. However, similar to the example previously given for the Ruddlesden-Popper phase $Na_2La_2Ti_3O_{10}$ in which the exchange Co^{2+} yields $CoLa_2Ti_3O_{10}$ (Figure 8.2) where the cobalt cations occupy half the tetrahedral interlayer sites, the cations that are exchanged in this work are of higher charges with respect to Na^+. This means that the vacancies in the A-sites are created as the reaction progresses. The cation transport in solids typically proceeds when an activated cation can hop into vacant sites through well-defined anion-bounded "bottle-necks".[136] Thus, although in three dimensional perovskite structures expansions similar to those in layered materials are not possible, the creation of vacancies in the A-sites favours the interdiffusion of cations and with this further cation exchange.

8.5 Conclusions

Cation exchanges of Na^+ for Ni^{2+} and Cu^{2+} were carried out topochemically in the three-dimensional perovskite-structure phase $NaTaO_3$.

Host phases comprised of robust yet "flexible" networks that can allow significant displacements or distortions without rearranging into thermodynamically stable phases at the reaction temperatures needed for cation mobility, are good candidates for topochemical cation exchange processes.

The absence of a structural transition in $Ni_{0.5}TaO_3$ to a polar phase highlights the challenge that the preparation of new ferroelectric materials represents. While local symmetry breaking distortions are a condition for ferroelectricity, the presence of such symmetry breaking units does not guarantee a resulting dipole moment.

The formulation of the compounds synthesised via the topochemical cation exchange reactions in this work, represents a route which has not yet been widely explored for the preparation of materials that could yield candidate multiferroic phases in which stronger magnetic interactions may be achieved by using a different combination of metal cations.

Chapter 9

Summary, Conclusions and Future Work

The work reported in this thesis uses the fact that the energy barriers to diffusion do not apply uniformly in solids. One or more of the sublattices contained in a 'host framework' may be more mobile with respect to the others yielding a difference in the reactivity for these species. The differing reactivity permits the removal, insertion or exchange of the more mobile species, with the outcome being a chemical process in which the main topology of the original framework is preserved. Such topochemical processes can take place at relatively low temperatures, and are kinetically rather than thermodynamically driven. The resulting metastable product phases have chemical compositions and structures that can be considered as modifications of the original host phase.[49]

While investigating the reaction conditions for the preparation of $LaSrNiRuO_4$, $SrV_{0.95}Ti_{0.05}O_{1.5}H_{1.5}$ phases and $Ni_{0.5}TaO_3$, the features of the starting materials ($LaSrNiRuO_6$, $SrV_{0.95}Ti_{0.05}O_3$ and $NaTaO_3$ respectively) were observed to be critical in the formation of the product phases. This is consistent with the kinetic control operating during structure conserving reactions.

The experiments discussed in Chapters 3 and 4 suggest that as the topochemical reduction of $LaSrNiRuO_6$ progresses during the formation of $LaSrNiRuO_4$ (Figure 3.14), there is a build-up in the lattice strain from the mismatch in the *c* lattice parameter between $LaSrNiRuO_6$ and the product $LaSrNiRuO_4$. This strain seems to increase the energy barrier for the formation of $LaSrNiRuO_4$ so that a microstructure comprised of small crystalline domains for the $LaSrNiRuO_6$ starting materials was found to be a requirement for the topochemical anion deintercalation to proceed.

The cooling method used in the final heating step during the synthesis of $LaSrNiRuO_6$ was observed to affect the size of the crystalline domains in the resulting materials. This is a consequence of the phase transition from the *R*-3 trigonal structure at high temperature to the $P2_1/n$ monoclinic structure upon cooling from the synthesis temperature to room temperature ($T_{transition}$ = 670 K). The growth of crystalline domains in

this case requires a reorientation, which in turn costs energy (*i.e.* an activation energy) and takes time. Therefore, a microstructure composed of small crystalline domains for $LaSrNiRuO_6$ can be achieved by quenching, which involves taking the system rapidly to temperatures low enough that the growth of large crystalline domains is impeded. Slow cooling on the other hand, provides enough time and thermal energy for the growth of large monoclinic crystalline domains as summarised in Figures 3.11 and 3.12. As the strain produced by oxide anion deintercalation scales with the size of the crystalline domains, the energy barrier to reduction is raised in slow-cooled samples which results in incomplete reduction of the latter as depicted in Figures 3.13 and 4.2.

The crystalline domains and particle sizes were not distinguishable in the X-ray diffraction data presented in this work. Future investigations could include dynamic light scattering to determine the particle size of slow-cooled and quenched $LaSrNiRuO_6$ samples, and electron microscopy techniques might be used to look at the crystalline domains. The study of partially reduced slow-cooled samples (phase separated sample depicted in Figure 4.2) by electron microscopy might also be of interest to confirm the influence of both microstructural aspects (particle and crystalline domain size) in the reactivity of $LaSrNiRuO_6$ towards the formation of $LaSrNiRuO_4$.

The synthesis and characterisation of $LaSrNiRuO_4$ was discussed in Chapter 5 and is, to the best of our knowledge, the first example of a B-cation ordered infinite-layer oxide phase. $LaSrNiRuO_4$ is composed of sheets of apex-linked NiO_4 and RuO_4 squares in a checkerboard arrangement (as depicted in Figure 5.4). Magnetisation data and DFT calculations are consistent with a spin moment of S = ½ for the nickel centres while an intermediate-spin S = 1 configuration can be proposed for the ruthenium cations analogous to the Ru^{2+} centres in $SrFe_{0.5}Ru_{0.5}O_2$.[38] The formation of $LaSrNiRuO_4$ via the reduction of $LaSrNiRuO_6$ demonstrates that the La-Sr-Ni-O lattice in $LaSrNiRuO_4$ is sufficiently robust to resist decomposition, and can thus stabilize the formation of Ru^{2+} centres in an extended oxide phase.

$LaSrNiRuO_4$ behaves paramagnetically at room temperature. However, upon cooling (T < 250 K) a phase transition is observed in which the nickel spins interact ferromagnetically, while the ruthenium cations appear to undergo a change in spin configuration to a diamagnetic spin state. A possible explanation is given for this observation based on an

ordered arrangement of local Jahn-Teller distortions driven by an orbitally degenerate state for Ru^{2+} as depicted in Figure 9.1.

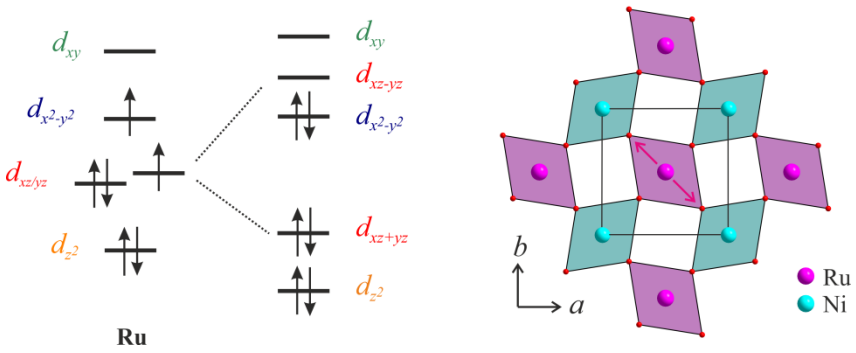


Figure 9.1. Schematisation of the proposed Jahn-Teller distortion for the ruthenium centres in $LaSrNiRuO_4$ (from the configuration $(d_z^2)^2(d_{xy/yz})^3(d_{x^2-y^2})^1(d_{xy})^0$ to the configuration $(d_z^2)^2(d_{xz+yz})^2(d_{x^2-y^2})^2(d_{xz-yz})^0(d_{xy})^0$). The expected structural distortion for a sheet of apex-linked NiO_4 and RuO_4 squares is shown at the right.

Nevertheless, no information about the presence of a distorted structure such as the one depicted in Figure 9.1 for $LaSrNiRuO_4$ is observed at low temperature in the powder diffraction data, or from the DFT calculations. Studying the proposed distorted structure would be intrinsically beyond the limits of the small model unit cell used for the DFT calculations. Additionally, the powder diffraction techniques used in this work characterise the average structure; therefore, given that the sheets of NiO_4 and RuO_4 squares are not mechanically linked with each other, no information about distortions arising in the individual sheets could be detected. A complete characterisation of the structure of $LaSrNiRuO_4$ requires some further work. Collection of synchrotron and neutron powder diffraction data as a function of temperature might be used to find evidence of a structural distortion upon cooling. A discontinuity in the change of the lattice parameters as a function of temperature is expected to be observed at a first approach. Additionally, EXAFS and XANES might be used to confirm the environment and oxidation states for the nickel and ruthenium centres. In the case that local ordering was observed, PDF analysis might also be useful to further understand the structure. Finally, the exploration of electron- and hole-doped $La_{1\pm x}Sr_{1\pm x}NiRuO_4$ phases could also lead to a better understanding of this system.

Chapters 6 and 7 discussed the topochemical oxide-for-hydride anion exchanges performed in $SrV_{0.95}Ti_{0.05}O_3$ samples, which resulted in the formation of oxyhydride phases of composition $SrV_{0.95}Ti_{0.05}O_{2-y}H_{1+y}$ ($y \approx 0.5$). These oxyhydride phases exhibit unexpectedly high contents of hydride with respect to the all-vanadium $SrVO_2H$ phase.[48]

As discussed in Chapter 6, the phase $SrVO_2H$ can be prepared from topochemical replacement of oxide anions for hydride in $SrVO_3$. The structure of $SrVO_2H$ can be described as sheets of apex-linked $V^{3+}O_4$ squares stacked with SrH layers (as depicted in Figure 6.3) and is analogous to that of the infinite-layer ABO_2 phases. However, in contrast to the growing diversity of ABO_2 materials in which the B cation has configurations of d^6 to d^9, $SrVO_2H$ is an electron-poor phase with d^2,V^{3+} centres.[38,39,107] $SrVO_2H$ is an insulator and exhibits long-range antiferromagnetic order between electrons in π-symmetry *d*-orbitals (Figures 6.2 and 6.4), with a transition temperature $T_N > 300$ K.[48] This phase thus represents an important extension for the investigation of materials with square-planar transition-metal centres with strongly interacting *d*-electrons in a low electron-count regime. A common approach to investigate such materials is to try to introduce electron holes by doping the A sites. In this work, a different approach was explored by investigating the effect of substitution of titanium onto the B-sites of $SrVO_2H$. Therefore, as detailed in Chapter 7, $SrV_{1-x}Ti_xO_3$ phases were prepared to be topochemically reduced.

However, the results from different attempts for preparing homogeneous $SrV_{1-x}Ti_xO_3$ solid solutions with x in the range $0.05 \leq x \leq 0.50$ suggest that incorporating titanium in $SrVO_3$ is challenging. Despite the end members $SrVO_3$ and $SrTiO_3$ fulfilling the structural requirements for long-range miscibility (same structure with the cations being substituted having the same charge), homogeneous $SrV_{1-x}Ti_xO_3$ ($0.05 \leq x \leq 0.50$) solid-solutions are not observed to form via the ceramic methods previously reported in the literature (Sections 6.2.1 and 7.2),[110,111] or via the arc-melt technique (Section 7.2.2).

The topochemical reduction with CaH_2 of two $SrV_{0.95}Ti_{0.05}O_3$ samples prepared by two different methods, the ceramic method described in Section 7.2.1 and the arc-melt technique, revealed important differences between the $SrV_{0.95}Ti_{0.05}O_3$ materials which were challenging to confirm from the characterisation via X-ray powder diffraction. The $SrV_{1-x}Ti_xO_2H$ reduction product which results from the $SrV_{0.95}Ti_{0.05}O_3$ starting material prepared via the ceramic method is very similar to $SrVO_2H$ (Figure 6.11, Tables 6.6 and

6.7). In contrast, the reduction of the $SrV_{0.95}Ti_{0.05}O_3$ starting material prepared via the arc-melt method yields a hydride-rich anion disordered phase of formula $SrV_{1-x}Ti_xO_{1.5}H_{1.5}$ (Figure 6.8, Tables 6.3 and 6.4). This differing reactivity between the $SrV_{0.95}Ti_{0.05}O_3$ samples prepared via the ceramic and arc-melt methods was confirmed to arise from a different content of titanium in the $SrV_{1-x}Ti_xO_3$ solid-solutions formed by each method.

During the formation of $SrVO_2H$ via topochemical anion-exchange of oxide for hydride in $SrVO_3$, a preferred substitution of the hydride ions to yield a *trans* configuration with respect to each other is observed, leading to distorted VO_4H_2 octahedra in $SrVO_2H$. The preference for this configuration can be explained from an energy gain for a square-planar array of the *p*-donor oxide ions around the d^2,V^{3+} centres as depicted in Figure 6.16. For d^1,Ti^{3+} cations, such stabilisation is not possible (Figure 6.18), and thus the electronic constraint for preferred insertion of hydride anions, *trans* or *cis* with respect to each other is lifted (as proposed in the diagram of Figure 6.19). Therefore, topochemical oxide-for-hydride exchanges in $SrV_{1-x}Ti_xO_3$ phases lead to further reduced $SrV_{1-x}Ti_xO_{2-y}H_{1+y}$ products such as the $SrV_{0.95}Ti_{0.05}O_{1.5}H_{1.5}$ phases prepared in this work.

The fact that the preparation of titanium-doped $SrV_{1-x}Ti_xO_3$ starting materials was more successful via the arc-melt technique was explained from the free energy associated with the formation of a mixture ($\Delta G = \Delta H - T\Delta S$), and the different cooling methods involved in each synthesis technique. At high temperatures the term "$-T\Delta S$" is dominant and the dispersion between the components of a mixture is thermodynamically favoured. However, if the formation of the mixture requires energy such that $\Delta H > 0$ and if the components of the mixture are immiscible, the segregation into separate components is thermodynamically favoured upon cooling. This seems to be the case in the $SrTiO_3$-$SrVO_3$ solid-solution system. By slow-cooling (which is the cooling method used during the ceramic syntheses), enough energy is available for the diffusion of the ions to form the separate phases $SrVO_3$ and $SrTiO_3$. In contrast, by quenching (inherent to the arc-melt technique), the $SrV_{1-x}Ti_xO_3$ solid-solutions rapidly reach temperatures at which insufficient energy is available for the diffusion of ions, and the high temperature dispersions are ‘frozen’ (Figure 7.14).

The temperature reached and the cooling rate during the arc-melt syntheses are therefore important variables for the formation of titanium containing $SrV_{1-x}Ti_xO_3$ starting materials. However, both variables are dependent on parameters that are not controlled

during the use of the arc-melt technique. For example, both the temperature reached and the cooling rate depend on the thermal and electric conductivity of the reaction mixtures (at the level of mixing of the samples), the water and gas flows used (Section 2.1.3) and the shape of the samples (*i.e.* thickness and geometry which affect the contact with the copper stage) also affect the change in temperature. None of the aforementioned parameters can be precisely controlled. The $SrV_{1-x}Ti_xO_3$ samples obtained after each particular arc-melt process are therefore likely to be different between them, and so are the $SrV_{1-x}Ti_xO_{2-y}H_{1+y}$ reduction products.

Alternative synthesis methods in which the temperature can be controlled more accurately and a quenching process is also possible might be attempted in order to further explore the solubility of titanium in $SrVO_3$. Electron microscopy could be used to study the composition and microstructure of the samples. Additionally, the substitution of vanadium by other transition metals and the study of the corresponding oxyhydride phases would also be interesting.

The ion exchanges studied in Chapter 8 are redox-neutral and concern cations rather than anions. In this chapter, the topochemical exchanges of Na^+ by divalent cations such as Ni^{2+} and Cu^{2+} in the three-dimensional perovskite-structure phases $NaTaO_3$ and $NaNbO_3$ were discussed. These topochemical cation exchange reactions were explored as a synthetic strategy to prepare magnetoelectric multiferroic materials: d^n magnetic cations were introduced in $NaNbO_3$ and $NaTaO_3$ in which the d^0 cations, Nb^{5+} and Ta^{5+}, are susceptible to SOJT effects (Section 1.1.1) and therefore can lead to polar structures.

Although cations are normally significantly less mobile compared to the anions in complex-oxide phases, under suitable conditions a sublattice of cations in a given phase may exhibit greater mobility. In particular, redox-neutral topochemical cation substitution reactions are not thermodynamically driven by electron transfer processes. Therefore, in addition to the species being significantly mobile within the host lattice at the reaction temperature and the product being kinetically stable additional conditions must be met. The redox-neutral reactions must be spontaneous ($\Delta G < 0$) and the latter can be achieved when large cations are substituted by smaller cations, which increases the lattice energy of the reaction products. The substitution of Na^+ for Co^{2+} in the Ruddlesden-Popper phase $Na_2La_2Ti_3O_{10}$ (Figure 8.2) is an example of such an equilibrium.[49] In this case, the Co^{2+} cations are inserted within the perovskite layers.

By utilising similar driving forces to the cation exchanges in $Na_2La_2Ti_3O_{10}$, cation exchanges of Na^+ for Ni^{2+} and Cu^{2+} in the three-dimensional perovskite-structure phase $NaTaO_3$ can be achieved. The gain in lattice energy from the substitution of Na^+ for cations of higher charge (with concomitant smaller size) makes the reaction spontaneous. Additionally, the electroneutrality condition generates vacancies in the A-sites as the reaction progresses (as for every divalent cation, two monovalent ones are exchanged). The cation transport in solids typically proceeds when an activated cation can hop into vacant sites through well-defined anion-bounded 'bottle-necks'. Thus, although in three dimensional perovskite structures expansions similar to those in layered materials are not possible, the creation of vacancies in the A-sites favours the interdiffusion of cations and with this further cation exchange.

The host phase must also be 'flexible' to undergo large distortions in order to accommodate the smaller species being introduced. The latter can be clearly observed from the structural characterisation of the product $Ni_{0.5}TaO_3$ (Figures 8.4 and 8.13, Table 8.1), and explains the failure of attempts to prepare $Ni_{0.5}NbO_3$ (Section 8.2.4) in which the metal-oxygen bonds are expected to be weaker. Thus, host phase networks suitable for the topochemical cation exchanges proposed in this work need to be flexible enough to allow significant displacements while being robust enough to prevent rearrangement to thermodynamically stable phases at the reaction temperatures needed for cation mobility.

The $NaTaO_3$ host phase exhibits an orthorhombic perovskite structure of space group *Pbnm* and as the cation exchanges of Na^+ for Ni^{2+} and Cu^{2+} take place, the TaO_6 octahedra tilt and twist to accommodate the smaller cations. In the case of Cu^{2+}, an orthorhombic structure of space group *Pmmm* results from the tilt system $a^+b^+c^-$. Rather than taking the A-sites, the copper centres occupy 4-coordinate square planar sites located at the centre of the faces and edges of the new unit cell (Figures 8.8 and 8.15, Table 8.3). Meanwhile, as the Na^+ cations are exchanged for Ni^{2+}, the latter cations do take the A-sites of the structure and a large distortion in the Ta−O−Ta framework leads to a triclinic unit cell of space group *P*-1 very similar to the rhombohedral cell of $LiTaO_3$ (*R*-3c). Analogous with the lithium site in the latter structure, the 12-coordinate sodium site present in $NaTaO_3$ converts into two pseudo-octahedral sites for the nickel in $Ni_{0.5}TaO_3$.

$LiTaO_3$ undergoes a structural transition to a polar (non-centrosymmetric, NCS) ferroelectric structure (space group *R3c*) in which the lithium cations occupy only one of

the two face-sharing "octahedral" A-cation sites (Figure 8.14). The displacement of the lithium cations in the A-sites in combination with the off-centring of the d^0 tantalum cations in the TaO_6 octahedral B-sites drives the net spontaneous electrical polarization observed in the material. Refinements of NCS models of $Ni_{0.5}TaO_3$ based on the ferroelectric phase of $LiTaO_3$ (using the space group $P1$) against neutron powder diffraction data collected at 5 K, showed no evidence for an analogous distortion for $Ni_{0.5}TaO_3$. SHG activity was tested and there was no observable measurable effect, consistent with the refined centrosymmetric structure. It was therefore concluded that $Ni_{0.5}TaO_3$ remains centrosymmetric over the entire measured temperature range.

The absence of a structural transition in $Ni_{0.5}TaO_3$ that results in a polar phase emphasises the challenge that coupling magnetism and ferroelectricity represents. Local symmetry breaking distortions are required for polarity; however the presence of such symmetry breaking units does not guarantee a resulting net dipole moment. Nonetheless, the phases discussed in this thesis represent an interesting approach to the preparation of materials that could yield candidate multiferroic composites. Stronger magnetic interactions in materials prepared using the approach presented in this work may be achieved by using different combinations of metal cations.

The preparation of all the investigated phases reported in this thesis shows that, the progress of, and products formed by, solid-state topochemical reactions can be influenced and directed by tuning the many features of the reagents and reaction conditions that come together to determine the reaction rates.

Appendix 1: Bibliography

(1) Rao, C. N. R.; Raveau, B. *Transition Metal Oxides: Structure, Properties, and Synthesis of Ceramic Oxides, 2nd Edition*; Wiley, 1998.

(2) Cox, P. A. *Transition Metal Oxides: An Introduction to Their Electronic Structure and Properties*; Oxford University Press, 2010.

(3) Peña, M. A.; Fierro, J. L. G. *Chemical Reviews* **2001**, *101*, 1981.

(4) Ishihara, T. *Perovskite Oxide for Solid Oxide Fuel Cells*; Springer, 2009.

(5) Hill, N. A. *The Journal of Physical Chemistry B* **2000**, *104*, 6694.

(6) Rao, C. N. R.; Cheetham, A. K.; Mahesh, R. *Chemistry of Materials* **1996**, *8*, 2421.

(7) Wu, M. K.; Ashburn, J. R.; Torng, C. J.; Hor, P. H.; Meng, R. L.; Gao, L.; Huang, Z. J.; Wang, Y. Q.; Chu, C. W. *Physical Review Letters* **1987**, *58*, 908.

(8) King, G.; Woodward, P. M. *Journal of Materials Chemistry* **2010**, *20*, 5785.

(9) Goodenough, J. B.; Zhou, J.-S. *Transport Properties*; Springer: Berlin, Heidelberg, 2001.

(10) Pearson, R. G. *Proceedings of the National Academy of Sciences of the United States of America* **1975**, *72*, 2104.

(11) Pearson, R. G. *Journal of Molecular Structure: THEOCHEM* **1983**, *103*, 25.

(12) Cohen, R. E. *Nature* **1992**, *358*, 136.

(13) Goldschmidt, V. M. *Naturwissenschaften* **1926**, *14*, 477.

(14) Woodward, P. *Acta Crystallographica Section B* **1997**, *53*, 32.

(15) Takata, K.; Azuma, M.; Shimakawa, Y.; Takano, M. *Journal of the Japan Society of Powder and Powder Metallurgy* **2005**, *52*, 913.

(16) Matar, S. F.; Subramanian, M. A.; Villesuzanne, A.; Eyert, V.; Whangbo, M. H. *Journal of Magnetism and Magnetic Materials* **2007**, *308*, 116.

(17) Burton, B. P.; Cockayne, E. *Physical Review B* **1999**, *60*, R12542.

(18) Sarma, D. D. *Current Opinion in Solid State and Materials Science* **2001**, *5*, 261.

(19) Valenzuela, R. *Magnetic Ceramics*; Cambridge University Press: Great Briatain, 1994; Vol. 4.

(20) Cox, P. A. *The Electronic Structure and Chemistry of Solids*; Oxford University Press, 1987.

(21) Dugdale, S. B. *Physica Scripta* **2016**, *91*, 13.

(22) Mackenzie, A. P.; Maeno, Y. *Reviews of Modern Physics* **2003**, *75*, 657.

(23) Wold, A.; Dwit, K.; Springer: 1993, p 90.

(24) Goodenough, J. B. *Metallic Oxides*; Pergamon, 1971; Vol. 5.

(25) Maeno, Y.; Rice, T. M.; Sigrist, M. *Physics Today* **2001**, 42.

(26) Huang, Q.; Soubeyroux, J. L.; Chmaissem, O.; Sora, I. N.; Santoro, A.; Cava, R. J.; Krajewski, J. J.; Peck, W. F. *Journal of Solid State Chemistry* **1994**, *112*, 355.

(27) Nakatsuji, S.; Maeno, Y. *Physical Review Letters* **2000**, *84*, 2666.

(28) Cao, G.; Bolivar, J.; McCall, S.; Crow, J. E.; Guertin, R. P. *Physical Review B* **1998**, *57*, R11039.

(29) Cava, R. J.; Batlogg, B.; Kiyono, K.; Takagi, H.; Krajewski, J. J.; Peck, W. F.; Rupp, L. W.; Chen, C. H. *Physical Review B* **1994**, *49*, 11890.

(30) Yuichi, S.; Masaichiro, M. *Journal of Physics: Condensed Matter* **2014**, *26*, 473203.
(31) Davies, P. K.; Wu, H.; Borisevich, A. Y.; Molodetsky, I. E.; Farber, L. *Annual Review of Materials Research* **2008**, *38*, 369.
(32) Denis Romero, F., University of Oxford, 2013.
(33) Goodenough, J. B. *Magnetism and the chemical bond* London, 1963.
(34) Anderson, P. W. *Physical Review* **1950**, *79*, 350.
(35) Hayward, M. A.; Green, M. A.; Rosseinsky, M. J.; Sloan, J. *Journal of the American Chemical Society* **1999**, *121*, 8843.
(36) Adkin, J. J.; Hayward, M. A. *Inorganic chemistry* **2008**, *47*, 10959.
(37) O'Malley, M.; Lockett, M. A.; Hayward, M. A. *Journal of Solid State Chemistry* **2007**, *180*, 2851.
(38) Denis Romero, F.; Burr, S. J.; McGrady, J. E.; Gianolio, D.; Cibin, G.; Hayward, M. A. *J Am Chem Soc* **2013**, *135*, 1838.
(39) Seddon, J.; Suard, E.; Hayward, M. A. *Journal of the American Chemical Society* **2010**, *132*, 2802.
(40) Gillie, L. J.; Wright, A. J.; Hadermann, J.; Van Tendeloo, G.; Greaves, C. *Journal of Solid State Chemistry* **2003**, *175*, 188.
(41) Dann, S. E.; Weller, M. T.; Currie, D. B. *Journal of Solid State Chemistry* **1992**, *97*, 179.
(42) Inoue, S.; Kawai, M.; Ichikawa, N.; Kageyama, H.; Paulus, W.; Shimakawa, Y. *Nature Chemistry* **2010**, *2*, 213.
(43) Matsumoto, K.; Haruta, M.; Kawai, M.; Sakaiguchi, A.; Ichikawa, N.; Kurata, H.; Shimakawa, Y. *Scientific Reports* **2011**, *1*.
(44) Hayward, M. A.; Cussen, E. J.; Claridge, J. B.; Bieringer, M.; Rosseinsky, M. J.; Kiely, C. J.; Blundell, S. J.; Marshall, I. M.; Pratt, F. L. *Science* **2002**, *295*, 1882.
(45) Helps, R. M.; Rees, N. H.; Hayward, M. A. *Inorganic chemistry* **2010**, *49*, 11062.
(46) Kobayashi, Y.; Hernandez, O. J.; Sakaguchi, T.; Yajima, T.; Roisnel, T.; Tsujimoto, Y.; Morita, M.; Noda, Y.; Mogami, Y.; Kitada, A.; Ohkura, M.; Hosokawa, S.; Li, Z.; Hayashi, K.; Kusano, Y.; Kim, J. e.; Tsuji, N.; Fujiwara, A.; Matsushita, Y.; Yoshimura, K.; Takegoshi, K.; Inoue, M.; Takano, M.; Kageyama, H. *Nat Mater* **2012**, *11*, 507.
(47) Sakaguchi, T.; Kobayashi, Y.; Yajima, T.; Ohkura, M.; Tassel, C.; Takeiri, F.; Mitsuoka, S.; Ohkubo, H.; Yamamoto, T.; Kim, J. e.; Tsuji, N.; Fujihara, A.; Matsushita, Y.; Hester, J.; Avdeev, M.; Ohoyama, K.; Kageyama, H. *Inorganic chemistry* **2012**, *51*, 11371.
(48) Denis Romero, F.; Leach, A.; Moller, J. S.; Foronda, F.; Blundell, S. J.; Hayward, M. A. *Angewandte Chemie* **2014**, *53*, 7556.
(49) Hayward, M. A. *Soft Chemistry Synthesis of Oxides.*; Elsevier: Oxford, 2013; Vol. 2.
(50) Cava, R. J.; Santoro, A.; Murphy, D. W.; Zahurak, S. M.; Roth, R. S. *Journal of Solid State Chemistry* **1983**, *50*, 121.
(51) Khomskii, D. I. *Journal of Magnetism and Magnetic Materials* **2006**, *306*, 1.
(52) Danks, A. E.; Hall, S. R.; Schnepp, Z. *Materials Horizons* **2016**, *3*, 91.
(53) Pechini, M. P. *US Patent* **1967**.
(54) Scott, H. G. *Journal of Materials Science* **1975**, *10*, 1527.
(55) ThermalArc*,150 TE DC Inverter Arc Welding Power Source User Manual,* **2016**.

(56) Clegg, W.; Blake, A. J.; Gould, R. O.; P., M. *Crystal Structure Analysis Principles and Practice*; Oxford Science Publications: New York, 2001.
(57) Whittaker, E. J. W. *Crystallography*; Pergamon: Amsterdam, 1981.
(58) Clegg, W. *Crystal Structure Determination*; Oxford University Press: Oxford, UK, 2002; Vol. 60.
(59) http://wwwpanalyticalcom/Empyrean/Specificationshtm.
(60) http://wwwpanalyticalcom/Xray-diffractometershtm.
(61) Thompson, S. P.; Parker, J. E.; Potter, J.; Hill, T. P.; Birt, A.; Cobb, T. M.; Yuan, F.; Tang, C. C. *Review of Scientific Instruments* **2009**, *80*, 075107.
(62) Tartoni, N.; Thompson, S. P.; Tang, C. C.; Willis, B. L.; Derbyshire, G. E.; Wright, A. G.; Jaye, S. C.; Homer, J. M.; Pizzey, J. D.; Bell, A. M. T. *Journal of Synchrotron Radiation* **2008**, *15*, 43.
(63) Rietveld, H. *Journal of Applied Crystallography* **1969**, *2*, 65.
(64) Larson, A. C.; Von Dreele, R. B. *General Structure Analysis System*; Los Alamos National Laboratory Report LAUR 86-748: The Regents of the University of California, 1985-2004.
(65) Toby, B. H. *Powder Diffraction* **2006**, *21*, 67.
(66) Sears, V. F. *Neutron News* **1992**, *3*, 26.
(67) Ekstein, H. *Physical Review* **1950**, *78*, 731.
(68) Rodríguez-Carvajal, J. *Physica B: Condensed Matter* **1993**, *192*, 55.
(69) https://wwwilleu/about/what-is-the-ill/.
(70) http://wwwisisstfcacuk/about/aboutisishtml.
(71) Caglioti, G.; Paoletti, A.; Ricci, F. P. *Nuclear Instruments* **1958**, *3*, 223.
(72) Bagayoko, D.; Callaway, J. *Physical Review B* **1983**, *28*, 5419.
(73) http://wwwisisstfcacuk/about/how-isis-works6313html.
(74) http://wwwisisstfcacuk/instruments/polaris/polaris4643html.
(75) Smith, R. In *Refinement of time-of-flight Profile Parameters in GSAS*; Rutherford Appleton Laboratory: Crystallography Group, ISIS Facility.
(76) Thompson, P.; Cox, D. E.; Hastings, J. B. *Journal of Applied Crystallography* **1987**, *20*, 79.
(77) Young, R. A. *The Rietveld Method* **1995**.
(78) Clarke, J. *Scientific American* **1994**, *271*.
(79) Bardeen, J.; Cooper, L. N.; Schrieffer, J. R. *Physical Review* **1957**, *108*, 1175.
(80) Crangle, J. *Solid State Magnetism*; Van Nostrand Reinhold New York, US, 1991.
(81) Dixon, E.; Hadermann, J.; Hayward, M. A. *Chemistry of Materials* **2012**, *24*, 1486.
(82) Orchard, A. F. *Magnetochemistry*; Oxford University Press: Oxford, UK, 2003; Vol. 75.
(83) Niwa, M.; Murakami, Y. *Journal of Catalysis* **1982**, *76*, 9.
(84) Vogel, A. I.; Bassett, J. *Vogel's textbook of quantitative inorganic analysis, including elementary instrumental analysis*; Longman, 1978.
(85) Brese, N. E.; Okeeffe, M. *Acta Crystallographica Section B-Structural Science* **1991**, *47*, 192.
(86) Brown, I. D.; Altermatt, D. *Acta Crystallographica Section B-Structural Science* **1985**, *41*, 244.
(87) https://wwwpsich/science/facilities-and-instruments.
(88) Ok, K. M.; Chi, E. O.; Halasyamani, P. S. *Chemical Society Reviews* **2006**, *35*, 710.

(89) Izumiyama, Y.; Doi, Y.; Wakeshima, M.; Hinatsu, Y.; Nakamura, A.; Ishii, Y. *Journal of Solid State Chemistry* **2002**, *169*, 125.

(90) Kobayashi, K. I.; Kimura, T.; Sawada, H.; Terakura, K.; Tokura, Y. *Nature* **1998**, *395*, 677.

(91) Pratt, J. A.; Shepherd, A. M.; Hayward, M. A. *Inorganic chemistry* **2015**, *54*, 10993.

(92) Gateshki, M.; Igartua, J. M. *Materials Research Bulletin* **2003**, *38*, 1893.

(93) Backhaus-Ricoult, M. *Annual Review of Materials Research* **2003**, *33*, 55.

(94) STOE; Cie; GmbH; Version 1.06 ed. 1999.

(95) Shiolv, A. L. *Russian Journal of Inorganic Chemistry* **1991**, *39*, 1256.

(96) Denis Romero, F.; Gianolio, D.; Cibin, G.; Bingham, P. A.; d'Hollander, J.-C.; Forder, S. D.; Hayward, M. A. *Inorganic chemistry* **2013**, *52*, 10920.

(97) Hayward, M. A. *Chemistry of Materials* **2005**, *17*, 670.

(98) Kresse, G.; Furthmüller, J. *Physical Review B* **1996**, *54*, 11169.

(99) Perdew, J. P.; Burke, K.; Ernzerhof, M. *Physical Review Letters* **1996**, *77*, 3865.

(100) Perdew, J. P.; Ruzsinszky, A.; Csonka, G. I.; Vydrov, O. A.; Scuseria, G. E.; Constantin, L. A.; Zhou, X.; Burke, K. *Physical Review Letters* **2008**, *100*, 136406.

(101) Tsujimoto, Y.; Tassel, C.; Hayashi, N.; Watanabe, T.; Kageyama, H.; Yoshimura, K.; Takano, M.; Ceretti, M.; Ritter, C.; Paulus, W. *Nature* **2007**, *450*, 1062.

(102) Tassel, C.; Goto, Y.; Kuno, Y.; Hester, J.; Green, M.; Kobayashi, Y.; Kageyama, H. *Angewandte Chemie* **2014**, *126*, 10545.

(103) Pruneda, J. M.; Íñiguez, J.; Canadell, E.; Kageyama, H.; Takano, M. *Physical Review B* **2008**, *78*, 115101.

(104) Lee, K. W.; Pickett, W. E. *Physical Review B* **2008**, *77*, 115101.

(105) Rodríguez-Carvajal, J.; Hennion, M.; Moussa, F.; Moudden, A. H.; Pinsard, L.; Revcolevschi, A. *Physical Review B* **1998**, *57*, R3189.

(106) Siegrist, T.; Zahurak, S. M.; Murphy, D. W.; Roth, R. S. *Nature* **1988**, *334*, 231.

(107) Dixon, E.; Hayward, M. A. *Inorganic chemistry* **2010**, *49*, 9649.

(108) Rey, M. J.; Dehaudt, P.; Joubert, J. C.; Lambert-Andron, B.; Cyrot, M.; Cyrot-Lackmann, F. *Journal of Solid State Chemistry* **1990**, *86*, 101.

(109) Ekuma, C. E.; Jarrell, M.; Moreno, J.; Bagayoko, D. *AIP Advances* **2012**, *2*, 012189.

(110) Hideyasu, T.; Koichi, K.; Kazuo, F. *Japanese Journal of Applied Physics* **1983**, *22*, 590.

(111) Hong, K.; Kim, S.-H.; Heo, Y.-J.; Kwon, Y.-U. *Solid State Communications* **2002**, *123*, 305.

(112) Ohashi, N.; Teramoto, Y.; Ikawa, H.; Fukunaga, O.; Tanaka, J. *Journal of Solid State Chemistry* **1992**, *97*, 434.

(113) Kato, K.; Kanke, Y.; Oka, Y.; Yao, T. *Zeitschrift fuer Kristallographie* **1998**, *213*, 399.

(114) Shannon, R. *Acta Crystallographica Section A* **1976**, *32*, 751.

(115) van Benthem, K.; Elsässer, C.; French, R. H. *Journal of Applied Physics* **2001**, *90*, 6156.

(116) Zhang, L.; Zhou, Y. J.; Guo, L.; Zhao, W. W.; Barnes, A.; Zhang, H. T.; Eaton, C.; Zheng, Y. X.; Brahlek, M.; Haneef, H. F.; Podraza, N. J.; Chan, M. H. W.; Gopalan, V.; Rabe, K. M.; Engel-Herbert, R. *Nature Materials* **2016**, *15*, 204.

(117) Onoda, M.; Ohta, H.; Nagasawa, H. *Solid State Communications* **1991**, *79*, 281.

(118) Busch‐Vishniac, I. J. *Physics Today* **1998**, *51*, 28.

(119) Fujimura, N.; Ishida, T.; Yoshimura, T.; Ito, T. *Applied Physics Letters* **1996**, *69*, 1011.

(120) Catalan, G.; Scott, J. F. *Advanced Materials* **2009**, *21*, 2463.

(121) Kimura, T.; Kawamoto, S.; Yamada, I.; Azuma, M.; Takano, M.; Tokura, Y. *Physical Review B* **2003**, *67*.

(122) Seshadri, R.; Hill, N. A. *Chemistry of Materials* **2001**, *13*, 2892.

(123) Wang, J. a. N., J. B. and Zheng, H. and Nagarajan, V. and Ogale, S. B. and Liu, B. and Viehland, D. and Vaithyanathan, V. and Schlom, D. G. and Waghmare, U. V. and Spaldin, N. A. and Rabe, K. M. and Wuttig, M. and Ramesh, R. *Science* **2003**, *299*, 1719.

(124) England, W. A.; Goodenough, J. B.; Wiseman, P. J. *Journal of Solid State Chemistry* **1983**, *49*, 289.

(125) Mitchell, R. H.; Liferovich, R. P. *Journal of Solid State Chemistry* **2004**, *177*, 4420.

(126) Johnston, K. E.; Tang, C. C.; Parker, J. E.; Knight, K. S.; Lightfoot, P.; Ashbrook, S. E. *Journal of the American Chemical Society* **2010**, *132*, 8732.

(127) Abrahams, S. C.; Buehler, E.; Hamilton, W. C.; Laplaca, S. J. *Journal of Physics and Chemistry of Solids* **1973**, *34*, 521.

(128) Wolcyrz, M.; Lukaszewski, M. *Zeitschrift für Kristallographie - Crystalline Materials* **1986**, *177*, 53.

(129) Inbar, I.; Cohen, R. E. *Ferroelectrics* **1997**, *194*, 83.

(130) Vincent, H.; Bochu, B.; Aubert, J. J.; Joubert, J. C.; Marezio, M. *Journal of Solid State Chemistry* **1978**, *24*, 245.

(131) Longo, J. M.; Sleight, A. W. *Materials Research Bulletin* **1975**, *10*, 1273.

(132) Langbeln, H.; Bremer, M.; Krabbes, I. *Solid State Ionics* **1997**, *101–103, Part 1*, 579.

(133) Mani, R.; Achary, S. N.; Chakraborty, K. R.; Deshpande, S. K.; Joy, J. E.; Nag, A.; Gopalakrishnan, J.; Tyagi, A. K. *Journal of Solid State Chemistry* **2010**, *183*, 1380.

(134) de Oliveira Neto, S. R.; Kinast, E. J.; Gusmão, M. A.; dos Santos, C. A.; Isnard, O.; da Cunha, J. B. M. *Journal of Magnetism and Magnetic Materials* **2012**, *324*, 3245.

(135) Amano Patino, M.; Smith, T.; Zhang, W.; Halasyamani, P. S.; Hayward, M. A. *Inorganic chemistry* **2014**, *53*, 8020.

(136) In *Solid State Electrochemistry I*; Wiley-VCH Verlag GmbH & Co. KGaA: 2009, p 279.

Appendix 2: Details of the Ferromagnetic Subtraction Experiment for $LaSrNiRuO_4$

As described in Section 2.6.1, the paramagnetic susceptibility of a bulk sample containing a ferromagnetic impurity (such as the $LaSrNiRuO_4$ sample characterised in Chapter 5) can be measured via a ferromagnetic subtraction experiment. The experiment carried out consisted of collecting magnetisation-field isotherms of the $LaSrNiRuO_4$ sample using fields at which the ferromagnetic impurity (nickel metal) was saturated (see Figures 2.9 and A.1). The magnetisation of the Ni impurity in the $LaSrNiRuO_4$ was observed to saturate at applied magnetic fields of 30000 Oe as can be observed from the 5 K isotherm shown in Figure A.1. Therefore, 5 fields within the range $30000 \leq H\ (Oe) \leq 50000$ (using 5000 Oe intervals) were applied to measure the magnetisation-field isotherms of the $LaSrNiRuO_4$ sample, at temperatures in the range $5 \leq T\ (K) \leq 300$ (using 5 K intervals).

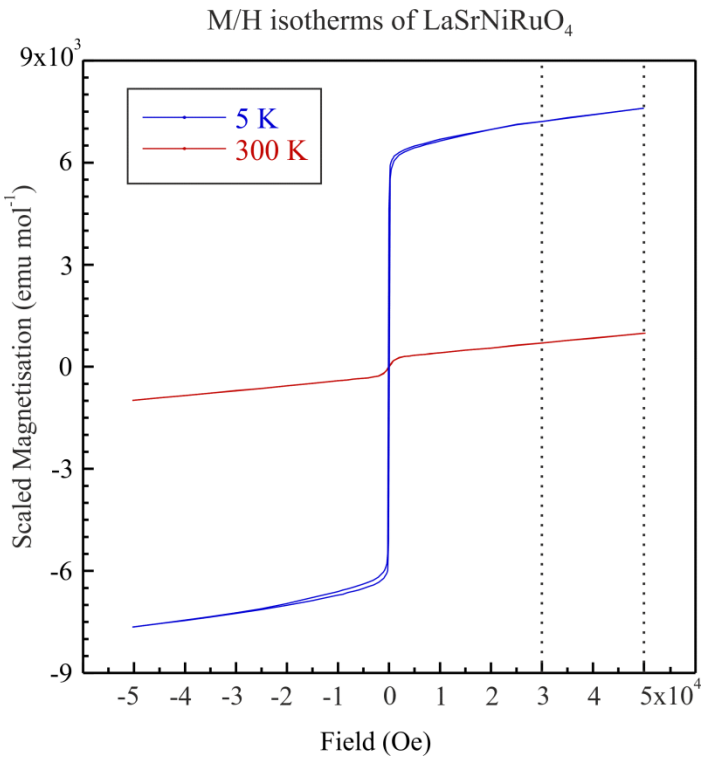


Figure A.1. Magnetisation-field isotherms collected from the $LaSrNiRuO_4$ sample at 5 K and 300 K. The field range used for the ferromagnetic subtraction experiment is indicated with dotted lines.

The magnetisation-field isotherms collected were fitted to a linear function as shown in Figure A.2 (See also Figure 2.9). The gradient of the as fitted lines corresponds to the paramagnetic susceptibility of $LaSrNiRuO_4$ and the intercept is equal to the saturated ferromagnetic moment. All fits had at least 4 data points and data points with large errors were excluded. The plots of the paramagnetic susceptibility and saturated ferromagnetic moment of $LaSrNiRuO_4$ as a function of temperature are given in Figure 5.6.

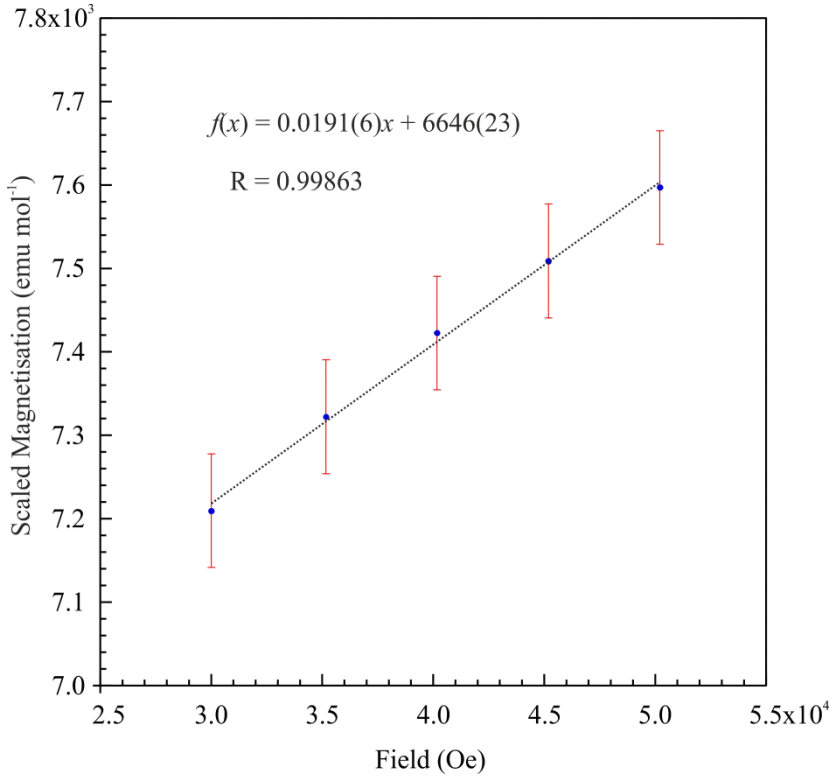


Figure A.2. Five data points within the high-field region of the M/H isotherm of $LaSrNiRuO_4$ collected at 5 K (blue curve in Figure A.1). The error bars are given in red and the linear function fitted to the data is indicated by the dotted line.

Appendix 3: Table of Figures

Figure 1.1. Schematisation of an example of (a) FOJT and (b) SOJT effects on a *d*-metal in an octahedral environment. The electrons in the *d* orbitals in (a) have been omitted for simplicity but d^0 configurations represent a good example. 2

Figure 1.2. Schematisation of the distortions that occur in the perovskite structure. Representative examples of space groups observed for the different values of the tolerance factor *t* are given in blue. 4

Figure 1.3. The Ruddlesden-Popper structures of Sr_2VO_4 and $Sr_3V_2O_7$. 5

Figure 1.4. Table of different ordering schemes in perovskites.[8] 6

Figure 1.5. Schematisation of atomic levels splitting into energy bands where the equilibrium interatomic distance is r_0.[20] 7

Figure 1.6. Schematisation of the hopping (*t*) and energy (*U*) terms in the Hubbard model.[21] 7

Figure 1.7. Hubbard sub-bands as a function of the band width *W*. On the energy coordinate *E*, *-I* represents the ionisation energy and *-A* the electron affinity.[2] 8

Figure 1.8. Structures of Sr_2RuO_4 (left), Ca_2RuO_4 (middle) and Sr_2IrO_4 (right).[33] 10

Figure 1.9. Schematic examples of M-O-M 180º and 90º, *d-p-d* orbital interactions resulting in the magnetic coupling predicted by the Goodenough-Kanamori rules. 11

Figure 1.10. Reaction of $LaNiO_3$ with NaH to form the reduction product $LaNiO_2$. 13

Figure 1.11. The reduction of $LaBaCo_2O_5$ with NaH resulting in the $LaBaCo_2O_{4.25}$ phase with square planar Co^+ centres (occupying 50% of the anion-defficient sites). 13

Figure 1.12. The structures of the topochemically reduced phases $LaBaCo_2O_{4.25}$ and $YBaCo_2O_{4.5}$. 14

Figure 1.13. The *n* = 2 Ruddlesden-Popper phases $Sr_3M_2O_7$ (M = Mn, Fe) and their reduction products.[33] 14

Figure 1.14. The structure of $ATiO_{3-y}H_y$ (A = Ba, Sr, Ca), $LaSrCoO_3H_{0.7}$ and $SrVO_2H$. 15

Figure 1.15. The lithium insertion into the ReO_3 and WO_3 perovskite structures.[52] 16

Figure 1.16. The cation exchange of Co^{2+} for Na^+ in the Ruddlesden-Popper phase $Na_2La_2Ti_3O_{10}$. The Co^{2+} cations occupy half of the tetrahedral interlayer sites.[52] 17

Figure 2.1. The arc-melt furnace 20

Figure 2.2. The venting apparatus 22

Figure 2.3. Bragg's construction for diffraction of monochromatic radiation by a set of parallel lattice planes.[61] 25
Figure 2.4. Schematisation of the Debye-Scherrer cones from diffraction by a powder sample, and their projection on a flat plate detector.[63] 26
Figure 2.5. Gas-tight holder for the collection of X-ray powder diffraction data from air-sensitive samples. 27
Figure 2.6. D2B diffractometer at ILL, Grenoble, France.[78] 32
Figure 2.7. New POLARIS instrument at the ISIS facility.[80] 33
Figure 2.8. Schematic representation of the principal component in a SQUID magnetometer.[85] 36
Figure 2.9. Schematisation of a magnetisation-field isotherm of a sample consisting of a paramagnetic phase and a ferromagnetic impurity phase. The dotted line indicates the region used for a ferromagnetic subtraction experiment. 37
Figure 2.10. Schematic representation of the experimental setup for the SHG measurements using a Kurtz-Powder Laser System. 42
Figure 3.1. Structures of $Sr(Ru_{0.5}Fe_{0.5})O_2$ and $Na_2La_2Ti_2RuO_8$. 44
Figure 3.2. Reduction of $LaSrNiRuO_6$ to form $LaSrNiRuO_4$. 44
Figure 3.3. Observed, calculated, and difference plots from refinement of the structural model of $LaSrNiRuO_6$ in space group $P2_1/n$ against X-ray powder diffraction data collected from a slow-cooled and a quenched samples. The upper set of tick marks corresponds to the NiO secondary phase. 47
Figure 3.4. Thermogravimetric data collected during the reduction of slow-cooled and quenched $LaSrNiRuO_6$ samples to La_2O_3, SrO, Ni and Ru. 49
Figure 3.5. Thermogravimetric data collected during the reduction of a quenched $LaSrNiRuO_6$ sample to La_2O_3, SrO, Ni and Ru. 49
Figure 3.6. Region $30 < 2\theta(^o) < 35$ of the X-ray powder diffraction patterns collected from a slow-cooled (left) and a quenched (right) $LaSrNiRuO_6$ sample. 50
Figure 3.7. Comparison of X-ray diffraction patterns of the slow-cooled subsequently quenched sample (top) and the original slow-cooled sample (bottom). Insets show expanded regions $32 < 2\theta(^o) < 33$, $56 < 2\theta(^o) < 59$, $84 < 2\theta(^o) < 86$, $93 < 2\theta(^o) < 96$. 51
Figure 3.8. Observed, calculated, and difference plots from refinement of the structural model of the 'SC-Q' $LaSrNiRuO_6$ sample in space group $P2_1/n$ against X-ray powder diffraction data. The upper set of tick marks corresponds to NiO (1.15% by weight). 52

Figure 3.9. Comparison of X-ray diffraction patterns of the slow-cooled subsequently quenched sample (top) and the result of slow-cooling again (bottom). Insets show expanded regions 32 < 2θ(º) < 33, 56 < 2θ(º) < 59, 84 < 2θ(º) < 86, 93 < 2θ(º) < 96. 53
Figure 3.10. The monoclinic $P2_1/n$ (left) and trigonal R-3 (right) structures of $LaSrNiRuO_6$. Curved, arrows describe the rotation of the BO_6 (B = Ni, Ru) octahedra about each Cartesian axis, in the Glazer notation. 55
Figure 3.11. Representation of the processes involved when cooling $LaSrNiRuO_6$ below the phase transition temperature. Region (1) schematises the formation of the monoclinic crystalline domains and region (2) their growth. The different patterns are parallel to the Cartesian axes x, y or z about which rotation can take place clockwise or anticlockwise. 56
Figure 3.12. Schematic representation of the crystalline domains in slow-cooled and quenched $LaSrNiRuO_6$ samples. The different patterns are parallel to the Cartesian axes x, y or z about which rotation can take place clockwise or anticlockwise. 57
Figure 3.13. Schematic representation of the reduction reactions carried out with slow-cooled and quenched $LaSrNiRuO_6$ samples. 58
Figure 3.14. Representation of the strain 'regions' at the reaction interface during reduction of $LaSrNiRuO_6$ to form $LaSrNiRuO_4$. Coloured arrows represent the two types of strain generated at each end composition and dotted lines of the corresponding colour represent the regions affected by each type of strain. 59
Figure 4.1. X-ray powder diffraction data collected from the reaction between $LaSrNiRuO_6$ and CaH_2 in the venting apparatus. A tetragonal phase could be indexed (○) using a tetragonal model of space group $I4/mmm$ (a = 5.65(1) Å, c = 6.92(1) Å). 63
Figure 4.2. X-ray powder diffraction data collected from the reaction of a $LaSrNiRuO_6$ slow-cooled (top) and a quenched (bottom) sample, with CaH_2 after 3 heating cycles at 360ºC in the venting apparatus. The dotted lines mark the position of the peaks used as reference. 64
Figure 4.3. X-ray powder diffraction data collected from the washed product of reduction a $LaSrNiRuO_6$ slow-cooled starting material after 10 heating cycles at 360 ºC. 65
Figure 4.4. The modified venting apparatus. 66
Figure 4.5. X-ray powder diffraction data collected from the reaction between a $LaSrNiRuO_6$ slow-cooled sample and CaH_2 after 3 heating cycles at 360 ºC, in the modified venting apparatus. 66

Figure 4.6. X-ray powder diffraction data collected from the reaction between a $LaSrNiRuO_6$ slow-cooled sample and CaH_2 after heating at the increased temperature of 375 ºC.....67
Figure 4.7. X-ray diffraction data collected from the washed reduction products of a slow-cooled (SC-R) and a quenched (Q-R) $LaSrNiRuO_6$ sample. The dotted line (2θ = 10.60º) marks the position of the extra peak observed in the SC-R data. 68
Figure 4.8. Thermogravimetric data collected during reductive decomposition of the SC-R and Q-R $LaSrNiRuO_{6-x}$ products.....69
Figure 4.9. Thermogravimetric data collected during oxidation of the SC-R and Q-R products.....69
Figure 4.10. Comparison of the X-ray powder diffraction data collected from the products from oxidation of the SC-R and Q-R samples. The X-ray diffraction pattern of a $LaSrNiRuO_6$ starting material is included at the top as a reference. 71
Figure 4.11. Observed, calculated and difference plots from the refinement of the *I*4/*mmm* structural model of $LaSrNiRuO_4$ against neutron powder diffraction data collected from the SC-R sample at 298 K using the D2B instrument. Black tick marks indicate the peak positions for the majority tetragonal phase; red elemental Ni (1.74(5)% by weight) and blue La_2O_3 (1.39(2)% by weight). The position of peaks of an *Fd*-3*m* cubic model (*a* = 8.378(2) Å) is indicated with arrows. 72
Figure 4.12. The reduction of (a) $SrFe_{0.5}Ru_{0.5}O_3$ and (b) $LaSrNiRuO_6$ via topochemical anion deintercalation using CaH_2.....73
Figure 4.13. Summary of the different outcomes observed from reduction of the slow-cooled and quenched $LaSrNiRuO_6$ starting materials. 77
Figure 4.14. Proposed reaction profile for the topochemical reduction of $LaSrNiRuO_6$. The path in red represents the extreme case of complete reductive decomposition. 78
Figure 5.1. Thermogravimetric data collected during reductive decomposition (left) and reoxidation (right) of the $LaSrNiRuO_{6-x}$ Q-R product. 82
Figure 5.2. Observed, calculated and difference plots from refinement of an *I*4/*mmm* structural model of $LaSrNiRuO_4$ against X-ray powder diffraction data. Black tick marks indicate the peak positions for the majority tetragonal phase; red, elemental Ni (2.5(4)% by weight) and blue, La_2O_3 (0.5(3)% by weight).....83
Figure 5.3. Observed, calculated and difference plots from refinement of an *I*2/*m* monoclinic structural model of $LaSrNiRuO_4$ against X-ray powder diffraction data. Black

tick marks indicate the peak positions for the majority phase; red, elemental Ni (2.7(3)% by weight) and blue, La_2O_3 (0.5(2)% by weight).....84
Figure 5.4. Representation of the crystal structure of $LaSrNiRuO_4$ at 300 K. Red ellipsoids represent the oxygen positions. 85
Figure 5.5. Observed, calculated and difference plots of the structural refinement of $LaSrNiRuO_4$ against neutron powder diffraction data collected at 300 K. Black tick marks indicate the peak positions for the monoclinic majority phase; red, elemental Ni (2.3(3)% by weight); blue, La_2O_3 (0.3(1)% by weight); and green, vanadium from the sample holder. 86
Figure 5.6. The paramagnetic susceptibility (a) and saturated ferromagnetic moment (b) of $LaSrNiRuO_4$ collected as a function of temperature. Inset in the left panel shows the fit to the Curie-Weiss law in the temperature range $250 < T(K) < 300$. 88
Figure 5.7. Neutron powder diffraction data collected from $LaSrNiRuO_4$ at 5 K exhibit enchanced intensity of the 110/-110 diffraction peak, compared to analogous data collected at 300 K, consistent with a magnetically ordered state at low temperature. 89
Figure 5.8. Base model for refinement of the magnetic structure of $LaSrNiRuO_4$. Arrows represent the magnetic moments on nickel and ruthenium centres. 89
Figure 5.9. Representation of the refined magnetic structure of $LaSrNiRuO_4$. 90
Figure 5.10. Observed, calculated and difference plots of the structural refinement of $LaSrNiRuO_4$ against neutron powder diffraction data collected at 5 K. Black tick marks indicate the peak positions for the monoclinic majority phase; red, elemental Ni (2.3% by weight); blue, La_2O_3 (0.3% by weight); green, vanadium from the sample holder; and orange, the magnetic cell of $LaSrNiRuO_4$.....92
Figure 5.11. Three distinct spin configurations of $LaSrNiRuO_4$ system. Spheres represent the nickel and ruthenium centres. The unit cells are monoclinic $I2/m$. 94
Figure 5.12. Representation of the most stable spin configuration. Dashed lines represent the exchange coupling interactions from which J_1 and J_2 are calculated. 95
Figure 5.13. Representation of the optimised bond lengths and net spin densities for the computed monoclinic unit cell (dotted line). 96
Figure 5.14. Spin-polarised projected density of states for nickel and ruthenium in $LaSrNiRuO_4$ (U_{eff}(Ni) = 6.0 eV, U_{eff}(Ru) = 3.0 eV. 97
Figure 5.15. Comparison of the crystal structure of $LaSrNiRuO_4$ at 300 K and 5 K. Red ellipsoids represent the oxygen positions 99

Figure 5.16. Schematisation of the proposed FOJT effect for the ruthenium centres in the low temperature structure of $LaSrNiRuO_4$. The relative position of the d_{z^2}, $d_{x^2-y^2}$ and d_{xy} orbitals has been adjusted for simplicity in showing the splitting of the $d_{xy/yz}$ manifold. 101
Figure 6.1. Reaction of the $SrO(SrVO_3)n$ (n = 1, 2, ∞) phases with CaH_2 to form the $Sr_{n+1}V_nO_{2n+1}H_n$ phases. 103
Figure 6.2. Local electronic structure (left) of the VO_4H_2 units (right). 104
Figure 6.3. An analogous coordination environment for the transition-metal centres can be observed by comparison of the $SrVO_2H$ and $Sr_{0.7}Ca_{0.3}CuO_2$ structures. 104
Figure 6.4. Magnetic structure of $SrVO_2H$. 105
Figure 6.5. Observed, calculated, and difference plots from refinement of the structural model based on a mixture of cubic phases with space group *Pm*-3*m* against data collected from the $SrV_{0.95}Ti_{0.05}O_3$ C and A samples. The bottom tick marks (black) correspond to the majority cubic phase in each case. 107
Figure 6.6. X-ray powder diffraction data collected during the reduction of the $SrV_{0.95}Ti_{0.05}O_3$ samples prepared via the ceramic (C, left panel), and arc-melt (A, right panel) methods. The diffraction pattern of a $SrVO_2H$ sample is shown (at the top) for comparison. The growth of the cubic phase at the expense of the tetragonal phase as the reaction progresses for the A sample is highlighted with the dotted lines (110 and 101 reflections respectively). 109
Figure 6.7. Observed, calculated and difference plots from refinement against synchrotron X-ray powder diffraction data collected from the C-R reduction product of the C starting material (prepared via the ceramic method). Bottom tick marks (black) correspond to peak positions for the tetragonal majority phase, bottom middle tick marks (red) to the vanadium secondary phase $SrVO_{3-y}$, top middle tick marks (blue) to the titanium secondary phase $SrTiO_{3-y}$, and top tick marks (green) to vanadium metal. 111
Figure 6.8. Observed, calculated and difference plots from refinement against synchrotron X-ray powder diffraction data collected from the A-R reduction product of the A starting material (prepared via the arc-melt method). Bottom tick marks (black) correspond to peak positions for the cubic majority phase, middle tick marks (red) to the tetragonal phase SrV_2OH, top tick marks (blue) to vanadium metal. 113
Figure 6.9. Thermogravimetric data collected during oxidative decomposition of the $SrVO_2H$ sample of Figure 6.6 (top panel), the C-R reduction product (bottom left), and the A-R reduction product (bottom right). The theoretical mass gain for the exact stoichiometric composition of $SrVO_2H$ (RMM 171.57) is 13.40%. 115

Figure 6.10. Zero-field cooled and field cooled susceptibility data as a function of temperature collected from $SrVO_2H$ (top panel), the C-R reduction product (bottom left) and the A-R reduction product (bottom right). The *C* and θ values result from the fit of the zero-field cooled data to the Curie-Weiss law over the whole range of T measured.120
Figure 6.11. Observed, calculated and difference plots from refinement of the C-R reduction product (top) and $SrVO_2H$ (bottom) against neutron powder diffraction data collected at 298 K. Black tick marks correspond to the peak positions of the majority phase, red to $SrVO_{3-y}$, yellow to $SrTiO_{2.88}H_{0.12}$, blue to the contribution from vanadium (both from the sample holder and the secondary phase), and green to the magnetic models. 121
Figure 6.12. The refined atomic and magnetic structures of $SrVO_2H$ at 298 K. 122
Figure 6.13. Observed, calculated and difference plots from refinement of the C-R reduction product (top) and $SrVO_2H$ (bottom) against neutron powder diffraction data collected at 298 K. Black tick marks correspond to the peak positions of the majority phase, red to $SrVO_{3-y}$, yellow to $SrTiO_{2.88}H_{0.12}$, blue to the contribution from vanadium (both from the sample holder and the secondary phase), green to the magnetic models. 125
Figure 6.14. Schematised reactivity of the $SrV_{0.95}Ti_{0.05}O_3$ samples prepared via the ceramic (C, top) and arc-melt (A, bottom) methods. 127
Figure 6.15. Schematic representation of the topochemical reduction of $SrVO_3$ via exchange of O^{2-} for H^-. Exchange takes place preferably on the apical positions of the original VO_6 octahedra to yield infinite VO_2 sheets connected by hydride ions which take the *trans* configuration around the vanadium centres. 129
Figure 6.16. Schematisation of the stabilisation via splitting of the octahedral t_{2g} orbitals which takes place for a square-planar array of the oxide anions around the vanadium centres in $SrVO_2H$. 130
Figure 6.17. Electronic configuration for the $\boldsymbol{d3}$,Cr^{3+} centres in $SrCrO_2H$. There is no preference for a *trans* or *cis* configuration of the hydride ions around the chromium centres. 130
Figure 6.18. On the left, the electronic configuration for the $\boldsymbol{d1}$,Ti^{3+} is shown. There is no stabilisation energy gain from a *trans* configuration and thus further substitution of O^{2-} for H^- can take place in the equatorial positions of the $V_{1-x}Ti_xO_4H_2$ units (as schematised on the right hand side diagram). 131
Figure 6.19. Proposed reaction profile for the topochemical reduction of $SrVO_3$ (pathway in dark blue) and $SrV_{1-x}Ti_xO_3$ (pathway in light blue). 132

Figure 7.1. The structure and composition of the characterised reduction products from $SrV_{0.95}Ti_{0.05}O_3$ samples synthesised via the ceramic method (C-R, left) and the arc-melt technique (A-R, right). 134
Figure 7.2. Observed, calculated, and difference plots from refinement of the structural model based on a mixture of cubic phases with space group *Pm*-3*m* against synchrotron X-ray diffraction data (λ = 0.8259 Å) collected from the $SrV_{0.95}Ti_{0.05}O_3$ C and A samples. The bottom tick marks (black) corresponds to the majority cubic phase in each case. ... 138
Figure 7.3. X-ray data collected from a $SrV_{0.95}Ti_{0.05}O_3$ sample prepared under a 10% H_2/Ar flow at 1550 ºC after (a) one 12-hour heating cycle (C-1550) and (b) two 12-hour heating cycles. Inset in (a) shows the observed, calculated, and difference plots from the refinement of C-1550. The black set of tick marks (bottom) corresponds to the majority cubic phase (a_1 = 3.845(1) Å), red (middle) to the minority cubic phase (a_2 = 3.900(1) Å) and blue to the secondary phase $SrV_{10}O_{15}$. 140
Figure 7.4. X-ray powder diffraction data collected from the $SrV_{0.95}Ti_{0.05}O_3$ C-1525 sample prepared under a 10% H_2/Ar flow at 1525 ºC after one 12-hour heating cycle. Inset shows the observed, calculated, and difference plots from the refinement of a model based on a mixture of $SrVO_3$ and $SrTiO_3$. The black set of tick marks (bottom) corresponds to the majority cubic phase (a_1 = 3.848(1) Å), red (middle) to the minority cubic phase (a_2 = 3.898(2) Å) and blue to the secondary phase $SrV_{10}O_{15}$. 141
Figure 7.5. X-ray powder diffraction data collected from $SrV_{1-x}Ti_xO_3$ samples with x = 0.40 (top) and x = 0.50 (bottom) prepared under a 10% H_2/Ar flow at 1525 ºC for 12 hours. 143
Figure 7.6. X-ray powder diffraction data collected from $SrV_{1-x}Ti_xO_3$ samples with x = 0.40 (top) and x = 0.50 (bottom) prepared via arc-melt. 143
Figure 7.7. Reflections observed from additional cubic phases revealed upon closer inspection of the X-ray powder diffraction data collected from $SrV_{0.60}Ti_{0.40}O_3$ sample prepared under a 10% H_2/Ar flow at 1525 ºC for 12 hours. 145
Figure 7.8. Observed, calculated, and difference plots (in the range $38 \leq 2\theta\ (^o) \leq 70$) from refinement of the model based on two cubic phases against the data collected from the $SrV_{1-x}Ti_xO_3$ (x = 0.40, 0.50) arc-melt samples. The black set of tick marks corresponds to the majority cubic phases (a_1) and red to the minority cubic phases (a_2). 145
Figure 7.9. Refined lattice parameters of the majority cubic phases observed in the $SrV_{1-x}Ti_xO_3$ ($0.10 \leq x \leq 0.30$) samples prepared via arc-melt. The lattice parameters of the

extreme compositions $SrVO_3$, $SrTiO_3$ and the x = 0.05, 0.40, 0.50 samples previously discussed have been included in the plot. 146
Figure 7.10. X-ray powder diffraction data collected from $SrV_{1-x}Ti_xO_3$ ($0.10 \leq x \leq 0.30$) samples prepared via arc-melt. 147
Figure 7.11. X-ray diffraction patterns collected from an arc-melt $SrV_{0.95}Ti_{0.05}O_3$ sample (a) before heating at 1100 ºC and slow-cooling (A_1), and (b) after this annealing process (A_1-SC). The overlaid diffraction patterns in the range $30 \leq 2\theta$ (º) ≤ 60 are shown in the inset of (a). 149
Figure 7.12. X-ray diffraction patterns of the $SrV_{0.50}Ti_{0.50}O_3$ sample prepared via the arc-melt method, before (top) and after (bottom) annealing at 610 ºC for 72 hours. 150
Figure 7.13. X-ray diffraction data collected from the reduction of the arc-melt A1 sample and the annealed (1100 ºC) slow-cooled fraction A_1-SC. Continuing the reduction of the A1 sample yields a cubic material consistent with that observed in the A-R reduction product characterised in Section 6.3. 151
Figure 7.14. Schematisation of the effect of the cooling rate on the $SrV_{1-x}Ti_xO_3$ samples. The circles represent particles of the samples, where the dispersion of $SrTiO_3$ (blue) in $SrVO_3$ (red) leads to $SrV_{1-x}Ti_xO_3$ phases in purple. 153
Figure 8.1. The structure of the perovskites $NaBO_3$ ($B = Nb^{5+}$, Ta^{5+}). 156
Figure 8.2. Reaction of the Ruddlesden-Popper phase $Na_2La_2Ti_3O_{10}$ with $CoCl_2$. The Co^{2+} substitutes in half the tetrahedral interlayer Na^+ sites.[52] 157
Figure 8.3. X-ray powder diffraction patterns collected from the washed products of reaction between $NaTaO_3$ and $NiCl_2$ at 450 °C, as a function of time. 160
Figure 8.4. Observed, calculated, and difference plots for refinement of structural models in space group *R*-3*c* (top; $\chi^2 = 9.12$) and *P*-1 (bottom; $\chi^2 = 4.088$) against neutron powder diffraction data collected from $Ni_{0.5}TaO_3$ at 298 K using the D2B instrument, ILL neutron source. 162
Figure 8.5. Magnetization data collected from $Ni_{0.5}TaO_3$ in an applied field of 100 Oe. The fit to the Curie-Weiss law is shown in the inset. 164
Figure 8.6. Observed, calculated, and difference plots for refinement of the structural model in space group *P-1* ($a = 5.468(1)$ Å, $b = 5.481(1)$ Å, $c = 5.501(1)$ Å, $\alpha = 55.68(1)$º, $\beta = 56.17(1)$º, $\gamma = 55.29(1)$º) against neutron powder diffraction data collected from $Ni_{0.5}TaO_3$ at 5 K using the D2B instrument, ILL neutron source. The features at $2\theta = 47.2$º, 71.2º correspond to reflections from the cryostat. $\chi^2 = 4.035$, *wRp* = 3.43%, *Rp* = 2.61%. 165

Figure 8.7. X-ray powder diffraction patterns collected from the washed products of reaction between $NaTaO_3$ and $CuCl_2$ at 450 °C, as a function of time. 166
Figure 8.8. Observed, calculated, and difference plots for refinement of structural models in space group *Pm-3* (top; χ^2 = 6.465) and *Pmmm* (bottom; χ^2 = 5.120) against neutron powder diffraction data collected from $Cu_{0.5}TaO_3$ at 298 K using the D2B instrument, ILL neutron source. Red tick marks correspond to a 6.17(3) % by weight of starting material $NaTaO_3$. 167
Figure 8.9. Magnetization data collected from $Cu_{0.5}TaO_3$ in an applied field of 100 Oe. The fit to the Curie-Weiss law is shown in the inset. 169
Figure 8.10. Extended range in the low temperature region of the magnetisation data collected from $Cu_{0.5}TaO_3$ in an applied field of 100 Oe. The isotherms collected at 300 K and 5 K are shown in the inset. 170
Figure 8.11. Expanded region ($5 \leq T\ (K) \leq 25$) of the magnetization data collected from $Cu_{0.5}TaO_3$ during a high resolution zfc-fc experiment in an applied field of 100 Oe. 170
Figure 8.12. Neutron powder diffraction data collected from $Cu_{0.5}TaO_3$ at 298 K (bottom) and 5 K (top). 171
Figure 8.13. Schematic representation of the distortion of the A-sites in $NaTaO_3$ into the product $Ni_{0.5}TaO_3$ 173
Figure 8.14. The paraelectric and ferroelectric structures of $LiTaO_3$. 173
Figure 8.15. The structure of $Cu_{0.5}TaO_3$ (space group *Pmmm*) refined against neutron powder diffraction data. 175
Figure 8.16. X-ray powder diffraction data collected from the washed product of reaction between $NaTaO_3$ and $CoCl_2$ carried out at 370 ºC and 380 ºC during 1 period of 7 days. 177
Figure 8.17. X-ray powder diffraction data collected from the reaction mixture of $NaTaO_3$ and $CoCl_2$ after 3 periods of 7 days at 350 ºC. 178
Figure 9.1. Schematisation of the proposed Jahn-Teller distortion for the ruthenium centres in $LaSrNiRuO_4$ (from the configuration $(d_{z^2})^2(d_{xy/yz})^3(d_{x^2-y^2})^1(d_{xy})^0$ to the configuration $(d_{z^2})^2(d_{xz+yz})^2(d_{x^2-y^2})^2(d_{xz-yz})^0(d_{xy})^0$). The expected structural distortion for a sheet of apex-linked NiO_4 and RuO_4 squares is shown at the right. 183

Appendix 4: Table of Tables

Table 2.1: Detector banks following the POLARIS upgrade. 33
Table 3.1. Lattice parameters and Ni/Ru atomic fractions in the structural model of $LaSrNiRuO_6$ in space group $P2_1/n$ refined against X-Ray powder diffraction data of a slow-cooled and a quenched sample. 48
Table 3.2. Summary of results from thermogravimetric analysis of slow-cooled and quenched $LaSrNiRuO_6$ samples. 49
Table 3.3. Ni/Ru atomic fractions in the structural model of $LaSrNiRuO_6$ refined against X-ray powder diffraction data of the 'SC-Q' sample. 52
Table 3.4. Comparison of the refined lattice parameters of the structural model of $LaSrNiRuO_6$ in space group $P2_1/n$ against X-ray powder diffraction data collected from the slow cooled and quenched samples. 53
Table 3.5. Calculated size and microstructural isotropic strain for slow-cooled and quenched $LaSrNiRuO_6$ samples. 54
Table 4.1. Estimated fractions of reduced product and unreacted starting material in SC-R and Q-R calculated from the relative intensity of the main peaks of each phase. 64
Table 4.2. Summary of the thermogravimetric data collected during reduction and oxidation of the SC-R and Q-R $LaSrNiRuO_{6-x}$ products. 69
Table 4.3. Comparison of the thermogravimetric data collected from the SC-R sample against the calculated values for $LaSrNiRuO_4$ 75
Table 5.1. Summary of the thermogravimetric data collected during reduction and oxidation of the Q-R $LaSrNiRuO_{6-x}$ product. 82
Table 5.2. The $I2/m$ structural model of $LaSrNiRuO_4$ refined against X-ray powder diffraction data. 84
Table 5.3. Structural parameters of $LaSrNiRuO_4$ refined against neutron powder diffraction data collected at 300 K. 87
Table 5.4. The magnetic structure of $LaSrNiRuO_4$ refined from neutron powder diffraction data collected at 5 K. 91
Table 5.5. Selected bond lengths and angles from the refined structures of $LaSrNiRuO_4$ at 300 K and 5 K. 91
Table 5.6. Structural parameters of $LaSrNiRuO_4$ refined against neutron powder diffraction data collected at 5 K. 93

Table 5.7. Energies computed for the ferromagnetic, and C-type and A-type antiferromagnetic spin models of $LaSrNiRuO_4$. 95
Table 5.8. Average M-O bond lengths in $LaSrNiRuO_4$ and $SrFe_{0.5}Ru_{0.5}O_2$ at 300 K.[39] ... 98
Table 6.1. Lattice parameters and weight fractions of the two cubic phases of a model based on $SrVO_3$ and $SrTiO_3$ refined against laboratory X-ray powder diffraction data collected from the $SrV_{0.95}Ti_{0.05}O_3$ C and A samples. The label '1' corresponds to the majority phase. 108
Table 6.2. Structural parameters refined against synchrotron X-ray powder diffraction data collected from the C-R reduction product. 111
Table 6.3. Structural parameters refined against synchrotron X-ray powder diffraction data collected from the A-R reduction product. 113
Table 6.4. Summary of the thermogravimetric data collected during oxidation of the C-R and A-R reduction products in combination with the results from X-ray powder diffraction of Figure 6.7 and Figure 6.8. 116
Table 6.5. Average vanadium oxidation state in the C-R and A-R reduction products from manganometric titration. 118
Table 6.6. Structural parameters from the refinement of the C-R reduction product against neutron powder diffraction data collected at 298 K. 122
Table 6.7. Structural parameters from the refinement of the $SrVO_2H$ sample against neutron powder diffraction data collected at 298 K. 123
Table 7.1. Lattice parameters and weight fractions of the two cubic phases of a model based on $SrVO_3$ and $SrTiO_3$ refined against laboratory X-ray powder diffraction data collected from the $SrV_{0.95}Ti_{0.05}O_3$ C and A samples. The label '1' corresponds to the majority phase. 136
Table 7.2. Lattice parameters and weight fractions of the two cubic phases of a model based on $SrVO_3$ and $SrTiO_3$ refined against synchrotron X-ray powder diffraction data (λ = 0.8259 Å) collected from the $SrV_{0.95}Ti_{0.05}O_3$ C and A samples. The label '1' corresponds to the majority phase 138
Table 7.3. Summary of results from refinement of the $SrV_{0.95}Ti_{0.05}O_3$ C-1550 sample. . 140
Table 7.4. Summary of results from refinement of the $SrV_{0.95}Ti_{0.05}O_3$ C-1525 sample. . 141
Table 7.5. Lattice parameters and weight fractions of the cubic phases refined for the arc-melt $SrV_{0.95}Ti_{0.05}O_3$ A_1 and A_1-SC samples. The label '1' corresponds to the majority phase. 149

Table 8.1. Structure of $Ni_{0.5}TaO_3$ refined against neutron powder diffraction data collected at 298 K using the D2B instrument, ILL neutron source. 162
Table 8.2. Selected bond lengths, angles and bond valence parameters (Section 2.9) from the refined structure of $Ni_{0.5}TaO_3$ at 298 K. 163
Table 8.3. Structure of $Cu_{0.5}TaO_3$ refined against neutron powder diffraction data collected at 298 K using the D2B instrument, ILL neutron source. 167
Table 8.4. Selected bond lengths, angles and bond valence sums (Section 2.9) from the refined structure of $Cu_{0.5}TaO_3$ at 298 K.....168